

Constitutive modeling of female pelvic floor dysfunctions and reconstructive surgeries using prosthetic mesh implants

Von der Fakultät für Ingenieurwissenschaften,
Abteilung Bauwissenschaften
der Universität Duisburg-Essen
zur Erlangung des akademischen Grades
Doktor-Ingenieur
genehmigte Dissertation

von

Aroj Bhattarai, M.Sc.

Hauptberichter: Prof. Dr.-Ing. habil. J. Schröder
Betreuer: Prof. Dr.-Ing. M. Staat
Korreferent: Univ.-Prof. Dr.-Ing. T. Ricken

Tag der Einreichung: 13. June 2018
Tag der mündlichen Prüfung: 23. November 2018

Fakultät für Ingenieurwissenschaften,
Abteilung Bauwissenschaften
der Universität Duisburg-Essen
Institut für Mechanik
Prof. Dr.-Ing. habil. J. Schröder

Herausgeber:

Prof. Dr.-Ing. habil. J. Schröder

Organisation und Verwaltung:

Prof. Dr.-Ing. habil. J. Schröder
Institut für Mechanik
Fakultät für Ingenieurwissenschaften
Abteilung Bauwissenschaften
Universität Duisburg-Essen
Universitätsstraße 15
45141 Essen
Tel.: 0201 / 183 - 2682
Fax.: 0201 / 183 - 2680

© Aroj Bhattarai
Biomechanics Laboratory
Institute of Bioengineering
FH Aachen, Campus Jülich
Heinrich-Mußmann-Straße 1
52428 Jülich

Alle Rechte, insbesondere das der Übersetzung in fremde Sprachen, vorbehalten. Ohne Genehmigung des Autors ist es nicht gestattet, dieses Heft ganz oder teilweise auf fotomechanischem Wege (Fotokopie, Mikrokopie), elektronischem oder sonstigen Wegen zu vervielfältigen.

ISBN-10 3-9818074-8-0
ISBN-13 978-3-9818074-8-6
EAN 9783981807486

Preface

The work presented in this thesis has been written while working as a research assistant at the Biomechanics Laboratory, FH Aachen University of Applied Sciences under the supervision of Prof. Dr.-Ing. Manfred Staat and in cooperation with Prof. Dr.-Ing. habil. Jörg Schröder, the director of Institute for Mechanics at the University of Duisburg-Essen. For this work, I have been financially supported by the research project BINGO (03FH073PX2): "Optimierung des Systems Netzimplantat-Beckenboden zur therapeutischen Gewebeverstärkung nach der Integraltheorie" (2013–2015) by the German Federal Ministry of Education and Research.

Working as a PhD candidate/research associate in the Biomechanics Lab, FH Aachen was a magnificent experience to me. Though this dissertation is an individual work, this multi-disciplinary research would not have been possible without the precious guidance and support from several personalities and organizations. Here is a small tribute and my heart-full gratitude to them.

Firstly, I would like to express my sincere gratitude to Prof. Dr.-Ing. Manfred Staat for introducing me to the Biomechanics and nonlinear mechanics. His continuous supervision, limitless patience and support, from the preliminary to the concluding level enabled me to develop an understanding of the topic, build up confidence and shape up my academic career. Moreover, I am also grateful to Prof. Dr.-Ing. habil. Jörg Schröder (University of Duisburg-Essen) and the member of the doctorate committee for their interest in my research and providing me the opportunity to present and defend it.

I wish to express my deepest gratitude to Univ.-Prof. Dr. Mircea Constantin Sora (Sigmund Freud University Vienna, Austria) for his valuable efforts on plastination of the female pelvic floor and providing the computer models for numerical studies. I am contented with the supports of the experts, Dr.-Ing. Boris Obolenski, Axel Dievernich, Dipl.-Ing. Manfred Grewe and Dr.-Ing. Andreas Müllen from the industrial project partner FEG Textiltechnik mbH, Aachen, Germany for providing the prostheses, their experimental data and regular discussions that help to shape the research work. Furthermore, I am obliged to the surgeons Univ.-Prof. Dr. med. Ruth Kirschner-Hermanns and Dr. med. Ralf Anding from the co-partner University Hospital Bonn, Germany for discussions on clinical issues. In addition, I thank PD Dr. med. Nils Andreas Krämer, (RWTH University Hospital Aachen, Germany) and Prof. Dr. med. sc. Dr. med. Peter Emanuel Papa Petros (University of NSW Sydney, Australia) for their permissions to use some beautiful medical images to illustrate the numerical results of the thesis.

Likewise, I would like to acknowledge my colleagues at the institute, Dipl.-Ing. Karl-Heinz Gatzweiler, Dipl.-Ing. Andreas Horbach, Dr.-Ing. Ralf Frotscher, Dr.-Ing. Minh Tuan Duong, Dr.-Ing. Ngoc Trinh Tran and Alexander Jung, M.Sc. and Stephanie Kahmann, M.Sc. at the Biomechanics Lab. Their support on technical aspects, experimental setup (construction and data analysis), numerical calculations, outstanding encouragement and pleasant working environment is very much appreciated. In this regard, I am also thankful to the students Christian Halbauer, M.Sc., Viola Gruben, M.Sc., and Medisa Jabbari, M.Sc., for their help with experiments and finite element simulations. I wish to express my deepest gratitude to Misses Angela Laabs and Misses Petra Rupp Couty for helping me

know-how to live in Germany. Similarly, I would like to acknowledge Dr.-techn. Bishoksan Kafle for his regular advices, encouragement and prompt responses to queries along the journey of my PhD.

Lastly, but not the least, I am indebted to my parents, family and friends for continuous encouragement and understanding in all aspects of my life and to God, who made things possible.

Jülich, in November 2018

Aroj Bhattarai

This dissertation is dedicated

to

my parents, Mr. Mukunda Bahadur Bhattarai, Mrs. Maiya Devi Arjel (Bhattarai) and
my family for their immense love

and to

Prof. Dr.-Ing. Manfred Staat (FH Aachen University of Applied Sciences) and
Dr.-Ing. Rainer Schlebusch (Technical University of Dresden) for encouraging me
to build my motivation towards Computational Mechanics.

Abstract

Female pelvic floor dysfunctions (PFDs) such as incontinence and prolapse are observed in multiparous elderly females caused by denervation injuries during childbirth and progressive tissue remodeling after menopause. With continuously increasing average life expectancy, these disorders have become an important public health issue that require high costs for the treatment and a standardized study. Minimally invasive surgery has become a more frequent repair procedure for which more than 20 million implants are implanted worldwide every year. However, serious postoperative mesh relative complications are reported.

This thesis reviews the static, functional and dynamic anatomy of the female pelvic floor. A detail methodology to construct a realistic computer model from sheet plastination of a female cadaver pelvic floor has been described. Based on the published literature and multi-disciplinary communication with surgeons and urologist, a most complete form of 3D finite element (FE) model has been constructed, which considers smoothed NURBS based surfaces for frictionless contacts between organs and internal self-contact of the hollow organs. Further, an isotropic, hyperelastic, incompressible multiscale modeling of the soft connective tissues is adopted. In addition, transversely isotropic and non-linear Humphrey's constitutive model has been implemented to describe the passive stretching of the pelvic skeletal muscle without neural excitation. Similarly, for the experimented surgical meshes with different pore characteristics and stress-strain curves, linearly elastic orthotropic and non-linear hyperelastic models are fitted and used in the numerical study. Various FE analyses are performed to investigate pathophysiological situations and surgical treatments using mesh implants to compare their biofunctionality and to optimize the preferred surgery. Hence, the presented models and the modeling approaches included in this thesis facilitate the work of surgeons and urologists by a biomechanical study of female PFDs.

Zusammenfassung

Weibliche Beckenbodendysfunktionen (PFDs) wie Inkontinenz und Prolaps werden bei mehrgebärende älteren Frauen beobachtet, die durch Denervierungsverletzungen während der Geburt und progressiven Gewebeumbau nach der Menopause verursacht werden. Mit einer kontinuierlich steigenden durchschnittlichen Lebenserwartung sind diese Erkrankungen zu einem wichtigen Problem der öffentlichen Gesundheit geworden, das hohe Behandlungskosten und eine standardisierte Studie erfordert. Die minimal-invasive Chirurgie ist zu einem häufigeren Reparaturverfahren geworden, bei dem jedes Jahr mehr als 20 Millionen Implantate weltweit implantiert werden. Es werden jedoch schwerwiegende postoperative Netzkomplicationen berichtet.

Diese Arbeit untersucht die statische, funktionelle und dynamische Anatomie des weiblichen Beckenbodens. Eine detaillierte Methodik zur Konstruktion eines realistischen Computermodells aus der Schichtplastination eines weiblichen Beckenbodens wird beschrieben. Basierend auf der veröffentlichten Literatur und der multidisziplinären Kommunikation mit Chirurgen und Urologen wurde eine vollständige Form des 3D Finite Element (FE) Modells erstellt, wobei die geglätteten NURBS-basierten Oberflächen für reibungsfreien Kontakt zwischen Organen und den inneren Eigenkontakt der Hohlorgane berücksichtigt. Ferner wird eine isotrope, hyperelastische, inkompressible Multiskalenmodellierung des weichen Bindegewebes verwendet. Außerdem wurde ein transversal isotropes und nichtlineares konstitutives Modell von Humphrey implementiert, um die passive Dehnung des Becken-Skelettmuskels ohne neurale Erregung zu beschreiben. In ähnlicher Weise werden für die experimentellen chirurgischen Netze mit unterschiedlichen Poreneigenschaften und Spannungs-Dehnungs-Kurven linear elastische orthotrope und nichtlineare hyperelastische Modelle eingesetzt und in den numerischen Studien verwendet. Verschiedene FE-Analysen werden durchgeführt, um pathophysiologische Situationen und chirurgische Behandlungen mit Netzimplantaten zu untersuchen, um ihre Biofunktionalität zu vergleichen und die bevorzugte Operation zu optimieren. Die in dieser Arbeit vorgestellten Modelle und Modellierungsansätze erleichtern somit die Arbeit von Chirurgen und Urologen durch eine biomechanische Untersuchung weiblicher PFDs.

Abbreviations

PFD	Pelvic Floor Dysfunction
SUI	Stress Urinary Incontinence
POP	Pelvic Organ Prolapse
FEM	Finite Element Method
UVJ	Urethro-Vesical Junction
FBGCs	Foreign Body Giant Cells
ECM	Extracellular Matrix
MRI	Medical Resonance Imaging
CT	Computed Tomography
US	Ultrasound
SEF	Strain Energy Function
RVE	Representative Volume Element
SE	Series Elastic Element
CE	Contractile Element
PE	Passive Parallel Element
PRS	DynaMesh [®] -PRS Soft
PRP	DynaMesh [®] -PRP Soft
CESA	DynaMesh [®] -CESA
PVDF	Polyvinylidendifluorid
PP	Polypropylene
GMC	Gelatin-Mesh Compound
PCL	Pubococcygeal line

Notations

$a, b, \dots A, B, \dots \alpha, \beta, \psi, \dots$	Scalars
\mathbf{n}	Normal unit vector
$\mathbf{F}, \mathbf{C}, \mathbf{E}, \dots$	Second order tensors
$\overline{\mathbf{C}}$	Fourth order constitutive tensor
σ	Cauchy stress
\mathbf{P}	First Piola-Kirchhoff stress
\mathbf{S}	Second Piola-Kirchhoff stress
ϵ	Infinitesimal Strain
\mathbf{E}	Green-Lagrange Strain
\mathbf{C}, \mathbf{B}	Right, Left Cauchy-Green strain
\mathbf{F}, \mathbf{I}	Deformation gradient, Identity tensor
$\mathbf{U}, \mathbf{V}, \mathbf{R}$	Right material stretch, left spatial, rotation tensor
$\lambda_i, i = 1, 2, 3$	Principal stretches
$I_i, i = 1, 2, 3$	Principal invariants of tensor
tr	Trace of a tensor
δ_{ij}	Kronecker symbol
E_L, E_T	Longitudinal and transverse Young's modulus of elasticity
ν	Poisson's ratio
G	Shear modulus
C_{10}, C_{01}, C_{20}	Hyperelastic material parameters
f_i	Volume fractions
J	Jacobian of a motion
det	Determinant of a tensor
W, ψ	Strain energy density function
p	Hydrostatic stress
$a_i, A_{ij}, \overline{C}_{ijkl}$	Index notation
$\mathbf{e}_1 \cdot \mathbf{e}_1 = 1$	Simple contraction or inner product
$a \otimes b = \mathbf{C}, C_{ij} = a_i b_j$	Tensor or dyadic product
$\mathbf{A}:\mathbf{B} = C, C = A_{ij} B_{ij}$	Double contraction or double inner product
$\overline{\otimes} = \frac{1}{2}(\otimes + \overline{\otimes})$	Symmetrized (squared) tensor product
\mathbf{T}^{-1}	Inverse of a tensor \mathbf{T}
\mathbf{T}^T	Transpose of a tensor \mathbf{T}
$\frac{\partial}{\partial \mathbf{C}}$	Partial derivative with respect to \mathbf{C}
$\frac{\partial}{\partial t}$	Partial derivative with respect to time (t)
T_0^M, a, A, b, c, D	Humphrey muscle model parameters
$\dot{\alpha}(t)$	Time dependent muscle activation function
$u(t)$	Muscle neural excitation
$\tau_{\text{rise}}, \tau_{\text{fall}}$	Time constants for activation and deactivation of muscle
f_L^{CE}	Force-length relation of skeletal muscle
f_V^{CE}	Force-velocity relation of skeletal muscle

Contents

1	Introduction	1
2	Female Pelvic Floor: Anatomy, Functions and Dysfunctions	9
2.1	Static anatomy of the female pelvic floor	9
2.1.1	Bony pelvis	9
2.1.2	Organs of the true pelvis	11
2.1.3	Muscles	13
2.1.4	Pelvic fasciae	16
2.1.5	Ligaments	19
2.2	Functional anatomy and pelvic floor dynamics	21
2.2.1	Micturition-continenence and urethral closure	22
2.2.2	Defecation-continenence and anorectal closure	25
2.3	Pelvic floor dysfunctions	26
2.3.1	Urinary incontinenence	26
2.3.2	Fecal incontinenence	27
2.3.3	Pelvic organ prolapse	27
2.4	Treatment of pelvic floor dysfunction	30
2.4.1	Non-surgical corrections	30
2.4.2	Reconstructive surgeries	32
3	Development of Computational Model Using Plastinates	35
3.1	Pelvic floor imaging techniques	35
3.2	Plastination technique	35
3.2.1	Benefits of plastination	37
3.2.2	Plastination methodology for 3D reconstruction of female pelvis	37
3.3	Volume rendered computer model from E12 plastinated slices	39
3.4	NURBS-based computational model	40
3.5	Computational model validation and adjustment	42
3.5.1	Comparison with anatomy	43
3.5.2	Shrinkage during plastination	45
3.5.3	Scaled model in WinSURF	45
3.5.4	Scale adjustment on the finite element mesh	46

3.6	Endopelvic fascia model as a single unit	46
4	Mathematical Modeling of Pelvic Tissues	47
4.1	Histomorphological study of pelvic structures	47
4.1.1	Anterior compartment: ureter, bladder and urethra	47
4.1.2	Middle compartment: uterus and vagina	48
4.1.3	Posterior compartment: rectum and anal canal	48
4.1.4	Ligaments	49
4.1.5	Endopelvic fascia	50
4.2	Finite deformation of pelvic tissues	52
4.2.1	Uniaxial tensile tests on female pelvic tissues	53
4.2.2	Non-linear strain energy	54
4.2.3	Parameter identification	61
4.3	Modeling of the endopelvic fascia	62
4.3.1	Fascia modeling according to collagen content	62
4.4	Fascia modeling according to tissue constituents: mixture theory	64
4.5	Modeling of tissue weakening: progressive remodeling of stronger collagen	68
4.6	Passive mechanical modeling of skeletal pelvic floor muscle	70
4.6.1	Passive stress component	71
4.6.2	Material tangent moduli for passive skeletal muscle	73
4.6.3	Implementation of anisotropic muscle model into a finite element framework	74
5	Anisotropic Modeling of Levator Ani Muscle	77
5.1	3D female pelvic floor muscle geometry	77
5.2	Boundary conditions	78
5.3	Finite element simulation of passive stretching of levator ani muscle	78
5.4	Limitations of the constitutive modeling	80
5.5	Active muscle contraction	81
5.5.1	Muscle activation simulation	82
5.5.2	Application to the pelvic muscle: future outlook	83
5.5.3	Calculation of the contractile stretch	85
6	Prosthetic Implants to Treat Pelvic Floor Disorders	91

6.1	Prosthetic meshes	91
6.1.1	An ideal polymer: polyvinylidene vs polypropylene?	91
6.1.2	Textile structures	92
6.1.3	Textile porosity	92
6.2	Specimen preparation and test set up	92
6.3	Mechanics of dry textiles	94
6.3.1	Uniaxial tensile test on rectangular pore mesh	94
6.3.2	Optical strain measurement	94
6.4	Mechanics of tissue surrogate-mesh specimen	97
6.4.1	Photoelastic uniaxial tensile test	97
6.4.2	Biaxial inflation test	99
6.5	Clinical comparisons	99
6.5.1	Mesh complications	100
7	Numerical Study of Stress Urinary Incontinence	107
7.1	Endopelvic fascia as a single unit	107
7.1.1	Pelvic fascia constituents	107
7.1.2	Finite element mesh of the female pelvic floor	108
7.1.3	Boundary conditions	108
7.2	Finite element simulations of SUI	109
7.2.1	Mobility of the urethro-vesical junction	110
7.2.2	Q-tip test for SUI	111
7.2.3	Levator plate angulation	112
7.2.4	Important discussions	112
8	Vaginal Vault Prolapse Correction	115
8.1	Sacrocolpopexy implant	115
8.2	Sacrocolpopexy implant in the pelvic floor model	116
8.3	Mechanical modeling of mesh implants	116
8.3.1	Parameters identification	117
8.4	Mesh implant and suture position	117
8.5	Prolapse definition	118
8.5.1	Surgical reconstruction technique	118
8.5.2	Biomechanical simulation of prosthesis to support weak pelvic tissues	119

8.5.3	Computational comparison of sacrocolpopexy with pectopexy technique	121
8.5.4	Numerical simulation after pectopexy surgery	122
9	Conclusions and Outlook	129
	References	135

List of Tables

2.1	Properties of ligaments to connect pelvic bone.	19
2.2	Surgical treatment procedures for various types of female PFDs.	33
3.1	Characteristics of different medical imaging techniques.	36
3.2	Pelvic bone measurement in females with and without pelvic floor disorders. Data are presented as mean \pm standard deviation. All values are in centimeters unless otherwise indicated.	44
4.1	Experimental studies performed to characterize the biomechanical behavior of female pelvic floor soft tissues.	56
4.2	Isotropic hyperelastic material models to describe incompressible soft tissue behavior.	60
4.3	Biomechanical properties of female pelvic structures. The stress-strain curves are adopted from experiment published from different literature listed below and is fitted with three term polynomial functions using the Hyperfit software.	61
4.4	Biomechanical properties of the endoplevic fascia. The stress-strain curves is adopted from experiments published in the KIRILOVA ET AL. [148] and is fitted with three term polynomial function using the Hyperfit software.	64
4.5	Biomechanical properties of endoplevic fascia constituents.	68
7.1	Comparison of the measured urethro-vesical junction movement ($UVJ = \sqrt{(VUVJ)^2 + (HUVJ)^2}$).	113
7.2	Comparison of the angle between the midpubic line with the bladder neck (α). The difference of the angle alpha between healthy and SUI simulation is computed as $\Delta\alpha_{\text{Valsalva}} = \alpha_{\text{SUI}} - \alpha_{\text{healthy}}$	114
8.1	Mechanical properties of prosthetic mesh implants fitted with elastic orthotropic and hyperelastic material behavior using eqn. (4.21) and Fig. 8.3.	118
8.2	Measurement of the bladder base (P_{Bb}), vaginal cuff resting position (VCRP), urethral (U_r) and vaginal axis (V_{ax}) during rest state and Valsalva maneuver simulation for pectopexy repair using DynaMesh [®] -PRP soft, Gynemesh [®] and Artisyn [®] (BHATTARAI AND STAAT [32]). Distances of the organs are measured as the perpendicular distance with respect to the PCL line and the angles are measured with respect to the vertical axis. Positive values of P_{Bb} and P_{VC} represent the perpendicular distance measured above the PCL line and negative values represent the distance measured below the PCL line. SI represents the direction of the vaginal axis towards I th sacrum bone.	123

8.3	Measurements of the bladder base (P_{Bb} in mm) and urethral axis (Ur in degrees) during Valsalva maneuver simulation for sacrocolpopexy and pectopexy repair using DynaMesh [®] -PRS soft, DynaMesh [®] -PRP soft, Gynemesh [®] and Artisyn [®] . Sign convention for P_{Bb} is same as in Table 8.2.	126
-----	---	-----

List of Figures

2.1	Sagittal anatomic representation of the female pelvic floor showing three anatomic compartments inside the bony pelvis. [Source: https://www.diagramcharts101.com]	10
2.2	a) Female pelvic bone (SOAMES [285]) b) Female true and false pelvis [Source: http://home.comcast.net/~wnor/pelvis.html].	10
2.3	Anatomy of the female urinary system. [Source: http://slideplayer.com/slide/9325705/]	11
2.4	Vaginal axis in a non-pathological state (FUNT ET AL. [105]).	12
2.5	This schematic shows the structure of the skeletal muscles in the female pelvic floor. Pelvic organs are supported by the pelvic diaphragm (green dotted line), sphincter and perineal muscles shown in a) cranial (superior) view (OTCENASEK ET AL. [218]) and b) caudal (inferior) view [Source: https://www.pinterest.com/pin/196751077454591498/]. TP=transverse perinei.	13
2.6	a) Superior view of the female pelvic floor showing the pelvic muscles, bony pelvis and parietal fascia coverings (orange, purple and green) (OTCENASEK ET AL. [218]). b) Mid-sagittal section of the female pelvic floor showing the anatomy and boundaries of the visceral fasciae (OTCENASEK ET AL. [218]). Abbreviations are described in the beginning of the thesis.	17
2.7	Detail illustration of DeLancey's three level of endopelvic fascia (BARBER [17]).	18
2.8	Schematic diagram of the visceral ligaments showing the three parts of the USL and its relation with the cardinal ligament (VU ET AL. [318]).	20
2.9	a) The schema of the cortex of the brain regulates closure and opening mechanisms by engaging all the muscles, nerves, ligaments and tissues (PETROS [239]). b) Superimposed tracings of radiographs in a healthy bladder function. Downward movement of the bladder base, obliteration of the posterior urethro-vesical angle and dilatation of the urethra during micturition. (ROBERTS [259]).	22
2.10	Schematic representation of the urethral and the bladder base support by various muscles and their effect during rest and micturition. At rest, the muscles contracts to elevate the UVJ, whereas, during micturition, muscles relaxes to descent the UVJ wide open as funnel (ROBERTS [259]).	24
3.1	Liver parenchyma images of a 8.5-year-old girl shown in a) US, b) CT and c) MRI (NIEVELSTEIN ET AL. [207]). LHV= left hepatic vein.	35
3.2	Flow chart schema of plastination technique.	38
3.3	E12 slice of female pelvis.	39

3.4	a)-g) E12 plastinated slices of female pelvis at different positions along caudocranial direction. Slice numbers (6-18) are provided on the right side of the figures. Vaginal outer surface is outlined by green curve. h) 3D geometry of the female pelvis showing organs, right pubic and coccyx-sacrum bone. The horizontal planes (gray) are the slice planes corresponding to E12 plastinated slices (a-g).	41
3.5	a) Computer model of the female pelvic floor including bony pelvis, pelvic viscera, muscles, ligaments and nerves. (BHATTARAI ET AL. [24], FEIL AND SORA [92]).	41
3.6	Preliminary model of the female pelvic organs right after plastination shown in Salome software, b) Magnified surface of urethra, vagina and pubourethral ligament with highly distorted triangles.	42
3.7	a,b) NURBS based smoother, regular and hollow female pelvic organ geometries, c) corresponding FE meshes generated in Salome software, d) Magnified meshes of urethra, vagina and pubourethral ligament with repaired aspect ratio.	43
3.8	Measurement of the distance between two points A and B in a) 2D and b) 3D space.	44
3.9	Measurement of the distance between two points A and B in a) 2D and b) 3D space.	45
4.1	Histologic cross section of the ureter stained with hematoxylin and eosin. [Source: University of Wisconsin Medical School-Department of Anatomy.]	48
4.2	The histological layers of a) the uterus, and b) the vagina.	49
4.3	The histological layers of a) the rectum [Source: Deltagen.Inc], and b) the anorectal junction [Source: Studyblue, Florida International University]. . .	49
4.4	Histomorphological analysis of the USL (a,b) and the CL (c). a) trichrome staining of the deep USL showing mainly nerve fibers (n), adipose tissue (ad), and a few vessels (v) (RAMANAH ET AL. [248]) b) hematoxylin staining (x100) of the superficial (cervical third) portion of USL showing considerable amount of smooth muscle (sm) cells and connective tissue (ct) (GABRIEL ET AL. [106]) c) trichrome staining of the CL showing mainly vessels (RAMANAH ET AL. [248]).	50

- 4.5 a) Histology of the female pelvic parietal fascia. Panel **A** shows topographical anatomy of pelvic tissues with HE staining. Panel **C-F** shows elastic fibers near bladder, vagina, rectum (asterisk=smooth muscle) and levator ani muscle, respectively with aldehyde-fuchsin staining (HIRATA ET AL. [118]). b) Histology of the visceral fascia at the level of lower paracolpium. Panel **A** shows topographical anatomy of pelvic tissues with HE staining. Panel **B** (star encircled in panel **A**) shows smooth muscle bundles of endopelvic fascia (EPF) with immunohistochemistry. Panel **C** shows elastic fibers (black) in the conjoint smooth muscle bundle in panel **B** stained with with elastica-Masson. Panel **D** shows nerves in the paracolpium or mesorectum with immunohistochemistry. (SASAKI ET AL. [270]). 51
- 4.6 Nonlinear stress-stretch response of soft biological tissues specimen in uniaxial tension showing the configuration of collagen fibers. Elastin is the major load bearing component at small stretch or toe region. Collagen fibers aligns towards loading direction in heel region and progressively recruits at large stretch (linear region) leading a J-shaped stress-stretch curve until failure. 52
- 4.7 Uniaxial stress-strain/stretch curves of female pelvic floor tissues a) Organs (RUBOD ET AL. [266]), b) Bladder (MARTINS ET AL. [192]), c) Ligaments (RIVAUX ET AL. [256]), and d) Fascia (KIRILOVA ET AL. [148]). 55
- 4.8 Fitting of pelvic floor organs ligaments, muscle and fascia using a) Ogden and Yeoh (BRANDÃO ET AL. [40]), b) three term Signorini hyperelastic constitutive model (BHATTARAI AND STAAT [29]). 62
- 4.9 a) Schematic representation of varying tissue density along the vaginal length. The distal pelvic viscera is supported by denser fibrous tissue support, while the mid and proximal visceral fascia is elastic with less collagen and more smooth muscle and elastin (PETROS [239]). b) Stress-stretch curve fit of elastin and collagen digested arterial tissue (NGUYEN ET AL. [206]) 63
- 4.10 Two constituent representation of a) the Voigt iso-strain and b) the Reuss iso-stress model and c) shows the rotation of axes from longitudinal system from 1-2 to X-Y. 65
- 4.11 Fitting of the nominal stress (P) vs stretch (λ) curve for a) elastin-collagen fascia applying a 0.13 mm/s elongation rate (KIRILOVA ET AL. [148]), b) adipose tissue applying strain at a rate of 5 $\mu\text{m/s}$ up to 30% strain (ALKHOULI ET AL. [4]) and c) smooth muscle without active contractility (elongation/strain rate not stated) is assumed during micturition (BUSH ET AL. [47]) using three term polynomial strain energy function (eqn. 4.21). 67

4.12	a) Stress-strain curves of vaginal tissue from nulliparous and parous rhesus macaques showing significant differences in tensile strength and tangent modulus (FEOLA ET AL. [93]), b) Progressive tissue impairment represented by reduced material stiffness. 0% Impairment represents healthy tissue state without any weakening.	69
5.1	a) Sagittal section of the female pelvic muscle model created from the data set of the plastinated reconstruction. ICM = iliococcygeus muscle, PCM = pubococcygeus muscle, PRM = puborectalis muscle, EAS = external anal sphincter, CCM = coccygeus muscle, ANOC = anococcygeal ligament, Ps = pubic symphysis, and Obt Int = obturator internus muscle. b) Sagittal section of the 3D finite element mesh of the levator ani muscle with two nodes EASc and ILISfix to compare muscle displacement and stress (BHATTARAI ET AL. [27]).	77
5.2	MR images showing levator ani muscle highlighted by the a) blue points at rest b) the red points during Valsalva maneuver. c) Anterior view of the finite elasticity simulations results showing the levator ani at rest (wire-frame) and under Valsalva (gold surface (NOAKES ET AL. [210])).	79
5.3	a) FE simulation of the levator ani displacement due to an IAP. (a) Undeformed state (gray wireframe) and displaced levator ani muscle (solid): anterior view. (b) Stress distribution along the muscle. The larger principal stress in the simulation is, $\sigma_1^{\max} = 0.03866$ MPa: superior view (BHATTARAI ET AL. [27]).	79
5.4	Principal stress variation at two points a) EASc: b) ILISfix (BHATTARAI ET AL. [26], BHATTARAI ET AL. [27]).	80
5.5	A simple bar mesh of linear tetrahedrons showing dimensions and boundary conditions.	83
5.6	a) Displacement (DY) of the bar along Y-axis vs muscle activation, $\alpha \in [0, 1]$	83
5.7	FE simulation showing the von Mises stress distribution in the bar with fully activated fibres ($\alpha = 1$). The black dotted line represents the position of the undeformed bar length.	84
5.8	Schematic of the Hill-type three element muscle model.	84
5.9	Relation of $f_L^{\text{CE}}(\lambda^{\text{CE}})$ with fiber stretches for different proposed models (BÖL AND REESE [36], MCLEAN ET AL. [195], Present model = PATO AND AREIAS [225]).	87
5.10	Representation of the force-velocity function (BÖL AND REESE [36], present model = PATO AND AREIAS [225]).	88
6.1	a) Mesh specimen preparation for inflation (bulge) test: a) Schematic drawing of PVC plastic plate and mesh; b) Dynamesh [®] -PRS soft specimen with gelatin; c) Dynamesh [®] -CICAT specimen with gelatin (BHATTARAI AND STAAT [28]).	93

6.2	Synthetic mesh clamped to a) uniaxial tensile and b) bulge test machines (BHATTARAI AND STAAT [28]).	94
6.3	Average stress-stretch curves of different dry meshes loaded in longitudinal and transverse direction for different meshes: a) CICAT; b) SD; and c) PRS (BHATTARAI AND STAAT [28]).	95
6.4	a) Uniaxial tensile test on dry SD mesh using DIC technique; b) The SD mesh elongates only by 40% if stretched to the thicker fiber (longitudinal) direction. In contrast, if rotated by 90°, an elongation of almost 100% occurs; c) Change of mesh porosity (BHATTARAI AND STAAT [28]).	96
6.5	a) Lagrangian strains under loading in b) longitudinal and b) transverse fiber direction of an anisotropic PVDF hernia mesh. Strain ϵ_x is extension in load direction and ϵ_y is contraction (BHATTARAI AND STAAT [28]).	97
6.6	Uniaxial tensile test on GMC specimen. DPRS mesh along a) longitudinal direction (left: 80.89 N); b) transverse direction (right: slippage of fiber (tearing out a seam) at less force, 15.89 N); c) debonding of the CICAT mesh from the gelatin due to large transversal contraction and pore collapse at tensile force 60.404 N (BHATTARAI AND STAAT [28]).	98
6.7	Failure of tissue surrogate-mesh under biaxial inflation test: a) Gelatin-CICAT mesh; b) Gelatin-PRS mesh (BHATTARAI AND STAAT [28]).	99
6.8	Tissue response after suture repair. Histological analysis of explanted heavy weight polypropylene mesh using Masson's trichrome staining procedure (with permission from (CASEY [52])).	101
6.9	Abdominal hernia repair using mesh implant: a) MRI image showing mesh wrinkled after placed in the abdomen: superior view [with permission of N. A. Krämer]; b) Representation of the position of the wrinkled mesh in abdomen (anterior-lateral view) (BHATTARAI AND STAAT [28]).	103
6.10	Area change under uniaxial tensile test on SIS direct soft mesh. A_0 and A are the initial and current surface area of the mesh (BHATTARAI AND STAAT [28]).	104
7.1	The organs, fasciae (pink) and muscles are cut in the sagittal plane (BHATTARAI AND STAAT [29]). For comparison of the fascia geometry refer to (OTCENASEK ET AL. [218]). The angle α measures the angle between the midpubic line to the bladder neck. Levator plate angle (LPA) is an angle subtended by the initial take off portion of the iliococcygeus from the coccyx to a horizontal reference line. Ut=Uterus; R= Rectum; B=Bladder; PCF=pubocervical fascia; RVF=rectovaginal fascia; U=Urethra; V=Vagina.	108
7.2	Sagittal section of the 3D finite element mesh showing a) pubocervical fascia (PCF) and rectovaginal fascia (RVF), ligaments and perineal structures, b) FE mesh loaded with intra-abdominal pressure (IAP). Endopelvic fascia is separated with different amount of elastin and collagen constituents, blue (elastin rich) and pink (collagen rich) (BHATTARAI AND STAAT [29]).	109

- 7.3 Sagittal section of a 3D pelvic model with results of the FE simulation showing the vertical movement of the pelvic floor during Valsalva manoeuvre for a) healthy tissues and b) 95% weakened ligaments and fasciae (BHATTARAI AND STAAT [29]). Urethral axis (Ur) $> 30^\circ$ with vertical line resembles positive Q-tip test. A great vertical descent ($DZ=38.79$ mm) of the anal orifice is observed in a dynamic MRI in a SUI patient (EL-GHARIB ET AL. [108]). The vertical displacement of the anal orifice in the SUI calculation (Fig. 7.4b) is 40.83 mm. 110
- 7.4 X-ray examination of an asymptomatic female pelvic floor urethral angle a) $Ur_{(Rest)}$ at rest and b) $Ur_{(Mict)}$ during micturition (PETROS [238], BHATTARAI AND STAAT [29]). 111
- 7.5 Effects of tissue impairment (*reduced stiffness*) on the vertical movement of the UVJ for the impairment of a) all connective tissues (fasciae and ligaments) b) and caused by individually impaired ligaments. *Maximum organ dislocation is achieved due to weakness in fasciae rather than the ligaments* (BHATTARAI AND STAAT [29]). 112
- 7.6 Plot of increased fascia impairment (*reduced stiffness*) on a) urethral axis, Ur and b) movement of the UVJ, (α) (BHATTARAI AND STAAT [29]). . . . 112
- 7.7 FE simulation results showing the sagittal section of increased levator plate angulation (LPA, the angle between the horizontal line and the line formed by two points between levator plate insertion point to the coccyx bone and anorectal junction) from rest (wireframe) to Valsalva manoeuvre (solid) for SUI female. $\Delta LPA=LPA_{SUI}-LPA_{Rest} = 22.5^\circ$ is obtained between the rest (green) and during Valsalva manoeuvre (red) (BHATTARAI AND STAAT [29]).113
- 8.1 Dimensions of a standard DynaMesh[®]-PRS soft mesh implant with right red panel represents the higher magnification view of the red square on the black left panel showing PVDF polymer fibers using a digital microscope VHX-600 (Keyence, Japan) (BHATTARAI ET AL. [30]). 115
- 8.2 Sagittal section of the female pelvic floor showing a) the smoothed NURBS-based visualisation geometry and b) the 3D FE mesh for simulation generated from smoothed NURBS-based geometry. Mesh implant suspends the vaginal cuff after hysterectomy from the first sacral (S1) bone (BHATTARAI ET AL. [30]). Prom=Promontory; Imp=DynaMesh[®]-PRS soft implant; Obt = Obturator internus muscle; Umb=Umbilical ligament; B=Bladder; PS=Pubic symphysis; F=Endopelvic fascia; U=Urethra; V=Vagina; Pm=Perineal membrane; Pb=Perineal body; USL=Uterosacral ligament; CCM=Coccygeus muscle; R=Rectum; ICM=Iliococcygeus; PCM=Pubococcygeus; PRM=Puborectalis; ANOC=Anococcygeal raphe; EAS=External anal sphincter. 116

- 8.3 Uniaxial tensile Cauchy stress-stretch curves of DynaMesh[®]-PRS soft (with regular rectangular pores), Gynecare Gynemesh[®] Prolene soft and Ultrapro[®] (irregular hexagonal pores) mesh implants loaded in longitudinal (Long) and transversal (Trans) directions (BHATTARAI ET AL. [30]). The tensile tests data have been provided by FEG Textiltechnik mbH, Aachen, Germany as force-elongation data. 117
- 8.4 MRI of the pelvic floor from a symptomatic female showing organs a) at rest and b) movement during Valsalva maneuver (BHATTARAI ET AL. [30]). The PCL white line is drawn from the inferior border of the pubic symphysis to the last coccygeal joint. It is adopted as a reference line to compare the normal pelvic floor and the prolapse. Asterisk (*) illustrates the position of the vaginal cuff. Source: Dr. med. Ralf Anding. 119
- 8.5 Sagittal section of MRI sequences with well depicted mesh (shown by red arrows) connecting the extraperitoneal structures, the sacral promontory and the vaginal cuff (BHATTARAI ET AL. [30]). Source: Dr. med. Ralf Anding. 119
- 8.6 Finite element simulation of the weak female pelvic floor showing the pelvic organ movement a) before surgery (prolapse) and b) after sacrocolpopexy repair using DynaMesh[®]-PRS soft mesh implant suspended at S1 bone below promontory (BHATTARAI ET AL. [30]). Positions of the vaginal cuff, bladder and urethra are compared with respect to their movement (DZ in mm) in vertical direction during Valsalva maneuver. The change of the urethral axis is measured by angle $U_r(^{\circ})$ with vertical line. 120
- 8.7 Sagittal slices showing the distances of the bladder base (P_{Bb}) and the vaginal cuff (P_{Vc}) from the reference PCL line (red line) inside the pelvic cavity before surgery or prolapse (orange), and after sacrocolpopexy repair using DynaMesh[®] (green) and Gynemesh[®] (blue) suspended at S1 bone below promontory (BHATTARAI ET AL. [30]). 121
- 8.8 Sagittal section of the female pelvic floor showing the smoothed NURBS-based geometry with DynaMesh[®]-PRP soft implant (abbreviated as Imp) suspending the cervical stump after hysterectomy from the iliopectineal ligament. (BHATTARAI AND STAAT [32]) For other abbreviations, see Fig. 8.2. 122
- 8.9 Dimensions of a standard DynaMesh[®]-PRP soft mesh implant (BHATTARAI AND STAAT [32]). 123
- 8.10 Finite element simulation of the pectopexy surgery after hysterectomy at rest, R/w (0.5 kPa) using a) DynaMesh[®]-PRP Soft and b) Gynecare Gynemesh[®] PS Nonabsorbable Prolene Soft[®] mesh materials (BHATTARAI AND STAAT [32]). DISP DZ represents the displacement in the vertical direction from the undeformed state. VCRP represents the perpendicular distance of the vaginal cuff resting position from red PCL line and * is drawn in Fig. 8.10b due to short perpendicular distance of bladder base from PCL. 124

- 8.11 Finite element simulation of the pectopexy surgery after hysterectomy during Valsalva maneuver (4.5 kPa) using a) DynaMesh[®]-PRP Soft and b) Gynecare Gynemesh[®] PS Nonabsorbable Prolene Soft[®] c) Artisyn[®] mesh materials (BHATTARAI AND STAAT [32]). DISP DZ represents the displacement in the vertical direction from the undeformed state. 125
- 8.12 Finite element simulation results showing differences in the vaginal axis (blue arrow) after sacrocolpopexy (a-c) and pectopexy (d-f) treatment using the DynaMesh[®]-PRS (a), DynaMesh[®]-PRP (d), Gynemesh[®] (b, e) and Artisyn[®] (c, f) meshes. (a-c) shows complete and (d-f) shows partial hysterectomy (BHATTARAI AND STAAT [32]). The red PCL line is shown to visualize the position of the vaginal cuff after different prolapse repair technique. 127

1 Introduction

The structure of the female pelvic floor is an inter-related system of bony pelvis, muscles, fasciae and ligaments with multiple functions. Unlike male, the female pelvic floor sustains the pregnancy and facilitates the fetal descent during delivery. From conception to delivery, the pelvic muscles, the connective tissues in the cervix and in between the pelvic organs undergo remodeling and softening induced by hormonal changes that widens the way out for fetal descent during vaginal delivery (DOWNING AND SHERWOOD [82], ULDBJERG ET AL. [308]). Muscles normally regain shape and function within a range of few days to months (PESCHERS ET AL. [232], PETROS [235]). However, significant denervation injury of the pelvic floor musculature during childbirth stresses the soft vaginal hammock and the ligaments to support the pelvic organs (WALL ET AL. [319]). The 'Integral theory' suggests that the loose insertions of the striated pelvic muscles due to the depolymerization of the collagen fibrils of the hammock tissues ultimately fail to transmit the muscle contraction to the organs and implications are seen in the form of pelvic floor dysfunctions (PFDs) (PETROS AND ULMSTEN [234]). Pelvic organ prolapse, incontinence, sexual dysfunction are some of the dysfunctions which progress with menopause and age (LIN ET AL. [177]) which leads to a significant effect on the quality of social life.

Incontinence and pelvic organ prolapse often coexist and affect 50% of parous women (SUBAK ET AL. [293]) with 19% women having the lifetime risk of undergoing POP surgery by the age of 80 years (SMITH ET AL. [283]). An estimated 20-40% of the world's female population is affected by stress urinary incontinence (KANE AND NAGER [144]), and a large percentage of symptomatic women are reported from the United States of America (41%) and Europe (over 30%) (DIOKNO [80]). These estimates are different from the Asian findings which show a predominance of mixed urinary incontinence ($\approx 64\%$) (LAPITAN AND CHYE [168]). Though, multiparous old females are mostly reported with such symptoms, a larger percentage of reproductive and postmenopausal females are also affected attributing the most common reasons to be multiple pregnancies, ageing, obesity (MANT ET AL. [187], OLSEN ET AL. [215], SWIFT ET AL. [295]), fetal weight (SMITH ET AL. [283]), instrumental delivery (MACLENNAN ET AL. [180]) and connective tissue disorder (NORTON ET AL. [213]), or a combined effect of these factors. The prevalence of the pelvic floor dysfunction varies widely across studies with ethnicity (DELANCEY ET AL. [74]) and is difficult to determine: many women do not seek medical advice and treatment due to embarrassment and misunderstanding regarding treatment (DENG [76], ELENSKAIA ET AL. [86]). Specific obstetric risk factors of the pelvic organ prolapse remain unclear. Weakened or damaged pelvic support-suspension system is observed in the symptomatic females as a consequence of denervation injuries during delivery, prolonged second stage of labour and collagen-estrogen reduction in old ages.

Though, non-surgical treatment or conservative therapy methods such as Kegel exercise are still in practice, for PFDs that cannot be treated with non-surgical procedures, minimally invasive surgery (MIS) has become a more frequent and the safest repair procedure. These new treatments are more effective than their traditional counterparts, with a variety of benefits: improved anatomical outcome, higher quality of post-operation life, smaller or no abdominal cut, minimal scars, less tis-

sue damage, and shorter recovery time (GADONNEIX ET AL. [107], PRICE ET AL. [246], ROSS AND PRESTON [262]). Gaining popularity on MIS technique among surgeons, more than 20 million net implants are implanted worldwide every year to correct pelvic floor problems (KLINGE ET AL. [153]). However, numerous cases of postoperative complaints were reported to the US food and drug administration (FDA) against such restoration surgery (FDA [90], ZIMMERMAN [340]). Apart from the ability of the surgeon, the success of such treatment techniques depends on various factors such as adequate treatment, biocompatibility of the prosthesis material and sufficient information on the postoperative behavior of the nets in the body. Unwanted events are closely linked to chronic foreign body reaction, with an increased formation of scar tissue around the surgical meshes, manifesting as pain, mesh erosion in adjacent structures (with organ tissue cut), shrinkage of nets, rejection of nets, and finally recurrence. More than 29% of the females undergoing surgery is reported to require reoperation (OLSEN ET AL. [215]). Multiple complicated surgeries are required to repair such complications including complete mesh removal that significantly impair the patient's quality of life and sometimes death (FDA [91]). As a result, some of the transvaginal mesh products including Bard Avaulta, Gynemesh overlay and Prolift have been recently withdrawn from the market and more than 40 mesh products are involved in federal lawsuits. Repeated operation on huge women population with increased life expectancy augments total cost of surgery (SUBAK ET AL. [293]) that leads to a growing need of high-quality and cost effective treatment.

In initial days, the prosthetic meshes constructed from stronger material such as polypropylene (PP) were popularly used due to excellent biocompatibility, lowest failure rates, improved tolerance to bacterial infection and good cost/benefits of the polymer (ALAEDEEN ET AL. [3]). However, such mesh constructions were heavy weight with small pore size, larger mesh area and high mesh stiffness which were related to the likelihood of post-operative pain, unnatural or difficult organ movements, central mesh ruptures and biomechanical and biological degeneration of host tissue such as erosion and exposure (AMID [6], COBB ET AL. [62], FEOLA ET AL. [94], LIANG ET AL. [173]). Over the seven-year period between 1997 and 2005, influence of mesh weight and mesh porosity were identified to be decisive for biocompatibility and stabilization of the surgical treatment (AMID [5], KLINGE ET AL. [153], KLOSTERHALFEN ET AL. [159]). The concept has been widely accepted among surgeons and manufacturers who systematically updated the mesh design changing polymer type (polytetrafluoroethylene, polyethylene terephthalate, expanded polytetrafluoroethylene and polyvinylidene fluoride (PVDF)), pore size, pore geometry and biocompatibility of the mesh implants (COBB ET AL. [61], KLINGE ET AL. [154]). Clinical trials showed the superiority of the light weight large porous textile constructions with significantly improved integration of the mesh into recipient tissues, decreased risk of bacterial colonization, reduced inflammation and fibrous reaction, and improved quality of life after repair (KLOSTERHALFEN ET AL. [158], KLOSTERHALFEN ET AL. [159], PATEL ET AL. [224], POST ET AL. [244]).

In the 21st century, with the development of sophisticated 2D/3D medical imaging techniques such as magnetic resonance imaging (MRI), ultrasonography (US) and X-rays have greatly improved the ability to understand the anatomic defects that may correlate to female PFDs. Such techniques not only provide a unique insight inside the pelvic

cavity showing every possible structures, but also outlines its static, functional and dynamic pathological mechanisms. Moreover, using the plastination method, the anatomic-topographic structures, biological composition of the tissues and their correlation with the neighboring structures can be also measured in great detail (FEIL AND SORA [92]). Although these improvements have indeed help clinicians for the optimization of the surgical procedures, mechanics of normal and various pathological conditions in female pelvic system is still unclear for which standardized biomechanical study is required.

Biomechanics serves as a best technique to improve understanding of normal tissue function, the causes and effects of physiopathology, the impact of treatment in a variety of body systems and to allow virtual clinical trials to eliminate potential risks before clinical deployment. Three-dimensional computational models constructed from medical imaging in living patients and plastination techniques in cadaver samples have been used as an powerful tool to study different anatomical and clinical questions. Offered a free selection of imaging plane (TAN ET AL. [298]), most of models are reconstructed using MRI (CHEN ET AL. [58], LUO ET AL. [179], NOAKES ET AL. [210], OTCENASEK ET AL. [218], PENG ET AL. [230]) and quite few using X-rays (BUSH ET AL. [47]) and plastination (BEYERSDORFF ET AL. [23], BHATTARAI ET AL. [24], FEIL AND SORA [92]). Such models have been extensively used to study different pelvic floor behaviors such as: urethral opening mechanisms (BUSH ET AL. [47]), prolapse (CHEN ET AL. [58], LUO ET AL. [179]), incontinence (PENG ET AL. [230], SPIRKA ET AL. [289]), vaginal delivery (ASHTON-MILLER AND DELANCEY [11], SILVA ET AL. [280]), normal defecatory mechanisms (NOAKES [209], NOAKES ET AL. [210]), sports (ROZA ET AL. [263]) and ligament impairment (BRANDÃO ET AL. [40]). Although, such patient specific models are of huge benefit, but are limited by an incomplete anatomical structures (RUBOD ET AL. [266]), idealised boundary conditions (CHEN ET AL. [58], LUO ET AL. [179], NOAKES ET AL. [210]) and simplified tissue mechanics (NOAKES ET AL. [210], PENG ET AL. [230]) that widely vary the quantitative results from one study to another.

Developments in the mechanical testing and the mathematical modeling of soft tissues have significantly improved the computational accuracy and the understanding of the female pelvic behavior. Uniaxial tensile experiments on every pelvic structures, namely, pelvic organs (MARTINS ET AL. [192], RUBOD ET AL. [266]), ligaments (RIVAUX ET AL. [256]) and fasciae (KIRILOVA ET AL. [148]) shows a wide range of non-linear mechanical response depending on the tissue constituents, mainly elastin, collagen and smooth muscle cells. Isotropic hyperelastic constitutive models, such as neo-Hookean, Yeoh, Fung, Mooney-Rivlin, and Ogden are most commonly and widely used to characterize the tissue behavior and to fit the nonlinear stress-strain test curves (BRANDÃO ET AL. [40], CHEN ET AL. [58]). Although these type of models are most popular for rubber, the real material behavior of soft pelvic tissues under loadings has been well approximated.

For transversely anisotropic skeletal muscles, recent modifications of the continuum constitutive models are mostly based on the Hill's three-element-model. Skeletal mus-

cle mechanics is described by three elements: the contractile element (CE) and two elastic spring elements, one in series (SE) and another one in parallel (PE) with the contractile element (HILL [116]). Furthermore, Humphrey and Yin accomplished major improvements in Hill's model by including the influence of the muscle fibres on muscle contraction. They split the pseudostrain-energy function into densely distributed extensible fibres and an isotropic ground matrix (HUMPHREY AND YIN [127]). MARTINS ET AL. [191] modified Humphrey's model and proposed a three-dimensional muscle model consistent with the one-dimensional model of the skeletal muscles model proposed by Hill (HILL [116]) and Zajac (ZAJAC [337]). Several modifications and new developments of the skeletal muscle model were proposed; see e.g. (BLEMKER AND DELP [35], YUCESYOY ET AL. [335], MCLEAN ET AL. [195]). Similarly, the skeletal muscle fiber constitutive laws have been decomposed into an active and a passive part, considering different muscle fibre types (BÖL AND REESE [36]), actin-titin interaction on force-length relation (HEIDLBAUF AND RÖHRLE [114]), macroscopic active and passive behavior (SPYROU ET AL. [290]), tissue injury (RAMASAMY ET AL. [249]), microstructural homogenisation in a continuummechanical framework (BLEILER ET AL. [34]). Numerous computational studies have been performed to analyze the behavior of the pelvic floor muscles ranging from Valsalva maneuver (NOAKES ET AL. [210]) to extreme deformation condition such as sports (ROZA ET AL. [263]), different stages of labor (JING ET AL. [138], KROFTA ET AL. [164]) and various fetal head shape (YAN ET AL. [331]). On this basis, the implementation of the modified Humphrey model may be relevant to investigate the passive relaxation of the levator ani muscle without activating the muscle using FE simulation.

There has always been conceptual arguments among the experts from the medicine and biomechanics regarding tissue behavior of symptomatic female pelvic floor. Clinicians and anatomists emphasize structural damage (growth and laxity) behind pelvic floor dysfunctions whereas engineers point mechanical alterations: reduced tissue stiffness due to collagen depolymerization. Histological investigations on healthy and prolapsed tissue samples evidenced altered tissue components (SILITONGA ET AL. [279]) leading to changed mechanical response of soft tissues (BRIEU ET AL. [42]). Whereas, MRI examinations shows anatomical or structural defects is also present in women with genital prolapse (CHEN ET AL. [57]). So far very few histological studies have been conducted, tissue impairment (weakness or softening) has been well adopted for computational studies (BRANDÃO ET AL. [40], CHEN ET AL. [58], (PENG ET AL. [230]). However, much more information on histological, experimental and multiscale modeling will be needed to precisely model the tissue mechanics in order to better understand the female pelvic floor behavior.

This thesis presents a computational framework to predict the complex female pelvic floor abnormalities due to mechanical weakening of the support structures that are clinically and pathologically relevant. Though a variety of models, computational and mathematical models exists, the effectiveness of the calculations depends on the understanding of the female pelvic anatomy. Here, the author focus on the existing Mooney-Rivlin model for the mechanical characterization, paying special attention to the pelvic anatomy, especially supporting fascia unit, realistic boundary conditions and appropriate tissue constituents

based on histological studies. The importance of this thesis is due to following reasons:

- Available computer models are simplified at anatomical level that does not fully incorporate the realistic boundary conditions. Complete anatomy in this thesis not only fulfills the boundary conditions but also provides realistic support to the organs and thus improves the effectiveness of the computational approach.
- The characteristic geometry of the endopelvic fascia is clinically important but difficult to assess and therefore has not been described previously in any computational model or at least has been simplified. With proper definition of the main supporting structure, computational studies presented in this thesis settle several limitations.
- Soft connective tissue constitutes varying amount of collagen-elastin fibre and adipose (fat) tissue in the pelvic cavity (OTCENASEK ET AL. [218], PETROS [239]) that has never been incorporated by any previous computational studies. Different forms of pelvic floor physiopathologies can be greatly simulated with the presented model.
- Histological information of the elastin-collagen density has been taken into account on the mathematical modeling of soft tissue composition and its weakness.
- Isotropic hyperelastic models for the skeletal muscles have been long extended in literature into more advanced anisotropic muscle modeling and one of them has been adopted in this study to improve the understanding of pelvic behavior.
- Simulations on incontinence and genital prolapse and their reconstruction using prosthetic devices provide information on pelvic floor mechanics to surgeons that helps to minimize the risk of surgical complications.

Motivated by these facts and improvements, this thesis deals with the construction of the most realistic computational model of the female pelvic floor so far. In this regard, the anatomical and mechanical importance of every structural components, for example, fascia, ligament and muscles, has been considered. Based on existing literature, a mixture model comprising of adipose tissue, elastin-collagen variation and their respective contribution on the tissue mechanics has also been adopted for the simulation, but certain simplifications have been done. Moreover, experiments on prosthetic devices are also performed in the Lab of Biomechanics at Aachen University of Applied Sciences for the mechanical characterization of dry implants and for the evaluation of their effectiveness and failure modes during reconstructive surgeries through FE simulation.

This thesis further investigates some physiopathologies such as stress urinary incontinence and vaginal vault prolapse on the computational model and compares the mechanisms of healthy and damaged supporting tissues to understand and evaluate critical factors causing these female pelvic floor disorders. In addition, this study aims to examine the biomechanical efficacy of artificial urethral support and cervical suspension system using standard prosthetic devices constructed by FEG Textiltechnik mbH, Aachen, Germany to correct urinary incontinence and genital prolapse. Positions of the implant connected to organs, implant fixation to the bone and muscles, loading directions of orthotropic

implants are some of the field of study that significantly affect the simulation and the reconstruction procedure. Simulations conducted in this thesis assists surgeons to optimize the reconstruction and minimize the post-operation complications. Moreover, the computer model, modeling approach and the computational results provide directions for future research in the field of medicine and biomechanics.

Structure of the thesis

This thesis is divided in nine chapters.

The first chapter explains the motivation and the objectives of this work, and introduces the outline of this document.

The chapters 2-4 regard the anatomical, mechanical and computational details of the female pelvic floor. In chapter 2, the anatomy, functions and dysfunction mechanisms of the female pelvic floor are described. The computational methodology of the construction of the three dimensional simulation model using ultra-thin slice plastination technique is introduced in chapter 3. In chapter 4, the histological and experimental literature has been reviewed with great detail to understand the healthy and pathophysiological mechanics of female pelvic floor tissues. Focus is given in the mathematical modeling of the pelvic floor soft connective tissue, divided into constituents, the elastin-collagen fiber components, the adipose tissue and the smooth muscle at microscopic level. Later, homogenization of the components is performed using an isotropic, incompressible and hyperelastic Mooney-Rivlin type polynomial function to describe the overall fascia mechanics at structural level.

In chapters 5-8, the computational model of the female pelvic floor is applied to study different physiological phenomena and is validated using clinical findings. More specifically, these chapters include result obtained during this thesis work. It begins by description and implementation of an anisotropic constitutive law for the skeletal pelvic muscle in open-source finite element software *Code_Aster*^{1.)} in chapter 5. The passive stretching of the skeletal levator ani muscle during normal pelvic maneuver is presented for which muscle activation is not considered. This chapter closes with a discussion that active muscle excitation is necessary in the mathematical formulation to describe the pathophysiology of the female pelvic floor disorders. Chapter 6 deals with the mechanical characterization of some of the prosthetic meshes which are used to repair pelvic floor disorders and abdominal hernia. Experiments are performed on meshes to study their local response on the host tissue after surgery. Literature has been reviewed to compare our findings and to relate with various post-operative mesh related complications. Finally, in chapter 7 and 8, the three dimensional female pelvic floor model is extensively used for the simulation of healthy and two common pathological conditions, stress urinary incontinence and vaginal vault prolapse. They are assumed to be due to weakened supporting tissues which is modeled by reducing tissue stiffness. Furthermore, the model is also used to simulate the surgical intervention using prosthetic meshes to repair the vaginal vault prolapse.

^{1.)} www.code-aster.org

The final chapter 9 concludes the work. The author presents some of the important conclusions, suggesting some future developments related to the employed models, methodologies and optimization techniques.

2 Female Pelvic Floor: Anatomy, Functions and Dysfunctions

The normal functions of the female pelvic organs, such as urination, defecation, maintenance of the intra-abdominal pressure, conception, pregnancy and delivery, depends on the integrated system of bony pelvis, the fibro-muscular connective tissues, the fibro-elastic ligaments, the urogenital diaphragm and the muscular diaphragm. Unique pre-menopausal and post-menopausal physical, mental and hormonal changes, injuries and severe damages during delivery affects the normal functioning of the female pelvic floor system. Symptoms are aggravated in ageing females and are commonly seen in the form of pelvic organ prolapse, (urinary and faecal) incontinence, sexual dysfunctions, which are medically termed as pelvic floor dysfunctions (PFDs). Such situations greatly affect their quality of life. Surgical interventions are usually performed by inserting prosthetic mesh implants to reinforce and strengthen the function of weakened or damaged supporting tissues. This chapter describes the (static and functional) anatomy of the female pelvic floor in brief. It also discusses the phenomena, types and causes of PFDs in detail. Lastly, some clinical procedures and treatment methods to correct such dysfunctions are presented.

2.1 Static anatomy of the female pelvic floor

The pelvic floor is the area between the trunk or the main body and the lower extremities or legs. It is a complex anatomic-functional entity that consists of an interrelated system of muscles, ligaments and connective tissues, which span along cranio-caudal and ventro-dorsal direction in the three dimensional bony pelvis. In female, the pelvic floor supports three vital anatomic compartments: the lower urinary tract (bladder and urethra), the female reproductive organs (vagina and uterus), and the lower gastrointestinal tract (rectum and anal canal). Figures 2.1 to 2.8 illustrate the organs and supporting tissue structures in the female pelvic floor.

2.1.1 Bony pelvis

The bony pelvis (or the pelvic skeleton) is formed posteriorly by the sacrum-coccyx bone and laterally and anteriorly by two mirror image hip or innominate bones. Hip bone on each side consists of the ilium, the ischium and the pubis that are separate bones during childhood and later fuse together to form a single bone, see Fig. 2.2. The two hip bones joined each other at the pubic symphysis anteriorly and fuses with the sacrum bone at the sacroiliac joints posteriorly to form the pelvic ring. The *pelvic brim* is an apple-shaped line passing through the prominence of the sacrum, the arcuate and the pectineal lines, and the upper margin of the pubic symphysis. The anatomical region near to the pelvic brim can be further differentiated by function into two parts: the greater or false pelvis above pelvic brim that basins the abdominal organs and the lesser or true pelvis below pelvic brim that contains and protects the pelvic organs., see Fig. 2.2a and 2.2b. In Figure 2.2b, lines 1 and 2 delineate the pelvic inlet and the pelvic outlet, respectively. The pelvic inlet travels from the sacral promontory to the superior pubic symphysis, whereas the pelvic outlet travels from the tip of the tail bone or coccyx to the inferior border of the pubic

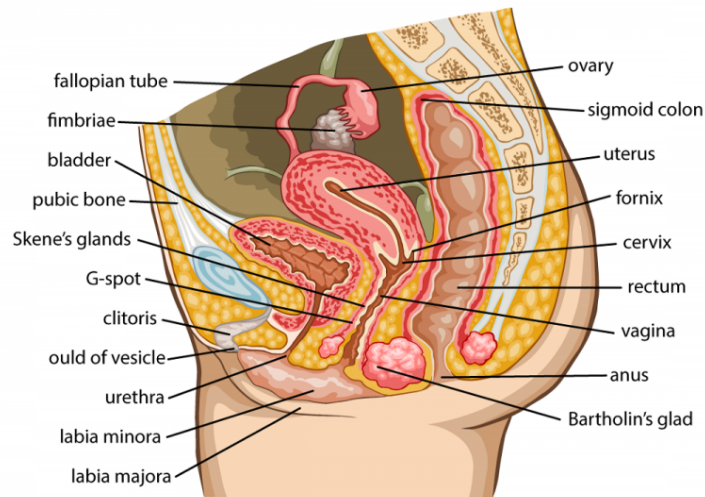


Figure 2.1: Sagittal anatomic representation of the female pelvic floor showing three anatomic compartments inside the bony pelvis. [Source: <https://www.diagramcharts101.com>]

symphysis and is larger in females for childbirth.

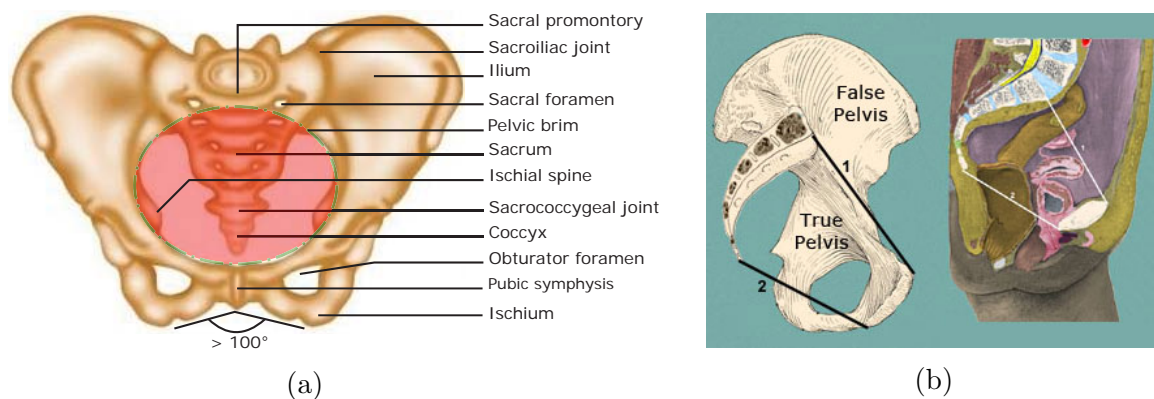


Figure 2.2: a) Female pelvic bone (SOAMES [285]) b) Female true and false pelvis [Source: <http://home.comcast.net/wnor/pelvis.html>].

The female pelvis is more circular and is evolved to its maximum width for childbirth, whereas the male pelvis is narrower, nearly heart shaped and has been optimized for bipedal locomotion. The angle beneath the ischial bones (the pubic arch) forms a much more acute angle in the male ($< 90^\circ$) while in the female, the pubic arch forms an obtuse angle ($> 100^\circ$), and the pubic arch is higher in the male. Additionally, the obturator foramen in the male are round, whereas in the female they are oval. The strong and rigid pelvis is adapted to serve a number of roles in the human body as:

- transmit the weight of the upper body bidirectionally to lower body by ways of the femurs (WOODBURNE [328]);

- anchors muscles, fasciae and ligaments, and;
- serves as a basin to support and protect the pelvic viscera.

2.1.2 Organs of the true pelvis

The pelvic viscera inside the bony pelvis are the lower urinary organs (ureters, bladder and urethra), reproductive organs (uterus, fallopian tubes, ovaries, cervix and vagina), and the lower alimentary tracts (sigmoid colon, rectum and anal canal), see Fig. 2.1. These integrated pelvic structures can be categorized clinically as landmarks to evaluate the functioning of the pelvic floor. Depending on the support system, DeLancey differentiated the pelvic viscera into two compartments separated by the anterior and posterior vaginal walls (DELANCEY [69]). The anterior compartment contains the bladder and urethra while the posterior compartment contains the rectum and the anal canal.

Anterior compartment

The anterior compartment in the female pelvic floor starts with a pair of ureter and ends

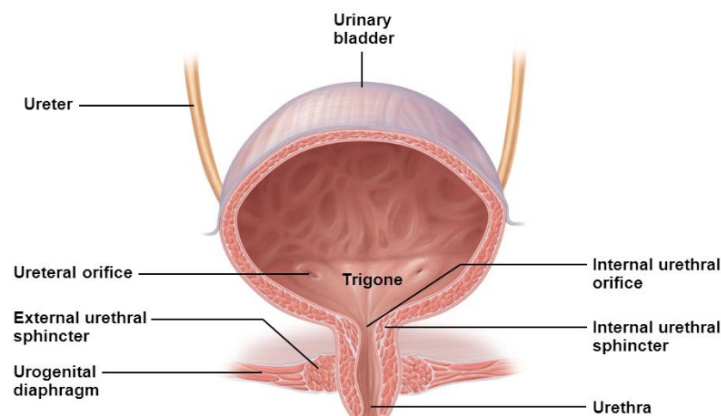


Figure 2.3: Anatomy of the female urinary system. [Source: <http://slideplayer.com/slide/9325705/>]

with the urethral meatus, where urine exits the body. The ureters are muscular duct that carries urine from the kidneys to the urinary bladder, see Fig. 2.3. They are usually 25-30 cm long and runs posteroinferiorly on the lateral pelvic wall, finally curves anteromedially to enter to the bladder. The urinary bladder is largely reperitonetial which lies posterior to the pubic bone just beneath the uterus which is separated by the vesico-uterine pouch. It serves as a reservoir for the urinary system which can hold up to 500-600 ml of urine. During urination, the internal urethral orifice at the bladder neck relaxes to pass the urine through the urethral duct, which is directed obliquely downward and forward behind the pubic symphysis and is embedded in the adventitia of the anterior vaginal wall. The female urethra is about 2.5-4 cm long and ends to the external urethral orifice at the proximal urethra consisting of smooth muscle and voluntary skeletal muscle.

Middle compartment

The middle compartment in the female pelvic floor is made up of internal and external sex organs which mainly comprises of the uterus, the cervical ring and the vagina. The uterus or the womb ($7.6 \times 4.5 \times 3$ cm) is a pear-shaped organ, which provides mechanical protection, nutritional support and waste removal from the developing embryo. It is held in position within the pelvis by the condensations of the endopelvic fascia called as ligaments, such as pubocervical, cardinal and uterosacral ligaments. The lowermost, cylindrical and narrow neck of the uterus is called the cervix which is around 2-3 cm in length. It has a cervical canal, which opens into the cranial end of the anterior vaginal wall through the *external os*. Other than passing menstrual flow and preventing bacterial infiltration inside the uterus, during childbirth, it dilates widely around 10 cm in diameter to pass baby through the vagina.

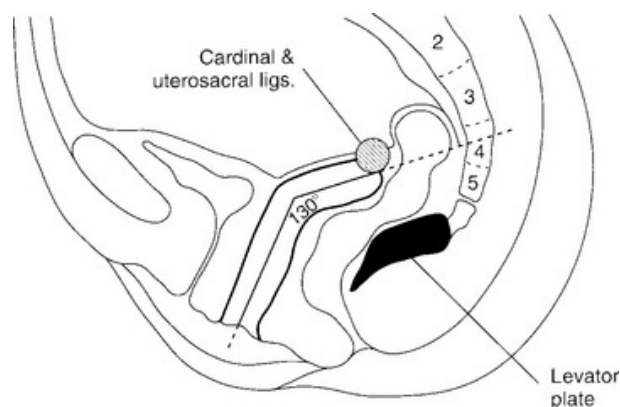


Figure 2.4: Vaginal axis in a non-pathological state (FUNT ET AL. [105]).

Anatomically, the vagina is the most important structure, providing a stable base for the bladder and urethra, anteriorly and the rectum and the perineal body, posteriorly. Normally, the vagina is a curved organ with a nearly horizontal upper part directed towards the S3 and S4 vertebrae, see 2.4. The position and the orientation of the vagina is critical: distorted normal vaginal axis predisposes women to the development of pelvic organ prolapse and incontinence. In a non-pathological state, the lower one-third of the vagina is approximately 45° from the horizontal (FUNT ET AL. [105], SZE ET AL. [296]) making an angle of $130^\circ - 145^\circ$ with the nearly horizontal upper vaginal part.

Posterior compartment

The sigmoid colon, the rectum and the anus are the components of the lower gastrointestinal tract that forms the posterior compartment in the female pelvic floor, see Fig. 2.1. At the level of S3 sacrum, the sigmoid colon loses its mesentery at the distal segment of the large intestine and gradually becomes the rectum and terminates into the anal canal of about 3 cm in length. The rectum is approximately 15 cm long, which follows the sacrococcygeal curve and ends at the perineum. The rectum has two flexures: the sacral flexure (dorsal bend) results from the concave form of the sacrum, the perineal flexure (ventral bend) from the encirclement of the rectum by the puborectal sling. Here is the

point of transition to the anal canal (anorectal junction). At the anorectal junction, the gut curves backward and its concavity is held by the puborectalis muscle. The posterior compartment acts as a temporary storage site for feces before excretion. Complaints of obstructed defecation, bowel dysfunction and rectal prolapse are common symptoms due to defected posterior compartment.

2.1.3 Muscles

The striated pelvic floor muscles span the area underneath the pelvis, separating the pelvic cavity from the perineal region below. They serve as a floor for the abdominal viscera including the rectum, maintains continence mechanism to the urethral, anal

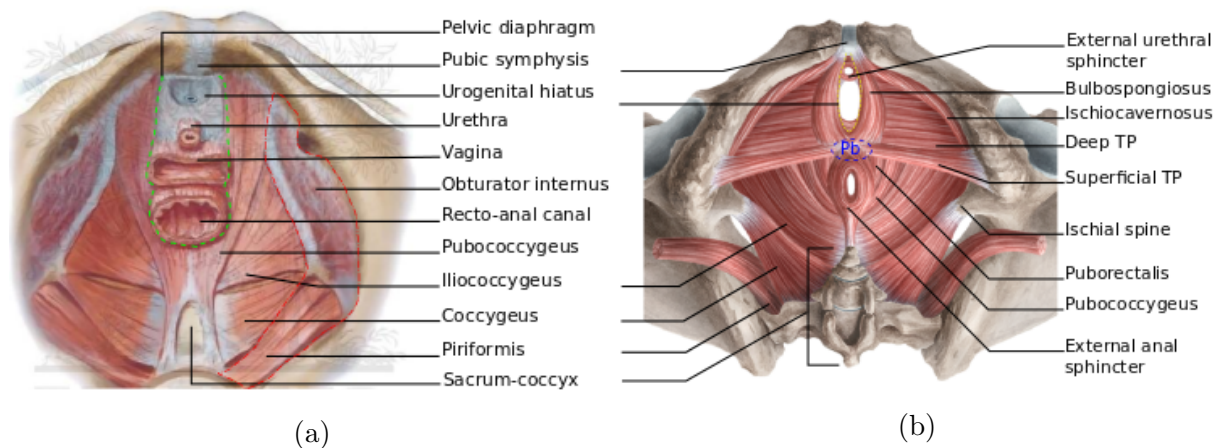


Figure 2.5: This schematic shows the structure of the skeletal muscles in the female pelvic floor. Pelvic organs are supported by the pelvic diaphragm (green dotted line), sphincter and perineal muscles shown in a) cranial (superior) view (OTCENASEK ET AL. [218]) and b) caudal (inferior) view [Source: <https://www.pinterest.com/pin/196751077454591498/>]. TP=transverse perinei.

and vaginal orifice and facilitates birth. The pelvic muscles are composed of both slow-twitch (66 %) and fast-twitch (34 %) muscle fibers (DIMPFL ET AL. [79]). The slow-twitch fibers maintains the tone of the LA muscles to support the pelvic organs at rest (DIXON AND GOSLING [81]). The fast-twitch fibers are of the rapidly contracting type which are mainly activated on demand during sudden increase in intra-abdominal pressure, such as in coughing, straining or sneezing. They can maintain contractions only for a shorter period of time (DIXON AND GOSLING [81]). The perfect muscle tone by high proportion of the slow-twitched striated muscle fibers and stable fascial structure prevents the ligaments becoming over-stretched and damaged by constant tension (DELANCEY [71]).

The pelvic musculature can be functionally classified into two groups: a) the pelvic wall muscles and b) the pelvic diaphragm (WILLIAMS ET AL. [326]). The piriformis and the obturator internus muscle form the pelvic wall, which assists hip flexion-extension during leg movement rotating the femur and the thigh, respectively. However, these muscles play no role in the structural support of the pelvic organs and only close the upper

posterior and lateral pelvic outlet. Inferiorly, a group of the muscle fibers from the levator ani (LA) muscle, the coccygeus muscle and the perital pelvic fascia forms a U-shaped, hammock-like structure, known as the pelvic diaphragm, see dotted curve in Fig. 2.5a. It stretches between the pubis and coccyx along the lateral walls of the bony pelvis, separates the pelvic cavity from the perineal region below and contains the urogenital hiatus or diaphragm (UH) that contains the urethra, the vagina and the anal canal. UH is a muscular membrane that occupies the area between the symphysis pubis and ischial tuberosities and stretches across the triangular anterior portion of the pelvic outlet, see yellow dotted curve in Fig. 2.5b.

Two triangular shaped coccygeus muscles are located posteriorly, which originate from the pelvic surface of the ischium spine and the sacrospinous ligament moving medially to insert into the fifth sacral vertebra and the coccyx. The bilateral action of the coccygei muscle induces the flexion of the coccyx bone that abducts and elevates the pelvic diaphragm during and after defecation. Another category of the diaphragm is the LA muscle, which is the most important muscle of the pelvic floor. The levator ani supports the abdominal pressure and stabilizes pelvic organs by regulating the size of the levator hiatus. It plays a crucial role in the preservation of the urinary and bowel continence. The literature in old days portray the LA muscle as a hammock structure lying in the horizontal plane and closing the inferior pelvic floor, these are incomplete and controversial. Once, surgeons, anatomists and radiologists have precisely recognized the origins and insertions of the broad muscle fibers and have distinguished them using radiological techniques and cadaver studies (JANDA ET AL. [134], OELRICH [214], PETROS AND ULMSTEN [236]), the actual anatomy and the the physio-pathology these days are found to be very consistent among the different studies. The description of such standardized categories are:

Pubococcygeus muscle

The pubococcygeus muscle (PCM), also termed as pubovisceral muscle (PVM) is the bulkier medial portion and the most important part of the levator ani that originates approximately 1.5 cm above the inferior pubic symphysis (ZACHARIN [336]) and the anterior portion of the arcus tendineus. It runs back almost horizontally to insert in some regions of the lateral vaginal walls and posterior rectum, see Fig. 2.5. Fibers of PCM from each side sweep behind the rectum to find its attachment at the coccyx. An U-shaped space formed by the inner margin of the PCM is known as the levator hiatus which holds the vagina, and the ano-rectal canal in vertical plane. The PCM with perfect tone creates a forward force, which elevates the mid-vagina to hammock the urogenital hiatus in order to close the urethral lumen and to control urine flow.

Iliococcygeus muscle

The iliococcygeus muscle (ICM) is the thin lateral part of the levator ani, which begins at the lateral margin of the PCM and the arcus tendineus of the levator ani or *levator arch*. It spans medially and attaches to the last 3 segments of the coccyx bone posteriorly (Fig. 2.5a). At the midline, the fibers from both sides fuses to form iliococcygeal raphe which

gets connected with the superior surface of the sacrum and coccyx and contribute to the anococcygeal ligament. At this level, the iliococcygeal and the posterior pubococcygeus fibers intertwine to form a small, flat and nearly horizontal musculature, known as the levator plate. The levator plate serves as a shelf on which the pelvic organs rest: weakness of this plate may loosen the muscular sling behind the anorectum that enlarges the levator ani and the urogenital hiatus. Discussion of the functional anatomy associated with the levator plate will be provided in the next sections.

Puborectalis muscle

The lowest medial level of the levator ani muscle is the puborectalis muscle (PRM), which closes the pelvic diaphragm. The fibers of the PRM originates from the symphysis and the superior fascia of the urogenital diaphragm on both sides (Fig. 2.5a). It passes medially backward and loops around the rectum like a sling at the level of the anorectal junction (PETROS [239]). The inferior fibers of the PRM around the rectum and the fibers of the longitudinal muscle of anus (LMA) are anchored to the external anal sphincter (EAS) muscle. This U-shaped sling creates an angulation of the rectum at the level of the anorectal junction that elevates the pelvic organs towards pubis on contraction. On relaxation, the anorectal angle increases, thus allowing the relaxation of the internal and external anal sphincter to defecate.

Sphincter and perineal muscles

The outlet of the pelvis below the levator ani muscles is a diamond shaped perineum, constructed by the deep and the superficial muscles of the perineum and external sphincters for each pelvic organ orifice, see Fig. 2.5b. This perineum is anteriorly originated from the pubic symphysis, anterolaterally from the interior pubic ramus, the ischial ramus and the ischial tuberosity. Muscles within the perineum space include bulbospongiosus or bulbocavernosus, ischiocavernosus, deep and superficial transverse perineal (TP). These muscles and overlaying fasciae from each pelvic bone meet to form the *perineal body* (as Pb in Fig. 2.5b) which anchors the external sphincter muscles of the vagina and the anus and separates their orifices. During childbirth, the perineal body distends: damage or defects in the perineal body leads to pelvic organ dislocation (DELANCEY [73]). The bilaterally contracting perineal muscle stabilizes the perineal body (superficial transverse perineal), regulates/closes the urogenital hiatus, provides a sphincter-like effect at the distal vagina, provides structural support for the distal urethra and compresses the deep dorsal vein of the clitoris, thereby assisting the erection in the clitoris (bulbospongiosus), tense the vagina during orgasm (ischiocavernosus) and regulates the external urethral and anal sphincters to urinate and defecate. The perineum contains an abundance of nerve endings in the special regions such as dorsum of clitoris, deep perineal pouch and gluteal that make them sensitive. Below the muscular layer of the perineum lies a triangular, flat and fibromuscular perineal membrane, or inferior fascia of urogenital diaphragm in older texts. It is attached to the either side of the inferior rami of the pubis and ischium and continues at the level of the perineal body. Perforated by the urethra and the vagina, it provides aperture for their orifice and attaches the muscles of the superficial external

genitalia to support the distal pelvic viscera. The fibers of the perineal membrane connect through the perineal body, thereby providing a layer that resists downward descent of the rectum.

2.1.4 Pelvic fasciae

Fasciae refers to a layer of fibrous tissue that permeates the body. It surrounds and interpenetrates muscles, joints, vascular beds, nerves and organs to bind them together. In the female pelvic floor, it is superiorly continuous with abdominal wall fascia and inferiorly with the fascia of the perineum. The fasciae are mainly of two groups: parietal pelvic fascia and visceral pelvic fascia that can be further categorized into different components depending on their anatomical location and function (KLINGLER ET AL. [156]). It is an important structure in the pelvic floor that

- provides a firm base to maintain the proper position of the urethro-vesical junction, particularly during straining;
- fills the organ-organ and the muscle-organ spaces in the pelvic floor and divide the pelvic floor into anterior and posterior compartments (OTCENASEK ET AL. [218]) and;
- prevents the urethral and the bladder hypermobility (RECHBERGER ET AL. [251]).

Parietal fascia

The parietal pelvic fascia primarily covers the walls of the pelvis and can be subdivided into the superior fascia of the pelvic diaphragm (levator ani and coccygeus muscle), the obturator muscle and the piriformis muscle, 2.6a. It is named according to the muscles it covers, for example, over the obturator internus muscle it is dense and strong and is known as the obturator internus fascia. These connective tissues are condensed at different regions on the overlaying pelvic walls to form thick bands: the arcus tendinous fascia pelvis (ATFP), the arcus tendinous levator arch (ATLA), and the arcus tendinous fascia rectovaginalis (ATFR). The anatomical origin and insertions of these condensations are shown in Fig. 2.6b. These structures mainly suspend the vagina laterally (ATFP) and posteriorly (ATFR) and the levator ani muscle fibers (ATLA).

Visceral fascia

Visceral fascia is the covering of the various pelvic viscera/organs, which is a loose continuous network of connective tissue strand that suspends organs to the pelvic musculature. The integrated structure is commonly known as the *endopelvic fascia* (DELANCEY [69]). It lies just beneath the peritoneum with a semifrontally oriented septum in shape surrounding the vagina and part of the uterine cervix (OTCENASEK ET AL. [218]) with varying thickness or condensations in specific regions. The regions of the endopelvic fascia and its associated peritoneum have been named by anatomists in accordance with the viscera to

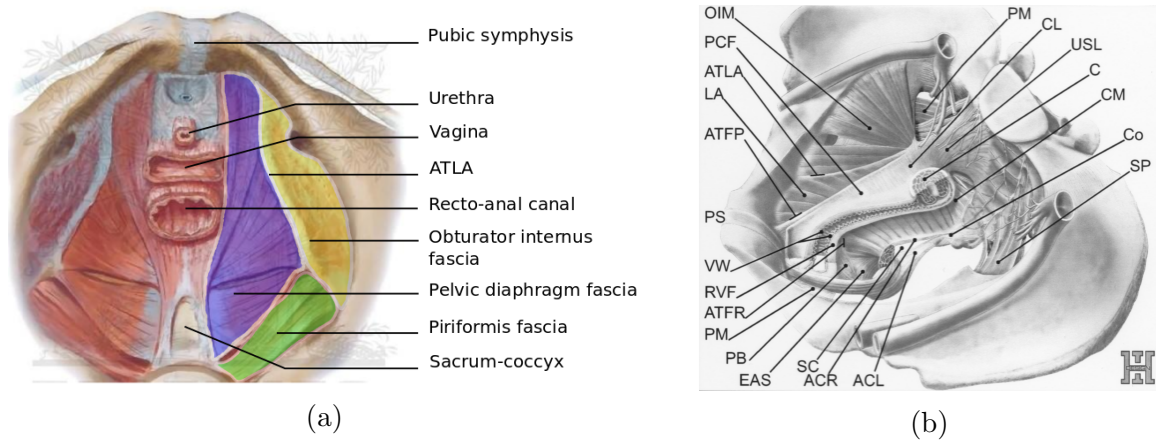


Figure 2.6: a) Superior view of the female pelvic floor showing the pelvic muscles, bony pelvis and parietal fascia coverings (orange, purple and green) (OTCENASEK ET AL. [218]). b) Mid-sagittal section of the female pelvic floor showing the anatomy and boundaries of the visceral fasciae (OTCENASEK ET AL. [218]). Abbreviations are described in the beginning of the thesis.

which it is related. They are pubocervical fascia, rectovaginal fascia, Waldeyer fascia, rectosacral fascia, mesorectum, paracolpium, pubourethral ligament, pubocervical ligament, cardinal ligament, uterosacral ligament. The listed ligaments are the real condensations of the endopelvic fascia constituents rather than true ligaments (ERCOLI ET AL. [87]). The ligaments are discussed in detail in the next sections.

The endopelvic fascia is a heterogeneous network of collagen interlaced with elastin, fibroblasts, nerves, lymph channels, and non-vascular smooth muscle cells (BERGLAS AND RUBIN [22]). It extends between the pubic symphysis, the sacrum and the ischial spine and is laterally attached to the arcus tendinous fascia pelvis (ATFP). The vagina acts as a middle compartment of the female pelvic floor and the support system along its length are different in different regions (DELANCEY [69]). With respect to the fascial attachment on the vagina, the endopelvic fascia can be categorized into three different anatomical levels (DELANCEY [69], TUNN ET AL. [306]). Level I refers the intermingling fibers of the endopelvic fascia and its specific condensations originated from the region of the greater sciatic foramen of the bony pelvis that inserts into the lateral walls of the proximal third of vagina and the cervix (when present), see Fig. 2.7. At this level I, the part of the endopelvic fascia can be subdivided into *the parametrium* and *the paracolpium* that suspend the uterus and the vagina to the pelvic side walls, respectively. The parametrium is composed of the anatomically contiguous uterosacral and the cardinal ligaments whereas the paracolpium is a relatively long sheet of tissue. Additional support to the uterus comes from the broad (round and ovarian) ligament. Together, these suspensory structures hold the uterus and upper vagina in proper positions over the levator plate: damage or weakness in this complex may result in abnormal bladder emptying and uterine prolapse (PETROS [240]).

The visceral or the endopelvic fascia at level II forms a hammock that stretches the mid-

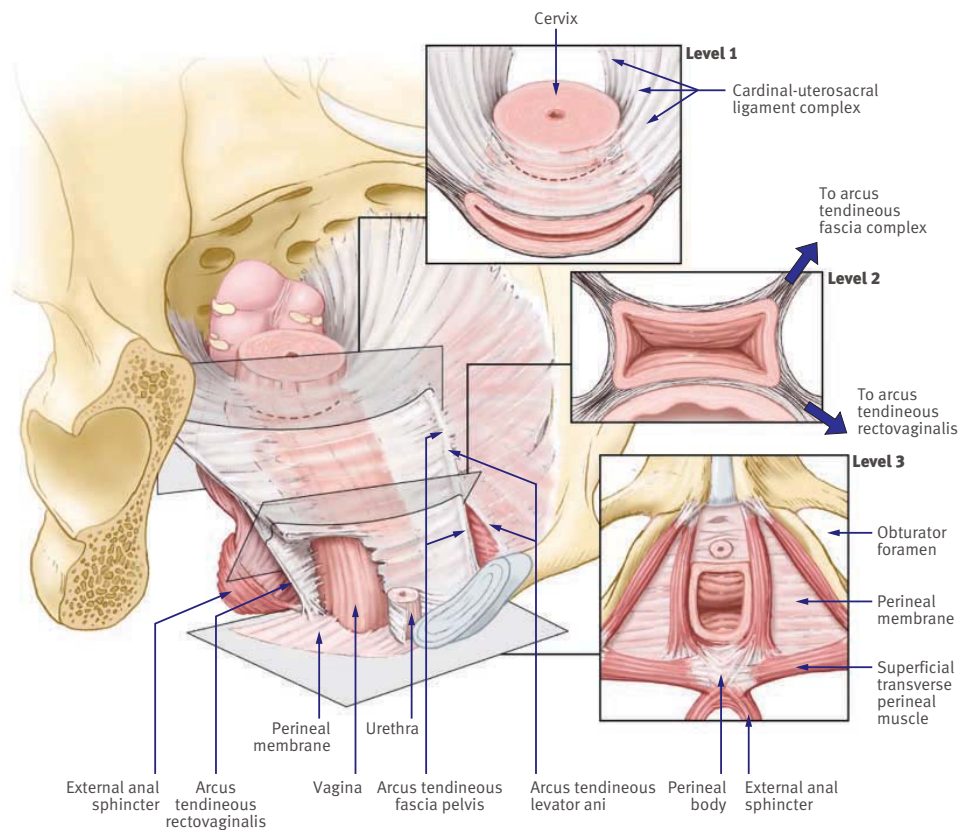


Figure 2.7: Detail illustration of DeLancey's three level of endopelvic fascia (BARBER [17]).

vagina dorso-ventrally between the bladder and the rectum. Superiorly, it is continuous with the downward reflections of the paracolpium that changes its configuration and forms a direct lateral attachments of the mid third of the vagina to the pelvic side walls at levator and fascial arches, ATRP anteriorly and ATRP posteriorly. This part of the endopelvic fascia is a larger, functionally continuous structural layer which supports the anterior vaginal wall directly to the ATRP, and is called as paravaginal fascial attachment (RICHARDSON [254]). It can be divided into a) anterior pubocervical fascia (PCF) and b) posterior rectovaginal fascia (RVF). Figure 2.6b show the spatial connections of the PCF and the RVF at both sides of the vagina, which fades cranio-dorsally into the cardinal and the uterosacral ligaments. Most importantly, the PCF generates a strong base for the urethra embedded on the anterior vaginal wall and the urinary bladder connected via bladder pillars of the adventitious layer at bladder base. Posteriorly, the RVF or the posterior leaf of the endopelvic fascia is attached to the rectum by the rectal pillars or lateral ligaments of the rectum (CHAPUIS ET AL. [54]). Laxity, damage or weakness at this level cannot properly hammock/support the anterior/posterior compartment, which often induces prolapse, hypermobility and incontinence related to the urinary bladder and the rectum. Further details of the tissue damages are provided later.

The support of the distal third vaginal segment includes the attachment to the perineal

membrane, the levator ani muscles and the perineal body. At level III of the endopelvic fascia, the visceral fascia from each side of the distal vagina and the parietal fascia of the levator ani muscle confluences together at the urethral surface to form the *pubourethral ligament*, which extends to the pubic symphysis. Posterior support is acquired from the rectovaginal fascial sheet. However, there is also agreement that in the distal vagina (level III), the vaginal wall is directly attached to surrounding structures without any intervening paracolpium (HSU AND DELANCEY [119]). Defects in the integrity of the level III produce rectocele, stress urinary incontinence and vaginal wall-urethral prolapse.

2.1.5 Ligaments

In the female pelvic floor, ligaments are the most important structures and are differentiated into two types according to their functions: *articular or skeletal* ligaments that hold or stabilize the pelvic bones together and *visceral* ligaments formed by fascial condensations (ERCOLI ET AL. [87]) that support organs in their correct anatomical positions. In anatomy, unlike muscles, articular ligaments are passive structures that are band of dense fibrous regular connective tissues similar to knee ligaments mainly composed of elastin and collagen fibers. However, the presence of nerves, smooth muscle, adipose tissue and blood vessels intermingled with irregular connective tissue makes visceral ligaments active contractile structures to support the functioning of pelvic organs. The articular type of ligaments in the pelvic floor are completely passive and play an important role on the movement of the joints. Some of their anatomic characteristics are described in Table 2.1.

Table 2.1: Properties of ligaments to connect pelvic bone.

Ligaments of bony pelvis	Properties
Anterior longitudinal	connects upper and lower edges of each vertebrae and limit extension of the vertebral column and reinforce the intervertebral disc
Sacroiliac	connect the anterior surface of the lateral part of the sacrum to the margin of the auricular surface of the ilium and to the preauricular sulcus
Iliolumbar	origins from tip of transverse process of 5th lumbar vertebra to posterior part of inner lip of iliac crest and strengthens the lumbo-sacral joint
Sacrococcygeal	starts from the surface of sacrum to the front of the coccyx and continuation of the longitudinal ligament of spine at different regions
Inguinal	runs from the pubic tubercle to the anterior superior iliac spine and important for operating on hernia patients
Sacrospinous	attaches ischial spine to the lateral margin of sacrum and coccyx and fibers are intermingled with the sacrotuberous ligament
Sacrotuberous	connects posterior inferior spine of ilium to 4th-5th transverse tubercles of sacrum and lower lateral margin of sacrum and coccyx

Pelvic ligaments by fascial condensation

The suspensory ligaments of the pelvic viscera are formed by the localized thickening or confluence of the endopelvic fascia at three distinct anatomical spaces in the pelvic cavity: anterior (pubourethral), medial (cardinal, uterosacral, broad ligament of uterus and ATFP, ATLA and ATFR) and posterior (anococcygeal ligament). When these structures are on tension, they form condensations that surgeons refer to as ligaments, however they are widely different from the true ligaments in any traditional sense such as articular ligaments. The morphological composition of these ligaments are similar to the fascia, except the amount of tissue constituents vary depending on their function.

In the anterior compartment of the female pelvic floor, the endopelvic fascia at the mid-urethra condenses to form the pubourethral ligament (PUL). It is a fan like structure, originates from the lower part of each pubic symphysis which bifurcates to insert into the midpart of the urethra approximately 1 cm short of the bladder (PETROS [237]) and lateral vaginal walls or vaginal hammock. It is generally between 5 and 7 mm in width and 3-4 mm in thickness. The urethral part is approximately 2 cm long and the vaginal part is approximately 3-4 cm long. Histological biopsies from Petros shows that the PUL consists of smooth muscle, elastin, collagen, nerves and, blood vessels (PETROS [237]). Anatomically, it tightly anchors the anterior wall of the urethra thereby kinking the mid-urethra to control the urine flow during sudden increase in abdominal pressure.

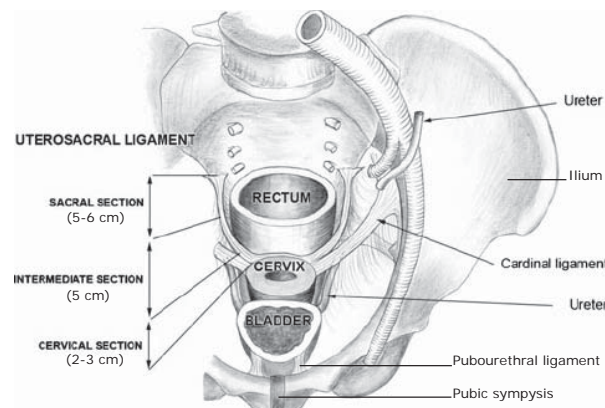


Figure 2.8: Schematic diagram of the visceral ligaments showing the three parts of the USL and its relation with the cardinal ligament (VU ET AL. [318]).

Broad ligament of the uterus is one of the largest fascial ligaments in the female pelvic floor that lies in the middle compartment. It is a two layered flat sheet of peritoneum, which extends from the lateral aspect of the uterus to either side of the pelvic walls. Broad ligament contains the round and the ovarian ligaments and serves as the mesentery for the uterus, ovaries, and the fallopian tubes. It helps in keeping the uterus anteverted and antiflexed; however, it is not the major factor to maintain the uterine anatomical position that is mostly suspended by the *cardinal* (CL) and the *uterosacral* ligaments (USL). The CL and USLs are part of the suspensory ligaments formed by the condensation of the endopelvic fascia at level I, see Fig. 2.7. They together form the parametrium and support the cervix and upper third of the vagina in their proper places over the levator

plate (CAMPBELL [51], RANGE AND WOODBURNE [250]). Similarly, these same tissues resist downward descent of the vaginal vault after hysterectomy. Weakness and laxity of these ligaments can contribute to uterine prolapse: the drop of the uterus into the vaginal canal.

The USL is a multifaceted, mesentery-like structure that originates from the tissues in the region of S2-S4 sacral vertebrae, with no direct insertion of the bone (FRITSCH AND HÖTZINGER [100]). It passes around the lateral rectum, medial to the ureter and has a superficial component covered by peritoneum and a deep retroperitoneal component. According to thickness and attachments with the intermediate section suitable for surgical use, particularly for vaginal vault support, it can be subdivided into three sections (VU ET AL. [318]), see Fig. 2.8. VU ET AL. [318] performed dissection of the nonembalmed and formalin-fixed pelvis and found a pair of 12-14 cm long USL originate distally from either side of the posterolateral aspect of the cervix and lateral vaginal fornix or upper vagina. At this region, some fibers of the USL gets interdigitate with fibers from the cardinal ligament and the thickness is measured to be 5-20 mm. Proximally, the USL is a thin (0 to 0.5 cm) fan shaped attached in the region between sacrococcygel joint-S4 vertebra (BULLER ET AL. [45]) and transversely from sacral foramina -5 cm to sacroiliac joint (FRITSCH AND HÖTZINGER [100]). The intermediate portion averaged 5 mm thick aligns antero-posteriorly at least 2.5 cm away from the ureter that provides sufficient space for surgical procedures.

The CL is another mesentery-like structure at the level I of the endopelvic fascia also known as the transverse cervical or Mackenrodht's ligament that extends laterally below the base of the broad ligament and superiorly covered by the visceral fascia. Anatomically, it is defined as a perivascular sheath with a proximal insertion at approximately the origin of the internal iliac artery and a distal insertion on the cervix and/or vagina (YABUKI ET AL. [330]). The two apical ligaments (CL and USL) fuses together into one single unit for a distance of 2 cm from the lateral aspect of the cervix. Beyond that point, the CL remained a thick bundle of connective tissue which ran posterolaterally to a broad triangular area of attachment on the lateral wall of the pelvis high up to the point where the internal iliac artery began to branch.

2.2 Functional anatomy and pelvic floor dynamics

The female pelvic organs alone behaves as a lump or formless mass when removed from the body. Their shape, position and function inside the body of a living female is determined by their three dimensional attachment to the pelvic bones through muscular and connective tissue structures, the anatomical relations are described in section 2.1. Mechanically, these support system can be categorized into two types according to their functions: (I) *supporting* system of the levator ani (LA) muscle, and (II) the *suspension* system of the endopelvic fascia (DELANCEY [71], TANSATIT ET AL. [301]). The muscle system provides normal resting contraction and reflex contraction to maintain the urogenital hiatus (CORTON [66]). On the other hand, the soft fascial tissues along with their localized condensations hold the pelvic organs and mobilize the pelvic viscera to store and excrete

urine and stool on demand. These actions must be maintained under the quasi-static gravitational and hydrostatic loading associated with upright standing and intra-abdominal pressure loading associated with dynamic activities such as walking, jumping, or sneezing. Certain support systems, such as pubococcygeus muscle, levator plate, pubourethral ligaments must relax to allow micturition and/or defecation.

2.2.1 Micturition-continence and urethral closure

Micturition, or normal urination is a dynamic process consisting of alternate storage and expulsion of urine outside the body through urethra. This periodic storage and elimination of urine depend on the structural organization and functional characteristics of smooth and striated muscles in the bladder, urethra, corresponding watertight sphincters, anchoring ligaments, fascial hammock and guiding levator ani muscles. These structures are mediated by a complex neural circuitry located in the brain, the spinal cord and the peripheral ganglia throughout filling and excretion. Although, micturition process includes the opening of the vesico-urethral ducts to expel out the urine, it is not exactly similar to

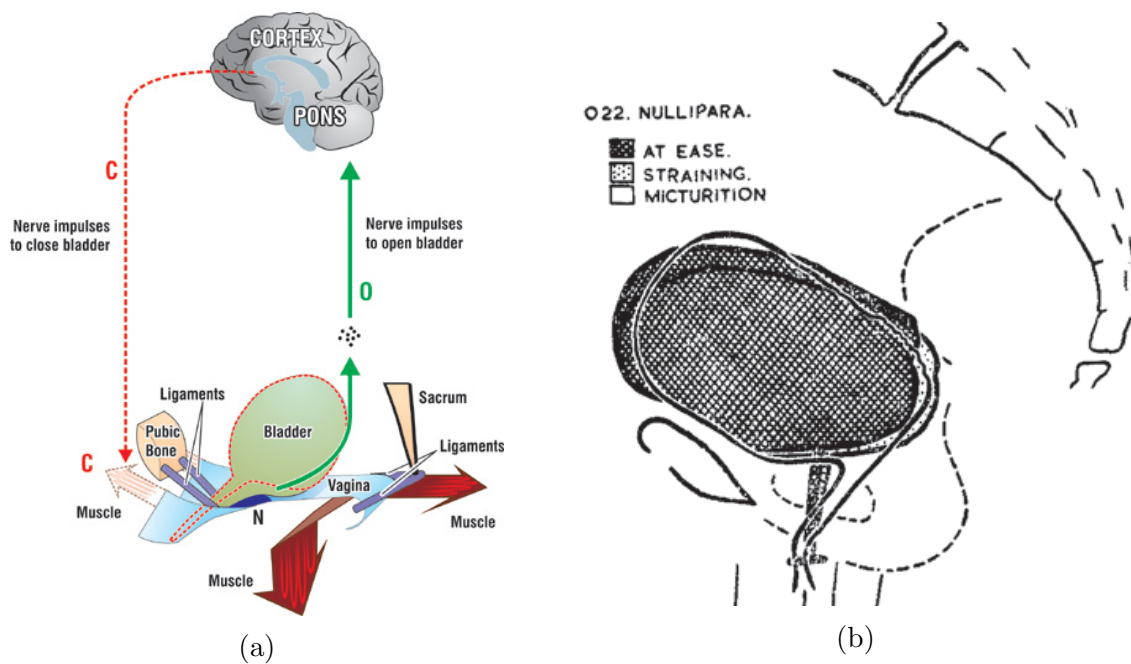


Figure 2.9: a) The schema of the cortex of the brain regulates closure and opening mechanisms by engaging all the muscles, nerves, ligaments and tissues (PETROS [239]). b) Superimposed tracings of radiographs in a healthy bladder function. Downward movement of the bladder base, obliteration of the posterior urethro-vesical angle and dilatation of the urethra during micturition. (ROBERTS [259]).

the term 'opening' (PETROS [239]). There lies phenomenological differences: micturition is driven by neurological reflex whereas the opening state is fully mechanical, for example, *genuine stress incontinence*.

Pressure variation inside bladder

As bladder gradually fills with urine, its muscular wall passively distends to maintain its tone at constant level so the intravesicular pressure remains below 10 cm of water (ROBERTS [259]). The stretch receptors nerve endings distributed throughout the bladder walls and mainly concentrated in the trigone and urethral meatus responds the desire to micturate that depends on the rate of filling and the volume of urine in the bladder (VON ZEISSL [317]). *If the bladder fills quickly, desire to micturate may be experienced even at a lower volume.* Cystometric studies in nulliparous adults show the normal or first desire to micturate appears when the average volume of filling in the bladder is 250 ml. When the bladder is completely filled up to its distension limit (usually 450-500 ml), there is a sharp increase in intravesicular pressure of 30 - 50 cm of water. At this stage, the contraction of the bladder detrusor begins micturition to outflow the urine at a steady pressure until emptying the bladder. After emptying, the bladder may still retain about 50 ml residual volume. The intravesicular pressure is temporarily raised from resting pressure of less than 10 cm of water to 70 -100 cm of water due to suddenly increased intraabdominal pressure by straining, coughing or other violent muscular activities. Intact sphincter muscles around bladder neck and compressor urethrae resists the increased intravesicular pressure force to maintain the continence, otherwise involuntary urine leakage occurs.

Structural changes in the bladder and urethra during micturition

The micturition phenomena in female is observed as structural and anatomical changes in the bladder and the urethra initiated by sequence of events such as, nerves stimulation, activation of micturition reflex, detrusor contraction, abdominal muscles contraction and an active relaxation of the levator ani muscle and the pubourethral ligaments (PETROS [239], ROBERTS [259]). Setting up the detrusor contraction due to stretch receptors, the bladder assumes an ovoid or egg shape to create the posterior outline of the bladder base, see Fig. 2.9b. The intrinsic voluntary muscle fibers that embraces the urethra above the perineal membrane or so called triangular ligament passes diagonally to insert backwards in to the vaginal wall. It modulates the relative opening of the urethra and regulates the micturition, see Fig. 2.10. During micturition, relaxation of the pubourethral ligaments and the voluntary levator muscles, especially anterior part of the pubococcygeus muscle inserted into the lateral wall of the vagina relaxes. The levator plate and the longitudinal muscle of anus stretches the urethro-vesical junction (UVJ) through its fascial insertion to the vaginal walls to move downwards and backwards, see Fig. 2.9a. The internal urethral meatus in the proximal urethra is rotated backwards and downwards that bring the trigone and upper urethra in line between two fixed points which are situated at the supravaginal cervix and at the triangular ligament, see Fig. 2.10. At the onset of micturition, the posterior urethro-vesical angle, approximately 100° at rest starts to diminish and the intrinsic muscle around the UVJ relaxes that allows the urethra to dilate as funnel up to the urogenital diaphragm. However, the anterior urethro-vesical angle does not change significantly and loss of the posterior urethro-vesical angle, either at rest or on straining, is considered to be the characteristic of stress incontinence (JEFFCOATE AND ROBERTS [136]).

When micturition is well established due to voluntary muscular pull, four structural

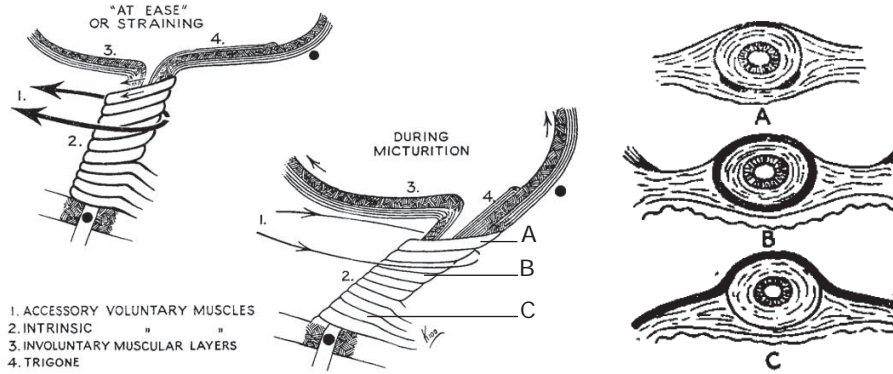


Figure 2.10: Schematic representation of the urethral and the bladder base support by various muscles and their effect during rest and micturition. At rest, the muscles contracts to elevate the UVJ, whereas, during micturition, muscles relaxes to descent the UVJ wide open as funnel (ROBERTS [259]).

changes around the UVJ becomes distinct: a) the UVJ position is backward and downward, b) the posterior urethro-vesical angle disappears completely, c) the urethra dilates fully as funnel, and d) the urinary stream angulates downward and is ready for outflow of urine. The outflow of urine at a steady pressure begins once the compressor urethrae is relaxed, which is called the *opening* of the urethra. Immediately after the outflux of the urine, partial restoration of the posterior urethro-vesical angle occurs, and the funnelling of the internal meatus and dilatation of the urethra become less manifest (ROBERTS [259]).

After urination is complete with complete voiding, stretch receptors activates to restore the anatomical changes of the muscles and ligaments around the bladder base and urethra. The release of the muscular stretching pulls the anterior vaginal wall and urethra forward and upwards to re-establish the angulation of the urethral stream with elevated UVJ at its normal position. The posterior urethro-vesical angle is set back to rest value at 100° . The tone of the urethra returns and the funnelling disappears. The sphincters along the urethra and the bladder neck contracts watertight to close the urethra and the bladder for another influx of urine in the bladder. During strong effort, the urethra adequately anchored by pubourethral ligament, vaginal hammock and pubococcygeus, sustains the backward and downward stretching of the UVJ at closed state to maintain continence, see Fig. 2.9a. In 1990, the integral theory of female incontinence hypothesized two closure mechanisms. The distal urethra is closed by forward stretching of the distal vagina by the pubococcygeus muscle against the pubourethral ligament. Whereas the proximal urethra can also be control closed by kinking around the pubourethral ligament for which backward and downward forces by levator plate and longitudinal muscle of anus are activated. Surgical interventions around these urethral regions might influence the urethral closing mechanisms.

2.2.2 Defecation-continnence and anorectal closure

Defecation is the final act of digestion, by which organisms eliminate solid, semisolid, or liquid waste material from the digestive tract via the anus. Actions associated with defecation involves excitation of reflex mechanisms and sequential activation of number of muscles in the anorectum that are involuntary and voluntary. The contraction of the abdominal diaphragm to raise the intra-abdominal pressure and to close the airway is voluntary in action, whereas the relaxation of the internal anal sphincter and the peristaltic contraction that empties the rectum are involuntary. In all cases, defecation is controlled by the autonomic nervous system which is always under voluntary control in healthy or continent people. For incontinent patients, the feces arriving from the sigmoid colon cannot be effectively retained in the rectum due to malfunctioning of the voluntary and striated external anal sphincter muscles. Such events are observed especially in ageing females during sudden physical activities where voluntary contraction is not sufficient enough.

Defecation or anorectal continence normally describe the ability to both reflexively and intentionally retain the bowel contents to release them at an appropriate time. Normally, the rectum is inactive and empty for most of the time. After each evacuation, rectum is filled very slowly with small amount of feces at long intervals. Defecation is initiated by neural receptors in the rectal ampulla, assisted by voluntary contraction of the abdominal muscles that raises intra-abdominal pressure to distend the rectum to receive the feces arriving from the sigmoid colon. The central nervous system then coordinates the action of the rectal ampulla and the anal canal allowing for the desired elimination of the rectal contents. When the rectal filling is sufficient, the internal anal sphincter relaxes as a result of activation of the rectoanal reflex and a powerful and evacuating peristaltic contraction sweeps the rectum. This is the defecation reflex.

The internal anal sphincter muscle made up of smooth muscle fibers a) contracts involuntarily at slower rate when rectum fills, b) maintains tone and c) contract with spasms. Most importantly, this muscle allows continuous maximal involuntary contraction, however the closure of the anal orifice on effort or straining can be intentionally employed by contraction of the external anal sphincter muscle. The external anal sphincter muscle joining the fibers from the anoccygeal ligament and the striated puborectalis muscle are voluntary in action. The puborectalis muscle surrounding the anorectal junction relaxes to allow the straightening of the anorectal angle from 90° to about 130° to 140° and moving the anorectal junction downwards and backwards. Finally, the external anal sphincter relaxes to evacuate the feces out of the external anal orifice.

Following defecation, both sphincters contracts and the puborectalis assumes its normal tone to constrict the rectum and the anus. The puborectalis and the external anal sphincter forms a distal sling to produce a flexing or kinging of the bowel between the rectum and anal canal. This is sometimes known as anorectal flexure that is required for the maintenance of the continence during effort or activities with raised intra-abdominal pressure. This closure can consciously maintained until another defecation is desired. Fecal filling beings in small amount for long period.

2.3 Pelvic floor dysfunctions

The perfect tone of the female pelvic supporting structures, such as muscles, ligaments and soft connective tissues maintain the normal functioning of the organs for urination, defecation and sexual activities. However, the remodeling and softening of these structures together with some pelvic organs during pregnancy facilitate a normal vaginal delivery (DOWNING AND SHERWOOD [82], ULDBJERG ET AL. [308]). Structures normally regain shape and function within a range of few days to months (PESCHERS ET AL. [232], PETROS [235]). However, significant denervation injury and structural damages during childbirth are vulnerable (WALL ET AL. [319]) in long run. The 'Integral theory' suggests that the loose insertions of the striated pelvic muscles due to the depolymerization of the collagen fibrils of the hammock tissues ultimately fail to transmit the muscle contraction to the organs and implications are seen in the form of pelvic floor dysfunctions (PFDs) (PETROS AND ULMSTEN [234]). Some of the most common disorders are urinary incontinence, fecal incontinence, pelvic organ prolapse and sexual dysfunctions that progress with menopause and age (LIN ET AL. [177]). Such conditions are distressing problem, which may have a large impact on quality of life in female.

Incidence and prevalence

It is estimated that 11.1% of American women have a lifetime risk of undergoing pelvic floor dysfunction surgery by the age of 80 (OLSEN ET AL. [215]). More than 200,000 surgeries are performed annually for pelvic organ prolapse (BOYLES ET AL. [39]). POP is a very costly condition, the annual estimated cost for these operations exceeds 1 billion US dollars (SUBAK ET AL. [293]). The POP surgery is a complicated procedure with high failure rate and reoperation (30%). The prevalence and incidence of pelvic organ prolapse is increasing; over the next 30 years, it is predicted that the number of women seeking care for the treatment of pelvic floor disorders will increase by 45% (LUBER ET AL. [178]).

2.3.1 Urinary incontinence

Urinary incontinence (UI) can be defined as involuntary urine leakage affecting an estimated 20-53 % of female aged 20-60 (MARKLAND ET AL. [189]). It is far more common among women than men (1.5-5%). Between 15-50% of women experience urinary incontinence during their lifetimes, with the highest rates occurring in women who have had children. Severe urinary continence affects 7-10% of women. There are mainly three types of urinary incontinence: urge UI, stress UI and mixed (stress+urge) UI. Urge UI is a sudden and strong need to urinate. It occurs when the overactive detrusor muscle of the partially full bladder contracts too early with enough force to override the sphincter muscles of the urethra. The potential causes of urge UI include bladder infection, irritation, stone, obstructed bladder opening and diseases or injuries to the nervous system. Although urge UI may occur in anyone at any age, it is more common in women, older adults and obese individuals. Another most common UI in female is stress UI that mostly develops in aging female where significant urine leakage occurs involuntarily during sudden increase

in intra-abdominal pressure. The cause for SUI in old ages are weak support at the mid-urethra and failed bladder neck closure from the collagen deficient pubourethral ligament, vaginal hammock, vaginal wall, and denervated or damaged levator ani (DELANCEY [70], DELANCEY [72]).

The prevalence rate of UI is high and varies widely from 15% to 67%, depending on the type of incontinence (WESNES ET AL. [323]). The stress UI is the most common affecting 39.4% followed by urge UI at 23.7% and mixed UI at 18.9% (WU ET AL. [329]). More specifically, the white women have higher rates of SUI (41 % American and 30 % European) compared to African American women with higher rates of urge UI. The prevalence of UI is different in the Asian women with a predominance of mixed urinary incontinence ($\approx 64\%$) (LAPITAN AND CHYE [168]). Unfortunately, the prevalence of urinary incontinence (UI) is difficult to determine; many women do not seek medical advice and treatment because of embarrassment and misconception regarding treatment (DENG [76], ELENSKAIA ET AL. [86]). The major studied risk factors for urinary incontinence include: gender, ageing, obesity, hysterectomy, smoking, late pregnancy and others.

2.3.2 Fecal incontinence

The fecal incontinence, also known as bowel incontinence is the inability to control bowel movements causing accidental or involuntary leak of solid (or feces) from the rectum. People of any age can be affected and nearly 18 million US adults about one in 12 have fecal incontinence (WHITEHEAD ET AL. [324]). But the prevalence is more common in older adults especially in women. As discussed in section 2.2.2, the internal and external anal sphincter muscles maintains the anorectal closure. Injury or weakness to one or both of them cannot effectively keep the anus closed and prevent stool from leaking. Trauma, childbirth injuries, cancer surgery, diarrhoea, constipation and muscle or nerve damage are possible causes of injury to the sphincters. Whatever be the cause, it is an embarrassing situation that decreases the quality of life. Some of the common risk factors for fecal incontinence are chronic diarrhoea, prolonged constipation, rectal prolapse, obesity, muscle damage during childbirth, nerve injuries controlling defecation due to diabetes or multiple sclerosis, physical disability, Alzheimer's disease and dementia.

2.3.3 Pelvic organ prolapse

Pelvic organ prolapse (POP) is a hernia or abnormal protrusion of the pelvic organs from their normal attachment sites to or through the vaginal opening. Multiparous old females are mostly reported with such symptoms attributing the most common reasons to be multiple pregnancies, ageing, obesity (OLSEN ET AL. [215], SWIFT ET AL. [295]), fetal weight (SWIFT ET AL. [295]), instrumental delivery (HENDRIX ET AL. [115], MACLENNAN ET AL. [180]) and connective tissue disorder (NORTON ET AL. [213]). Weakened or damaged pelvic support-suspension system is observed in the symptomatic females as a consequence of denervation injuries during delivery, prolonged second stage of labour and collagen remodeling in old ages. The pelvic organs supported by a weaker levator ani muscles, ligaments and fasciae pushes the anterior and posterior vaginal wall.

Further pushing either due to gravity or an increased intra-abdominal pressure with exertion protrudes vaginal tissue out of vaginal opening. Depending on the size of dropping organs outside the vaginal orifice, pelvic organ prolapse are asymptomatic (no protrusion outside the vaginal opening) and symptomatic (clearly visible tissue protrusion beyond the vaginal opening). The prevalence of the POP varies widely across studies. 43-76% of the female population may have some degree of prolapses (BARBER [18]), however, most prolapses are not clinically bothersome without specific symptoms. Though, it is difficult to determine its prevalence as many women do not seek medical advice, 19% of women have the lifetime risk of undergoing POP surgery by the age of 80 years (SMITH ET AL. [283]) with larger percentage of reproductive and postmenopausal females affected by different forms of POP (SHAH ET AL. [276]).

Cystocele: bladder prolapse

Anterior vaginal wall prolapse or also known as central defect is clinically common as cystocele that develops when the supportive tissue between bladder and anterior vaginal wall (central portion of the pubocervical fascia) weakens or softens, allowing the bladder to bulge into the vagina. It is the most common form of the POP (DELANCEY [69]) with 34.3-53.4% of repairs (HENDRIX ET AL. [115], LIEN ET AL. [175]). Weakening or damage of the fascia tissue occurs due to the phenomenological reduction of the estrogen hormone after menopause and successive remodeling of the stronger collagen in older age. In early stage, cystocele may be asymptomatic that progresses to various symptoms such as fullness or pressure in the pelvis or vagina, object protruding from the vagina, lower back pain or pressure, problems with bladder emptying, dyspareunia, or vaginal bleeding. For a severe cystocele cases, the prolapsed bladder can appear outside the vaginal opening for which surgery may be necessary. Radiographically, cystocele is confirmed when the bladder base descend below the inferior margin of the symphysis pubis (MACURA K.J. [181]) and is more than 1 cm vertically below the pubococcygeal line (YANG ET AL. [332]). Bladder neck descent more than 1 cm refers to the bladder neck hypermobility and the urinary symptoms often associated with such situations are stress UI (60%), urge UI (15%), frequent or urge urination (35%), and difficulty voiding (23%) (ROMANZI ET AL. [260]).

Urethrocele: urethral prolapse

A urethrocele is characterized by a protrusion of the urethral segment and the surrounding connective tissue into the anterior distal vaginal wall. When the urethra is not held properly in its position by the muscles and tissues, it curves and widens to descend on the anterior distal vaginal wall. Urethrocele often occurs with cystoceles, which is collectively termed as cystourethrocele. In most cases, urethrocele are not serious health problems and possess no particular symptoms. Large urethrocele includes symptoms such as stress incontinence, increased urinary frequency, difficulty in emptying the bladder, and pain during sex. Urethroceles are often caused by childbirth, congenital weakness in the pelvic supporting tissues, and the movement of the baby through the vagina causing damage to the surrounding tissues. This condition may also occur due to obesity, parturition, or poor muscle tone.

Uteroceles: uterine prolapse

Uterine prolapse, a herniation or protrusion of the uterus into the vaginal canal, is the second most common type of pelvic organ prolapse after cystourethrocele (32-34%) affecting 14% of parous women (HENDRIX ET AL. [115]). The prevalence of POP varies widely across studies. 11% of women have a lifetime risk of undergoing POP surgery by the age of 80 years (OLSEN ET AL. [215]) with a larger percentage of reproductive and postmenopausal women affected by different forms of POP (SHAH ET AL. [276]). The pathological cause of uterine prolapse is loss of integrity of the supporting tissues around the cervical ring mainly the broad ligaments, uterosacral-cardinal ligament complex, pelvic diaphragm, parametrium and paracolpium damaged either during surgery or stretched or weakened due to vaginal delivery and hormonal changes on ageing. Uterine descent is a consequence rather than the cause of pelvic organ prolapse: the symptom is generally a sensation of vaginal bulge that is observed as a large ball protruding out of the vagina causing pain in the lower back or over the tailbone, urinary (urethral kinking, difficult or incomplete urination), bowel (difficult bowel movements) and sexual complaints.

The anatomical position of the uterus is located between the bladder and the bowel, the descent of the uterus inside the vaginal canal pulls the bladder and the superior rectum that are connected by the superior complex of the endopelvic fascia. This abnormal dislocation of the bladder and rectum is termed as cystocele and rectocele (rectal prolapse, refer 2.3.3). Physiologically, the cystocele, rectocele and uterocele are three different conditions aggravating the functionality of anterior, posterior and middle compartment in the female pelvic floor respectively, but sometimes cystocele and rectocele may follow the uterine prolapse. Depending on the size of the uterine descent from its normal anatomical position, the severity of the uterocele can be categorized into five stages (PERSU ET AL. [231]):

- Stage 0: no prolapse is demonstrated
- Stage 1: the most distal portion of the prolapse is more than 1 cm above the level of the hymen
- Stage 2: the most distal portion of the prolapse is 1 cm or less proximal or distal to the hymenal plane
- Stage 3: the most distal portion of the prolapse protrudes more than 1 cm below the hymen but protrudes no farther than 2 cm less than the total vaginal length (for example., not all of the vagina has prolapsed)
- Stage 4: vaginal eversion is essentially complete

Rectocele: rectal prolapse

A rectocele occurs when the rectovaginal septum or Denonvillier's fascia that separates the rectum from the vagina weakens or becomes thin, allowing the posterior vaginal wall to bulge or herniate (KAHN AND STANTON [143], POLLAK AND DAVILA [242]). The events that may cause rectocele, also known as the posterior prolapse, include tearing of the rectovaginal septum during childbirth, longer and difficult labour, multiple babies delivery,

chronic constipation, ageing, hysterectomy and parturition (ROSATO [261]). When rectoceles are small and asymptomatic, rectum temporarily stores and transfers the waste material to the anal canal for defecation through bowel movement. In severe cases, the herniated pouch abnormally holds the stool rather than passing out to the anus. This may cause constipation and incomplete or difficult defecation for which individual may have to push manually by placing a finger in the vagina and press against the rectum to have a proper bowel movement. In some cases, women with rectocele may also experience painful intercourse (dyspareunia).

The prevalence and incidence of rectocele is widely ranged between 12-80%. Clinical examination and radiological imaging suggests that the symptoms of rectocele is evident mainly in parous female between 20-80% due to true rectovaginal septum defect (MOLLEN ET AL. [201]). However, other study shows that some (12%) young nulliparous women are also affected by rectal prolapse due to defects of rectovaginal septum and perineal hypermobility that are assumed to be congenital (from birth) in nature (DIETZ AND CLARKE [77]). Recent ultrasound methodology showed a fourfold increase in prevalence after a first delivery (DIETZ AND LANZARONE [78]). Therefore, vaginal childbirth and ageing indeed is very likely to be a major aetiological factor, but damages, such as uterocele and enterecole (intestine prolapse) might also aggravate the situation.

Risk factors for POP

Physiologically and anatomically, the development of POP in the vaginal compartments is due to the loss of integrity and the support of the pelvic organs that occurs singly or in combination of following factors (BUMP AND NORTON [46]):

- predisposing (genetics, race, gender),
- inciting (pregnancy, delivery, surgery, myopathy, neuropathy),
- promoting (obesity, smoking, chronic cough, constipation, repetitive occupational or recreational activities),
- decompensating (aging, menopause, debilitation and medications).

2.4 Treatment of pelvic floor dysfunction

Several approaches to correct/treat female PFDs are available these days. Depending on the symptoms affecting the normal functions of the pelvic organs and severity of the situation, non-surgical and surgical methods are widely popular among physiotherapists and surgeons. Such methodology not only avoids unnecessary operations and saves huge amount of money but also provides optimal comfort to the patients after the treatment.

2.4.1 Non-surgical corrections

Asymptomatic and mild cases of female PFDs have been successfully managed by non-surgical treatment procedures. Although the majority of treatment options for PFDs are

surgical, conservative therapies are available for those patients who are not appropriate surgical candidates or those who do not desire corrective surgery. These methods significantly improve organ function and reduce the symptoms getting worst. Some of the treatments options are:

Kegel exercise and behavioral techniques

Kegel exercise consists of repeated, high intensity, pelvic muscle contractions of slow-twitch and fast-twitch muscle fibers. It strengthens weakened or damaged muscle due to pregnancy, childbirth, surgery, ageing, straining from constipation, chronic coughing and obesity. Kegel exercises are usually done to reduce stress UI especially after childbirth but no way correct prolapse. This is recommended to women generally after pregnancy to promote perineal healing, regain bladder control, and strengthen pelvic muscles. Identifying and training the right muscle that manages the involuntary leakage can be helpful, however, improper exercise and forceful stop of urination might lead to incomplete bladder emptying and urinary tract infection. In addition, double voiding (waiting for next urination), scheduled toilet trips, bladder training (delay urination on urge) and fluid and diet management are other behavioral change techniques for the management of the incontinence.

Medication

Medicines are often prescribed to treat asymptomatic urge UI, mixed UI and fecal incontinence, however, medicine varies with the types of incontinence to cure. Some of the commonly used medicines to treat UI are Topical estrogen, Imipramine (Tofranil), Alpha blockers and Anticholinergic drugs. These medications mainly rejuvenate tissues in the urethra and vaginal area and calm/relax bladder muscle to hold more urine against urge. For fecal incontinence, Anti-diarrheals, Laxatives and Stool Softeners may be used to treat diarrhoea and facilitate chronic constipation. Nevertheless, medicines are always prone to certain side effects, detail investigation on the necessity of the medication is essential.

Pessary

Vaginal pessary is a small, removable silicone or plastic device that are inserted into the vagina to support the vagina and increase tightness of the pelvic tissues and muscles. It is a non-surgical approach used for mild symptoms of PFDs, for women who have serious chronic health problems, such as heart or lung disease, that make a surgical procedure more dangerous and for young women who have not finished having children and want to avoid surgery for other reasons. However this procedure may be ineffective for severe prolapse and only 14% of the patients continue to use pessaries in long-term (SARMA ET AL. [269]). Pessaries do not cure pelvic organ prolapse but slow down the progression of prolapse. Varieties of pessaries are available that can be fitted comfortably to reduce stress UI and correct uterine prolapse (LIANG ET AL. [172]). To treat uterine prolapse, pessary holds the uterus in the correct position before it enlarges and becomes trapped in the vaginal canal. Possible complications from wearing a pessary

include open sores in the vaginal wall, bleeding, rectovaginal and vesicovaginal fistulae (WEBER AND RICHTER [320]) that can be minimized by having a pessary that fits correctly and estrogen (cream, ring or tablets).

2.4.2 Reconstructive surgeries

Patients whose symptoms of PFDs fail to improve with non-surgical treatment and gets severe, reconstructive surgery is only option to restore the pelvic floor functions. Different operation techniques such as transvaginal, abdominal, laparoscopic and robotic are available. Among all, laparoscopic and robotic are the minimally invasive techniques that offers a pile of benefits such as small incisions, less injury to tissue, low risk of infection, minimal scarring, reduced blood loss, quick recovery time and short hospital stay. It is done through one or more small incisions, using small tubes and tiny cameras and surgical instruments. Though, the purpose of the surgery is to correct the anatomy as well as to provide better bowel, bladder, and vaginal function, it must be noted that there is higher recurrence rate of 30-41%. Some of the surgical treatments for the reconstruction of the female pelvic floor dysfunctions are listed in Table 2.2.

Uterine prolapse treatment surgery as an example

To correct severe uterine prolapse, hysterectomy (uterine removal surgery) is commonly performed, but a very high rate (43%) of posthysterectomy prolapse complaints have been recognized (TOOZS-HOBSON ET AL. [303]). The use of transvaginal prosthetic mesh is often associated with complications such as mesh erosion, pain, infection, bleeding, organ perforation, and even recurrence (FDA [90], ZIMMERMAN [340]). Extensive reoperations may be required to repair such complications including complete mesh removal that further put the patient's health at risk (FDA [90]).

Abdominal sacrocolpopexy appears to result in lower rates of mesh complications compared to the transvaginal POP surgery with mesh (MAHER ET AL. [184]). Laparoscopic sacrocolpopexy (LSC) that evolved from classical abdominal sacrocolpopexy has been widely performed as a minimally invasive surgical technique to address vaginal vault prolapse safely and effectively after hysterectomy. It offers a profound success rate of 83-98% in treating symptoms (GADONNEIX ET AL. [107], PRICE ET AL. [246], ROSS AND PRESTON [262]) and usually provides faster recovery times for patients. Nevertheless, foreign body reaction, urinary incontinence, dyspareunia, bowel dysfunctions, mesh tension, development of prolapse in new compartments are reported to be the major reasons for reoperations in POP surgery (GADONNEIX ET AL. [107]). It has been reported that 29.2% of women undergoing surgery require reoperations (OLSEN ET AL. [215]).

Table 2.2: Surgical treatment procedures for various types of female PFDs.

Treatments	Objectives	Surgery	Outcomes	Risks
Burch colposuspension	Stress UI	Abdominal or laparoscopic	relocated UVJ to stronger ligaments using sutures	bladder or urethral injury during surgery
Anterior-posterior vaginal repair	prolapses in all compartments	mostly vaginal	organs lifted/supported by prosthetic meshes and sutures	foreign body reactions (FBRs), organ injuries, recurrence (41%)
Sub-urethral sling	Stress UI	Vaginal	reduced incontinence due to urethral support	difficult urination due to excessively tight mesh, FBRs
Sacrospinous fixation	Uterus and vaginal vault prolapse	Vaginal	cervix/vaginal vault well attached to the stronger sacrospinous ligament with/without hysterectomy	painful buttock, short term constipation, vaginal infection, bladder infections
Sacrocolpopexy	Uterus and vaginal vault prolapse	Abdominal or laparoscopic	elevated vaginal vault sutured by a Y-shaped mesh to the sacrum bone	mesh erosion/extrusion, FBRs, bowel obstruction, organ injuries

3 Development of Computational Model Using Plastinates

This chapter discusses the state-of-art in utilizing plastinated tissue slices of the female pelvic floor and methodology to construct the computer model for 3D visualization of its anatomy in vitro. The tissue origin, insertion, dimension and arrangement/composition can be estimated that are differentiated by various tissue colors in plastinated slices. The generated 3D computer model provides a stereoscopic view to study the adjacent relationship of the pelvic structures which is relevant to gynaecologists, surgeons, urologists and engineers who deal with the treatment/reconstruction of the female pelvic floor dysfunction.

3.1 Pelvic floor imaging techniques

Advances in radiological imaging techniques such as magnetic resonance imaging (MRI), computed tomography (CT) scanning, and three-dimensional ultrasound sonography (US) imaging have provided novel insights into the anatomy, static and dynamic function of the pelvic floor. MRI uses strong magnetic fields, radio waves and field gradients, its use is favored in preference to CT over a wide range of applications in medical diagnosis such as: neuroimaging, cardiovascular, musculoskeletal, and gastrointestinal imaging. However, MRI is expensive, time consuming, and claustrophobia-exacerbating than CT that uses ionizing radiations such as X-rays. On the other hand, US uses high-frequency sound waves to diagnose the movement of the body's internal organs, as well as blood flowing through vessels and to capture and to produce their 3D pictures in real-time. They are used to diagnose a variety of conditions and to assess organ damage following illness and symptoms such as, pain, swelling and infection. No particular type of imaging technique is always better. As shown in Fig. 3.1, different imaging techniques can generate different forms of medical images each having different pros and cons that are mentioned in Table 3.1.



Figure 3.1: Liver parenchyma images of a 8.5-year-old girl shown in a) US, b) CT and c) MRI (NIEVELSTEIN ET AL. [207]). LHV= left hepatic vein.

3.2 Plastination technique

Computerised modeling using imaging techniques have become highly useful for generating electronic representations of anatomical structures, but they plays a limited role

Table 3.1: Characteristics of different medical imaging techniques.

Imaging	Characteristics
MRI	<p>Advantages</p> <ul style="list-style-type: none"> • non-invasive, painless and does not use ionising radiation • provides outstanding soft tissue contrast including neurologic pathologies • ideal technique for imaging brain without bone artifacts <p>Disadvantages</p> <ul style="list-style-type: none"> • not suited for imaging of dense tissue, such as bone • slight movement may ruin image, requiring retesting • injection of a contrast medium (dye) if needed can cause kidney problems or result in allergic or injection-site reactions • not recommended for patients with magnetic foreign bodies, metallic implants and cardiac pacemakers
US	<p>Advantages</p> <ul style="list-style-type: none"> • non-invasive, safe, relatively painless and less expensive technique • not exposed to the harmful effects of ionising radiation and injection of contrast medium (dye) • produces a dynamic, real time image of soft tissues imaging (cardiac, renal, musculo-skeletal, reproductive, ophthalmic and gastrointestinal systems), superficial structures (testicles, thyroid, salivary glands and lymphs) and moving images of an unborn baby inside a mother's body <p>Disadvantages</p> <ul style="list-style-type: none"> • non-thermal damage followed by cavitation causes disruption of cell membranes and an acute inflammatory reaction • special probe is required for ultrasounds of oesophagus, rectum or vagina)
CT	<p>Advantages</p> <ul style="list-style-type: none"> • eliminates superimposed images of structures outside the area of interest • better clarity of bone pathologies and enhanced images compared to X-ray • can be used to check if a previously treated disease has recurred <p>Disadvantages</p> <ul style="list-style-type: none"> • risk of cancer in future from exposure to ionising radiation due to DNA mutations. • kidney problems and allergic response at injection site due to radioactive contrast dye • radiation dose in a single CT scan is ≈ 100 times more potent than a single X-ray

in the histo-morphology and pathology. These methods rely on tissue cross section from live specimen body, little error arising due to sudden movement, instant cavitation during data collection makes the study useless. Also, these databases are time consuming to generate and require labour-intensive manual digitisation. Plastination, first developed by Gunther von Hagens, serves as a novel method of tissue preservation from cadaver specimen (VON HAGENS [314], VON HAGENS ET AL. [316]). It can be used as a best alternative for generating three-dimensional computerised models where tissue fat and water are replaced by certain plastics or polymerizable resins without changing most of the properties of the original sample. These preserved tissue structures are then sliced into desirable thickness depending on histological or morphological studies or if 3D reconstruction is desired. Many different techniques can be used in plastination depending on the the favourable polymers such as silicon, epoxy and polyster-copolymer (VON HAGENS ET AL. [316]).

3.2.1 Benefits of plastination

Plastination today has proved to be very useful in anatomy as well as serving as models in teaching and research purposes. Plastinates even communicate more than untreated anatomical specimens. Transparent slices of tissue, for example, allow observers to trace the course of even the most minute nerves into the depths of the body. When the physical/chemical process is performed properly, even small, microscopic bundles of cells retain their original form. Some of the major benefits of plastination over imaging techniques are as follows:

- It preserves the rare or historically imperative materials/specimens with completely visible surfaces and highly durability for museum display, evidence and instructional use.
- A visually arresting plastinate serves as an *ideal and novel method for anatomical display* of a preserved body in a way that sheds light on the functions of its structures.
- It allows distinction of connective tissue, muscles and pelvic organs down to a microscopic level
- The specimens are odorless, non-toxic and mechanically resistant to a high degree.
- The structures remain intact and the decalcifying of bony tissue is not necessary.
- It preserves the topography and integrity of a target region in a complete and uninterrupted state with all interconnected structures on a given plane preserved.
- The use of plastinated material for generating 3-D computerised models has distinct advantages compared to cross-sectional tissue images.

3.2.2 Plastination methodology for 3D reconstruction of female pelvis

Plastination has been widely implemented for different anatomical applications ranging from small tissues (MAETA ET AL. [183], SHANTHI ET AL. [226]), bones (SCALI ET AL. [271]), organs (SANKAT ET AL. [268]) and complete human body (RIEDERER [255]). In order to understand the complete anatomy of the female pelvic floor and its physiopathologies, the medical university of Vienna for the first time constructed a three-dimensional model of the female pelvis based on thin slice plastination cross-section (1.5 mm). Plastination of specimens was done by the standard ultra-thin E12 slice plastination method (SORA [287]). In general, four steps involve in the standard process of plastination and are described in the flow chart diagram, (figure 3.2).

The female pelvis is separated from a 70 year old female cadaver specimen, which is a part of the human donation program of the Medical University of Vienna (FEIL AND SORA [92]). The Ethical Committee of the university provided approval for using the pelvis for 3D reconstruction: EK Nr: 1191/2011. The specimen is then optionally fixed in formalin depending on the plastination procedure to stop decomposition. E12

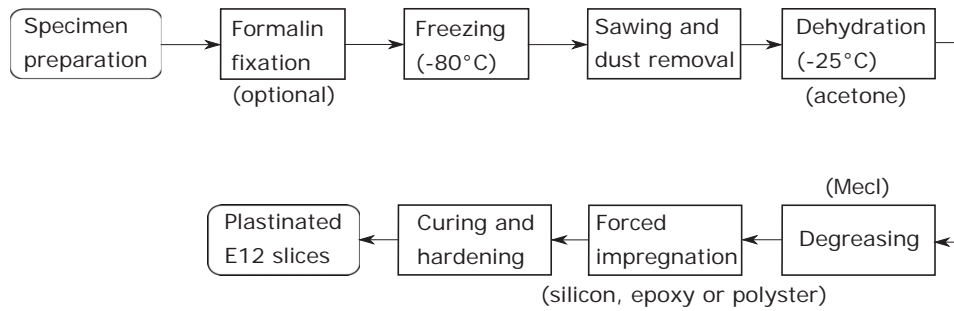


Figure 3.2: Flow chart schema of plastination technique.

sheet plastination does not require fixation for the production of the transparent body slices. Generally, formalin fixation prevents any potential biohazard risk during handling and sawing of tissue, however it is also associated with marked loss of tissue color and increased specimen freezing point. Afterwards, the female pelvis is frozen at 80°C for one week. It is important to freeze the specimen uniformly without or less ice crystals. The frozen block is cut into slices of an ideal thickness of 2-3 mm which assures a transparency of the connective tissue in the finished formation. Sections thicker than 3 mm are typically too dense and contain many superimposed structures that substantially decrease clarity. Such freshly sawn slices usually contains a covered layer of tissue shavings on each side that appear as artifacts in the finished layer and should be cleaned either with a small cool water tap or brush using scalpel or a sharp broad knife. Using the EPSON GT-10000+ Color Image Scanner and UTHSCSA MAGE TOOL v.2.0 for Windows software (The University of Texas Health Science Center in San Antonio), the area of the slices can be measured to evaluate the tissue shrinkage associated with plastination.

The next step for the preparation of the plastinate slices is to dehydrate and remove the tissue fats from the slices. The standard dehydration procedure include freeze substitution (SORA AND COOK [288]), where specimen are submerged in (-25°C) 90-100% cold *acetone* bath for 3 days each. Once the bath reaches equilibrium, the specimen is moved to another two set of acetone bath until the acetone purity is above 98.5%. Hence after three dehydration baths, the slices are brought to the atmospheric pressure for fat removal. Certain amount of fats/lipids are removed during acetone bath and slices with higher amount of fats are degreased with stronger lipid remover, methylene chloride (MeCl) for one week after dehydrating process.

Forced impregnation is the central process in plastination where the solvent in gaseous state is then continuously extracted from the cellular and interstitial space of the slice. Under vacuum conditions at 5°C in Heraeus VT 6130 M vacuum chamber, this space inside the tissue with negative pressure is filled by the resin impregnation-mixture, an epoxy Biodur (Heidelberg, Germany) mixture: E12 (resin)/ E6 (hardener)/ E600 (accelerator) (VON HAGENS [315], SORA [287]). Sometimes other reactive polymers such as silicon, polyster resins and glycerine are often used. The impregnation duration lasts for 2 days. After impregnation, the tissue block containing slices are removed out of the vacuum chamber. The impregnated specimen and resin-mix is casted in a mold constructed by heavy polythene foil sandwiched by two glass plates. This mold is then cured in a 45° -

65°C oven for next four days to harden the resin-mix. Once hardened, the tissue/resin block is cooled to room temperature and is cut into 1.6 ± 0.26 mm thin slices by a contact point diamond blade saw (Exact 310 CP, Exact Apparatebau GmbH, Norderstedt, Germany). To determine shrinkage resulting from the plastination process, the images were remeasured following plastination. Excellent high quality and perfectly transparent E12 slices as shown in Fig. 3.3 can be constructed with properties (SORA ET AL. [286]):

- high-resolution anatomical images
- greater anatomical details in submacroscopic level
- adipose tissue perfectly contrasted with muscle and epithelial tissue
- no evident tissue shrinkage (total area shrinkage is 6.65%)
- average tissue loss between sections is 1 mm due to saw blade.

3.3 Volume rendered computer model from E12 plastinated slices

The finished E12 (epoxy) slices are scanned from both sides using an EPSON GT-10000+ Color Image Scanner at 600 dpi. A ruler (cm) was included in every scan as a calibration marker. Scanned images of the plastinated tissue slices were imported as BMP files and are loaded into WinSURF soft ^{2.)} for the reconstruction step. Each features/structures to be reconstructed are traced manually on every slice images by using a graphic table (Wacom Cintiq 24HD) and are numbered accordingly on every BMP file. Once all contours are traced and outlined layer by layer, for example green curves on vaginal cross-section along entire vaginal length in Fig. 3.4a-3.4g, the reconstruction is rendered and visualized as a 3D model/geometry as shown in Fig. 3.4h. This 3D model is qualitatively checked for surface discontinuities by rotating it. Reconstructed geometries of the structure are transformed in .OBJ format.

The pelvic structures as outlined in Fig. 3.5 are reconstructed: pelvic bone, levator ani muscle, pelvic side wall muscles, organs, ligaments, ureter, arteries and nerves. The description of the abbreviations used in the figures are described in the abbreviation section in the beginning of this thesis. The UTHSCSA IMAGE TOOL v.2.0 for Windows software (The University of Texas Health Science Center in San Antonio) is used for the morphological measurement of the pelvic structures and their anatomical relations with adjacent structures. These measurements were compared with the anatomical literatures and verified for computational purpose.

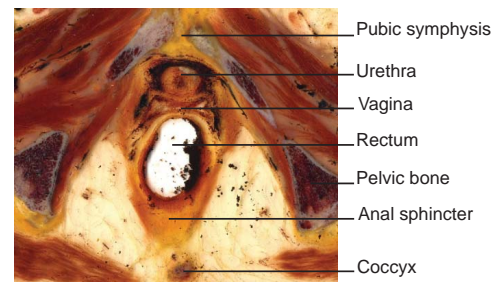
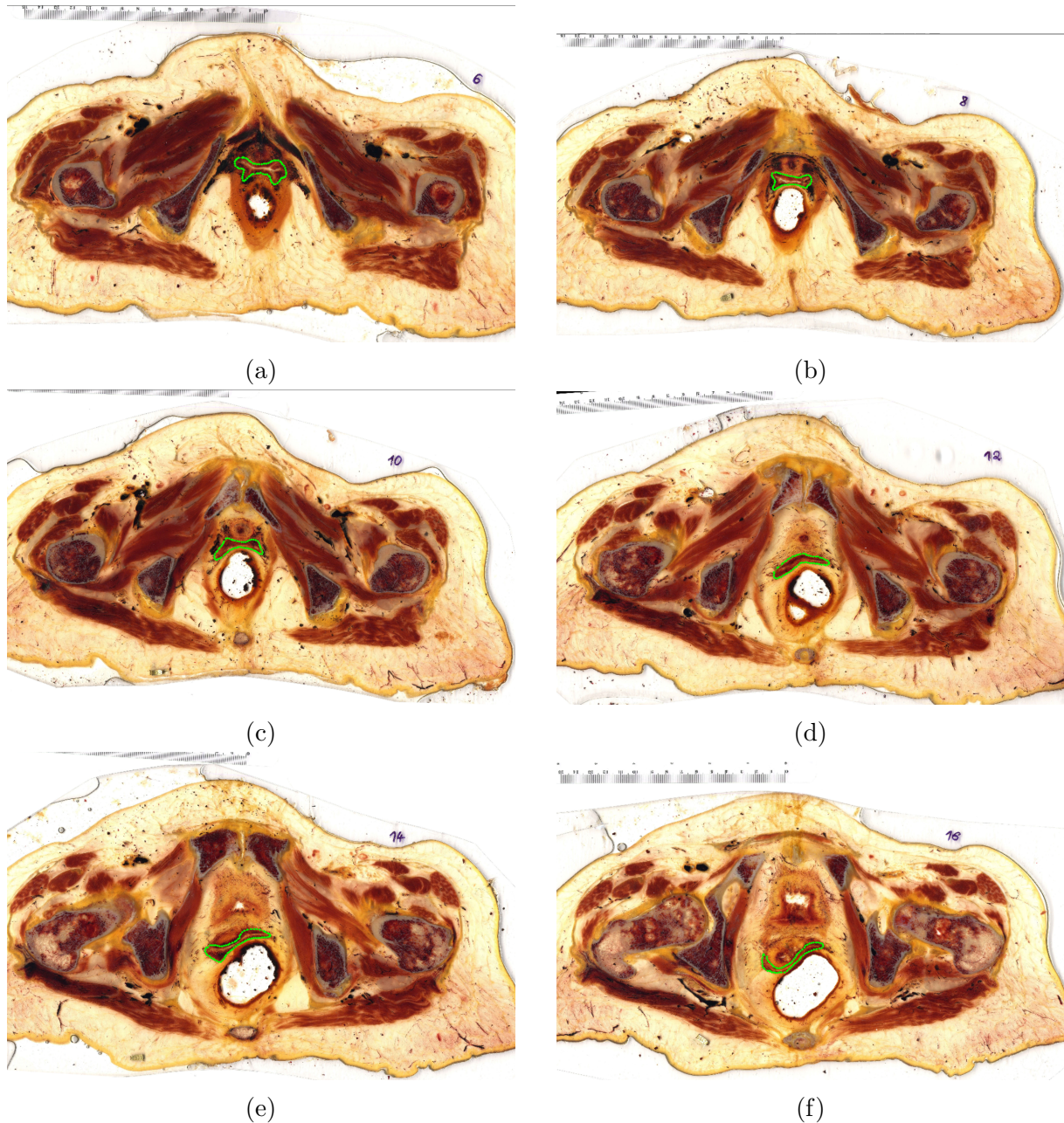


Figure 3.3: E12 slice of female pelvis.

^{2.)} <http://www.surfdriver.com>



3.4 NURBS-based computational model

The model shown in Fig. 3.5 is well suited to map the pelvic floor anatomy into a finite element model for biomechanical analyses. Due to the complex geometry, reconstructed triangular surfaces show artefacts such as high aspect ratio, holes and intersecting faces, see Fig. 3.6. Finite element (FE) simulations are known to fail or at least affect the convergence due to distortion of the mesh under extreme deformations. The convergence problems of bad shaped finite elements can be overcome by the newly proposed smoothed finite element method which has been applied also to problems of soft tissues. Nonsmooth surfaces of the geometric models of the organs is the more relevant problem because it



Figure 3.4: a)-g) E12 plastinated slices of female pelvis at different positions along caudo-cranial direction. Slice numbers (6-18) are provided on the right side of the figures. Vaginal outer surface is outlined by green curve. h) 3D geometry of the female pelvis showing organs, right pubic and coccyx-sacrum bone. The horizontal planes (gray) are the slice planes corresponding to E12 plastinated slices (a-g).

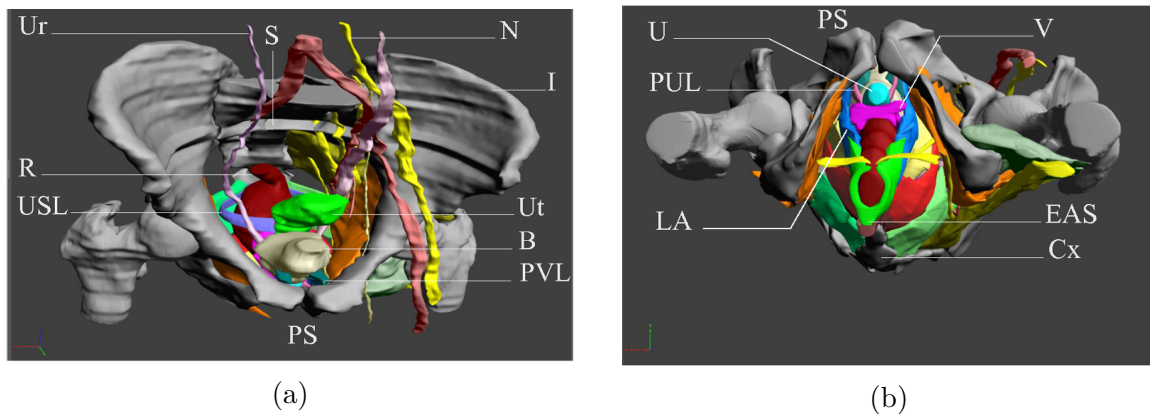


Figure 3.5: a) Computer model of the female pelvic floor including bony pelvis, pelvic viscera, muscles, ligaments and nerves. (BHATTARAI ET AL. [24], FEIL AND SORA [92]).

will prevent convergence in the analysis of the contacts between organs and self-contacts of hollow organs.

Pre-smoothing of the triangular FE geometry reconstructed from the plastinated slices is done by using the 3D mesh processing software MeshLab ^{3.)}. MeshLab not only smoothens the geometries but also transforms the 3D structures into .IGES format that is compatible with the open source pre-processor and postprocessor software Salome ^{4.)} and Rhinoceros 3D or simply Rhino3D software ^{5.)}. Using Rhino software is an important step to repair and convert irregular surfaces into smooth free-form surfaces based on non-uniform rational B-splines (NURBS) as shown in figures 3.7a and 3.7b. NURBS are much easier to handle and

^{3.)} <http://meshlab.sourceforge.net/> ^{4.)} www.salome-platform.org ^{5.)} <http://www.rhino3d.com>



Figure 3.6: Preliminary model of the female pelvic organs right after plastination shown in Salome software, b) Magnified surface of urethra, vagina and pubourethral ligament with highly distorted triangles.

provide smoother geometrical models for the FE calculations. The smoothed geometries are then imported into Salome *to join adjoining pelvic structures, to make organs hollow and to generate three dimensional FE meshes.*

Considering the significant thickness of each pelvic constituents, volume discretization of the geometries have been adopted. A smooth FE mesh as shown in figure 3.7c is constructed from linear tetrahedrons (>900,000 elements only organs are shown in the figure) except for the vagina that has been discretized with quadratic tetrahedral elements (>22,000) which are required for high precision due to contact between the anterior and posterior walls. The bony pelvis can be considered to be rigid thus it is excluded from the mesh for computation, however the attachments to the muscles, ligaments and fasciae are provided at corresponding regions.

The presented model of the female pelvic floor is huge and consists of 24 structures: 5 organs, 8 ligaments, 8 muscles, 1 fasciae and 2 perineal structures (perineal membrane and perineal body). All the tissues possess highly non-linear mechanical behavior. FE simulation on such bulky model requires huge computation time and memory. Higher order finite elements such as quadratic elements are much better than the linear constant stress elements, however, in order to reduce the complication arising from the computation, the FE meshes are constructed with 4 noded three dimensional tetrahedrons. These are also called as linear tetrahedrons since their shape functions are linear polynomials between the nodes.

3.5 Computational model validation and adjustment

The final form of the computational model illustrated in Fig. 3.7 appeared after a series of procedures: plastination, reconstruction, smoothing and meshing that adopts multiple utilities and software. Chances of erroneous model might occur due to two main reasons: firstly, human error by improper handling during plastination and 3D reconstruction and

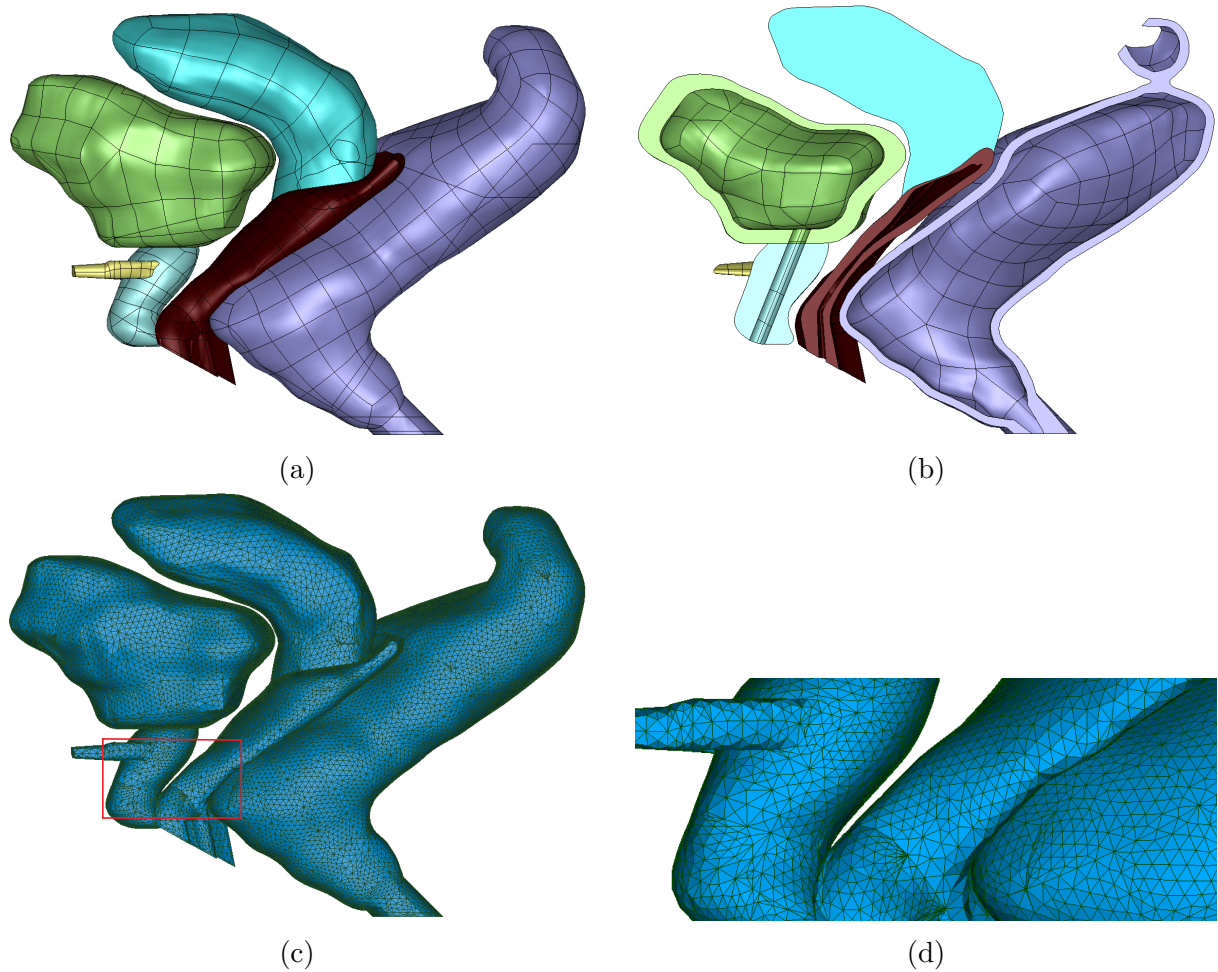


Figure 3.7: a,b) NURBS based smoother, regular and hollow female pelvic organ geometries, c) corresponding FE meshes generated in Salome software, d) Magnified meshes of urethra, vagina and pubourethral ligament with repaired aspect ratio.

secondly, inefficient software communications of data in various formats. Human error can often be minimized from skill personnel, however, technical error from data migration process of data export and import between software in different file formats is inevitable. This leads to a range of negligible to severe damage on the data/model sometimes with a complete mismatch between the original and final information/anatomy. Also, every software are designed to perform specific tasks, available FE software offers limited compatibility to different CAD software; wrong selection might not correctly consider geometrical properties. Therefore, reconstructed geometry must be thoroughly compared with anatomy and adjusted if necessary.

3.5.1 Comparison with anatomy

The dimensions (length, width, height and thickness) of every reconstructed pelvic structures can be measured in the FE meshes that can be compared with anatomical literatures

obtained either by the dissection of the cadaver bodies or medical imaging on living females. Though study may vary between subjects (nulliparous, parous, asymptomatic and symptomatic), average values provides the accuracy of the modeling technique using plastination sheet. For an example, the architecture of the bony pelvis has been compared by HANDA ET AL. [112] and STEIN ET AL. [292]. The topology of the bony pelvis serves as a benchmark for the attached pelvic structures such as ligaments, muscles and connective fasciae. Figure 3.8 provides the measurement of the pelvic bone dimensions at important anatomical sections in females with and without pelvic floor disorders. These measurements can be compared with that performed on the FE mesh in Salome and WinSURF geometry, see Table. 3.2.

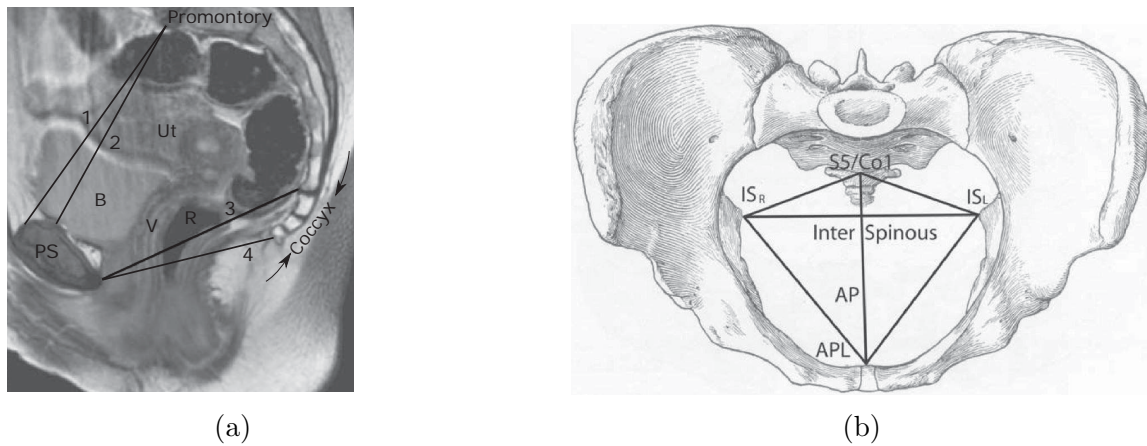


Figure 3.8: Measurement of the distance between two points A and B in a) 2D and b) 3D space.

Table 3.2: Pelvic bone measurement in females with and without pelvic floor disorders. Data are presented as mean \pm standard deviation. All values are in centimeters unless otherwise indicated.

Bony measurement	With PFD	Without PFD	WinSURF	Salome mesh
AP conjugate	12.1 \pm 0.9	12.2 \pm 1.1	10.088	19.745
Obstetrical conjugate	11.9 \pm 1.0	12.0 \pm 1.2	10.0426	19.47
AP diameter	11.7 \pm 0.7	11.7 \pm 0.8	11.1561	21.872
AP outlet	9.7 \pm 1.3	10.3 \pm 1.6	7.899	16.3255
Interspinous diameter	11.4 \pm 1.0	10.7 \pm 0.9	7.8888	16.221
Intertuberous diameter	13.2 \pm 1.5	12.3 \pm 1.4	8.9159	17.837
PS-IS	9.5 \pm 0.45	9.5 \pm 0.45	8.4281	16.328
S5/Co1-IS	7.0 \pm 0.6	6.95 \pm 0.45	5.4501	10.516

Abbreviations: PFD=pelvic floor disorders; AP= anteroposterior, PS=pubic symphysis, IS=ischial spine, S5/Co1=sacral-coccyx junction. AP conjugate=sacral promontory to most superior pubic symphysis, Obstetrical conjugate=shortest distance between promontory to symphysis, AP outlet=shortest distance between symphysis to coccyx tip, AP diameter=distance between inferior symphysis to sacro-coccyx joint.

3.5.2 Shrinkage during plastination

After initial slicing and after three of the processing steps (both acetone baths and curing), the morphological measurement of the anatomical details in the E12 impregnated sheets are recorded using UTHSCSA IMAGE TOOL v.2.0 software. Although, E12 sheet plastination process is a well-established preservation technique for producing transparent slices, *it offers a major disadvantage of shrinkage that can be minimized by proper polymer selection but cannot be completely avoided.* SORA ET AL. [286] computed an average surface shrinkage (decrease in area) of $6.65\% \pm 1.123$ on ultra-thin E12 plastinated sheet of male pelvis, the main factors were assumed due to shrinkage of the epoxy polymer and body slices. However, they also found the E12 polymer shrinkage was less than 0.2%, most of the tissue shrinkage during plastination was summed up by the cold acetone dehydration (2.13%) and room temperature acetone and Methylene chloride bath (4.52%).

3.5.3 Scaled model in WinSURF

The architecture of the female pelvis can also be measured with the help of the measuring tool offered by the WinSURF software. It has the ability to record the position of any anatomical feature in 2D-3D space. As shown in Fig. 3.9a, a ruler (cm) placed in the 2D Bitmap image calibrates the real distance between two points AB=10 cm. This distance can also be measured from 3D visualization in order to estimate the deviation between

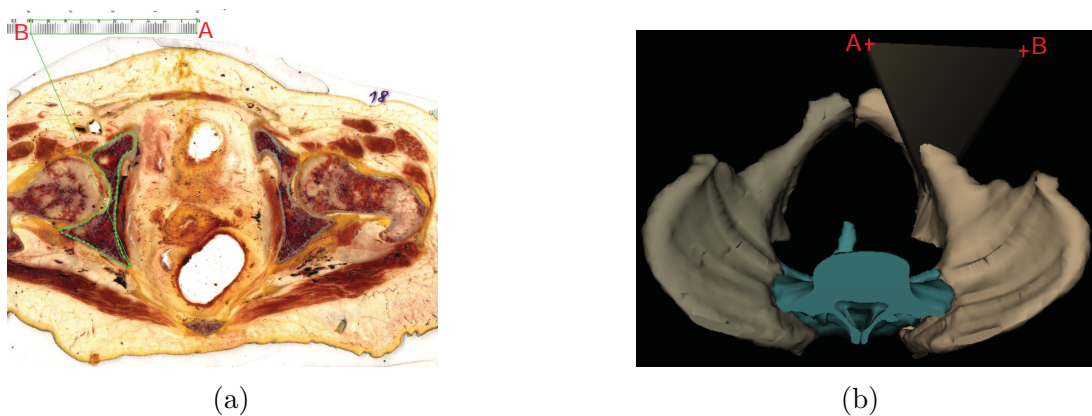


Figure 3.9: Measurement of the distance between two points A and B in a) 2D and b) 3D space.

UTHSCSA IMAGE TOOL v.2.0 and WinSURF. The 3D object of the selected structures (for example bony pelvis in Fig. 3.9b) is reconstructed along with the gray triangular plane constructed by five lines from bony contour to the calibration scale in Fig. 3.9a. In 3D preview, XYZ coordinates of any point can be measured to estimate the position of other structures. For example three dimensional position of selected points A and B in Bitmap scan image 3.9a can again be obtained in 3D plot as A (17.0202362,5.4152225,19.2614456) and B (8.1078880,5.4147778,19.2301285) with a length of AB=8.9124032 cm.

3.5.4 Scale adjustment on the finite element mesh

As shown in Table. 3.2, the size of the pelvic bone in Salome software (and other pelvic structures, accordingly) is larger than the bone measurement from the WinSURF software and the literature. This means uniform or isotropic scaling of the Salome model is necessary when an anatomically realistic computer model is intended. For this purpose, a linear transformation or scale factor can be evaluated from the error occurred during plastination to the Salome. The average linear shrinkage correction factor on E12 slices is $\sqrt{1.0665}=1.03272$, corresponding to a surface area shrinkage of 6.65%. Also, the three dimensional geometry of the pelvic structures reconstructed in WinSURF is reduced by $\approx 11\%$ than the actual size in scanned E12 slices. Lastly, after smoothing and repairing the geometries in CAD software (MeshLab and Rhino3D) and the FE mesh generated in preprocessor software (Salome) is double the size from WinSURF model which requires the mesh to be reduced by half in order to obtain a final computer model representing an actual anatomy. Therefore, assuming the bone features measured in the literature as mentioned in Table 3.2 is correct, an overall scale factor (F) is given as,

$$F = F_{\text{Shrinkage}} \cdot F_{\text{WinSURF}} \cdot F_{\text{CAD-preprocessor}} = 1.03272 \cdot 1.11 \cdot 0.5 = 0.58. \quad (3.1)$$

3.6 Endopelvic fascia model as a single unit

The behavior of the conventional radiological imaging techniques on pelvic tissues depends on their densities; the denser the tissue, the whiter (more radiopaque) the image. The range of densities, from most to least dense, is represented by bone cortex (1.75 g/cm^3 =less white), muscles, organs and fluid (1.0599 g/cm^3 - 1.0 g/cm^3 =gray), fat (0.9094 g/cm^3 =darker gray), and air or gas ($1.225 \cdot 10^{-3} \text{ g/cm}^3$ =black, radiolucent or transparent). The organs, bones and muscles in radiological instruments are clearly distinct, but comparatively softer connective tissue are not easily diagnosed, cannot be easily separated from the connecting organs and muscles. This makes almost impossible to reconstruct fascial geometry in similar fashion of other pelvic structures. Also, cadaver studies are generally performed to estimate the locations and anatomy of the organs, ligaments and muscles, for which soft tissue layers are removed. Both (radiological and cadaver) approach limit the understanding of the pelvic floor support system. Based on the anatomical boundaries and relevant scientific literature (DELANCEY [69], OTCENASEK ET AL. [218]), the space inside the pelvic cavity is defined with a continuous network of soft connective tissue, known as the endopelvic fascia. The created single functional unit fascia geometry envelops the urethra, bladder neck, vagina, cervical ring and rectum. The static and functional anatomy and tissue constituents of the endopelvic fascia is described in section 2.1.4. Fascia and its condensation (ligaments) are later weakened locally and globally in its material level to investigate the development of the pelvic floor disorders.

4 Mathematical Modeling of Pelvic Tissues

Mathematical modeling is the art of translating problems from an application area into tractable mathematical formulations whose theoretical and numerical analysis provides answers useful for the originating application. In other words, it is an activity that has both principles behind it and methods that can be successfully applied. Soft biological tissues, such as female pelvic floor structures exhibit complex mechanical behavior, characterized by highly nonlinear stress-strain response, large strains, hysteresis, rate sensitivity and stress softening. Modeling of soft tissues is a very active field of research continuously increasing in the biomechanics where tissue constituents vary widely among muscles, organs, ligaments and fasciae, and within themselves depending on their functions. In this chapter, continuum constitutive models that describe the biomechanical behavior of the female pelvic structures are presented. In doing so, adequate histomorphological study of every soft tissue are performed, appropriate but simplest constitutive models able to consider experimental data from in-vitro uniaxial tests are taken into account and material parameters are identified via fitting procedures.

4.1 Histomorphological study of pelvic structures

Effective constitutive description of the *in vitro* soft biological tissues to define their deformation process require a fundamental understanding and an intensive knowledge of the tissue histology and morphology. Soft tissues such as organs, ligaments and fasciae in the female pelvic floor contain smooth muscle cells, vascular network, water, extracellular matrix components and proteins mainly elastin and collagen (LANIR [167]). The fibroblasts tissue constituents are abundant and are mainly responsible for the mechanical properties of soft tissues to perform specific physiological functions such as to store and excrete biological waste on demand and to maintain structural support and stability of the pelvic organs. These functions completely depend on the type and proportion of cells the structures are made of and are discussed in this section. For anatomical descriptions, reader can refer to section 2.1.

4.1.1 Anterior compartment: ureter, bladder and urethra

Histologically, the lumen of the ureter is lined by the transitional epithelium (also called urothelium), and has a longitudinal and circular smooth muscle layer that creates the peristaltic contractions to move the urine into the bladder without an aid of gravity, see Fig. 4.1. Similarly, the bladder is also lined with transitional epithelium and lamina propria but it is well covered by fat cells, serosa and thicker, irregular crisscrossing bands of smooth muscle known as the detrusor muscle that contracts to allow the urine to come out through urethra. However, tissue constituents of the urethra vary widely along its length. The proximal 2/3rd of the urethra near the bladder neck is lined with transitional epithelium cells. As one moves to caudal, the epithelium becomes stratified squamous along the proximal 1/3rd of the urethral length. The mucosa here is highly folded and the muscularis consists of two layers of smooth muscle and is reinforced by the striated

muscles.



Figure 4.1: Histologic cross section of the ureter stained with hematoxylin and eosin. [Source: University of Wisconsin Medical School-Department of Anatomy.]

4.1.2 Middle compartment: uterus and vagina

Histological images of the uterus as shown in Fig. 4.2a is composed of three layers: a) outer serosa or perimetrium layer, b) middle muscularis or myometrium layer and c) inner mucosal or endometrium layer. The endometrium itself is divided into two layers, the stratum functionalis and stratum basalis. During the menstrual cycle, the stratum functionalis expands and vascularizes and is subsequently sloughed off during the process of menstruation, whereas the stratum basalis remains relatively constant. The powerful muscles of the uterus dilates and contracts to accommodate a growing fetus and push it through the birth canal. On the other hand, the vagina is lined by vaginal mucosa which is composed of an upper layer of stratified squamous non-keratinized epithelium and a thick embedded layer of dense connective tissue or elastic lamina propria, see fig. 4.2b. Larger veins are located in this layer. The cells of the vaginal wall typically contain a relatively large amount of cytoplasm because they produce and store glycogen. The fibromuscular and the adventitia provides mechanical strength and neighbours to the surrounding structures. The cervix is an important site of epithelial transition. The upper cervix (endocervix) is lined by a simple columnar epithelium that contains mucous-secreting cells. In contrast, the lower cervix (ectocervix) is lined by a stratified squamous epithelium. The transition point between these two epithelia is known as the external os.

4.1.3 Posterior compartment: rectum and anal canal

The rectum-anal canal features an important overlay of the epithelial lining, see Fig. 4.3. The mucosa forms the innermost layer of the rectum that is in contact with fecal matter. The mucosa is composed of the simple columnar epithelium that secretes mucus from specialized cells known as goblet cells. Next is the muscularis layer, which contains layers of visceral (smooth) muscle. Contractions of the muscularis allow the rectum to expel

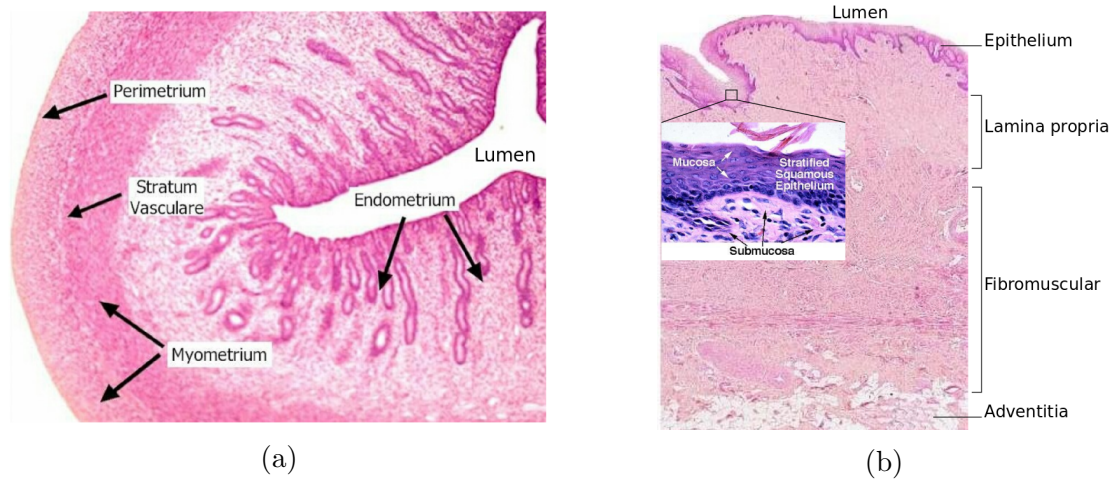


Figure 4.2: The histological layers of a) the uterus, and b) the vagina.

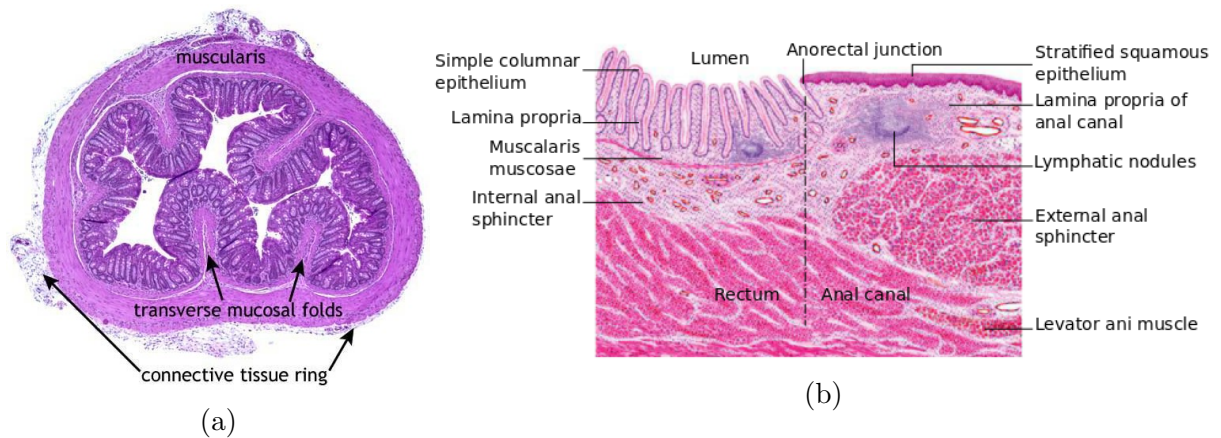


Figure 4.3: The histological layers of a) the rectum [Source: Deltagen.Inc], and b) the anorectal junction [Source: Studyblue, Florida International University].

feces during defecation. The anus, on the other hand, has a variety of mucosa layers: upper simple columnar epithelium, middle stratified squamous non-keratinized epithelium and lower part covered by true skin. The external anal sphincter regulates the anal canal to relax during defecation, whereas, the internal anal sphincter is made of visceral (smooth) muscle and is continuous with the muscularis layer of the rectum. Also, the levator ani muscle at the recto-anal junction fuses with the longitudinal smooth muscle coat of the rectum. The anorectal junction is the site where there is a transition from the simple columnar epithelium of the colon to the stratified squamous epithelium of skin.

4.1.4 Ligaments

Histologically, the CL and USL are visceral ligaments with bilateral mesentery-like structures containing blood vessels, connective tissue, lymphatics and nerves embedded in adipose (fat) tissue that run under the rectovaginal peritoneum (CAMPBELL [51]), see

Fig. 4.4. They connect the apical part of the female genital to the pelvic side walls

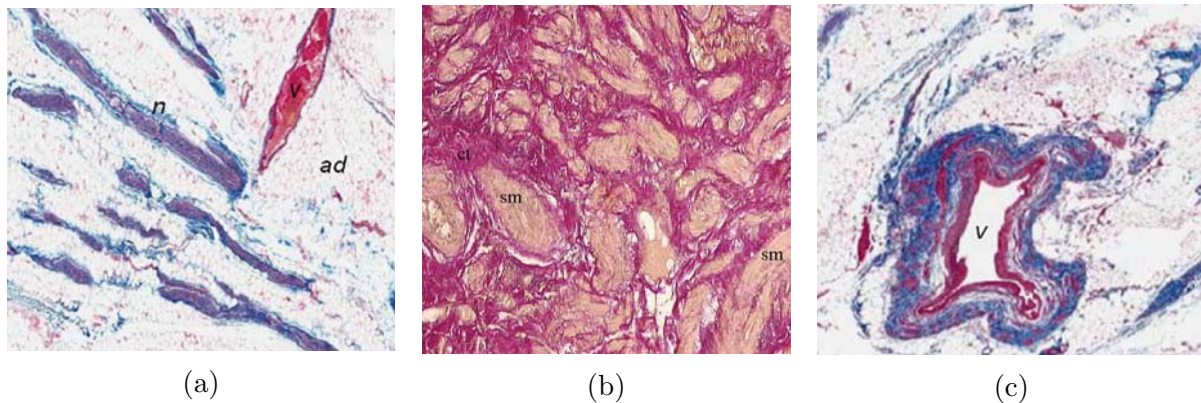


Figure 4.4: Histomorphological analysis of the USL (a,b) and the CL (c). a) trichrome staining of the deep USL showing mainly nerve fibers (n), adipose tissue (ad), and a few vessels (v) (RAMANAH ET AL. [248]) b) hematoxylin staining (x100) of the superficial (cervical third) portion of USL showing considerable amount of smooth muscle (sm) cells and connective tissue (ct) (GABRIEL ET AL. [106]) c) trichrome staining of the CL showing mainly vessels (RAMANAH ET AL. [248]).

where the tissue constituents vary in the amount of each of them from place to place. The USL is a multifaceted, mesentery-like structure containing loose connective tissue, smooth muscle, vessels and autonomic nerve fiber from the IHP, with contributions from sacral nerves (RAMANAH ET AL. [248]). A large amount of adipose tissue in USL is evident from histological evaluation (COLE ET AL. [64]), see Fig. 4.4a. The distal or cervical attachment of the ligament is composed of closely packed bundles with smooth muscle peritoneal connective tissue, abundant medium-sized and small blood vessels, and small nerve bundles, see Fig. 4.4b (CAMPBELL [51], IWANAGA ET AL. [131]). The intermediate part is predominantly composed of connective tissue and a few scattered smooth muscle fibers, nerve elements, and blood vessels. The sacral third is almost entirely composed of loose strands of connective tissue and intermingled fat, with few vessels, nerves, and lymphatics. Whereas, the CL consists mainly of vascular, neural and areolar tissue containing fat and a delicate network of connective tissue between different structures, see Fig. 4.4c. It can be divided into vascular and neural sections: the cranial portion and parametrium is more vascular and the caudal portion and paracervix is more neural which contains part of the inferior hypogastric plexus (IHP). Though, the deep USL and the caudal CL are closely related to the IHP, the deep part has more autonomous nerve fibers (BUTLER-MANUEL ET AL. [48]).

4.1.5 Endopelvic fascia

Independent studies have been performed to demonstrate the morphology, fiber types and proportion of the pelvic soft tissues (BRIEU ET AL. [42], NAGATA ET AL. [205], SASAKI ET AL. [270]). As an important structural component in the female pelvic floor, the soft fascia tissue is composed of elastin, collagen and non-vascular smooth muscle

fibers, penetrated by nerves, blood and lymph vessels (BERGLAS AND RUBIN [22]). A wide variety of tissue constituents exists along the vaginal walls depending on the function (NAGATA ET AL. [205], PETROS [239]). Histological examinations on the female parietal fascia of the pelvic floor shows abundance of elastic fibers irrespective of parity, see Fig. 4.5a (HIRATA ET AL. [118], SASAKI ET AL. [270]). These elastic fibers are perpendicular

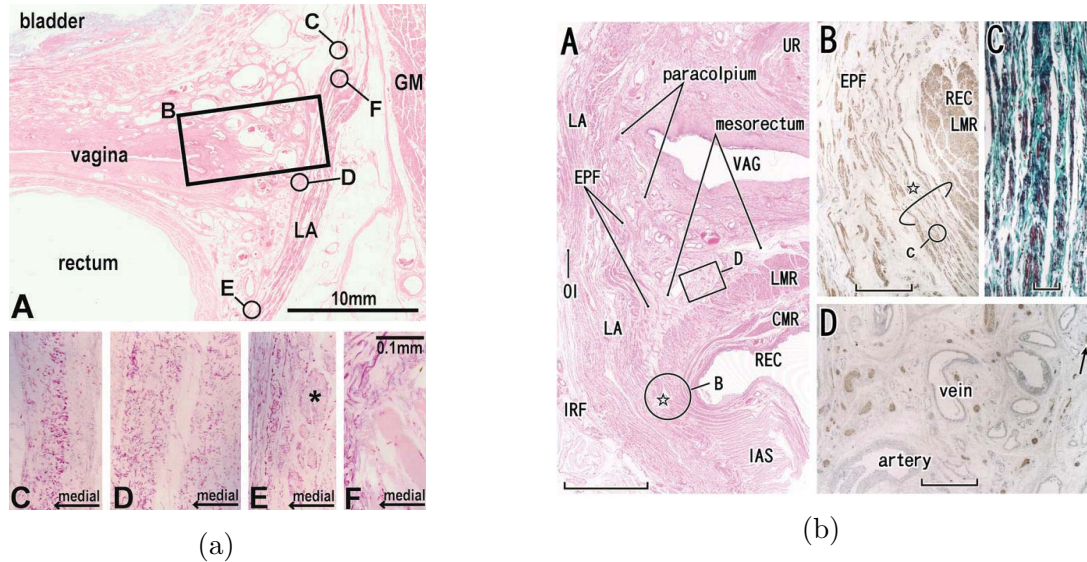


Figure 4.5: a) Histology of the female pelvic parietal fascia. Panel **A** shows topographical anatomy of pelvic tissues with HE staining. Panel **C-F** shows elastic fibers near bladder, vagina, rectum (asterisk=smooth muscle) and levator ani muscle, respectively with aldehyde-fuchsin staining (HIRATA ET AL. [118]). b) Histology of the visceral fascia at the level of lower paracolpium. Panel **A** shows topographical anatomy of pelvic tissues with HE staining. Panel **B** (star encircled in panel **A**) shows smooth muscle bundles of endopelvic fascia (EPF) with immunohistochemistry. Panel **C** shows elastic fibers (black) in the conjoint smooth muscle bundle in panel **B** stained with with elastica-Masson. Panel **D** shows nerves in the paracolpium or mesorectum with immunohistochemistry. (SASAKI ET AL. [270]).

to most of the levator ani muscle fibers running along the superoinferior axis. On the other hand, the smooth muscles are exceptionally abundant only in the parietal fascial space enclosed by the vagina, rectum, and levator ani and fiber bundles run almost parallel to each other. The thickening of the parietal fascia, such as ATRFP is mainly comprised of collagen (84 % with abundance of type III collagen), elastin (13 %), and smooth muscle (3 %) (MOALLI ET AL. [198]).

There is some disagreement with the concept of pubocervical and rectovaginal fascia. Some authors described their absence from their histological studies (KRANTZ [163], RICCI ET AL. [253]), however some authors strongly agree on the existence as a dissectable layer between vagina and adjacent organs (OTCENASEK ET AL. [218], RICHARDSON [254], UHLENHUTH ET AL. [307]). Three layers have been found on a dissection of the anterior vaginal wall: outer muscosal layer (nonkeratinized squamous ep-

ithelium overlying a lamina propria), middle muscular layer (smooth muscle, collagen and elastin) and inner adventitial layer (collagen and elastin) (WEBER AND WALTERS [321]). The visceral (pubocervical and rectovaginal) fascia, also referred as the adventitial layer of the vagina, is composed of collagen and elastin that separates the muscular wall of the vagina and the paravaginal tissues.

Types I and III are the most common collagen fibers in vaginal tissues. Type I fibers are the more abundant, and type III contributes more of the elastic properties of the tissue (LIAPIS ET AL. [174]). Collagen metabolism, breakdown and turnover to abundance of type III are markers of pelvic floor dysfunctions (PFDs) (CHEN ET AL. [55]). Elastin on the other hand provides much of the elastic properties, but has little or no role in the development of PFDs (JACKSON ET AL. [132]). The smooth muscle as shown in Fig. 4.5b is a major component of the endopelvic fascia (MILLEY AND NICHOLS [196], SASAKI ET AL. [270]). There is a considerable variations in the thickness and densities of the smooth muscle on the vaginal wall (MORGAN ET AL. [202]), on women with prolapse compared to healthy women (BOREHAM ET AL. [38]). On the other hand, dissection of the paracolpium shows the pubocervical and the rectovaginal septum as a fibrous network of thick elastin and collagen fibers with few or no smooth muscles (HINATA ET AL. [117]). These difference are likely due to specimen variations in age, parity and staining methods: women with prolapse have lesser smooth muscle contractility and force maintenance (BOREHAM ET AL. [37]).

4.2 Finite deformation of pelvic tissues

One of the most common material characteristic of soft tissue is its potential to undergo large, non-linearly elastic deformation which is termed as hyperelastic material response if a strain energy exists. When subjected to uniaxial mechanical load, they gain a J-shaped stress-strain curve, which can be figuratively subdivided into a toe, heel and linear region,

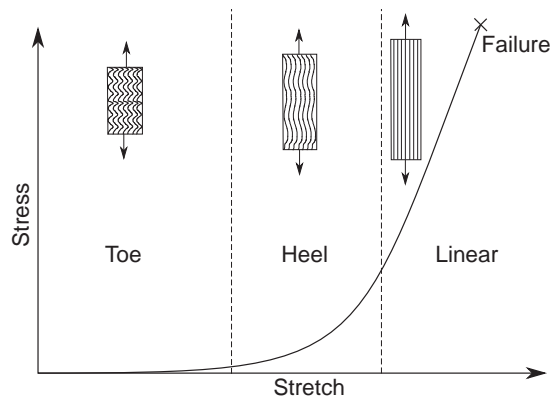


Figure 4.6: Nonlinear stress-stretch response of soft biological tissues specimen in uniaxial tension showing the configuration of collagen fibers. Elastin is the major load bearing component at small stretch or toe region. Collagen fibers aligns towards loading direction in heel region and progressively recruits at large stretch (linear region) leading a J-shaped stress-stretch curve until failure.

see Fig. 4.10 (HOLZAPFEL [120], MISOF ET AL. [197]). At the characteristic toe region, the mechanical behavior of the tissue is largely dominated by elastin fibers that uncoils reversibly when loaded. The specimen undergoes large deformation or stretch with a small increase in stress. The collagen fibers remains relaxed and undulated or coiled until loaded to the heel region. The stress-stretch relation is approximately linear and the slope of the curve is low. At higher stretch level, collagen fibers are progressively aligned in the loading direction and recruited. The stress-strain behavior becomes linear again with a dramatic increase of the slope. The material behaves stiffer and becomes more difficult to extend which dominates the mechanical response.

The J-shaped curve can vary at a number of different structural levels, in soft fibrous tissues depending on the tissue constituents mainly elastin and collagen. Tissue rich in elastin network and unorganized collagen filaments behaves isotropic in nature with longer toe region, whereas, tissue abundance of collagen fibers form stronger fibrous networks with shorter toe region and a rapid tissue stiffening whenever a stretching force is applied (HUMPHREY [128], FUNG ET AL. [103], HOLZAPFEL ET AL. [121], ZENINALI-DAVARANI ET AL. [338]). Also, the overall stiffness depends on the number of collagen fibers aligned along loading direction to share appreciable loads. Collectively, tissue proteins together with smooth muscles, water and vascular network, their individual properties and structural management also comprise other mechanical characteristics such as anisotropy, incompressibility, softening, viscoelasticity (relaxation, creep and hysteresis), active contractility, growth and remodeling.

4.2.1 Uniaxial tensile tests on female pelvic tissues

In order to characterize the real finite deformation behavior of any material via experimental methods, the selected loading modes should be similar to the functional loading in the desired case of application. Typical test setup for the characterization of soft biological tissues includes uniaxial and planar biaxial machines for isotropic and orthotropic tissues, respectively. Among them, uniaxial tensile test is most commonly used in which a strip of tissue specimen is stretched from both ends and the load-extension readings are recorded to compute the stress and strain measures to describe the finite deformation. Two stress measures widely used in the literatures are the Cauchy (or true) stress ($\sigma = F/A$) and the engineering (or first Piola-Kirchhoff, or nominal) stress ($P = F/A_0$), where F , A and A_0 are the applied force, current and initial cross-sectional area. The nonlinear strain measures to describe finite deformation are the stretch ratio ($\lambda = L/L_0$), the nominal strain ($\epsilon = \lambda - 1$) and the Green-Lagrange strain ($E = \frac{1}{2}(\lambda^2 - 1)$), where L and L_0 are the current and the initial length of the specimen. The stress vs strain/stretch curve as shown in Fig. 4.10 is plotted to determine the parameters that fit the mechanical response of the test. As an advantage, this type of characterization eliminates size effects, which means different size of specimens from the same material will have the same stress-strain/stretch curve.

Collection of every type of human pelvic tissue for the experimental study with desired level of physiopathology (healthy, incontinence or prolapse) is realistically impossible. Following the code of ethics, specimens are generally obtained surgically either as a

futile body part from the living volunteer or from a cadaver dissection as a human donor for scientific study. As an alternative, animals mostly rat (FEOLA ET AL. [93], MOALLI ET AL. [199], POELLMANN ET AL. [241], YOSHIDA K. [334]) rabbit (RAJASEKARAN ET AL. [247]), monkey (VARDY ET AL. [310]), pig (BECKER AND DE VITA [20], MANOOGIAN ET AL. [186]) and sheep (KNIGHT ET AL. [160], RUBOD ET AL. [265]) are often used as experimental subjects. Though animal specimens possess certain benefits over human testing as i) fresher subjects to raise for scientific testing and ii) larger source of tissue samples from many animals, the morphology and physiology of the pelvic cavity from these quadrupeds differ significantly from human (ABRAMOWITCH ET AL. [1]). The typically used preservation of tissues by freezing and refrigeration before mechanical testing is known to modify the composition of the tissue and changes the mechanical behavior of most tissues considerably (NGUYEN ET AL. [206]). Also, ethical committees on human and animal testing sometimes limit the study for which desired data from literatures are useful. In this manner, biomechanical characterization of the pelvic tissues used for the numerical study in this thesis are collected from literature as recent as possible that are cited wherever required, see Fig. 4.7.

Recent advances in soft tissue mechanics provides a wealth of information on the mechanical characterization of pelvic tissues in vitro. Different methods and testing protocols have been described depending on the type and constituents of tissue to be tested, see Table 4.1. But the material characterization in many cases is fairly superficial due to lack of robust constitutive models that can collectively integrate the influence of water, smooth muscles, elastin and collagen fibers. Attempts have been made to develop physiologically relevant models that account for the histological and morphological structure of the pelvic tissues causing non-linear elasticity, tissue anisotropy (BRIEU ET AL. [42], HOLZAPFEL ET AL. [121]), viscoelasticity (PENA ET AL. [228]) and smooth muscle contractility (VINK ET AL. [312]), however none of them fully considers the overall in-vivo mechanics of the soft tissue. Herein, studies still implement the simple isotropic mathematical formulations ranging from linearly elastic (MARTINS ET AL. [193], PENG ET AL. [230]) to hyperelastic models (MARTINS ET AL. [192], RIVAUX ET AL. [256], RUBOD ET AL. [264]) to describe the characteristics of the curves obtained from the uniaxial tensile tests on soft tissue specimens.

4.2.2 Non-linear strain energy

An appropriate modeling of the soft tissue mechanical response is of critical importance. For such materials, neither the force-elongation nor the stress-strain/stretch relationship agrees with the linearly elastic Hooke's law. Macroscopically, for these so called *Green elastic or hyperelastic materials*, the highly nonlinear, incompressible and elastic stress-strain relation can be widely derived using the *Helmholtz free-energy function* (W) defined per unit reference volume rather than per unit mass. The scalar-valued energy function (W) is referred as the strain energy function (SEF) or stored energy function if it depends only on the deformation gradient \mathbf{F} , i.e. $W := W(\mathbf{F})$ (GREEN [109], GREEN [110]). For

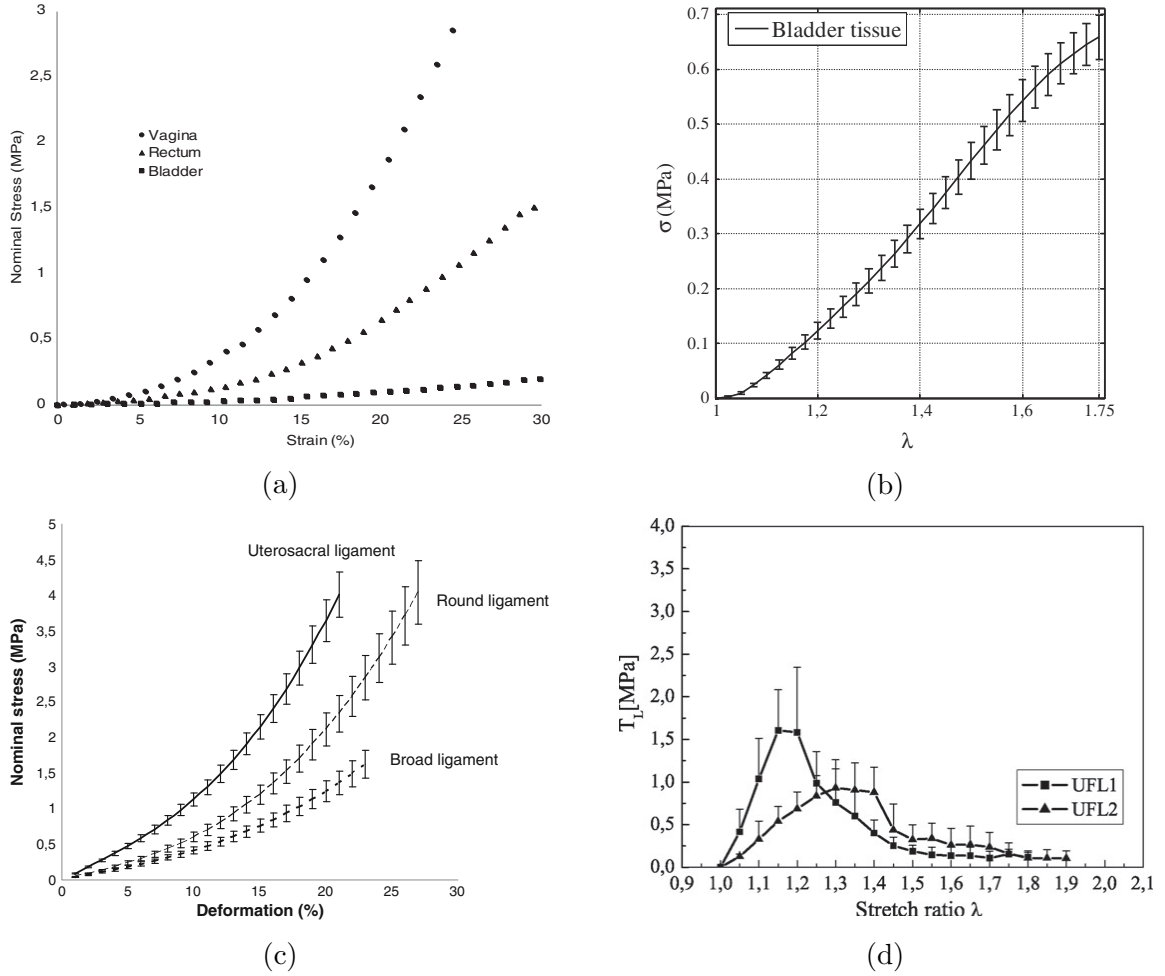


Figure 4.7: Uniaxial stress-strain/stretch curves of female pelvic floor tissues a) Organs (RUBOD ET AL. [266]), b) Bladder (MARTINS ET AL. [192]), c) Ligaments (RIVAUX ET AL. [256]), and d) Fascia (KIRILOVA ET AL. [148]).

incompressible hyperelastic materials, the stress is determined by the deformation only to within a hydrostatic pressure p (TRUSDELL AND NOLL [305]), which gives the strain energy function as:

$$W = W(\mathbf{F}) - p(J - 1). \quad (4.1)$$

Here, the scalar p is an indeterminate *Lagrange multiplier* and can be determined from the equilibrium equations and the boundary conditions. $J := \det[\mathbf{F}]$ is the determinant of the second order deformation gradient tensor. In reference or stress-free configuration, the deformation gradient equalises to the identity tensor rendering the strain energy function zero, i.e.

$$W(\mathbf{F}) \begin{cases} = 0, & \text{if } \mathbf{F} = \mathbf{I} \\ \geq 0, & \text{if } \mathbf{F} \neq \mathbf{I}. \end{cases} \quad (4.2)$$

For any scalar-valued function W depending on the deformation gradient \mathbf{F} , the derivative with respect to the deformation gradient tensor gives the first Piola-Kirchhoff stress tensor

Table 4.1: Experimental studies performed to characterize the biomechanical behavior of female pelvic floor soft tissues.

Literature	Structure	Material properties measured
BRANDÃO ET AL. [40]	Uterus	passive stress relaxation
KAUER ET AL. [147]	Uterus	viscoelastic, nonlinear, nearly incompressible, isotropic continuum
PEARSALL AND ROBERTS [227]	Uterus	elastic moduli and tensile strength are measured
CHANTEREAU ET AL. [53]	Vagina	Hyperelastic behavior is observed and tissue stiffness is measured
CHUONG ET AL. [59]	Vagina	Viscoelastic properties
RUBOD ET AL. [265]	Vagina	Hyperelastic parameters
MARTINS ET AL. [192]	Bladder	Nonlinear mechanical response, tissue stiffness is measured
RUBOD ET AL. [266]	Bladder	Hyperelastic parameters
CHANTEREAU ET AL. [53]	Ligaments	Hyperelastic behavior is observed and tissue stiffness is measured
MARTINS ET AL. [193]	Ligaments	Stiffness is measured
RIVAUX ET AL. [256]	Ligaments	Hyperelastic parameters
KIRILOVA ET AL. [148]	Fascia	Young's modulus is measured
JANDA [135]	Muscles	-

(or *Lagrangian stress tensor*) (FUNG [102]):

$$\mathbf{P} := \frac{\partial W(\mathbf{F})}{\partial \mathbf{F}} - \frac{\partial p(J-1)}{\partial \mathbf{F}} \equiv \frac{\partial W(\mathbf{F})}{\partial \mathbf{F}} - p\mathbf{F}^{-T}, \quad (4.3)$$

which relates the forces in current configuration with area in reference configuration. The first Piola-Kirchhoff stress tensor is not symmetric and is generally inconvenient to use in a stress-strain law in which the strain tensor is always symmetric. However, this stress tensor is usually used for the reduction of laboratory experimental data (FUNG [104]).

The deformation gradient tensor can be decomposed into positive definite and symmetric right material stretch \mathbf{U} or left spatial stretch tensor \mathbf{V} and a rotation tensor \mathbf{R} as $\mathbf{F} = \mathbf{R} \cdot \mathbf{U} = \mathbf{V} \cdot \mathbf{R}$. Here, \mathbf{R} is proper orthogonal tensor satisfying, $\mathbf{R}^T \mathbf{R} = \mathbf{I}$ and $\det[\mathbf{R}] = 1$. Introducing the symmetric and positive definite right Cauchy-Green stretch tensor $\mathbf{C} = \mathbf{F}^T \mathbf{F} = \mathbf{U}^2$, the SEF can be alternatively expressed in terms of \mathbf{C} (for simplicity of notation the name of the function W is not changed) (GREEN [109], GREEN [110])

$$W := W(\mathbf{F}) \equiv W(\mathbf{C}). \quad (4.4)$$

According to the Doyle-Ericksen formula, the SEF depending on the finite strain tensor if differentiated with respect to the finite strain tensor, for example the right Cauchy-Green

stretch tensor gives the second Piola-Kirchhoff stress tensor

$$\mathbf{S} = 2 \frac{\partial W(\mathbf{C})}{\partial \mathbf{C}} - p \mathbf{F}^{-1} \mathbf{F}^{-T}, \quad (4.5)$$

where $\mathbf{F}^{-1} \mathbf{F}^{-T} = \mathbf{C}^{-1}$. This form of stress relates forces in initial configuration to the experimented area in initial configuration.

Constitutive equations in terms of invariants

A scalar-valued isotropic tensor function $W(\mathbf{C})$ is invariant under an orthogonal rotation tensor \mathbf{Q} (HOLZAPFEL ET AL. [121])

$$\text{i.e.} \quad W(\mathbf{C}) := W(\mathbf{Q} \mathbf{C} \mathbf{Q}^T), \quad (4.6)$$

then the SEF of an isotropic hyperelastic material equations 4.1, 4.4 and 4.6 can be expressed in terms of the principal invariants I_1, I_2, I_3 of its arguments (for example, \mathbf{C} or \mathbf{B}) (TRUSDELL AND NOLL [305] SIMO AND HUGHES [281]) as

$$W(\mathbf{C}) = W(I_1(\mathbf{C}), I_2(\mathbf{C}), I_3(\mathbf{C})), \quad (4.7)$$

with $I_1(\mathbf{C}) := \text{tr}[\mathbf{C}]$, $I_2(\mathbf{C}) := \frac{1}{2} \{(\text{tr}[\mathbf{C}])^2 - \text{tr}[\mathbf{C}^2]\}$ and $I_3(\mathbf{C}) := \det[\mathbf{C}] = (\det[\mathbf{F}])^2 = J^2$. For the stress-free reference configuration, the invariants $I_1 = I_2 = 3$ and $I_3 = 1$ results $W = 0$.

Incompressible, isotropic, hyperelastic material

The strain-energy function for the incompressible material using equation 4.1 can be expressed in terms of invariants of its argument as:

$$W = W(\mathbf{C}) - p(J - 1) = W(I_1(\mathbf{C}), I_2(\mathbf{C}), I_3(\mathbf{C})) - p(J - 1). \quad (4.8)$$

When the material is incompressible, its volume (V) remains constant throughout deformation process

$$\text{i.e.} \quad J = \frac{V_{\text{current}}}{V_{\text{reference}}} = \det \mathbf{F} = 1, \quad (4.9)$$

leading kinematic constraint $I_3 = \det \mathbf{C} = \det \mathbf{B} = (\det[\mathbf{F}])^2 = J^2 = 1$ and therefore the SEF equation 4.8 only dependent on two invariants:

$$W = W(I_1(\mathbf{C}), I_2(\mathbf{C})) - p(J - 1). \quad (4.10)$$

The second Piola-Kirchhoff stress in terms of invariants can be derived using chain rule as:

$$\mathbf{S} = 2 \frac{\partial W(\mathbf{C})}{\partial \mathbf{C}} - p \mathbf{F}^{-1} \mathbf{F}^{-T} = 2 \sum_{i=1,2} \frac{\partial W}{\partial I_i(\mathbf{C})} \frac{\partial I_i(\mathbf{C})}{\partial \mathbf{C}} - p \mathbf{C}^{-1}. \quad (4.11)$$

The partial derivatives of the invariants with respect to \mathbf{C} are

$$\begin{aligned}\frac{\partial I_1}{\partial \mathbf{C}} &= \frac{\partial \text{tr}[\mathbf{C}]}{\partial \mathbf{C}} = \mathbf{I} \\ \frac{\partial I_2}{\partial \mathbf{C}} &= \frac{1}{2} \left(2\text{tr}[\mathbf{C}]\mathbf{I} - \frac{\partial \text{tr}[\mathbf{C}^2]}{\partial \mathbf{C}} \right) = I_1\mathbf{I} - \mathbf{C}.\end{aligned}\quad (4.12)$$

where \mathbf{I} is the identity tensor. Substituting the partial derivatives in Eqn.(4.11), the constitutive model to characterize the isotropic hyperelastic materials at finite strain can be given as

$$\begin{aligned}\mathbf{S} &= 2 \sum_{i=1,2} \frac{\partial W}{\partial I_i} \frac{\partial I_i}{\partial \mathbf{C}} - p\mathbf{C}^{-1} \\ &= 2 \left[\left(\frac{\partial W}{\partial I_1} + I_1 \frac{\partial W}{\partial I_2} \right) \mathbf{I} - \frac{\partial W}{\partial I_2} \mathbf{C} \right] - p\mathbf{C}^{-1}.\end{aligned}\quad (4.13)$$

In the current or spatial configuration, the true or Cauchy stress $\boldsymbol{\sigma}$ uses the left Cauchy-Green strain tensor. It follows the second Piola-Kirchhoff stress \mathbf{S} by the Piola transformation $\boldsymbol{\sigma} = J^{-1}\mathbf{F}\mathbf{S}\mathbf{F}^T$ to get

$$\boldsymbol{\sigma} = 2J^{-1} \left[\left(\frac{\partial W}{\partial I_1} + I_1 \frac{\partial W}{\partial I_2} \right) \mathbf{B} - \frac{\partial W}{\partial I_2} \mathbf{B}^2 \right] - p\mathbf{I}, \quad (4.14)$$

where, $\mathbf{B} = \mathbf{F}\mathbf{F}^T = \mathbf{V}^2$ is the left Cauchy-Green stretch tensor.

Constitutive equations in terms of principal stretches

Isotropic nonlinear elastic models can also be expressed in terms of principal stretch ratios for simplicity as:

$$W = W(\lambda_1, \lambda_2, \lambda_3) - p(J - 1), \quad (4.15)$$

where $\lambda_i, i = 1, 2, 3$ are the eigenvalues of the right material stretch tensor \mathbf{U} and can be expressed as:

$$\mathbf{U} := \begin{bmatrix} \lambda_1 & 0 & 0 \\ 0 & \lambda_2 & 0 \\ 0 & 0 & \lambda_3 \end{bmatrix}.$$

Then the right Cauchy-Green tensor, $\mathbf{C} := \mathbf{U}^2$ can be rewritten as:

$$\mathbf{C} := \begin{bmatrix} \lambda_1^2 & 0 & 0 \\ 0 & \lambda_2^2 & 0 \\ 0 & 0 & \lambda_3^2 \end{bmatrix},$$

In terms of the principal stretches, the invariants takes the form

$$\begin{aligned}I_1(\mathbf{C}) &= \lambda_1^2 + \lambda_2^2 + \lambda_3^2 \\ I_2(\mathbf{C}) &= \lambda_1^2\lambda_2^2 + \lambda_2^2\lambda_3^2 + \lambda_3^2\lambda_1^2 \\ I_3(\mathbf{C}) &= J^2 = \lambda_1^2\lambda_2^2\lambda_3^2.\end{aligned}\quad (4.16)$$

Then the first Piola-Kirchhoff stress becomes:

$$\mathbf{P} = \frac{\partial W(\lambda_1, \lambda_2, \lambda_3)}{\partial \mathbf{F}} - p\mathbf{F}^{-\text{T}} \equiv \sum_{i=1,2,3} \frac{\partial W}{\partial \lambda_i} \frac{\partial \lambda_i}{\partial \mathbf{F}} - p\mathbf{F}^{-\text{T}}, \quad (4.17)$$

where $\frac{\partial \lambda_i}{\partial \mathbf{F}} = n_i \otimes N_i$ with n_i and N_i are the eigenvectors of \mathbf{B} and \mathbf{C} stretch tensors, respectively and corresponding to the eigenvalues λ_i^2 . Similarly, the other forms of stresses, second Piola-Kirchhoff stress \mathbf{S} and Cauchy stress $\boldsymbol{\sigma}$ can be expressed using $\mathbf{S} = \mathbf{F}^{-1}\mathbf{P}$ and $\boldsymbol{\sigma} = \mathbf{P}\mathbf{F}^{\text{T}}$ as:

$$\begin{aligned} \mathbf{S} &= \mathbf{F}^{-1} \sum_{i=1,2,3} \frac{\partial W}{\partial \lambda_i} \frac{\partial \lambda_i}{\partial \mathbf{F}} - p\mathbf{F}^{-1}\mathbf{F}^{-\text{T}} \equiv \sum_{i=1,2,3} \frac{1}{\lambda_i} \frac{\partial W}{\partial \lambda_i} \frac{\partial \lambda_i}{\partial \mathbf{F}} - p\mathbf{C}^{-1} \\ \boldsymbol{\sigma} &= \sum_{i=1,2,3} \frac{\partial W}{\partial \lambda_i} \frac{\partial \lambda_i}{\partial \mathbf{F}} \mathbf{F}^{\text{T}} - p\mathbf{F}^{-\text{T}}\mathbf{F}^{\text{T}} \equiv \sum_{i=1,2,3} \lambda_i \frac{\partial W}{\partial \lambda_i} \frac{\partial \lambda_i}{\partial \mathbf{F}} - p\mathbf{I}. \end{aligned} \quad (4.18)$$

Single phase tissue mechanics

Assuming the pelvic tissues to be isotropic, hyperelastic and incompressible materials, a three term polynomial strain energy function (TRUSDELL AND NOLL [305]):

$$W = C_{10}(I_1 - 3) + C_{01}(I_2 - 3) + C_{20}(I_1 - 3)^2 - p(J - 1), \quad (4.19)$$

is used to model the mechanical behavior of tissues under load, where C_{10} , C_{01} and C_{20} are the material parameters with dimensions of stress (MPa). For an incompressible hyperelastic material with preserved volume ($\lambda_1\lambda_2\lambda_3 = 1$) under uniaxial tension, assuming $\lambda_1 = \lambda$, the stretch along the direction to the loading or tensile stress gives transversal stretch ratios (TREOLAR [304]):

$$\lambda_2 = \lambda_3 = \frac{1}{\sqrt{\lambda}}, \quad (4.20)$$

resulting the two stretch invariants from Eqn. 4.16;

$$\begin{aligned} I_1 &= \lambda^2 + \frac{2}{\lambda} \\ I_2 &= 2\lambda + \frac{1}{\lambda^2}. \end{aligned}$$

In terms of principal stretches, the SEF can be expressed as:

$$W = C_{10}\left(\lambda^2 + \frac{2}{\lambda} - 3\right) + C_{01}\left(2\lambda + \frac{1}{\lambda^2} - 3\right) + C_{20}\left(\lambda^2 + \frac{2}{\lambda} - 3\right)^2 - p(J - 1). \quad (4.21)$$

Finally, the magnitude of the first Piola-Kirchhoff stress \mathbf{P} along the loading direction can be written using chain rule with a single stretch ratio λ (Eqn. 4.17),

$$P = 2C_{10}\left(\lambda - \frac{1}{\lambda^2}\right) + 2C_{01}\left(1 - \frac{1}{\lambda^3}\right) + 4C_{20}\left(\lambda - \frac{1}{\lambda^2}\right)\left(\lambda^2 + \frac{2}{\lambda} - 3\right) - \frac{p}{\lambda}, \quad (4.22)$$

Similarly, using Eqns. 4.18, the magnitudes for the second Piola-Kirchhoff and the Cauchy stress can be expressed as:

$$\begin{aligned}
S &= 2C_{10} \left(1 - \frac{1}{\lambda^3}\right) + 2C_{01} \left(\frac{1}{\lambda} - \frac{1}{\lambda^4}\right) + 4C_{20} \left(1 - \frac{1}{\lambda^3}\right) \left(\lambda^2 + \frac{2}{\lambda} - 3\right) - \frac{p}{\lambda^2} \\
\sigma &= 2C_{10} \left(\lambda^2 - \frac{1}{\lambda}\right) + 2C_{01} \left(\lambda - \frac{1}{\lambda^2}\right) + 4C_{20} \left(\lambda^2 - \frac{1}{\lambda}\right) \left(\lambda^2 + \frac{2}{\lambda} - 3\right) - p. \quad (4.23)
\end{aligned}$$

Different forms of large strain elasticity can be derived from the general Rivlin equation by considering the expansion of the strain energy function in power series of $(I_1 - 3)$ and $(I_2 - 3)$ terms that are illustrated in Table 4.2. The equations of motion, boundary

Table 4.2: Isotropic hyperelastic material models to describe incompressible soft tissue behavior.

Model	Strain energy function (W)	Nominal stress (P)
Neo-Hookean	$C_{10}(I_1 - 3)$	$2C_{10}(\lambda - 1/\lambda^2)$
Mooney-Rivlin	$C_{10}(I_1 - 3) + C_{01}(I_2 - 3)$	$2(\lambda - 1/\lambda^2)[C_{10} + \frac{C_{01}}{\lambda}]$
2 nd order Mooney-Rivlin	$C_{10}(I_1 - 3) + C_{02}(I_2 - 3)^2$	$2(\lambda - 1/\lambda^2)[C_{10} + 2\frac{C_{02}}{\lambda}(2\lambda + \frac{1}{\lambda^2} - 3)]$
Rivlin-Saunders	$C_{10}(I_1 - 3) + C_{20}(I_1 - 3)^2$	$2(\lambda - 1/\lambda^2)[C_{10}\lambda + 2C_{20}\lambda(\lambda^2 + \frac{2}{\lambda} - 3)]$
Signorini	$C_{10}(I_1 - 3) + C_{01}(I_2 - 3) + C_{20}(I_1 - 3)^2$	$2(\lambda - 1/\lambda^2)[C_{10}\lambda + C_{01} + 2C_{20}\lambda(\lambda^2 + \frac{2}{\lambda} - 3)]$
1 st order Ogden	$\sum_{p=1}^1 \frac{\mu_p}{\alpha_p} (\lambda_1^{\alpha_p} + \lambda_2^{\alpha_p} + \lambda_3^{\alpha_p} - 3)$	$\mu_1(\lambda^{\alpha_1-1} - \lambda^{\frac{\alpha_1}{2}-1})$
Yeoh	$\sum_{p=1}^3 C_{p0}(I_1 - 3)^p$	$2(\lambda - \frac{1}{\lambda^2})[C_{10} + 2C_{20}(\lambda^2 + \frac{2}{\lambda} - 3) + 3C_{30}(\lambda^2 + \frac{2}{\lambda} - 3)^2]$

μ_p and α_p are constants and may have any value including non-integer values. The degree of the sum may be adjusted as needed to fit the data at hand.

conditions and stress-strain relations for such highly elastic material can also be expressed in terms of the SEF that may be defined entirely in terms of the principal stretch ratios $(\lambda_i, i = 1, 2, 3)$. All of these hyperelastic constitutive models assumes the material to be isotropic and incompressible where the collagen fiber orientation on the tissue mechanics are not included. More recently, structurally motivated, non-linear elastic, anisotropic models including collagen fiber has been developed and used for wide range of soft tissues (HOLZAPFEL ET AL. [121]).

Neglecting temperature, viscous and time-dependent effects, Neo-Hookean, Ogden, Yeoh, Mooney-Rivlin, Rivlin-Saunders and Signorini model are the most widely used strain

energy functions to characterize the pelvic tissue mechanics in the context of non-linear hyperelasticity. Consequently, the stress and constitutive tangent matrix for them are obtained by derivation of a strain-energy function per unit reference volume with respect to strain tensors or stretch tensors. These equations can then be implemented into finite element models to predict the behavior of the pelvic floor under a variety of mechanical stimuli that emulate both normal and pathological conditions.

4.2.3 Parameter identification

The stress-strain curves of the pelvic structures are adopted from the experiments published on different literature and are fitted with three term polynomial function (Eqn. (4.22)) in Hyperfit software^{6.)} to obtain isotropic hyperelastic parameters that are later used in the numerical study, see Table 4.3. The aim of fitting a stress-strain/stretch curve of an experimented tissue is to fit the parameters of any selected constitutive model in such a way that the fitted curve is as close to the measured curve as possible i.e. the fitted model equation should yield the same stress values as the measured curve through experiment and given as:

$$P_{\text{fit}}(\lambda, C_{10}, C_{01}, C_{20}\dots) = P_{\text{experiment}}(\lambda), \quad (4.24)$$

where C_{pq} are the parameters and have to be determined through regression analysis.

Table 4.3: Biomechanical properties of female pelvic structures. The stress-strain curves are adopted from experiment published from different literature listed below and is fitted with three term polynomial functions using the Hyperfit software.

Structure	C_{10} (MPa)	C_{01} (MPa)	C_{20} (MPa)	References
Uterosacral	1.6	-	8.0	RIVAUX ET AL. [256]
Cardinal, perineal body	0.2288	-	1.144	TAN ET AL. [299]
Pubourethral	0.68	-	5.0	RIVAUX ET AL. [256]
Uterus, vagina	0.4	-	3.2	RUBOD ET AL. [266]
Rectum	0.73	-	1.4	RUBOD ET AL. [266]
Vesica, urethra	0.0835	-	0.092	MARTINS ET AL. [192]
Pelvic muscle	0.0625	-	-	BRANDÃO ET AL. [40]

Common challenges often faced in modeling the mechanical response of the soft tissues are: i) the selection of an appropriate constitutive laws that can sufficiently capture the experimental material behavior of the tissue without being over-parameterized and ii) the definition of such tissue behavior in finite element software that allows the solution of the three-dimensional finite deformation mechanics in a reasonable time on parallel architectures. The hyperelastic material behavior based on the Rivlin function possess an advantage over other strain energy functions readily available, easily and widely implemented constitutive law in commercial and open source finite element codes. Also, such material behavior uses comparatively lesser number of parameters to define the large strain behavior for rubber material and soft tissues such as pelvic floor tissues.

^{6.)} <http://www.hyperfit.wz.cz/>

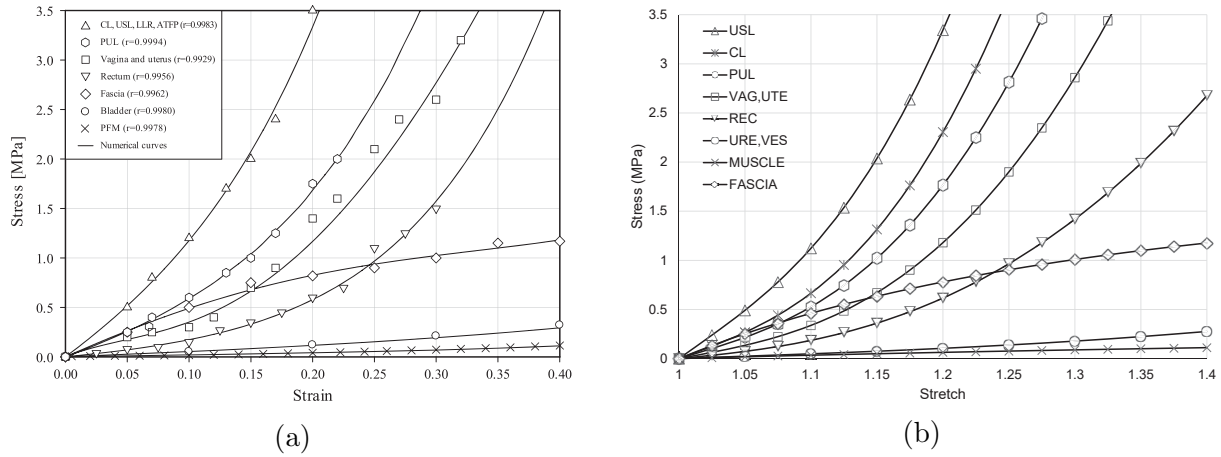


Figure 4.8: Fitting of pelvic floor organs ligaments, muscle and fascia using a) Ogden and Yeoh (BRANDÃO ET AL. [40]), b) three term Signorini hyperelastic constitutive model (BHATTARAI AND STAAT [29]).

The curve fitting capability in the Hyperfit software using a hyperelastic strain energy function allows to fit the uniaxial tensile test data obtained for the pelvic organs and other soft tissues. The test data, specified as nominal stress-nominal strain/stretch pairs are used as X-Y variables in Hyperfit to determine the hyperelastic coefficients (C_{pq}). For each stress-strain/stretch data pair, the software generates a correlation coefficient which can compare the effectiveness of the curve fit as shown in Table 4.3. Herein, the Signorini model with adjusted ($C_{pq} = 0$) appeared to be sufficient enough to predict the behavior of the experimented tissue at small and large strain/stretch values, see Fig. 4.8.

4.3 Modeling of the endopelvic fascia

4.3.1 Fascia modeling according to collagen content

The endopelvic fascia is a very thin structure measuring from 1.43 ± 0.41 mm to 1.56 ± 0.17 mm (KIRILOVA ET AL. [148]). The main load bearing components in the soft fascia are the elastin and the collagen fibers arranged in a random fashion that align along the loading direction when loaded. The density and stiffness of each major constituent vary along the length of the vagina depending on the interaction of the fascia with bladder, urethra and rectum, see Fig. 4.9a (NAGATA ET AL. [205], OTCENASEK ET AL. [218], PETROS [239]). The composition of the fascia lining and its mechanical behavior is responsible for the phenomenological differences of the incontinence and prolapse. Since it is not easy to obtain stress-strain relations of soft connective tissues which consider anisotropy, wherever possible, such models are not readily available in the FE software. Therefore, focus is given on the simplest but widely adopted non-linear and isotropic hyperelastic material laws.

To estimate the mechanical behavior of such elastin-rich fascia and collagen-rich fascia along the vaginal length, comparison can be made from the experiments after digesting or removing each fiber type from tissue specimen, for example collagen-elastin digestion

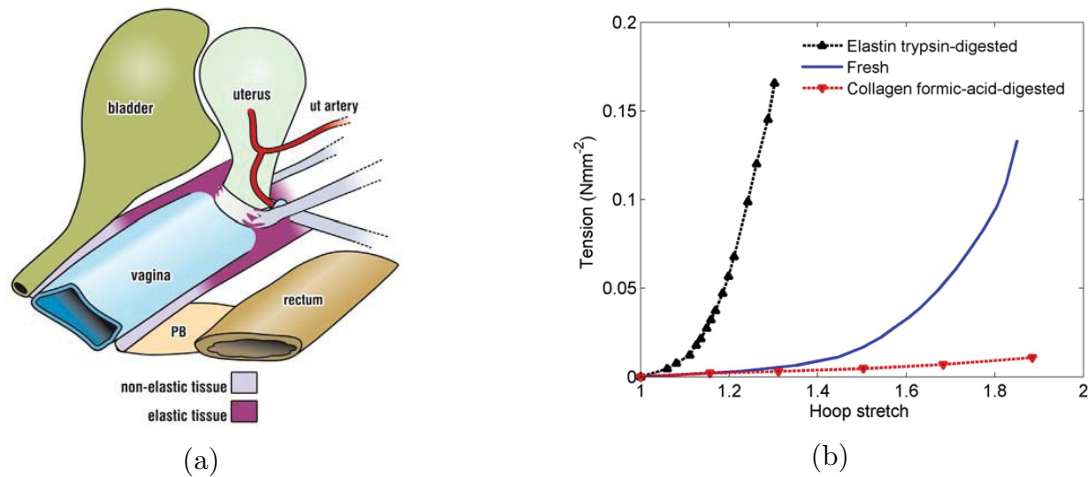


Figure 4.9: a) Schematic representation of varying tissue density along the vaginal length. The distal pelvic viscera is supported by denser fibrous tissue support, while the mid and proximal visceral fascia is elastic with less collagen and more smooth muscle and elastin (PETROS [239]). b) Stress-stretch curve fit of elastin and collagen digested arterial tissue (NGUYEN ET AL. [206])

from artery, elastin-rich spleen and collagen-rich liver samples (NGUYEN ET AL. [206], ROACH ET AL. [258], DUONG ET AL. [83]). Tissue stiffness is found to be substantially varying after digestion phenomena. Due to elastin removed, the initial stiffness at toe region is greatly reduced and the linear stiffness is immediately gained due to the recruitment and alignment of the leftover collagen fibers, see Fig. 4.9b. In such remodeled tissues, the specimen distensibility (only 4%) comes only from the rearrangement of the stiff collagen fibers. Similarly, samples after collagen reduction shows nearly linear stress-stretch curve with very low overall stiffness and is highly stretchable by more than 80% due to elastin fibers. Though, no analytical relation has been discussed in the cited publications to describe the relative changes in the mechanical response from elastin-collagen reduction, comparing the experimental stress-stretch curves of the collagen digested tissue shows stiffness reduction by more than 90% compared to the elastin digested tissue.

In the healthy endopelvic fascia, elastin and collagen vary without complete removal along the vaginal wall. In addition, other tissue components (adipose and smooth muscle) can be assumed to be unchanged. Thus, 90% or more stiffness reduction due to complete removal of other components would be an overestimation for the fascia composition. In addition, SILITONGA ET AL. [279] measured 68% difference in the collagen content in prolapsed and healthy ligament. Therefore, we adopted an average stiffness difference of 70% between the elastin-rich and the collagen-rich fascia, thus maintaining the general non-linearity of the stress-stretch curve.

Table 4.4: Biomechanical properties of the endopelvic fascia. The stress-strain curves is adopted from experiments published in the KIRILOVA ET AL. [148] and is fitted with three term polynomial function using the Hyperfit software.

Structure	C_{10} (MPa)	C_{01} (MPa)	C_{20} (MPa)
Collagen-rich endopelvic fascia, perineal membrane	-	0.64785	-
Elastin-rich endopelvic fascia	-	0.194355	-

4.4 Fascia modeling according to tissue constituents: mixture theory

Pelvic connective tissues are made up of cells linked by the extracellular matrix (ECM). While the cells provide biochemical functions, the non-cellular ECM provides (structural and mechanical) support and physical scaffolding for the cellular constituents. It is mainly composed of macromolecules of biopolymers including elastin-collagen fibers and a varying amount of adipose (fat) tissue and smooth muscle organized in a nonhomogeneous fashion to form a complex composite microstructure. At structural level, its biomechanical behavior depends on the components, since each of them possess unique mechanical properties; the collagen significantly contributes to the stiffening response (limited extension or stretch), elastin to the distensibility, the smooth muscle to the continuous contractility and the softest adipose tissue serves as a cushion with much lower stiffness than other constituents. In anatomical pelvic fascia, fatty (adipose) tissue is found outside the adventitia of the distal and lateral bladder and the rectum. The region of the uterosacral ligament is found to be diffused in the surrounding subperitoneal fat and contains mostly smooth muscles and elastin. In this section, an attempt is made to describe the theory of immiscible mixture where the tissue constituents retain their unique identity and mechanics, but provide an integrated effect to the structural tissue mechanics.

Continuum modeling of such biological tissues is notoriously intimidating as it possess a number of challenges related to its structure and composition. Modeling the overall mechanical response of such multiple constituent tissue need I) to obey individual balance and constitutive relation by each constituent and II) to agree for mass, momentum and energy by the overall mixture (TRUSDELL AND NOLL [305]). In general terms, the mixture as a whole should behave as a pure substance with an exchange of mass, momentum and energy between constituents. In addition, based on the continuum theories of heterogeneous substances, all constituents coexist at every point in the microstructurally small volume also known as representative volume element (RVE). The architecture of the soft tissue RVE composed of elastin-collagen fiber, fat tissues and smooth muscles that are weighted by their volume fractions (f_i). To model the large, elastic strain mechanical response of the fiber reinforced CT two approaches can be followed; firstly, the homogenization technique that assumes an equivalent single material with a common reference/stress-free configuration and secondly, mixing the constituents with their respective reference configuration and material symmetries (PENCE AND WINEMAN [229]). Under both assumptions, the derived constitutive theory should coincide with the constitutive theory of the connective tissue for which a precise knowledge of the histology and the mechanics of each constituents is required. For the homogenization of such heterogeneous biological materials

and to determine the effective mechanical parameters, classically the Voigt upper bounds and the Reuss lower bounds have been widely used.

The Voigt and the Reuss averages are interpreted as the ratio of average stress and average strain within the composites, i.e., elastin-collagen fiber fascia, fat tissues and smooth muscles. The stress and the strain are generally unknown in the composite and are expected to be non-uniform. The parallel Voigt model as shown in Fig. 4.10a assumes equal kinematics and uniform strain everywhere in the composite. It is an upper bound of the mixture theory. Whereas the lower bound Reuss model (Fig. 4.10b) assumes equal statics and uniform stress for all components. In Reuss series model, the total composite deformation gradient \mathbf{F} in the structure can be written with Kröner's multiplicative decomposition [165] as

$$\mathbf{F} = \mathbf{F}^{\text{elas-coll}} \mathbf{F}^{\text{ad}} \mathbf{F}^{\text{sm}} \quad (4.25)$$

where *elas-coll*, *ad* and *sm* are the representation for the elastin-collagen fiber fascia, the adipose tissue and the smooth muscle^{7.)}. This model is less practical for solids because the inverse constitutive equation $\mathbf{B}(\sigma)$ or the complementary SEF cannot generally be written as an analytical equation and is mostly applicable for fluid mixtures. Therefore, the Voigt isostrain mixture rule possess some technical advantage over the Reuss isostress rule (CALVO-GALLEGO ET AL. [50], FATA ET AL. [89], NOBLE ET AL. [211]).

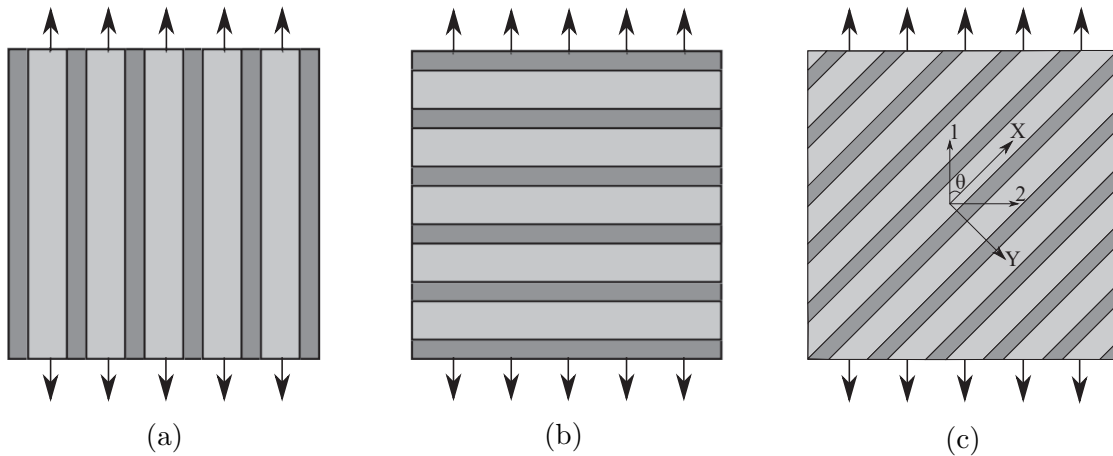


Figure 4.10: Two constituent representation of a) the Voigt iso-strain and b) the Reuss iso-stress model and c) shows the rotation of axes from longitudinal system from 1-2 to X-Y.

An other possibility of arbitrarily aligned tissue components to the loading direction (for example by an angle θ , Figure 4.10c) has been discussed in literature SINCLAIR AND CHAMIS [282] where the influence on the material parameters can be computed at the desired co-ordinate system through a series of transformation (for isotropic

^{7.)} Separate stress-strain curves of elastin and collagen fibers with their global and local volume fraction in the fascia is difficult to obtain. Therefore, the decomposition in this thesis has been performed on the fascia sample after the reduction of the adipose tissue as in KIRILOVA ET AL. [148]

to orthotropic angle-ply or cross-ply laminate subjected to unidirectional tensile stress, see HULL [126]).

Also, the author would like to point out that the homogenization technique discussed in this thesis is purely analytical (for more examples, see CALVO-GALLEGO ET AL. [50], FATA ET AL. [89]) in order to evaluate the average material mechanics of the multi-constituent tissue composite: no numerical validation using the finite element method on micro-structure mesh is performed.

The SEF of the soft tissue (W) is the sum of the SEF of the constituents, i.e.

$$W = \sum_{i=\text{fas,ad,sm}} f_i W_i(\mathbf{C}) - p(J - 1), \quad (4.26)$$

In Voigt's isostrain rule the deformation of the constituents is kinematically compatible, i.e. they have the same \mathbf{C} or \mathbf{B} for each constituent, i.e. $\mathbf{C}^{\text{elas-coll}} = \mathbf{C}^{\text{ad}} = \mathbf{C}^{\text{sm}} = \mathbf{C}$ or $\mathbf{B}^{\text{elas-coll}} = \mathbf{B}^{\text{ad}} = \mathbf{B}^{\text{sm}} = \mathbf{B}$ so that in terms of \mathbf{C}

$$\begin{aligned} W &= \sum_{i=\text{fas,ad,sm}} f_i W_i(\mathbf{C}) - p(J - 1) \\ &= f_{\text{fas}} W_{\text{fas}}(\mathbf{C}) + f_{\text{ad}} W_{\text{ad}}(\mathbf{C}) + f_{\text{sm}} W_{\text{sm}}(\mathbf{C}) - p(J - 1), \end{aligned} \quad (4.27)$$

where, f_{fas} , f_{ad} and f_{sm} are the volume fractions of the elastin-collagen fascia, adipose tissue and smooth muscle satisfying the total volume fraction $f = f_{\text{fas}} + f_{\text{ad}} + f_{\text{sm}} = 1$. In this study, the strain energy for the smooth muscle is solely because of the passive contribution, no activation of the smooth muscle is considered, so that $(\sigma_{\text{active}})_{\text{sm}} = 0$.

Several hyperelastic material models are available, e.g. Neo-Hookean, Arruda-Boyce, Mooney-Rivlin, Ogden models for the constitutive modeling of soft biological tissues similar to rubber material. The choice of the strain energy function should fulfil the numerical stability of the selected model. For finite-valued, continuous energy function, this is determined by the concept of polyconvexity which implies quasiconvexity (associated functional to be minimized is weakly lower semi-continuous) and rank one convexity (the Euler equations of the associated functional are elliptic, i.e. the associated projection maps non-zero, positive semi-definite, symmetric second-order tensors to positive definite, symmetric tensors) BALL [14], BALZANI [15], SCHRÖDER AND NEFF [273]. All these isotropic hyperelastic material functions satisfy the polyconvexity concept SCHRÖDER AND NEFF [273]. Therefore, we present here the simplest models (the Mooney-Rivlin type polynomial function) which has been typically applied for many biological tissues. Elastin and collagen fibers are sparsely distributed in the matrix of the soft tissues, several anisotropic constitutive models have been implemented to characterize their mechanical behavior (BRIEU ET AL. [42], FATA ET AL. [89]). Intense histological study is required to evaluate the proportion, orientation and distribution of the tissue constituents for soft fascia and is yet to be done. Assuming the elastin-collagen fascia, adipose and smooth muscle are to be isotropic, hyperelastic and incompressible materials, the composite soft tissue can be modeled using a three term polynomial strain energy function as expressed in Eqn. 4.21

$$W_i = \sum_{i=\text{fas,ad,sm}} f_i \left(C_{10}^i (I_1 - 3) + C_{01}^i (I_2 - 3) + C_{20}^i (I_1 - 3)^2 \right) - p(J - 1). \quad (4.28)$$

For an incompressible hyperelastic material with preserved volume ($\lambda_1\lambda_2\lambda_3 = 1$) under uniaxial tension, assuming $\lambda_1 = \lambda$ gives $\lambda_2 = \lambda_3 = \frac{1}{\sqrt{\lambda}}$. Then the distortional magnitude of the first Piola-Kirchhoff or nominal stress \mathbf{P} along the stretch direction can be written as:

$$P = \sum_{i=\text{fas,ad,sm}} f_i \left[2C_{10}^i \left(\lambda - \frac{1}{\lambda^2} \right) + 2C_{01}^i \left(1 - \frac{1}{\lambda^3} \right) + 4C_{20}^i \left(\lambda - \frac{1}{\lambda^2} \right) \left(\lambda^2 + \frac{2}{\lambda} - 3 \right) \right] - \frac{p}{\lambda}. \quad (4.29)$$

The constants $C_{10}^i, C_{01}^i, C_{20}^i$ for the elastin-collagen fascia, adipose and smooth muscle are fitted from the tensile experiments adopted from literature and are listed in Table 4.5. Figure 4.11 shows the capability of the three term hyperelastic polynomial function to capture the mechanical response of experimented tissue components. The fascia is a very thin

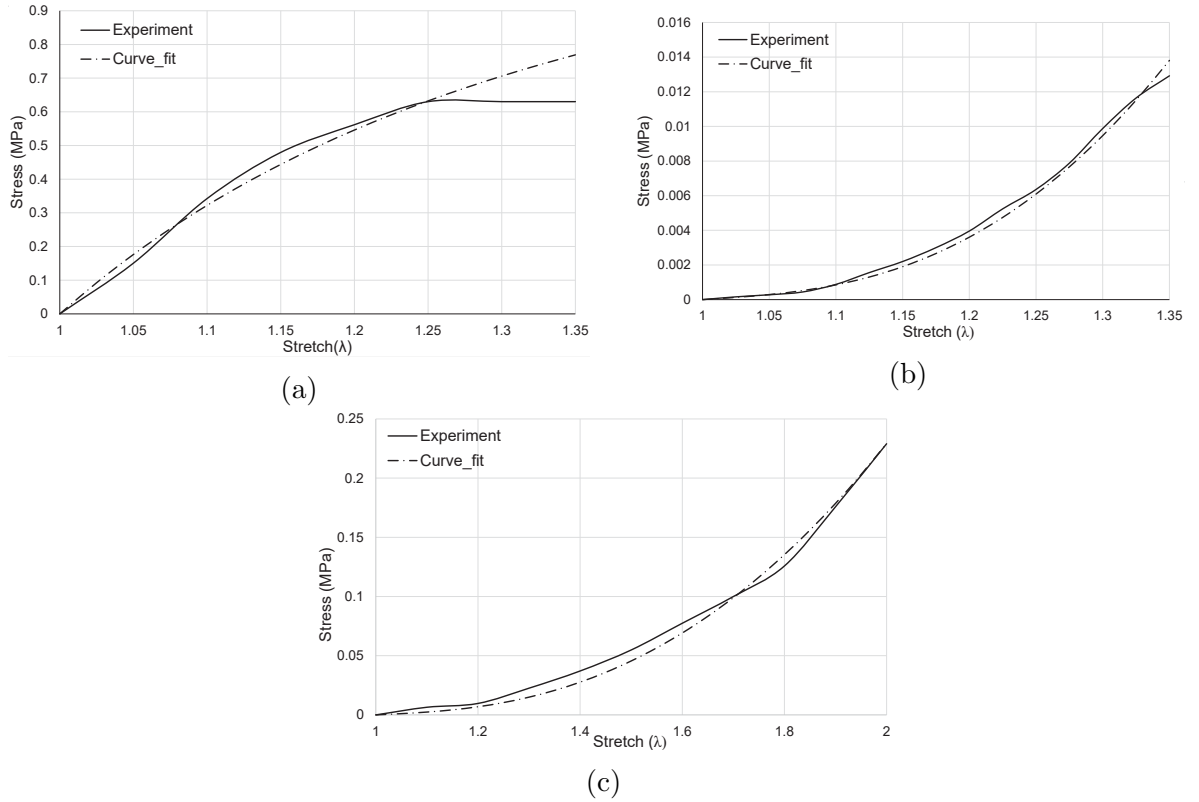


Figure 4.11: Fitting of the nominal stress (P) vs stretch (λ) curve for a) elastin-collagen fascia applying a 0.13 mm/s elongation rate (KIRILOVA ET AL. [148]), b) adipose tissue applying strain at a rate of 5 $\mu\text{m/s}$ up to 30% strain (ALKHOULI ET AL. [4]) and c) smooth muscle without active contractility (elongation/strain rate not stated) is assumed during micturition (BUSH ET AL. [47]) using three term polynomial strain energy function (eqn. 4.21).

structure measuring from 1.43 ± 0.41 mm to 1.56 ± 0.17 mm (KIRILOVA ET AL. [148]), it is not easy to determine the exact proportion of the tissue constituents. Separate staining

protocols are necessary for each components and histological studies are always not consistent. For example, for structurally similar uterosacral and ATRP ligaments, wide ranges of collagen densities (23% (GABRIEL ET AL. [106])-48.75% (SILITONGA ET AL. [279]) vs 84% (MOALLI ET AL. [198])) and smooth muscle cells (20% (GABRIEL ET AL. [106]) vs 5% (MOALLI ET AL. [198])) were measured. At this stage, with the personal advice from the experience of (anatomist and urologist) Prof. Dr. med. Mircea Constantin Sora (Sigmund Freud University Vienna, Austria) approximation of the fascial components were

Table 4.5: Biomechanical properties of endopelvic fascia constituents.

Tissue component	C_{10} (MPa)	C_{01} (MPa)	C_{20} (MPa)	References
Collagen-elastin fascia	-	0.64785	-	KIRILOVA ET AL. [148]
Adipose (fat) tissue	0.000835	-	0.0128	ALKHOULI ET AL. [4]
Smooth muscle	0.0035	-	0.0155	BUSH ET AL. [47]

done to have a more realistic model. In a total volume of the endopelvic fascia, the adipose tissue is assumed abundance ($\approx 85\%$) and serves as a cushion to the adjoining organs. The thin layer of the fascia formed by elastin and collagen fibers embedded in the ground matrix occupies about 10% of the endopelvic fascia volume. Whereas, the remaining 5% is estimated to be occupied by the randomly distributed smooth muscles. Therefore, the mechanical behavior of the fat-free endopelvic fascia consisting of elastin and collagen embedded in the ground matrix is adopted from the curve fit of the uniaxial tensile experiment performed on the human transversalis fascia (KIRILOVA ET AL. [148]) that is directly continuous with the pelvic fasciae. For adipose tissue and smooth muscle, corresponding literatures (ALKHOULI ET AL. [4], BUSH ET AL. [47]) were reviewed and fitted with Eqn. 4.29. Finally, the stress-stretch relationship of the composite fascia tissue, made up of elastin-collagen fascia, adipose tissue and smooth muscle is given by equation (4.29) and its behavior can be defined by fitted three hyperelastic parameters C_{10}, C_{01}, C_{20} . The deviations of the fit from the elastin-collagen curve in Fig. 4.11a suggests that care should be taken, not to use the composite mixture relation as extrapolation far beyond $\lambda = 1.2$.

4.5 Modeling of tissue weakening: progressive remodeling of stronger collagen

Female pelvic floor disorders are associated with the denervation injuries (DELANCEY [72], SNOOKS ET AL. [284]) of the support and suspension system in the pelvic cavity during childbirth and weakening or laxity in old ages (MARTINS ET AL. [192], OLSEN ET AL. [215], PETROS AND ULMSTEN [234]). Biochemical data and clinical experience suggests that the soft supportive tissues of women with disorders are weaker and/or more distensible than the healthy tissues (JAMESON ET AL. [133], JONES ET AL. [139]). The resilience of the pelvic organs and supporting connective tissues are affected due to i) remodeling of the larger and stronger type I collagen fibers into smaller and weaker collagen type III that are damaged during vaginal delivery (BARLOW AND WILLOUGHBY [19]), ii) reduction of the total stronger collagen after menopause (BRINCAT ET AL. [43], KONDO ET AL. [162],

RECHBERGER ET AL. [251]) and iii) decrease of collagen fiber size (diameter) on ageing. Increased amount of weaker collagen type III increases the tissue elasticity and extensibility that is responsible for the increased tissue laxity in symptomatic females (GABRIEL ET AL. [106], MOALLI ET AL. [199]).

Collagen is the most abundant protein in the human body and is an important structural unit of the skin, muscle, bone, tendons, blood vessels, soft tissues (ligament and fascia) and organs. Depending on the fibrous, sheets and globular architecture, about 20 different types of collagen families can be categorized into different classes and types. Amongst others, type I and III are abundant in soft tissues that together copolymerizes to form fibrils with controlled diameters, which influences the biomechanical characteristics of a given tissue when stressed (BIRK ET AL. [33], WENSTRUP ET AL. [322]). Type I collagen provides mechanical strength to tissues while type III contributes to elasticity and regulates collagen fibril diameter during fibrillogenesis. Balanced proportion of these fibrillar collagen maintains the architecture and functions of the body parts and control their biomechanical properties when loaded. However, faulty collagen metabolism during sickness, pregnancy and old ages after menopause produces a pathologically altered extracellular matrix (ECM) with higher amount of weaker type III collagen (GABRIEL ET AL. [106], KÖKÇÜ ET AL. [161]). This process i) modifies the Collagen I/III ratio, an indicator of tensile strength (BIRK ET AL. [33], KLINGE ET AL. [151], KLINGE ET AL. [152], ZHENG ET AL. [339]) and ii) creates an abnormal quantity and organization of collagen fibers that significantly affects the tensile strength due to reduced fiber size (NIYIBIZI ET AL. [208]).

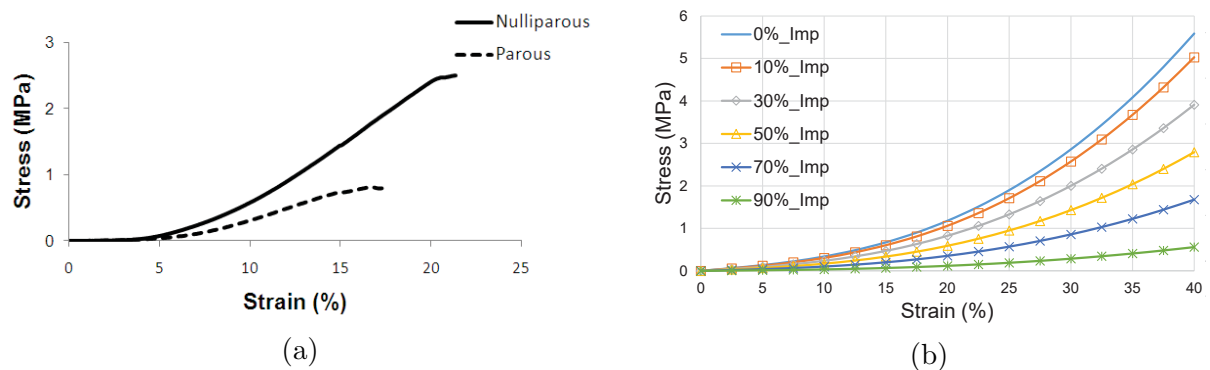


Figure 4.12: a) Stress-strain curves of vaginal tissue from nulliparous and parous rhesus macaques showing significant differences in tensile strength and tangent modulus (FEOLA ET AL. [93]), b) Progressive tissue impairment represented by reduced material stiffness. 0% Impairment represents healthy tissue state without any weakening.

In a vast majority of histological studies on pelvic tissues, active remodeling of the tissues is also responsible for changes in smooth muscle cells. Tenderness of smooth muscle content reduction and disorganization of the muscle bundles in women with pelvic floor prolapse are reported (BOREHAM ET AL. [38], KAPLAN ET AL. [146], OZDEGIRMENCI ET AL. [220], REISENAUER ET AL. [252], TAKACS ET AL. [297]). In contrast to the ECM alterations due to collagen fibril and smooth muscle turn

over in a lifespan, there is no strict evidence about significant elastin metabolism (KANNAN ET AL. [145], KÖKÇÜ ET AL. [161], LIN ET AL. [176]). Only few have found decreased elastin content and reduced fiber width (TAKACS ET AL. [297]) in prolapsed females. Thus, female pelvic floor disorders are profoundly associated with weakening of the tissue mechanics due to loosely arranged collagen fibers, less dense extracellular matrix, and impaired smooth muscle cells. Such alterations by active remodeling is significantly evident in females with pregnancy, menopause and ageing, see Fig. 4.12a.

To model the progressive weakening of the pelvic tissues, reduced material stiffness is implemented successively between 0% and 95%. The reduced material stiffness is obtained by multiplying the respective material parameters/coefficients in Tables 4.3 and 4.4 from 0.9 (10% impairment) up to 0.05 (95% impairment), see Fig. 4.12b. Similar methodology of tissue impairment has been implemented by BRANDÃO ET AL. [40], CHEN ET AL. [58] and PENG ET AL. [230] which is obtained by multiplying the stress/strain curve of corresponding healthy tissues by same coefficients (0.9 up to 0.05).

4.6 Passive mechanical modeling of skeletal pelvic floor muscle

The majority of computer modeling studies of the levator ani muscle assumes their mechanical behavior to be passive and isotropic. Hyperelastic constitutive relations, with either isotropic or anisotropic material properties, are often used to model large deformation of such tissues. Numerous early attempts have been made on cadaver dissections to describe the information about the fiber organization of the levator ani muscle, for which JANDA ET AL. [134] were among the first to construct a useful model on the basis of the fiber arrangements. However, the development of the transversely isotropic constitutive models by HUMPHREY AND YIN [127] and their successive improvements have put forward novel idea of fiber contractility to evaluate the behavior of skeletal muscles. The passive Helmholtz free energy in the model proposed by Humphrey and Yin for the skeletal muscle can be additively decomposed into

$$W_{\text{muscle}} = W_{\text{incomp}} + W_{\text{matrix}} + W_{\text{passive}}, \quad (4.30)$$

with the incompressible (W_{incomp}), ground matrix (W_{matrix}), active fiber contraction (W_{active}), and passive relaxation (W_{passive}) to the muscle strain energy. Considering the muscle to be quasi-incompressible, the incompressibility contribution of the free energy takes the form

$$W_{\text{incomp}} = \frac{1}{D} (J - 1)^2, \quad (4.31)$$

where D is the compressibility constant and the Jacobian $J = \det \mathbf{F}$ is the volume change. \mathbf{F} is the deformation gradient. Since most of the soft tissues are regarded as perfectly incompressible, the free energy is equal to $\tilde{p}(J - 1)$, where \tilde{p} is the Lagrange multiplier, which has the physical meaning of hydrostatic pressure. The mechanical response of the matrix material is assumed to be isotropic, therefore a hyperelastic model adopted by Humphrey and Yin (HUMPHREY AND YIN [127]) is used as

$$W_{\text{matrix}} = c [\exp \{b (\bar{I}_1 - 3)\} - 1], \quad (4.32)$$

where c and b are the material constants and \bar{I}_1 is the first principal invariant of the unimodular part of the right Cauchy-Green tensor $\mathbf{C} = \mathbf{F}^T \mathbf{F}$. It can be calculated as $\bar{I}_1 = \text{tr}[\bar{\mathbf{C}}] = \text{tr}[\bar{\mathbf{F}}^T \bar{\mathbf{F}}] = J^{-\frac{2}{3}} \text{tr}[\mathbf{C}]$, where $\bar{\mathbf{F}} = J^{-\frac{1}{3}} \mathbf{F}$ is the unimodular part of the deformation gradient. Further, the strain energy stored in the muscle fiber is

$$W_{\text{passive}} = \begin{cases} T_0^M A \left[\exp \left\{ a (\bar{\lambda}_f - 1)^2 \right\} - 1 \right], & \forall \bar{\lambda}_f \geq 1 \\ 0, & \text{otherwise,} \end{cases} \quad (4.33)$$

where A and a are the material constants, T_0^M is the peak stress when the muscle is fully activated and $\bar{\lambda}_f = \sqrt{\mathbf{N}^T \bar{\mathbf{C}} \mathbf{N}} = \sqrt{\mathbf{n}^T \mathbf{B} \mathbf{n}}$ is the fiber stretch ratio given as

$$\bar{\lambda}_f = \sqrt{\mathbf{N}^T \bar{\mathbf{C}} \mathbf{N}} = \sqrt{\bar{\mathbf{C}} : (\mathbf{N} \otimes \mathbf{N})}, \quad (4.34)$$

where, \mathbf{N} is the unit vector parallel to the preferred muscle fiber direction in the reference configuration which is directed antero-posterior (Fig. 5.1). And \mathbf{n} is the unit vector parallel to the preferred muscle fiber direction in the deformed configuration in accordance to the left Cauchy-Green tensor \mathbf{B} .

The muscle fiber direction \mathbf{N} in the three dimensional Euclidean reference configuration can be uniquely represented by a linear combination of the basis vectors $\mathbf{e}_i, \forall i = 1, 2, 3$, i.e., $\mathbf{N} := N_i \mathbf{e}_i = N_1 \mathbf{e}_1 + N_2 \mathbf{e}_2 + N_3 \mathbf{e}_3$. In matrix form this vector can be expressed as $[\mathbf{N}] = [N_1, N_2, N_3]^T$. The global unit muscle fiber vector as shown in Fig. 5.1 is $[\mathbf{N}] = [0, 1, 0]^T$. Similarly, the unimodular part of the right Cauchy-Green tensor $\bar{\mathbf{C}}$ can also be written in the 3×3 square matrix as

$$\bar{\mathbf{C}}_{ij} = \begin{vmatrix} \bar{C}_{11} & \bar{C}_{12} & \bar{C}_{13} \\ \bar{C}_{21} & \bar{C}_{22} & \bar{C}_{23} \\ \bar{C}_{31} & \bar{C}_{32} & \bar{C}_{33} \end{vmatrix} \quad (4.35)$$

This leads to the calculation of the fiber stretch ratio (Eqn. 4.34) as

$$\bar{\lambda}_f^2 = \mathbf{N}^T \bar{\mathbf{C}} \mathbf{N} = \bar{\mathbf{C}} : (\mathbf{N} \otimes \mathbf{N}) = [N_1, N_2, N_3] \begin{vmatrix} \bar{C}_{11} & \bar{C}_{12} & \bar{C}_{13} \\ \bar{C}_{21} & \bar{C}_{22} & \bar{C}_{23} \\ \bar{C}_{31} & \bar{C}_{32} & \bar{C}_{33} \end{vmatrix} \begin{bmatrix} N_1 \\ N_2 \\ N_3 \end{bmatrix}. \quad (4.36)$$

4.6.1 Passive stress component

The second Piola-Kirchhoff stress \mathbf{S} is widely used to describe the finite strains of highly non-linear materials such as skeletal muscles and can be generally obtained as:

$$\mathbf{S} := \frac{\partial W}{\partial \mathbf{E}} \quad \Leftrightarrow \quad S_{ij} = \frac{\partial W}{\partial E_{ij}}, \quad (4.37)$$

where \mathbf{E} is the symmetrical material tensor known as the Green-Lagrange strain tensor. For skeletal muscle comprising of fiber, matrix and incompressible part as shown in Eqn. 4.30, the second Piola-Kirchhoff stress can be computed as:

$$\mathbf{S}_{\text{muscle}} := \frac{\partial W_{\text{muscle}}}{\partial \mathbf{E}} = \frac{\partial W_{\text{incomp}}}{\partial \mathbf{E}} + \frac{\partial W_{\text{matrix}}}{\partial \mathbf{E}} + \frac{\partial W_{\text{passive}}}{\partial \mathbf{E}} = \mathbf{S}_{\text{incomp}} + \mathbf{S}_{\text{matrix}} + \mathbf{S}_{\text{passive}}, \quad (4.38)$$

Applying chain rule of differentiation on the incompressible strain energy function 4.31 as a function of right Cauchy-Green tensor expressed in terms of Jacobian determinant ($J(\mathbf{C})$)

$$\begin{aligned}\mathbf{S}_{\text{incomp}} &= \frac{1}{D} \frac{\partial (J-1)^2}{\partial J} \frac{\partial J}{\partial \mathbf{C}} : \frac{\partial \mathbf{C}}{\partial \mathbf{E}} \\ &= \frac{2}{D} J (J-1) \mathbf{C}^{-1},\end{aligned}\quad (4.39)$$

where $\frac{\partial J(\mathbf{C})}{\partial \mathbf{C}} = \frac{1}{2} J \mathbf{C}^{-1}$ and $\frac{\partial \mathbf{C}}{\partial \mathbf{E}}$ can be computed using the relation $\mathbf{E} := \frac{1}{2} (\mathbf{C} - \mathbf{I})$ as,

$$\frac{\partial \mathbf{C}}{\partial \mathbf{E}} = 2 \frac{\partial \mathbf{E}}{\partial \mathbf{E}} = 2 \mathbf{I} \underline{\otimes} \mathbf{I}. \quad (4.40)$$

This fourth order supersymmetric identity tensor^{8.)} $\mathbf{I} \underline{\otimes} \mathbf{I}$ when assigned to the symmetric right Cauchy-Green tensor gives the tensor itself as $\mathbf{I} \underline{\otimes} \mathbf{I} : \mathbf{C} = \mathbf{I} \cdot \mathbf{C} \cdot \mathbf{I}^T = \mathbf{C}$. The $\underline{\otimes}$ symbol may look a bit strange and has been introduced here to distinguish the *symmetrized dyadic or tensor product* according to the rule

$$\begin{aligned}\mathbf{I} \underline{\otimes} \mathbf{I} &= \frac{1}{2} (\mathbf{I} \underline{\otimes} \mathbf{I} + \mathbf{I} \underline{\otimes} \mathbf{I}) \\ (\mathbf{I} \underline{\otimes} \mathbf{I})_{ijkl} &= \frac{1}{2} (I_{il} I_{jk} + I_{ik} I_{jl}) = \frac{\partial C_{ij}}{\partial E_{kl}}.\end{aligned}\quad (4.41)$$

Similarly for the isotropic ground matrix, the strain energy is the function of the tensor \mathbf{C} expressed in terms of unimodular principal invariant $(\bar{I}_1(\bar{\mathbf{C}}) = J^{-\frac{2}{3}}(\mathbf{C}) I_1(\mathbf{C}))$.

Using the product rule of differentiation, $\frac{\partial I_1}{\partial \mathbf{C}} = \mathbf{I}$ and the derivative properties $\frac{\partial J^{-\frac{2}{3}}}{\partial \mathbf{C}} = -\frac{1}{3} J^{-\frac{2}{3}} \mathbf{C}^{-1}$,

$$\frac{\partial \bar{I}_1}{\partial \mathbf{C}} := \frac{\partial (J^{-\frac{2}{3}} I_1)}{\partial \mathbf{C}} = J^{-\frac{2}{3}} \frac{\partial I_1}{\partial \mathbf{C}} + \frac{\partial J^{-\frac{2}{3}}}{\partial \mathbf{C}} I_1 = J^{-\frac{2}{3}} \mathbf{I} - \frac{1}{3} \bar{I}_1 \mathbf{C}^{-1}. \quad (4.42)$$

Therefore, the second Piola-Kirchhoff stress due to isotropic matrix can be obtained as

$$\begin{aligned}\mathbf{S}_{\text{matrix}} &= \frac{\partial c \left[\exp \left\{ b (\bar{I}_1 - 3) \right\} - 1 \right]}{\partial \bar{I}_1} \frac{\partial \bar{I}_1}{\partial \mathbf{C}} : \frac{\partial \mathbf{C}}{\partial \mathbf{E}} \\ &= bc \exp \left\{ b (\bar{I}_1 - 3) \right\} \left(J^{-\frac{2}{3}} \mathbf{I} - \frac{1}{3} \bar{I}_1 \mathbf{C}^{-1} \right) : 2 \mathbf{I} \underline{\otimes} \mathbf{I} \\ &= 2bc \exp \left\{ b (\bar{I}_1 - 3) \right\} \left(J^{-\frac{2}{3}} \mathbf{I} - \frac{1}{3} \bar{I}_1 \mathbf{C}^{-1} \right).\end{aligned}\quad (4.43)$$

Finally, the second Piola Kirchhoff passive muscle stress with the strain energy function expressed in terms of the fiber stretch ($\bar{\lambda}_f$) can be computed as

$$\mathbf{S}_{\text{passive}} = \frac{\partial T_0^M A \left[\exp \left\{ a (\bar{\lambda}_f - 1)^2 \right\} - 1 \right]}{\partial \bar{\lambda}_f} \frac{\partial \bar{\lambda}_f}{\partial \bar{\mathbf{C}}} : \frac{\partial \bar{\mathbf{C}}}{\partial \mathbf{C}} : \frac{\partial \mathbf{C}}{\partial \mathbf{E}}, \quad (4.44)$$

^{8.)} For any symmetrical second order tensor, for example \mathbf{C} , such supersymmetric identity tensor as a product of symmetric second order tensors \mathbf{A} and \mathbf{B} obeys $\mathbf{A} \underline{\otimes} \mathbf{B} : \mathbf{C} = \mathbf{A} \cdot \mathbf{C} \cdot \mathbf{B}^T$.

where the derivative of the fiber stretch with respect to the unimodular part of the \mathbf{C} tensor is:

$$\frac{\partial \bar{\lambda}_f}{\partial \bar{\mathbf{C}}} = \frac{\partial \left\{ \bar{\mathbf{C}} : (\mathbf{N} \otimes \mathbf{N}) \right\}^{1/2}}{\partial \bar{\mathbf{C}}} = \frac{1}{2\bar{\lambda}_f} \mathbf{N} \otimes \mathbf{N}, \quad (4.45)$$

and the derivative of the modified or unimodular right Cauchy-Green tensor $\bar{\mathbf{C}}$ relative to the symmetric tensor \mathbf{C} gives the fourth-order tensor using the relation $\frac{\partial \alpha \mathbf{A}}{\partial \mathbf{B}} = \alpha \frac{\partial \mathbf{A}}{\partial \mathbf{B}} + \mathbf{A} \otimes \frac{\partial \alpha}{\partial \mathbf{B}}$ ^{9.)}

$$\frac{\partial \bar{\mathbf{C}}}{\partial \mathbf{C}} = \frac{\partial J^{-\frac{2}{3}} \mathbf{C}}{\partial \mathbf{C}} = J^{-\frac{2}{3}} \frac{\partial \mathbf{C}}{\partial \mathbf{C}} + \mathbf{C} \otimes \frac{\partial J^{-\frac{2}{3}}}{\partial \mathbf{C}} = J^{-\frac{2}{3}} \left(\mathbf{I} \otimes \mathbf{I} - \frac{1}{3} \mathbf{C} \otimes \mathbf{C}^{-1} \right). \quad (4.46)$$

Substituting the partial derivatives (4.40, 4.45 and 4.46) in Eqn. 4.44, the second Piola-Kirchhoff stress due to passive muscle fibers can be finally obtained as:

$$\mathbf{S}_{\text{passive}} = 2aAT_0^M (\bar{\lambda}_f - 1) \exp \left\{ a (\bar{\lambda}_f - 1)^2 \right\} \left(\frac{J^{-\frac{2}{3}}}{\bar{\lambda}_f} \mathbf{N} \otimes \mathbf{N} - \frac{\bar{\lambda}_f}{3} \mathbf{C}^{-1} \right). \quad (4.47)$$

The spatial counterpart of constitutive equation 4.38 is the Cauchy stress $\boldsymbol{\sigma}$ that follows from the second Piola-Kirchhoff stress $\mathbf{S}_{\text{muscle}}$ by the Piola transformation

$$\boldsymbol{\sigma}_{\text{muscle}} = J^{-1} \mathbf{F} \mathbf{S}_{\text{muscle}} \mathbf{F}^T. \quad (4.48)$$

The constitutive relation for the skeletal muscle can also be derived from the partial derivative of the strain energy equation (4.30) with respect to the left Cauchy-Green tensor $\mathbf{B} = \mathbf{F} \mathbf{F}^T$. In Voigt notation VOIGT [313], the overall muscle stress can be calculated as

$$[\boldsymbol{\sigma}_{\text{muscle}}]_{ij} = \begin{bmatrix} \sigma_{11} \\ \sigma_{22} \\ \sigma_{33} \\ \sigma_{23} \\ \sigma_{13} \\ \sigma_{12} \end{bmatrix} \quad (4.49)$$

4.6.2 Material tangent moduli for passive skeletal muscle

Unlike elastic materials, material tangent moduli or the gradient of the function \mathbf{S} for hyperelastic materials can be evaluated as:

$$\bar{\mathbf{C}} = \frac{\partial \mathbf{S}}{\partial \mathbf{E}} \quad \Leftrightarrow \quad \bar{C}_{ijkl} = \frac{\partial S_{ij}}{\partial E_{kl}}. \quad (4.50)$$

It measures the change in stress resulting from a change in strain and is a tensor of rank four provided with four indices. It possess major and minor symmetries following from the

^{9.)} It is valid for a smooth scalar-valued function α and a tensor \mathbf{A} , where \mathbf{A} is the smooth tensor-valued function of a tensor variable \mathbf{B} .

second Piola-Kirchhoff stress tensor \mathbf{S} and the Green-Lagrange strain tensor \mathbf{E} or the right Cauchy-Green tensor \mathbf{C} i.e. $\bar{\mathbf{C}}_{ijkl} = \bar{\mathbf{C}}_{klij} = \bar{\mathbf{C}}_{jikl} = \bar{\mathbf{C}}_{ijlk}$ (HOLZAPFEL ET AL. [121]). Differentiating each terms of Eqn. 4.38 yields the incompressible part

$$\bar{\mathbf{C}}_{\text{incomp}} = \frac{\partial \mathbf{S}_{\text{incomp}}}{\partial \mathbf{E}} = -\frac{4}{D} (J^2 - J) \mathbf{C}^{-1} \underline{\otimes} \mathbf{C}^{-1} + \frac{2}{D} (2J^2 - J) \mathbf{C}^{-1} \otimes \mathbf{C}^{-1}, \quad (4.51)$$

the isotropic ground matrix part

$$\begin{aligned} \bar{\mathbf{C}}_{\text{matrix}} &= \frac{\partial \mathbf{S}_{\text{matrix}}}{\partial \mathbf{E}} \\ &= 4b^2 c \exp \left\{ b (\bar{I}_1 - 3) \right\} \left\{ J^{-\frac{4}{3}} \mathbf{I} \underline{\otimes} \mathbf{I} - \frac{J^{-\frac{2}{3}}}{3} \bar{I}_1 (\mathbf{C}^{-1} \otimes \mathbf{I} + \mathbf{I} \otimes \mathbf{C}^{-1}) \right. \\ &\quad \left. + \frac{1}{9} (\bar{I}_1)^2 \mathbf{C}^{-1} \otimes \mathbf{C}^{-1} \right\} + 4bc \exp \left\{ b (\bar{I}_1 - 3) \right\} \left\{ \frac{1}{9} \bar{I}_1 \mathbf{C}^{-1} \otimes \mathbf{C}^{-1} \right. \\ &\quad \left. - \frac{J^{-\frac{2}{3}}}{3} (\mathbf{C}^{-1} \otimes \mathbf{I} + \mathbf{I} \otimes \mathbf{C}^{-1}) + \frac{1}{3} \bar{I}_1 \mathbf{C}^{-1} \otimes \mathbf{C}^{-1} \right\}, \end{aligned} \quad (4.52)$$

and the passive muscle fiber part of the tangent matrix

$$\begin{aligned} \bar{\mathbf{C}}_{\text{passive}} &= \frac{\partial \mathbf{S}_{\text{passive}}}{\partial \mathbf{E}} \\ &= 2aA (\bar{\lambda}_f - 1) \exp \left\{ a (\bar{\lambda}_f - 1)^2 \right\} \left\{ -\frac{J^{-\frac{4}{3}}}{\bar{\lambda}_f^3} \mathbf{N} \otimes \mathbf{N} \otimes \mathbf{N} \otimes \mathbf{N} \right. \\ &\quad \left. - \frac{J^{-\frac{2}{3}}}{3\bar{\lambda}_f} (\mathbf{N} \otimes \mathbf{N} \otimes \mathbf{C}^{-1} + \mathbf{C}^{-1} \otimes \mathbf{N} \otimes \mathbf{N}) + \frac{1}{9} \bar{\lambda}_f \mathbf{C}^{-1} \otimes \mathbf{C}^{-1} + \frac{2}{3} \bar{\lambda}_f \mathbf{C}^{-1} \underline{\otimes} \mathbf{C}^{-1} \right\} \\ &\quad + 2aA \left(1 + 2a (\bar{\lambda}_f - 1)^2 \right) \exp \left\{ a (\bar{\lambda}_f - 1)^2 \right\} \left\{ \frac{J^{-\frac{4}{3}}}{\bar{\lambda}_f^2} \mathbf{N} \otimes \mathbf{N} \otimes \mathbf{N} \otimes \mathbf{N} \right. \\ &\quad \left. - \frac{J^{-\frac{2}{3}}}{3} (\mathbf{N} \otimes \mathbf{N} \otimes \mathbf{C}^{-1} + \mathbf{C}^{-1} \otimes \mathbf{N} \otimes \mathbf{N}) + \frac{1}{9} \bar{\lambda}_f^2 \mathbf{C}^{-1} \otimes \mathbf{C}^{-1} \right\}. \end{aligned} \quad (4.53)$$

Combining Eqns. 4.51, 4.52 and 4.53, a 6×6 square matrix of the material tangent moduli for anisotropic skeletal muscle can be obtained to implement into a finite element software.

4.6.3 Implementation of anisotropic muscle model into a finite element framework

The finite element (FE) software used in this thesis work is *Code_Aster* which is developed by the Électricité de France (EDF), France. It is an open source software and the user-defined material subroutines, describing the passive mechanical behavior of the skeletal muscle, as shown from Eqn. 4.30 to Eqn. 5.3 have been implemented in the aster version 12.4. Previous aster versions until 11.x has been written in FORTRAN 77 and starting from version 12.0 the core of *Code_Aster* is updated in FORTRAN 90. The pre-processing (geometry modification after Rhino software and meshing) and post-processor (graphical analysis of the results) have been employed in the SALOME software.

The mesh is only an topological entity with a collection of nodes, elements and their groups, one needs to instruct *Code_Aster* to solve a physical problem and output the results. For this, a python interpreted input file, so called command file is written to read the FE mesh, to define the material parameters, to establish the boundary conditions, to choose relevant analysis type and solution methodology and to print the results for post-processing in SALOME Post-Pro or ParaVis modules.

In order to reduce the complication arising from the computation of the non-linear anisotropic muscle model, the FE mesh is constructed with 4 noded three dimensional tetrahedrons. These are also called as linear tetrahedrons is named as TETRA4 in aster since its shape functions are linear polynomials between the nodes.

The passive model of the skeletal pelvic muscle as defined by the system of differential equations is implemented on the level of the constitutive equation. Besides some configuration implementations to allow aster to recognize the newly introduced material model, the whole implementation is limited to the user-defined constitutive subroutines. The algorithm of Newton-Raphson is used to solve the nonlinear equation systems in an iterative way with a user-defined precision (default relative error of $= 10^{-6}$) at any discrete time.

5 Anisotropic Modeling of Levator Ani Muscle

This chapter will present a 3D computational model of the female levator ani muscle with a focus on the anatomy and fibre organization, include an integrated discussion of the constitutive model based on the tissue constituents, fibre and ground substance; and emphasize the importance of the muscle fibres during increased IAP by comparing the passive relaxation of the levator ani muscle with the results of dynamic Magnetic resonance Imaging (MRI). This chapter will also discuss the possibility of a levator ani dysfunction due to lost support from the anococcygeal ligament and perineal structures, and also highlight further studies regarding active contraction of the levator ani muscles and related dysfunctions due to localized damages in the muscle fibres.

5.1 3D female pelvic floor muscle geometry

The NURBS-based model as shown in Fig. 5.1a is the part of the complete female pelvic floor model as described in section 3.4. The smooth geometry is imported into the open source pre- and post- processor SALOME to create a FE mesh (Fig. 5.1b). Considering the significant thickness of the levator ani muscle, the discretization of the volume is performed with 61538 linear tetrahedrons^{10.)}.

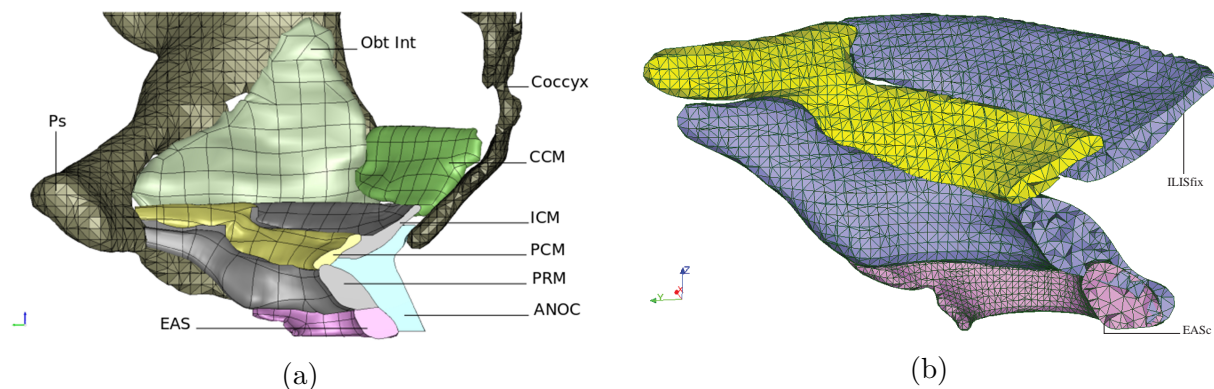


Figure 5.1: a) Sagittal section of the female pelvic muscle model created from the data set of the plastinated reconstruction. ICM = iliococcygeus muscle, PCM = pubococcygeus muscle, PRM = puborectalis muscle, EAS = external anal sphincter, CCM = coccygeus muscle, ANOC = anococcygeal ligament, Ps = pubic symphysis, and Obt Int = obturator internus muscle. b) Sagittal section of the 3D finite element mesh of the levator ani muscle with two nodes EASc and ILISfix to compare muscle displacement and stress (BHATTARAI ET AL. [27]).

^{10.)} Reasons behind using linear tetrahedrons to construct FE meshes of the female pelvic floor structures in this thesis is discussed in section 3.4

5.2 Boundary conditions

The anterior and posterior nodes of the levator ani muscle connected to the pubic symphysis and coccyx are completely fixed. Laterally, the levator ani muscle is connected to the obturator internus (OI) muscle by the condensation of the fascia, commonly known as arcus tendinous levator ani (ATLA). Though, the OI muscle forms the pelvic side wall, larger area of the OI muscle is unattached to the obturator foramen and ilium, which allows 3D movement of the levator ani muscle along the attachment of the ATLA. Therefore, the lateral constraint has been released to induce free deformation of the levator ani muscle. Suddenly increased IAP acts over the pelvic organs, which is supported by the levator ani muscle and suspended by connective tissues. This pressure is transferred to the levator ani muscle.

Pressure calculation

An average supine Valsalva pressure^{11.)} of 4 kPa has been averaged from the literature (COBB ET AL. [62], ZAJAC [337], NOAKES ET AL. [210]). Examinations of patients, either normal physical or using radiological equipment for grading the severity of the prolapse with pelvic organ prolapse quantification (POP-Q) system are usually performed in dorsal supine or standing positions. There is an excellent correlation in the evaluation of prolapse between two positions. However, performing measurements in standing position is physically more difficult. Therefore all the measurements of the pressure and the organ movements are established in supine position. In the present model, the area of the internal faces of the levator ani muscle that are connected to the pelvic organs via endopelvic fascia is summed up. Therefore, the IAP assumed in this numerical simulation was set equal to 3.1155 kPa.

5.3 Finite element simulation of passive stretching of levator ani muscle

The material parameters of the passive Humphrey model (Eqn. (4.30-4.33)) are derived from Pato et al. (PATO AND AREIAS [225]) and are: $a = 12.43$, $b = 23.46$, $c = 3.79517355 \times 10^{-4}$ MPa, $A = 5.7270836 \times 10^{-4}$ MPa, $T_0^M = 6556.872 \times 10^{-4}$ MPa and $D = 10^{-4}$ MPa. The finite deformation simulations for the computer model as shown in Fig. 5.2 were performed in BHATTARAI ET AL. [26], BHATTARAI ET AL. [27] with the open source FE software, *Code_Aster*. To verify the results obtained from the simulation, two points *EASc* and *ILISfix* on the FE mesh of the levator ani muscle are selected, see Fig. 5.1b. These points are also chosen as reference points (*EASc* and *ILISfix*) by NOAKES ET AL. [210] where larger deformation and stress were calculated. In the levator ani model, the vertical displacement of the reference point during Valsalva maneuver simulation is 27.616 mm, see Fig. 5.3a. As a reference, we used the vertical movement of the levator muscle of 27.9 mm set from a dynamic MRI acquisition in a nulliparous female during Valsalva maneuver (Fig. 5.2a-5.2b) from NOAKES ET AL. [210]. Figure 5.3a

^{11.)} It is characterized by a forced exhalation against a closed glottis which suddenly increases the intra-abdominal and intrathoracic pressures due to the contractions of the abdominal and respiratory muscles.

illustrates that the vertical displacement of the levator ani muscle which is quantitatively consistent with the MRI reading (NOAKES ET AL. [210]).

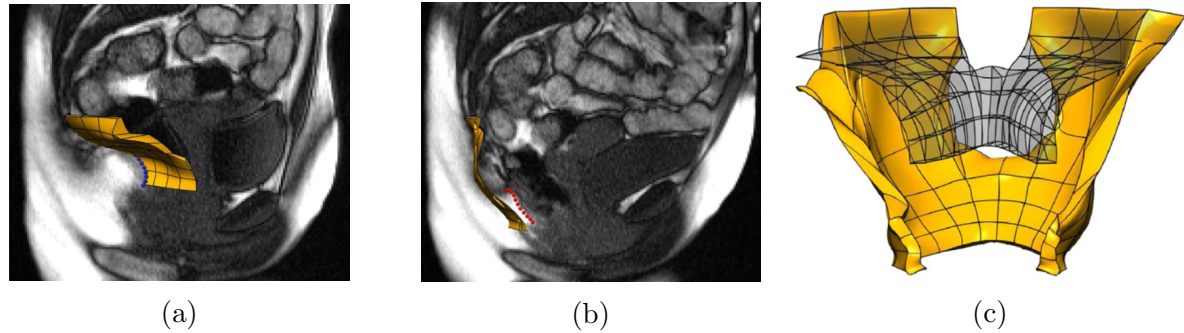


Figure 5.2: MR images showing levator ani muscle highlighted by the a) blue points at rest b) the red points during Valsalva maneuver. c) Anterior view of the finite elasticity simulation results showing the levator ani at rest (wireframe) and under Valsalva (gold surface) (NOAKES ET AL. [210]).

Noakes et al. simplified the pelvic muscle as an isotropic hyperelastic material and used the Mooney-Rivlin material model. Simulation result in the reference offered a significant difference (13.7 mm) of the movement of the posterior region of the muscle, and for that reason the paper explicitly recommended adopting fibre based constitutive models for improving the results. In that regard, the Humphrey model has been implemented by BHATTARAI ET AL. [27] for the assessment of the fibre-matrix contribution due to the



Figure 5.3: a) FE simulation of the levator ani displacement due to an IAP. (a) Undeformed state (gray wireframe) and displaced levator ani muscle (solid): anterior view. (b) Stress distribution along the muscle. The larger principal stress in the simulation is, $\sigma_1^{\max} = 0.03866$ MPa: superior view (BHATTARAI ET AL. [27]).

applied IAP. Despite of the fibre being orientated towards posterior direction, the levator ani muscle displaces about 2.5 times more than the one seen by Noakes et al. (11.64 mm vs. 4.7 mm, respectively). In both the Mooney-Rivlin and the Humphrey models the differences might be addressed due to the lack of any anterior-posterior support at the level of the EAS. Pelvic anatomy suggests that at this level, along with the posterior support from the fat tissues, the perineal body, the transverse perinei superficialis, skin

and the anal plate holds the EAS muscle anteriorly and posteriorly. All of these structures are absent in the computational model. Thus, one can predict a case with possible (extra) widening of the levator hiatus, which is due to the loss of structural integrity of the perineal structures and anal plate during vaginal delivery.

Stress contours in the deformed pelvic muscle due to IAP are plotted in Fig. 5.4. The Cauchy stresses are compared at two selected reference points on the muscle, ILISfix (which is fixed to the coccyx) and EASc (which moves according to the deformation of the whole muscle), see Fig. 5.4. The stress value at the external anal sphincter, the exit of the anal canal, is quite low, however, around ILISfix, whereas the part of the iliococcygeus muscle connected to the coccyx bone is highly stressed. Chances of localized damage of the levator ani muscle are certainly high during extreme physical activities such as heavy physical exercise and straining during obstructed defecation.

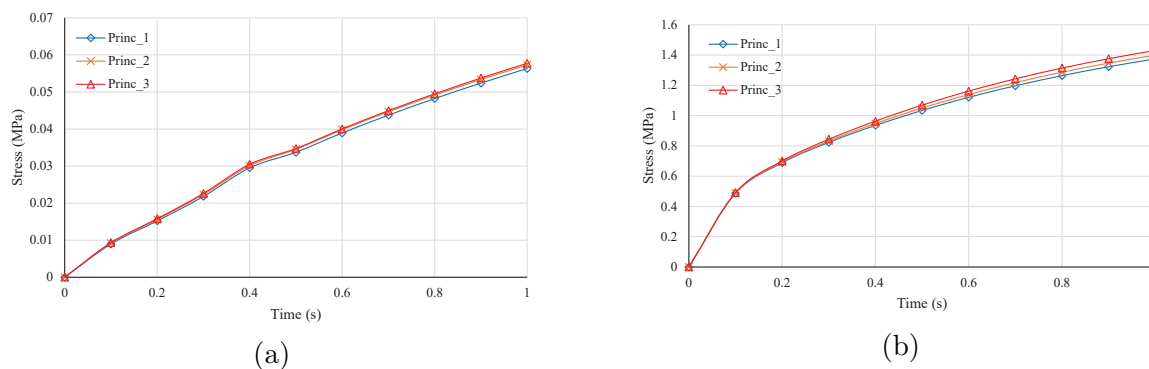


Figure 5.4: Principal stress variation at two points a) EASc: b) ILISfix (BHATTARAI ET AL. [26], BHATTARAI ET AL. [27]).

5.4 Limitations of the constitutive modeling

PFDs may be associated with impaired or injured muscles and connective tissues in the pelvic cavity due to overstretched pelvic floor by birth-related levator ani injury, chronic coughing, or obesity. Progressive weakening of the muscle, especially of pubococcygeus and its lateral connective tissue attachment to the vaginal walls fails to contract effectively to close the hiatal opening. As a result, vaginal walls move downward and are exposed to the differential pressure between abdominal and atmospheric pressure. This pressure difference further widens the levator hiatus and pulls the rest of the pelvic organs, which in turn, stresses and stretches the supporting ligaments. Over time, due to excessive stretching, ligaments lengthen permanently and fail to support. Results are often seen as (urinary and fecal) incontinence and prolapse (cystocele, urethrocele, rectocele and vaginal vault prolapse).

This chapter introduced some of the relevant physical and mechanical issues in the female levator ani muscle modeling which allowed studying its complex behavior during increased IAP. The results of the 3D levator ani muscle model developed from a subject-specific dataset of an old female cadaver qualitatively captured the passive relaxation of the pelvic

muscle. The implemented Humphrey model is very promising to describe the passive mechanics of the female pelvic muscle due to IAP. Muscle fibres are qualitatively and quantitatively able to resist the exerted pressure and restrict the vertical levator ani muscle movement.

Although the investigation of the passive response of the levator ani muscle has been done with great detail, its posterior movement was nevertheless larger than it has been observed in the reference MRI (11.64 mm vs. 4.7 mm), for which structural and mechanical reasons may have contributed. The presented model lacks some supporting structures such as perineal structures, fatty tissues and anococcygeal ligament. Due to hormonal changes in old ages weak support from such tissues and posterior shifting of the levator ani muscle is expected. Since, the material parameters used in the simulation are adopted from the autonomously contracting heart tissue, differences in the behavior might be the other reason of different displacement measurement in levator ani muscle. The presented pelvic model is adopted from the cadaver levator ani muscle; lack of the muscle tone or the neural excitation in the mechanical model cannot sufficiently represent the in vivo muscle deformation. Thus, decreased muscle tone from an aged female leads to a decreased ability to balance the muscle contraction and the induced IAP. Nevertheless, results obtained from this simulation are additionally helpful to predict the location of regions where the muscle is critically stressed during increased IAP.

5.5 Active muscle contraction

Clinically, PFDs is considered when the pelvic muscle is not able to support or hold the pelvic organs at their stable positions. The computed model present considers only the passive stretching of the pelvic muscle fibres in the structural level. However, it is presumed that the pelvic muscles stretching is influenced by the inactive muscle fibers that is fully extensible during IAP but capable of shortening when activated against the IAP. During sudden physical activities IAP increases for which muscle fibers neurally excite and contract to resist the pressure.

Active strain energy function

The constitutive model for the skeletal muscle presented before (Eqn. 4.30) needs to be extended with an active muscle contraction strain energy function AULIGNAC ET AL. [12] which adopts the activation function $\alpha \in [0, 1]$ given as

$$W_{\text{active}} = \alpha T_0^M \int_1^{\bar{\lambda}_f} 1 - 4(\bar{\lambda}_f - 1)^2 d\bar{\lambda}_f. \quad (5.1)$$

For $0.5 < \bar{\lambda}_f < 1.5$, the active strain energy is larger than zero. For other values of $\bar{\lambda}_f$, the muscle produces no active contraction force and, therefore, the strain energy is zero.

Active contraction second Piola-Kirchhoff stress

The stress contribution from the active fibre contraction can be computed as

$$\begin{aligned}
\mathbf{S}_{\text{active}} &= \frac{\partial W_{\text{active}}}{\partial \mathbf{E}} \\
&= \frac{\partial W_{\text{active}}}{\partial \bar{\lambda}_f} \frac{\partial \bar{\lambda}_f}{\partial \bar{\mathbf{C}}} : \frac{\partial \bar{\mathbf{C}}}{\partial \mathbf{C}} : \frac{\partial \mathbf{C}}{\partial \mathbf{E}} \\
&= \alpha T_0^M \left\{ 1 - 4(\bar{\lambda}_f - 1)^2 \right\} \left(J^{-\frac{2}{3}} \mathbf{N} \otimes \mathbf{N} - \frac{1}{3} \bar{\lambda}_f \mathbf{C}^{-1} \right). \tag{5.2}
\end{aligned}$$

The fibre vectors (\mathbf{N}) and other parameters has been already described in section 4.6.

Material tangent moduli for active skeletal muscle contraction

Finally, the fourth order material tangent moduli for the active contraction component of the skeletal muscle can be computed as

$$\begin{aligned}
\bar{\mathbf{C}}_{\text{active}} &= \frac{\partial \mathbf{S}_{\text{active}}}{\partial \mathbf{E}} \\
&= \alpha T_0^M \left\{ 1 - 4(\bar{\lambda}_f - 1)^2 \right\} \left\{ - \frac{J^{-\frac{4}{3}}}{\bar{\lambda}_f^3} \mathbf{N} \otimes \mathbf{N} \otimes \mathbf{N} \otimes \mathbf{N} \right. \\
&\quad \left. - \frac{J^{-\frac{2}{3}}}{3\bar{\lambda}_f} (\mathbf{N} \otimes \mathbf{N} \otimes \mathbf{C}^{-1} + \mathbf{C}^{-1} \otimes \mathbf{N} \otimes \mathbf{N}) + \frac{1}{9} \bar{\lambda}_f \mathbf{C}^{-1} \otimes \mathbf{C}^{-1} + \frac{2}{3} \bar{\lambda}_f \mathbf{C}^{-1} \underline{\otimes} \mathbf{C}^{-1} \right\} \\
&\quad + 8\alpha T_0^M (\bar{\lambda}_f - 1) \left\{ - \frac{J^{-\frac{4}{3}}}{\bar{\lambda}_f^2} \mathbf{N} \otimes \mathbf{N} \otimes \mathbf{N} \otimes \mathbf{N} \right. \\
&\quad \left. + \frac{J^{-\frac{2}{3}}}{3} (\mathbf{N} \otimes \mathbf{N} \otimes \mathbf{C}^{-1} + \mathbf{C}^{-1} \otimes \mathbf{N} \otimes \mathbf{N}) - \frac{1}{9} \bar{\lambda}_f^2 \mathbf{C}^{-1} \otimes \mathbf{C}^{-1} \right\}. \tag{5.3}
\end{aligned}$$

5.5.1 Muscle activation simulation

The constitutive model for the skeletal pelvic floor muscle adopted in this section is same (Eqn. (4.30-4.33)) as used for the FE simulation results in section 5.3. However, the active contraction of the cardiac tissue based material parameter might not perfectly approximate the pelvic muscle behavior. Parente et al. PARENTE ET AL. [223] investigated the influence of the varying muscle material behavior during vaginal delivery with an integrated system of passive stretching and active contraction (5.1-5.3). The constitutive parameters (the materials used in PARENTE ET AL. [223]) are: $a = 0.6215$, $b = 1.173$, $c = 1.85 \times 10^{-2}$ MPa, $A = 2.80 \times 10^{-2}$ MPa, $T_0^M = 6.82 \times 10^{-4}$ MPa and $D = 10^{-2}$ MPa.

In order to examine the influence of the active contraction energy, we performed a simple test on a bar of L (200 mm) \times B (20 mm) \times H (20 mm), see Fig. 5.5. The geometry is discretized into a FE mesh of 8000 linear tetrahedrons. The fibre direction is aligned along the length of the test geometry, i.e., Y-axis. The bar is fixed on one side and the other

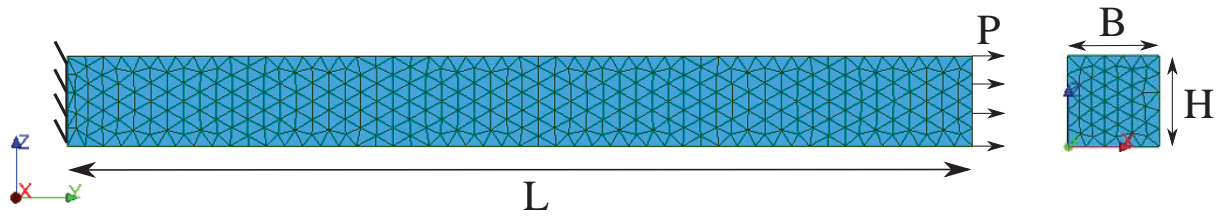


Figure 5.5: A simple bar mesh of linear tetrahedrons showing dimensions and boundary conditions.

side is uniaxially pulled with a pressure, $P=10$ kPa. In the first step, the bar is subjected to a uniaxial pull with a pressure P along positive Y -axis. An activation function α is considered to be zero which resembles a situation similar to the pure passive stretching. At the end of the simulation, the displacement of the free end of the bar at $\alpha = 0$ is calculated to be 11.45 mm as shown in Fig. 5.6.

In next step, the muscle contraction is activated by 10% with activation function $\alpha = 0.1$ on the same bar subjected to the same boundary conditions. The muscle fibres are activated to contract under prescribed neural stimulation. The displacement is again calculated at the end of the loading. In the same manner, simulations are performed with $\alpha=0.2, 0.3, \dots$ and so on until fully activated value $\alpha=1$ is gained. The displacements of the bar under all activation levels are calculated and plotted in Fig. 5.6.

The shortening effect due to the fibre activation can be clearly observed. It is important to observe that when the constitutive model is purely passive without activating fibre contraction ($\alpha = 0$), the deformation is significantly larger (11.45 mm vs 10.66 mm) than when the fibres are activated for contraction ($\alpha = 1$) and the distributed stress on the uni-axially loaded bar with fully activated muscle fibres is shown in Fig. 5.7.

5.5.2 Application to the pelvic muscle: future outlook

In the presented model, firstly, we simulate the purely passive deformation of the levator ani muscle when subjected to an intra-abdominal pressure under zero muscle stimulation.

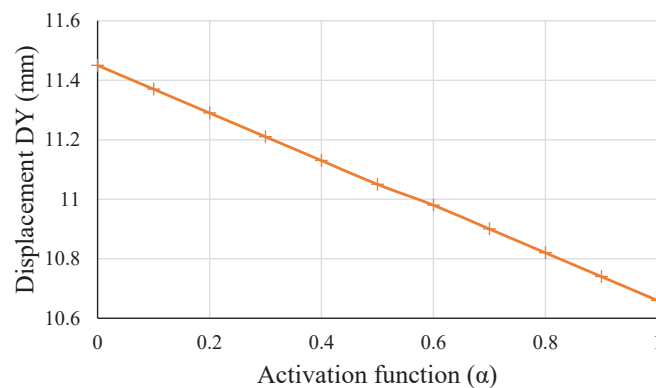


Figure 5.6: a) Displacement (DY) of the bar along Y -axis vs muscle activation, $\alpha \in [0, 1]$.

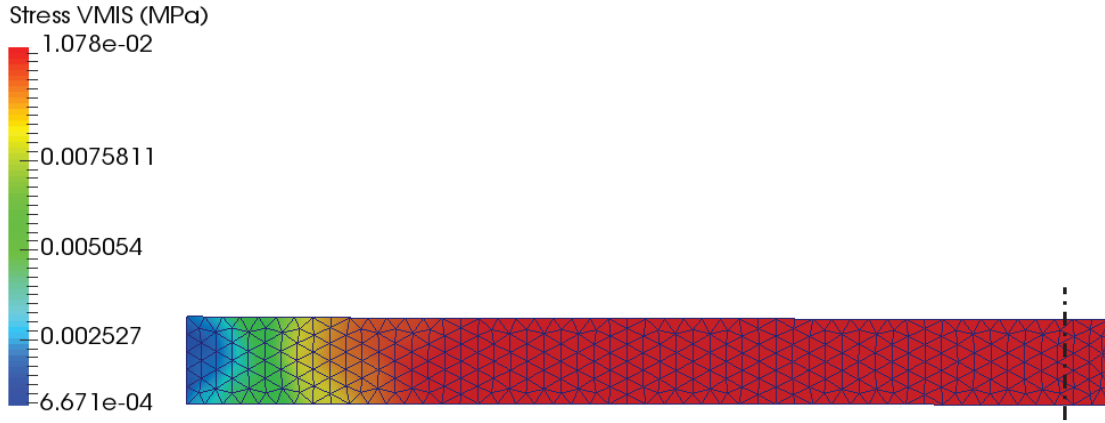


Figure 5.7: FE simulation showing the von Mises stress distribution in the bar with fully activated fibres ($\alpha = 1$). The black dotted line represents the position of the undeformed bar length.

Later, we extended the anisotropic skeletal muscle model by introducing a simple activation function, the value of the muscle activation ranges between 0 and 1. The model has been tested on a simple bar as an example. However, the time-dependent activation of the skeletal pelvic muscle involves a phenomenological stimulation of the contractile element resulting from the muscle neural excitation ($u(t) \in [0, 1]$) that is governed by the dynamics of the Ca^{2+} and is represented by the first-order ordinary differential equation PANDY ET AL. [221]

$$\alpha(t) = \frac{\alpha(0)\tau_{\text{rise}}\tau_{\text{fall}} + \Delta t\tau_{\text{fall}}u(t) + \Delta t\alpha_{\text{min}}\tau_{\text{rise}} - \Delta t\alpha_{\text{min}}\tau_{\text{rise}}u(t)}{\tau_{\text{rise}}\tau_{\text{fall}} + \Delta t\tau_{\text{fall}}u(t) + \Delta t\tau_{\text{rise}} - \Delta t\tau_{\text{rise}}u(t)}. \quad (5.4)$$

The characteristic time dependent constants τ_{rise} and τ_{fall} are for activation and deactivation of the muscle, and $\alpha_{\text{min}} = 0$ is the minimum value of the activation.

A *three-element skeletal muscle model* has been proposed by Hill (HILL [116]) where a passive parallel element (PE) is connected in parallel to both the contractile element (CE) and the series elastic element (SE), see Fig. 5.8. Under tension, the contractile element allows the free change in length of the muscle (when not activated) and for the active force production in the muscle (when activated) by the actin and the myosin cross-bridges at the sarcomere level. On the other hand, the passive part is represented by the connective tissues (fascia, epimysium, perimysium and endomysium) that surround the contractile element, which is PE, and other connective tissues in series (SE) with the sarcomeres,

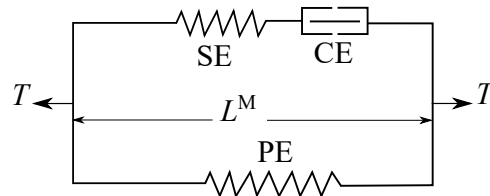


Figure 5.8: Schematic of the Hill-type three element muscle model.

which influence the force-length curve of the muscle. Together these passive elements have a soft tissue mechanical behavior, which can be described by nonlinear hyperelastic and incompressible constitutive relations, however, because of a single muscle fiber direction they may be considered as transversely isotropic. The net force-length characteristics of the skeletal muscle satisfy

$$F = f^{\text{SE}} + f^{\text{PE}} \quad \text{and} \quad f^{\text{CE}} = f^{\text{SE}}, \quad (5.5)$$

where F , f^{CE} , f^{SE} and f^{PE} are the forces in total muscle, contractile, series elastic and passive parallel element. Following Eqn. (5.5), the longitudinal muscle stress T and the stress in the components as shown in Fig. 5.8 also satisfy

$$T = T^{\text{SE}} + T^{\text{PE}} \quad \text{and} \quad T^{\text{CE}} = T^{\text{SE}}. \quad (5.6)$$

On the other hand, the muscle length (L^{M}) and the lengths of these components satisfy

$$L^{\text{M}} = L^{\text{PE}} = L^{\text{CE}} + L^{\text{SE}}. \quad (5.7)$$

5.5.3 Calculation of the contractile stretch

For an undeformed fiber length L_0^{M} , deformed fiber length in contractile element L^{CE} due to relative sliding in the actin-myosin contractile device, and a final length L^{M} due to elastic deformation of the myofibers superposed to their relative sliding, one can relate different stretches as:

$$\bar{\lambda}_f = \frac{L^{\text{M}}}{L_0^{\text{M}}}, \quad \lambda^{\text{CE}} = \frac{L^{\text{CE}}}{L_0^{\text{M}}}, \quad \text{and} \quad \lambda^{\text{SE}} = \frac{L^{\text{M}}}{L^{\text{CE}}}. \quad (5.8)$$

For the implementation of the active contraction of the skeletal muscle model, the deformation associated within the contractile element needs to be computed. Because of the large deformation involved in the muscle deformation, the fiber stretch $\bar{\lambda}_f$ can be multiplicatively split into a contractile stretch λ^{CE} and an elastic stretch λ^{SE} in the series element

$$\bar{\lambda}_f = \lambda^{\text{CE}} \lambda^{\text{SE}}. \quad (5.9)$$

Stress in the parallel element

It is assumed that when the muscle is not activated, $T^{\text{CE}} = T^{\text{SE}} = 0$. The muscle develops force/stress in the passive element when the muscle is stretched i.e. $\bar{\lambda}_f > 1$ and is essentially zero for other cases. The stress T^{PE} in the parallel elastic element can be defined as:

$$T^{\text{PE}}(\bar{\lambda}_f) = T_0^{\text{M}} f^{\text{PE}}(\bar{\lambda}_f), \quad (5.10)$$

where,

$$f^{\text{PE}}(\bar{\lambda}_f) = \begin{cases} 2aA \exp \left\{ a (\bar{\lambda}_f - 1)^2 \right\} (\bar{\lambda}_f - 1), & \forall \bar{\lambda}_f > 1 \\ 0, & \text{otherwise,} \end{cases} \quad (5.11)$$

is the passive non-dimensional force that is a rederived version of the proposal by PANDY ET AL. [221] and a modified version of MARTINS ET AL. [191]. The constitutive parameters a and A have been introduced for cardiac tissues by HUMPHREY AND YIN [127].

Stress in the series elastic element

The stress on the series elastic T^{SE} is given by:

$$T^{\text{SE}}(\lambda^{\text{SE}}, \lambda^{\text{CE}}) = T_0^M f^{\text{SE}}(\lambda^{\text{SE}}, \lambda^{\text{CE}}), \quad (5.12)$$

where

$$f^{\text{SE}}(\lambda^{\text{SE}}, \lambda^{\text{CE}}) = \frac{1}{10} \left[\exp \{ 100 \lambda^{\text{CE}} (\lambda^{\text{SE}} - 1) \} - 1 \right] \quad \forall \quad \lambda^{\text{SE}} \geq 1. \quad (5.13)$$

In terms of the muscle fiber stretch $\bar{\lambda}_f$,

$$f^{\text{SE}}(\bar{\lambda}_f, \lambda^{\text{CE}}) = \frac{1}{10} \left[\exp \{ 100 (\bar{\lambda}_f - \lambda^{\text{CE}}) \} - 1 \right] \quad \forall \quad \bar{\lambda}_f \geq \lambda^{\text{CE}}. \quad (5.14)$$

Stress in the contractile element

The stress in the contractile element follows the relatively standard form, adapted from PANDY ET AL. [221]:

$$T^{\text{CE}}(\lambda^{\text{CE}}, \dot{\lambda}^{\text{CE}}, \alpha) = T_0^M f_L^{\text{CE}}(\lambda^{\text{CE}}) f_V^{\text{CE}}(\dot{\lambda}^{\text{CE}}) \alpha, \quad (5.15)$$

where the functions $f_L^{\text{CE}}(\lambda^{\text{CE}})$ and $f_V^{\text{CE}}(\dot{\lambda}^{\text{CE}})$ are the force-length and force-velocity properties of the muscle and the time dependent muscle activation is caused by neural excitation with the activation variable $\alpha \in [0, 1]$. The function $f_L^{\text{CE}}(\lambda^{\text{CE}})$ has been proposed by PATO AND AREIAS [225] as a typical bell curve or inverted parabola with maximum value at the muscle rest length and is given as:

$$f_L^{\text{CE}}(\lambda^{\text{CE}}) = 8 \begin{cases} \lambda^{\text{CE}^2} - \lambda^{\text{CE}} + 0.25, & 0.5 \leq \lambda^{\text{CE}} < 0.75 \\ -\lambda^{\text{CE}^2} + 2\lambda^{\text{CE}} - 0.875, & 0.75 \leq \lambda^{\text{CE}} < 1.25 \\ \lambda^{\text{CE}^2} - 3\lambda^{\text{CE}} + 2.25, & 1.25 \leq \lambda^{\text{CE}} < 1.5 \\ 0, & \text{otherwise.} \end{cases} \quad (5.16)$$

Some other functions have also been proposed by BÖL AND REESE [36] and MCLEAN ET AL. [195] to describe the mechanical behavior of the skeletal muscle and its force-length property. However, only PATO AND AREIAS [225] and ROZA ET AL. [263] have used the modified Humphrey model to characterize the desired pelvic skeletal muscle and therefore has been adopted in this thesis. As shown in Fig. 5.9, the adopted *present model* by Pato et al. is closer to that formulated by Böl and Reese, however the consideration of stretches are widely different for both cases.

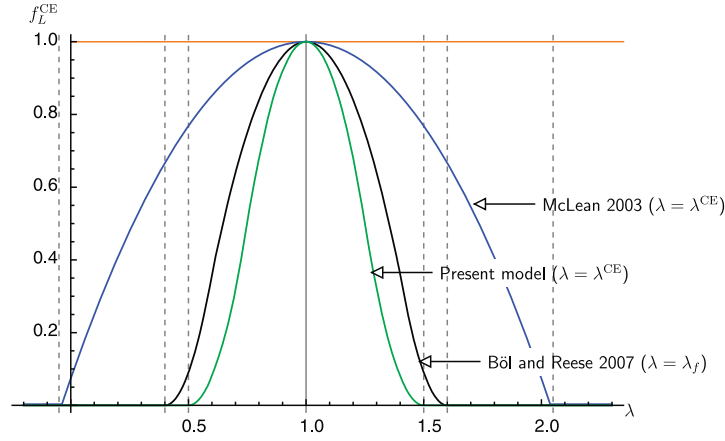


Figure 5.9: Relation of $f_L^{CE}(\lambda^{CE})$ with fiber stretches for different proposed models (BÖL AND REESE [36], MCLEAN ET AL. [195], Present model = PATO AND AREIAS [225]).

Similarly, the force-velocity property of the skeletal muscle during active contraction can be expressed as (PATO AND AREIAS [225]):

$$f_V^{CE}(\dot{\lambda}^{CE}) = \begin{cases} (\dot{\lambda}^{CE} + 10)\varepsilon, & \dot{\lambda}^{CE} \leq -10\text{s}^{-1} \\ -\frac{\arctan(-0.5\dot{\lambda}^{CE})}{\tan^{-1}(5)} + 1, & -10\text{s}^{-1} < \dot{\lambda}^{CE} < 2\text{s}^{-1} \\ (\dot{\lambda}^{CE} - 2)\varepsilon + \frac{\pi}{4\arctan(5)} + 1, & \dot{\lambda}^{CE} \geq 2\text{s}^{-1}, \end{cases} \quad (5.17)$$

where the value of ε is sufficiently small and is introduced to avoid $f_V^{CE}(\lambda^{CE}) = 0$ when $\dot{\lambda}^{CE} \leq -10\text{s}^{-1}$. Alternatives to this function have also been derived by Böl and Reese (BÖL AND REESE [36]), however the function has been simplified ($\dot{\lambda} = \dot{\lambda}_f$) to circumvent the singularity problem. In contrast, the smooth force-velocity function represented as shown in Fig. 5.10 solves the singularity problem without simplification by replacing $\dot{\lambda}_f$ with $\dot{\lambda}^{CE}$.

Time-dependent activation

The activation variable $\alpha \in [0, 1]$ results from the neural stimulation that is governed by the dynamics of the Ca^{2+} . At the macroscopic level, this time dependent activation is represented by the first-order differential equation

$$\dot{\alpha}(t) = \frac{1}{\tau_{\text{rise}}} (1 - \alpha(t)) u(t) + \frac{1}{\tau_{\text{fall}}} (\alpha_{\text{min}} - \alpha(t)) (1 - u(t)), \quad (5.18)$$

where, $\tau_{\text{rise}} = 20 \times 10^{-3}\text{s}$ and $\tau_{\text{fall}} = 200 \times 10^{-3}\text{s}$ are the characteristic time constants for activation and deactivation of the muscle. And $\alpha_{\text{min}} \geq 0$ is the minimum value of the activation. Experimental values for these parameters are given in HUMPHREY AND YIN [127] and PANDY ET AL. [221].

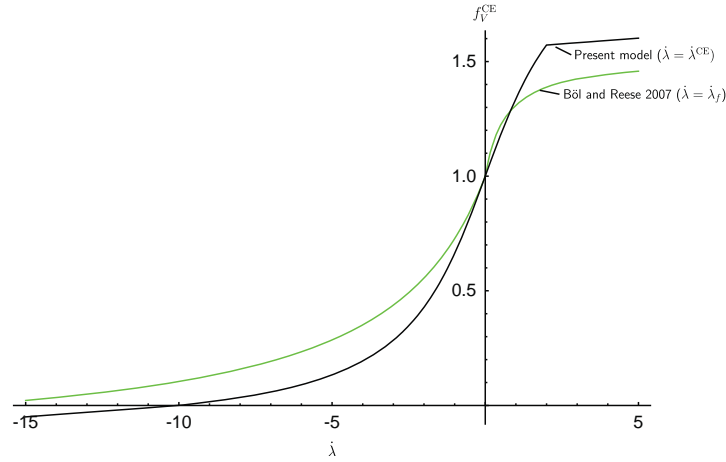


Figure 5.10: Representation of the force-velocity function (BÖL AND REESE [36], present model = PATO AND AREIAS [225]).

Solution for contractile stretch

The contractile stretch can be calculated by equating the stress of the series elastic T^{SE} (Eqn. 5.12) and the contractile T^{CE} element (Eqn. 5.15) adapted from PANDY ET AL. [221] and PATO AND AREIAS [225]

$$\begin{aligned} T^{\text{CE}}(\lambda^{\text{CE}}, \dot{\lambda}^{\text{CE}}, \alpha) &= T^{\text{SE}}(\lambda^{\text{SE}}, \lambda^{\text{CE}}) \\ \Rightarrow f_V^{\text{CE}}(\dot{\lambda}^{\text{CE}}) &= \frac{f^{\text{SE}}(\lambda^{\text{SE}}, \lambda^{\text{CE}})}{f_L^{\text{CE}}(\lambda^{\text{CE}}) \alpha}. \end{aligned} \quad (5.19)$$

The rate of contractile stretch can be calculated using Eqn. 5.17

$$\dot{\lambda}^{\text{CE}} = \begin{cases} \frac{f_V^{\text{CE}}}{\varepsilon} - 10, & \forall f_V^{\text{CE}} < 0 \\ 2 + \frac{f_V^{\text{CE}}}{\varepsilon} - \frac{\pi}{4\arctan(5)+1}, & \forall f_V^{\text{CE}} - \frac{\pi}{4\arctan(5)+1} > 0 \\ 2\tan\left[\arctan(5)(f_V^{\text{CE}} - 1)\right], & \text{otherwise.} \end{cases} \quad (5.20)$$

At initial condition when the muscle is not excited or activated for contraction, $\alpha(t=0) = u(0) = 0$ and $\bar{\lambda}_f(0) = 1$, the contractile stretch can be computed as $\lambda^{\text{CE}}(0) = 0.9959455676$ (PATO AND AREIAS [225]) using Eqn. 5.19 where $f_V^{\text{CE}}\alpha = 1$. Finally, the residual of the contractile element stretch follows the backward-Euler form

$$r_{\lambda^{\text{CE}}} = \lambda_{n+1}^{\text{CE}} - \lambda_n^{\text{CE}} - \Delta t \dot{\lambda}^{\text{CE}}, \quad (5.21)$$

to compute the updated contractile stretch. When the solution holds, $r_{\lambda^{\text{CE}}} \approx 0$ the final contractile stretch can be computed using *the Newton-Raphson method*.

Such an improved anisotropic muscle model has been implemented for different types of skeletal muscles PATO AND AREIAS [225]. At this stage, the author would like to consider

the advance muscle model as a future outlook on the project. Nevertheless, this thesis has succeed to implement and discuss the importance of the anisotropic model to describe the mechanical behavior of the skeletal pelvic muscle and to examine the development of the pelvic floor dysfunctions.

6 Prosthetic Implants to Treat Pelvic Floor Disorders

This chapter reviews some mesh related complications arising from the mechanical behavior of the mesh implants. A good mesh should optimally fulfil certain requirements, such as negligible foreign body reaction with no pathological fibrosis, flexibility with adaptable stiffness, adequate adhesion especially near the sutures, and mesh dynamics close to the anisotropic host tissue. Since, every prosthesis possess different mechanical properties, the response to the native tissues varies hugely making it difficult for surgeons to select the most appropriate mesh and its orientation for each type of patient with each type of disorder. To achieve a physiological behavior of the implanted mesh in the body, engineers and manufacturers should be aware of how the host tissue would respond with the implantation of such biomaterials. In this chapter, standard protocols for uniaxial tensile test in orthogonal symmetry directions are used to characterize the compressible dry meshes. The characterization should help predict how well a surgical mesh may contribute to the short-term and long-term success of the repair of hernia and urogynecological disorders.

6.1 Prosthetic meshes

Biologically and mechanically competent tissue-mesh response is a key factor in repairing herniation and pelvic floor dysfunctions. An ideal synthetic mesh should always provide structural support to the organs, restore anatomical function and treat physiological disorders with post-operation complications as less as possible. In order to achieve idealistic functionality and biological compatibility of prosthetic implants, properties of (type, dimensions and mechanics) polymer and (size and deformation under force) pores should be carefully understood.

6.1.1 An ideal polymer: polyvinylidene vs polypropylene?

Mechanically, an ideal synthetic meshes can be obtained from a mono filamentous large porous structure with anisotropic mechanical properties that mimics the mechanics of the host tissue. However, the biochemical compatibility of the meshes can be achieved through the choice of appropriate polymer material that affects the inflammatory response with granuloma formation. PP and PVDF are the mostly used polymer to construct surgical meshes due to their lesser amount of foreign body reaction compared to other available polymers. Though, PP shows inert response during infection, have excellent capacity for integration and are low cost meshes tested for years (LEBER ET AL. [171]), they results in an intensified inflammatory reaction characterized by pronounced foreign body granuloma and are less stable. On the other hand, PVDF filaments have excellent biocompatibility and reduced adverse foreign body reaction, such as scar formation or pain claiming a higher biocompatibility and biostability than polypropylene (KLINK ET AL. [157]). A PVDF meshes has been successfully used as composite scaffold for cell cultures (DUONG ET AL. [85]). Some long term advantages of the monofilament meshes against PP meshes are:

- reduced risk of infection due to lower bacterial adherence
- reduced mesh erosion (KLINGE ET AL. [154]).
- durability (lesser loss of tensile strength against PP: 7.5% vs. 46.6%) (LAROCHE ET AL. [169])
- no mesh curling under stress (OTTO ET AL. [219])

6.1.2 Textile structures

Textile constructions can be monofilament or multifilament. Monofilament mesh is very distensible, has thicker fibrils (100-150 μ) and large pore whereas, multifilament mesh is softer, non-distensible with thinner fibrils (20-30 μ) and smaller pores. Due to less inter-fiber space, multifilament meshes does not allow macrophages and neutrophils to enter through small pores. This provides comfortable environment for bacteria to survive within pores making such meshes at highest risk of infection.

6.1.3 Textile porosity

Porosity is defined as the amount of open space relative to the total area of the textile. It is an important parameter to predict the biocompatibility of the synthetic meshes. During healing stage, granulomas are formed around mesh fibers as part of the foreign body reaction that become confluent with each other and encapsulate the entire mesh. A stiff scar plate is formed which reduces the mesh flexibility (JERABEK ET AL. [137]). MÜHL ET AL. [203] introduced the concept of effective porosity that considers only the scar free or open pores. Effective porosity excludes all pores, which are smaller in diameter than a critical diameter which depends on the mesh material, 1 mm for Polypropylene mesh and 0.6 mm for polyvinylidene fluoride (OTTO ET AL. [219]). Meshes with large pores preserve effective porosity and exhibit less inflammatory infiltrate, connective tissue, fistula formation, calcification and scar bridging, which allows increased soft tissue ingrowth.

6.2 Specimen preparation and test set up

Specimen preparation

Three different DynaMesh[®]-SIS direct soft (SD), CICAT and PRS soft (PRS) products from FEG Textiltechnik mbH, Aachen, Germany have been tested. All of the selected meshes are monofilament made out of PVDF polymer but have a considerably different structure constructed for specific applications: SD is used for the repair of stress urinary incontinence, CICAT for hernia repair and PRS is used for uterine/vaginal vault prolapse correction. For uniaxial tensile tests specimens (70 mm x 30 mm) were cut out of each mesh in longitudinal direction and transverse direction with respect to knitted pattern. The thickness and the pore size was measured using a digital microscope VHX-600 (Keyence,

Japan). For inflation test, mesh specimen of 50 mm x 50 mm were cut and placed in the between two PVC plastic plate, see Fig. 6.1a. As alternative to animal testing, warm ballistic gelatin type 3 of GELITA (Eberbach, Germany) as a soft tissue surrogate is then poured inside the groove (1 mm deep), when cooled it forms a flexible gelatin-mesh complex (GMC), as shown in Fig. 6.1b and 6.1c. Gelatin has the practical advantage that its transparency and photoelasticity show detailed local behavior.

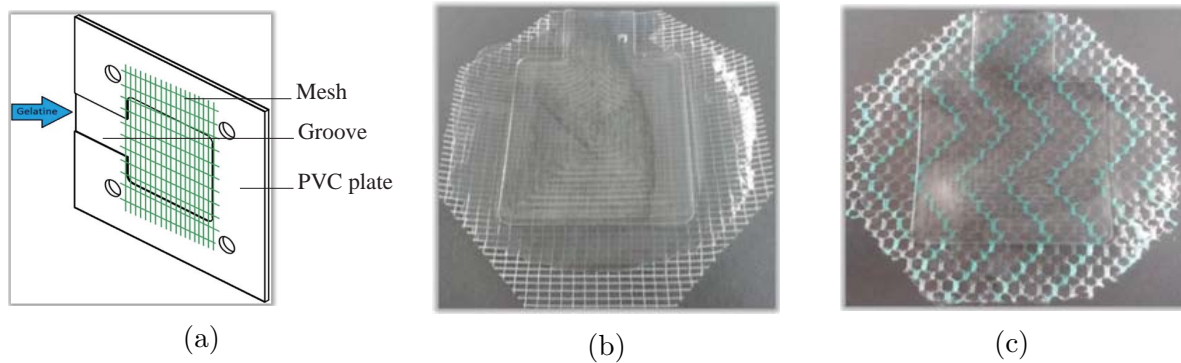


Figure 6.1: a) Mesh specimen preparation for inflation (bulge) test: a) Schematic drawing of PVC plastic plate and mesh; b) Dynamesh[®]-PRS soft specimen with gelatin; c) Dynamesh[®]-CICAT specimen with gelatin (BHATTARAI AND STAAT [28]).

Mechanical test set up

The uniaxial tensile tests are performed on tension testing machine Z 010 (Zwick Roell AG, Ulm, Germany) (BHATTARAI AND STAAT [28]). Two uniaxial tests protocols are followed on dry mesh and explants (dry mesh + ballistic gelatin). The two ends of the testing meshes are clamped properly at a distance of 50 mm, see Fig. 6.2a. For strong grip and to protect the mesh against cutting by the fixation, sand paper or PVC foils are used. BHATTARAI AND STAAT [28] used digital image correlation (DIC) technique to measure the stretch during tests that is based on the optical measurement of the deformation of a speckle pattern made by grey graphite spray. The camera has taken pictures during the test with a frequency of 1 Hz for DIC and the deformation is analyzed with the software ISTR 4D (Limes Messtechnik und Software GmbH, Krefeld, Germany) using a correlation algorithm.

Figure 2b shows biaxial test setup. GMC is clamped airtightly between two 2 mm thick stainless steel plates. Two cameras (uEye Modell UI-122xLE, WVGA (752x480); Fujinon lens HF25HA-1B) at two orthogonal observation planes measures the profile movement of the inflating GMC and captures the deformation of the anisotropic mesh. At the same time, air is blown to generate pressure inside the GMC that is measured by the pressure transducer. An automation program LabView (National Instruments, Austin, Texas) elaborates images with the predefined algorithm. The height of the inflated GMC was measured before gelatin layer bursts. Engineering parameters such as stress and strain are

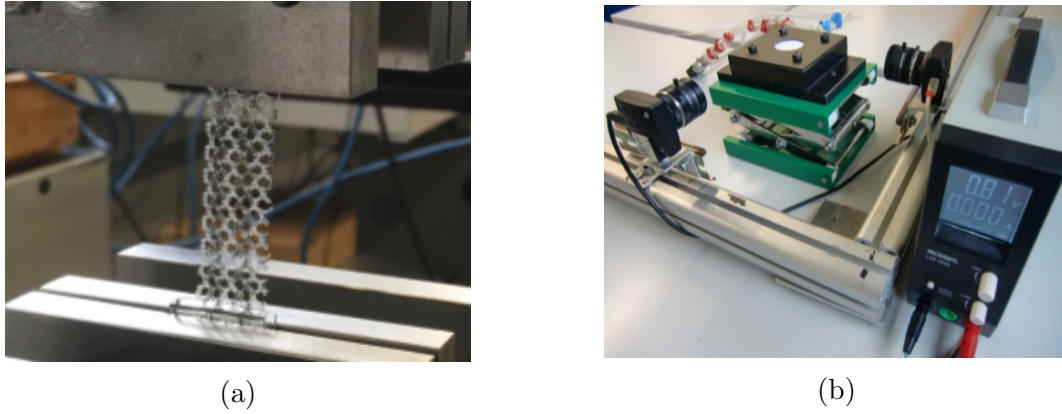


Figure 6.2: Synthetic mesh clamped to a) uniaxial tensile and b) bulge test machines (BHATTARAI AND STAAT [28]).

computed to evaluate the mechanical response of the GMC that can be compared with the in-vivo response of the tissue-mesh complex.

6.3 Mechanics of dry textiles

6.3.1 Uniaxial tensile test on rectangular pore mesh

Uniaxial tensile tests on structurally similar dry PRS and SD mesh provided qualitatively similar results. As shown in Fig. 6.3b and 6.3c, the characteristic stress-stretch curves are nearly linear and orthotropic. Curves are plotted until complete failure of the implant. The SD mesh has larger toe stiffness and larger strain at inflection than the PRS mesh. Linear stiffness is measured that determines the strength and clinical effectiveness of the implantation. The initial Young's modulus in longitudinal direction of the PRS mesh ($E_L=29.778$ MPa) is greater than for the SD mesh ($E_L=26.73$ MPa), whereas, the initial transverse modulus is larger for the SD mesh ($E_T=3.58$ MPa vs. $E_T=1.919$ MPa). The meshes show nonlinear orthotropic behavior for which a polyconvex hyperelastic material model has been successfully identified in (HORBACH ET AL. [123]). For simplicity we continue here to discuss the stiffness only linearly. On the other hand, the CICAT mesh with hexagonal pore shape shows highly nonlinear mechanical behavior under uniaxial tensile test, see Fig. 6.3a. Compared to stretched SD and PRS meshes in longitudinal direction, CICAT mesh possessed the largest toe region and lower stiffness ($E=13.207$ MPa) in the linear region.

6.3.2 Optical strain measurement

The traditional extensometer technique provides an average strain over the specimen gauge length. For accurate strain measurement over the whole area between extensometer probes, especially at positions of necking, DIC tracks the positions of the same physical points during test. Lagrangian strains and stretch for large deformation are calculated and visualized by the color scaling using DIC analyses which are later converted into stretches

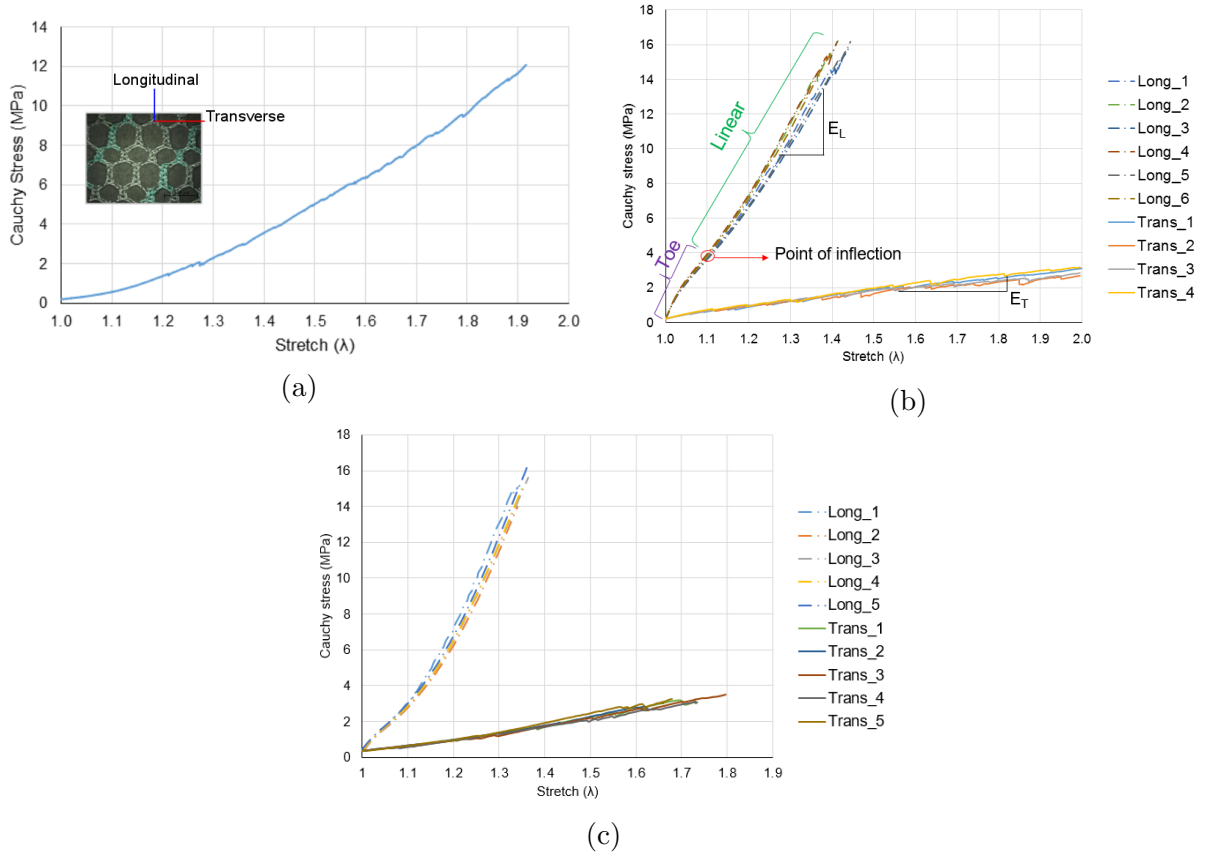


Figure 6.3: Average stress-stretch curves of different dry meshes loaded in longitudinal and transverse direction for different meshes: a) CICAT; b) SD; and c) PRS (BHATTARAI AND STAAT [28]).

for suitable presentation of results. In addition, for orthotropic prosthetic meshes, DIC technique benefits to measure the change of mesh porosity during tests.

SIS Direct soft mesh

In this part, the experiment performed using DIC technique on SIS direct soft mesh is presented BHATTARAI AND STAAT [28]. Two pairs of images at zero load and maximum load before failure of the mesh are compared when stretched in two orthogonal directions, see Fig. 6.4a. Due to lesser number of woven fibers along transverse direction, axial elongation and transverse contraction of the specimen is significant. As shown in Fig. 6.4b, the textile construct shows a wide range of nearly linear stress-stretch curves when subjected to tension in longitudinal ($E_L = 105.78$ MPa) and transverse direction ($E_T = 10.87$ MPa). The dry meshes are found to be compressible with significant volume change during tensile test. The stress-stretch behavior using uniaxial tensile test are qualitatively similar to that of DIC technique. However, computing Lagrangian strain and later converted into true strain and expressing them in terms of stretch reveals the maximum true stress is significantly large, see Fig. 6.3b and 6.4b. Under uniaxial tension load applied

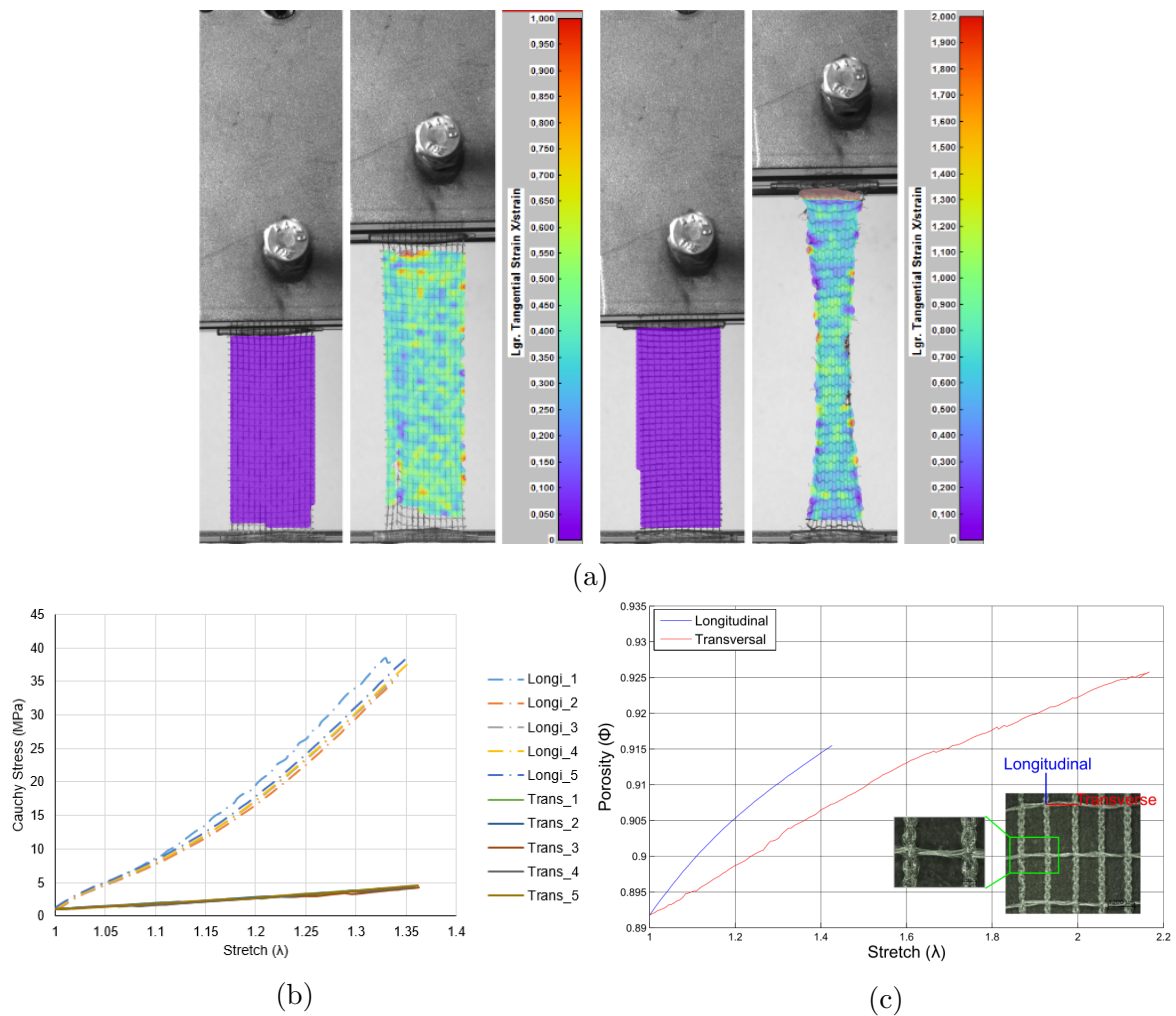


Figure 6.4: a) Uniaxial tensile test on dry SD mesh using DIC technique; b) The SD mesh elongates only by 40% if stretched to the thicker fiber (longitudinal) direction. In contrast, if rotated by 90°, an elongation of almost 100% occurs; c) Change of mesh porosity (BHATTARAI AND STAAT [28]).

in longitudinal and transverse direction, the rectangular pore of the SD mesh becomes progressively bigger with increased fiber stretch. Stretching up to a stretch of $\lambda = 1.4$ in longitudinal direction, an increase in porosity of 2.4% was measured, see Fig. 6.4c. Despite of significant mesh contraction, loading along transverse direction rather increases the mesh porosity by 3.93%.

Hernia mesh

The uniaxial tensile tests of a PVDF hernia mesh shows a nonlinear stress-stretch behavior when loaded in longitudinal and transverse direction. Due to hexagonal pore geometry, pore deformation is extreme in low load range. In both loading directions, increased length and reduced width of the specimen is observed. Fig. 6.5 shows deformed mesh when

stretched in the longitudinal and the transversal direction of the mesh. Longitudinal (Fig. 6.5a) and transverse Lagrangian strains (Fig. 6.5b) for loading along both directions are

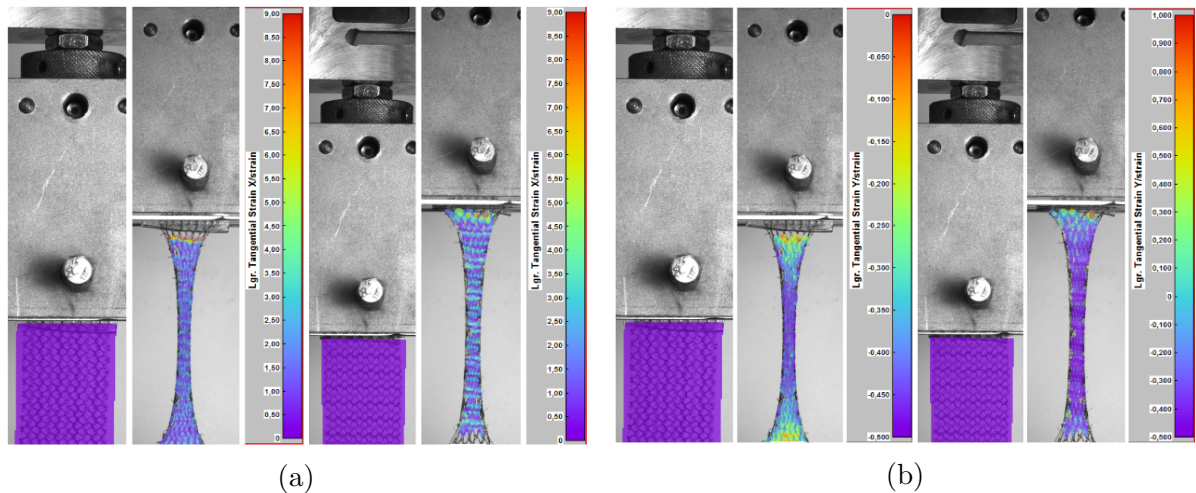


Figure 6.5: a) Lagrangian strains under loading in b) longitudinal and b) transverse fiber direction of an anisotropic PVDF hernia mesh. Strain ϵ_x is extension in load direction and ϵ_y is contraction (BHATTARAI AND STAAT [28]).

shown in Fig. 6.5. CIRITSIS ET AL. [60] performed uniaxial tensile tests on PVDF constructed hernia mesh with hexagonal pore shape. As per the study, the porosity decrease was found to be 10.4% and 7.2% to a minimum in longitudinal and transverse directions, respectively. In vivo hernia meshes loaded in biaxial tension show the increased porosity. In animal experiment, this led to an improved maturity of the scar indicated by a higher I/III collagen ratio which allowed the mesh implant to adapt to remain more flexible within the abdominal wall (CIRITSIS ET AL. [60]). With respect to scar formation the concept of effective porosity has been suggested which could be only measured ex vivo with a specially developed image processing. In (HORBACH ET AL. [123]) a new method has been presented which allows the calculation of effective porosity from measurement of the global mesh deformation. Again the uniaxial tension was found to be critical because the pores collapse and effective porosity decreases to zero for the two tested meshes at stretches around $\lambda = 1.4$.

6.4 Mechanics of tissue surrogate-mesh specimen

6.4.1 Photoelastic uniaxial tensile test

The mesh embedded in a transparent gelatin block behaves similar to soft biological tissue but is transparent and photoelastic BHATTARAI AND STAAT [28]. Two ends of the mesh are clamped into a tension machine Z010 (Zwick Roell AG, Ulm, Germany). Applying tension to the gelatin-mesh complex (GMC) between two polarizing filters leads to isochromatic lines that represent lines of equal shear stresses. As shown in Fig. 6.6a and 6.6b, PRS mesh shows very little transverse contraction. The mesh surface area is found to be increased by 18%. Since, there are no drastic reductions of the pore size, the

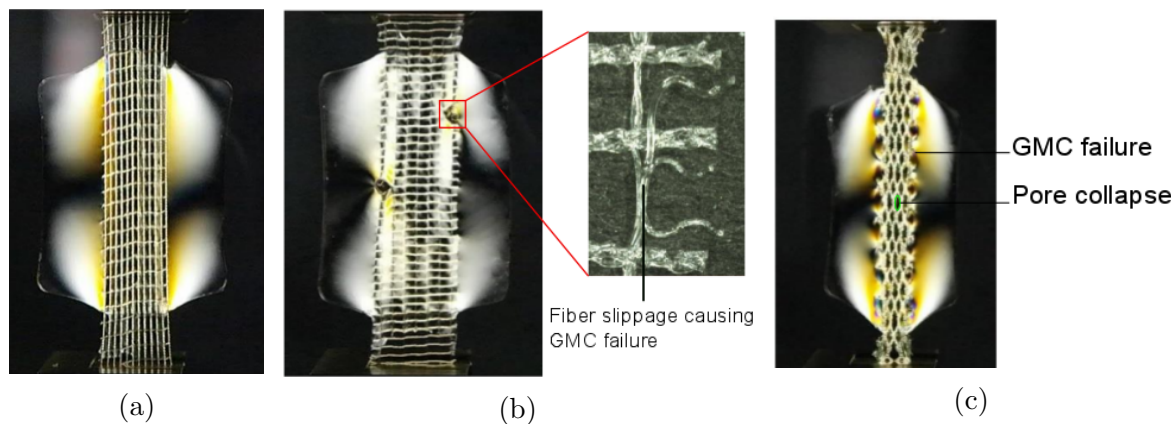


Figure 6.6: Uniaxial tensile test on GMC specimen. DPRS mesh along a) longitudinal direction (left: 80.89 N); b) transverse direction (right: slippage of fiber (tearing out a seam) at less force, 15.89 N); c) debonding of the CICAT mesh from the gelatin due to large transversal contraction and pore collapse at tensile force 60.404 N (BHATTARAI AND STAAT [28]).

mesh porosity and the effective porosity are satisfactorily preserved during uniaxial tensile test. Unlike PRS meshes, CICAT mesh has different pore shapes in the loading direction and is completely unable to preserve its porosity; almost all pores are collapsed already under small tensile force, see Fig. 6.6c. The mesh shows a strong dependency of the GMC failure on the loaded direction. For the PRS soft mesh, loading along longitudinal direction sustains larger tensile force (124 N) that stresses the softer gelatin. The GMC specimen ruptures at lower stretch ($\lambda_{\max} = 1.42$). Whereas, along the transversal loading, the GMC is highly stretched ($\lambda_{\max} = 2.05$). The zigzag (like steps of a staircase) orientation of transversal fiber families are unsupported at the boundaries and the mesh is pulled out at lower tensile load (22 N). This stresses the gelatin locally from where the rupture of the GMC begins, see Fig. 6.6b. On the other hand, the CICAT mesh with irregular hexagonal pores show large pore deformation along the loaded direction. High shear stresses are generated on the gelatin at the boundaries of the mesh due to unequal stretching of the gelatin and the mesh, see Fig. 6.6c. Further stretching the GMC debonds the gelatin from the mesh along its edges and rupture of the GMC specimen occurs.

Such mesh edge failure have been observed after repair with the heavyweight small porous textiles (BROWN AND FINCH [44]) due to the heavy scar tissue formation, mesh shrinkage, mesh-size (KLOSTERHALFEN ET AL. [159]) and the mesh anisotropy (ANUROV ET AL. [10]). However, pullout tensile tests and FE studies on monofilamentous and compliant Gynecare mesh (Ethicon, USA) shows a similar gradual debonding of the mesh from the tissue-surrogate gelatin in a zipper-like manner with huge pore deformation (FROTSCHER AND STAAT [101], STAAT ET AL. [291]). Furthermore, large shear stresses at the lateral edges are generated when the mesh is highly stretched that is responsible for the failure of the compliant GC mesh. These reasons for similar mesh failure in two different classes of meshes are most likely due to the geometry, loading direction, compliance of the meshes and the generation of the normal and shear stresses.

6.4.2 Biaxial inflation test

Unlike, incontinence repair that supports mostly uniaxial physiological loads, abdominal hernia or pelvic organ prolapse repair uses a flat sheet of prosthetic meshes. They are designed to support the biaxial function of weak abdominal wall and pelvic organ and to restrain increased abdominal pressure on those surfaces developed with physical activities such as exercise, coughing, lifting, straining, and others. An inflation (bulge) test setup as shown in Fig. 6.2b on tissue surrogate gelatin-mesh complex theoretically mimics the physiological abdominal pressure and helps to determine the mechanical behavior after the implantation. As shown in Fig. 6.7, the GMC specimen expands (inflates) with increased

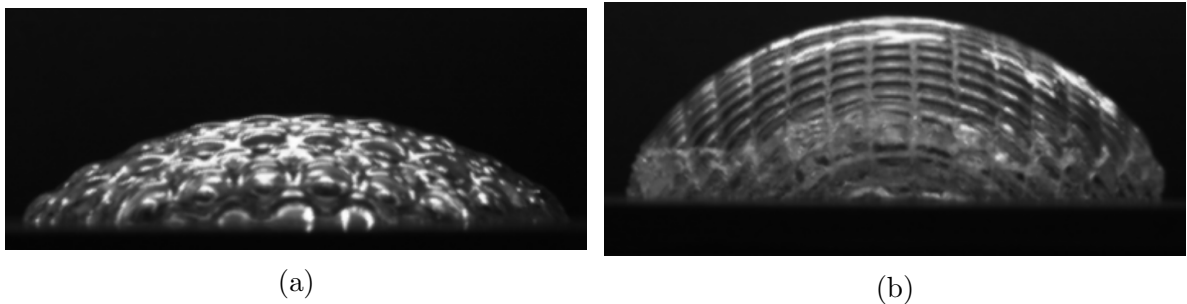


Figure 6.7: Failure of tissue surrogate-mesh under biaxial inflation test: a) Gelatin-CICAT mesh; b) Gelatin-PRS mesh (BHATTARAI AND STAAT [28]).

pressure from below. On the outer side of the GMC, small gelatin cups are formed across the mesh pores. Compliant CICAT-GMC specimen offers bigger cups due to (1.42 times in length and 2.41 times in width) larger pores than stiffer PRS-GMC specimen. The soft gelatin cups are highly stretched to burst at significantly lower pressure (97 kPa vs 116 kPa) for CICAT-GMC specimen, thus failing at lower inflation height (6.89 mm vs 11.44 mm), see Fig. 6.7a. For stiffer PRS mesh with small mesh pore the GMC bond is intact and bears larger stress. At high stress, the gelatin is scraped off from the edge of the cover plate to leak the pressure failing the GMC specimen. For inflation test, the maximum values of the principal stresses at the end of the experiment differ considerably in magnitude (483.79 MPa for CICAT and 1186.26 MPa for PRS). These differences are due to the pore geometry, pore size and the compliance of the two meshes.

6.5 Clinical comparisons

Immediately after implantation, biomaterials, such as prosthetic meshes are associated with the acute inflammation phase. Numerous blood and tissue proteins, such as cytokines or growth factors and leukocytes are deposited on the foreign body surface and injury site to form the provisional matrix and to clean the wound site (ANDERSON [7], JUNGE ET AL. [142]). The types and concentration of such proteins are dependent on mesh surface properties and polymer hydrophilicity (WILSON ET AL. [327]). These proteins modulate the adhesion of monocytes/macrophages cells on the protein absorbed foreign object that are fused together to form larger foreign body giant cells (FBGCs)

(CHEN ET AL. [56]), also known as chronic inflammation. The chronic inflammation period for biocompatible materials should not be more than two weeks, otherwise may cause infection (ANDERSON ET AL. [8]). Adherent macrophages and FBGCs secrete fibroblast attractants, and the incoming fibroblasts from the surrounding tissue create an organized collagenous matrix around the biomaterial (SHOSHAN [277]), called extracellular matrix (ECM) remodeling fibrosis. This vascular and collagenous capsule (usually 50-200 μm thick) isolates medical devices from the rest of the interstitial tissue at the end stage of wound healing process (WILLIAMS AND WILLIAMS [325]). Later, abundant amount of fatty tissues and significantly less connective tissues penetrates completely into the pores of the mesh to form a layer of neo-tissue unit. But, why does the host tissue not heal normally around implants and what are the reasons for post-operation complications? These are very critical questions in surgical interventions for which thorough understanding of the foreign body response and the biocompatibility of the medical devices is important.

6.5.1 Mesh complications

Inflammation

Almost all modern biomaterials trigger a wide variety of adverse responses in vivo mainly due to inflammation right after implantation (KLINGE ET AL. [155]). The biosafety of the mesh implant is characterized by the inflammation phase: acute and chronic, that are associated with the deposition of proteins and macrophages/monocytes. Longer acute inflammation directly enhances the development of a greater amount of fibrous tissue, whereas, longer chronic inflammation initiates infection (ANDERSON ET AL. [8]). An ideal, biocompatible material is assumed to deposit thin fibrous tissue around the mesh filament and to fill sufficiently larger pores mainly by fat tissues (KLOSTERHALFEN ET AL. [159]) that maintains the elasticity of the mesh even after the inflammation phase. These animal experiments with a low-weight, large pore size and monofilament made mesh reduces the inflammation, maintains the flexibility of the mesh and provides greater host tissue mobility during physiological loadings (KLINGE ET AL. [153]).

In contrast, heavy-weight, multifilament made mesh with small pores increases the surface areas in contact with the recipient host tissue that basically aggravate the acute and chronic inflammatory phase. The adverse effects are seen in the form of a) huge macrophages and FBGCs deposition at the interface, b) intense fibrosis forming thicker connective tissue around filament, c) poor or no fat cell penetration to the pore, and d) disordered collagen metabolism with much lower collagen (I/III) ratio, see Fig. 8. Changes in this ratio affect both tensile strength and mechanical stability and may increase the risk of recurrence. This consequently forms a thick continuous connective tissue, also known as scar plate with tangled bundles of collagen fibers around the filaments which grow to the adjacent filaments (JUNGE ET AL. [142], MÜHL ET AL. [203]), a phenomena called 'bridging' (CASEY [52]). This bridging of newly formed inter-filament connective tissue (stiff scar plate) a) prevents the pores to deform freely, b) reduces the mesh compliance, c) restricts the mobility of the host tissue, d) prevents further tissue ingrowth and d) finally causes recurrence. As a result, the healing of the wound may be retarded.

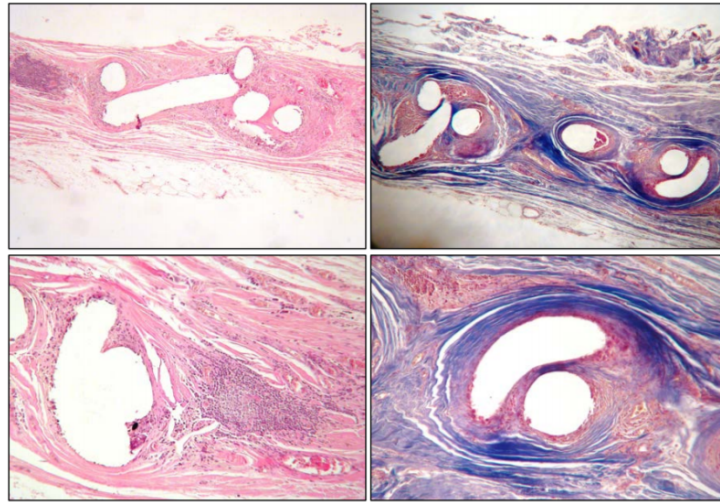


Figure 6.8: Tissue response after suture repair. Histological analysis of explanted heavy weight polypropylene mesh using Masson's trichrome staining procedure (with permission from (CASEY [52])).

The polymer and fiber surface greatly affect the inflammatory response. PVDF made meshes result in a significantly reduced foreign body granuloma size (KLINK ET AL. [157]) with reduced diameters of the inner (inflammatory infiltrate) and the outer (connective tissue infiltrate) ring of granulomas (JUNGE ET AL. [142]) compared to conventional PP (deposits more collagen, longer inflammation and scar neo-tissue) (BAKTIR ET AL. [13]), and polyester mesh (long-lasting chronic inflammatory response) (ORENSTEIN ET AL. [217]).

Seroma

Seroma is an ill-defined event, typically involving a collection of serous fluid in any potential fluid-occupying space that develops in the recipient body after surgery or any blunt injury. It usually appear under the surface of the skin as a swollen lump, like a large cyst when blood seeps out of the injured or ruptured blood vessels during operation. Seroma etiology remains unclear, its formation after incisional hernia repair with mesh is a most frequent problem due to local inflammatory response aggravated by the presence of the foreign body (BENDAVID AND KUX [21]) and lasts for several weeks (SUSMALLIAN ET AL. [294]). Chronic seromas are evidenced due to a long-term inflammatory reaction with heavyweight and small sized mesh monofilamentous PP and polyester meshes (KLINGE ET AL. [153], SALAMONE ET AL. [267]). Postoperative seroma formation anterior to mesh is very common up to 100% (SUSMALLIAN ET AL. [294]); however, deep seroma behind the mesh develops an infection which ultimately requires surgical removal of the mesh (MOHAMED ET AL. [200], SCOTT ET AL. [275]).

Adhesion

Postsurgical adhesions are serious and frequent complication resulting in a similar way that a scar tissue forms and vary from filmy to dense (JUNGE ET AL. [141]). Such adhe-

sions occur in almost all meshes as a result of inflammation (BROWN AND FINCH [44]) containing multiple foreign body granulomas that connect tissues or anatomic structures to the textiles. Studies shows 20%-80% of the subjects develop adhesions after ePTFE and PP mesh implantation (FISCHER ET AL. [96], MATTHEWS ET AL. [194]). Other than the polymer type, factors associated with adhesion formation include trauma, tight suturing, thermal injury, infection and foreign bodies. Traditional heavy PP meshes with small pores induce an intense fibrotic reaction that produce dense adhesion around 62% of the mesh area and provide a strong adherence to the abdominal (BROWN AND FINCH [44]). An anti-adhesion film-like barrier around the mesh filaments have been an alternate to reduce adhesions (BROWN AND FINCH [44]), however, light weight, large porous PVDF constructs with PP coating seem to be superior with regard to the induced intensity of inflammation and filmy adhesion of 34.6% mesh area that could be lysed with traction (JUNGE ET AL. [141]).

Collagen Metabolism

Collagen metabolism has an intense influence on the wound healing after mesh repair (KLINGE ET AL. [151]); decreased ratio of collagen I to III increases the risk of hernia recurrences (JUNGE ET AL. [140]). The inflammatory process after surgical implantation is accompanied by a pronounced fibrosis to deposit the fibrillary collagen molecule that are stabilized by intracellular hydroxylation reaction forming hydroxylysine and hydroxyproline (SHOULDERS AND RAINES [278]). Lysyl oxidase enzymes mediates a cross-linking process to form a strong, stable collagen fibrils and fibers that provides strength, integrity and structure. Among 20 different collagen types, I and III are synthesized in huge amount. Collagen type I is stronger, mature and thick whereas type III is less cross-linked and immature that provides less tensile strength predominantly found in early wound healing (FLEISCHMAJER ET AL. [97]). Balanced collagen maturation and degradation by matrix metalloproteinases (NAGASE ET AL. [204]) to form type I collagen is a requirement for normal scar formation (FLEISCHMAJER ET AL. [97], FRIEDMAN ET AL. [99]). Reduced ratio of collagen type I to III lead to thinner collagen fibrils, changed geometrical arrangement (HURME ET AL. [129]) with higher levels of non-polymeric soluble collagen (FLEISCHMAJER ET AL. [97]) that contributes to a decreased tensile strength and instability of the connective tissue and induced scar tissue (BIRK ET AL. [33]). It has been proven that the fibroblastic ingrowth, chronic inflammation and scar formation is dependent on the weight and structure of the implanted mesh (BROWN AND FINCH [44], JUNGE ET AL. [142], KLINGE ET AL. [153], MÜHL ET AL. [203], POST ET AL. [244]), but the quality and mechanics of such scar tissues are characterized by the extent of collagen type I/III (BIRK ET AL. [33], PANS ET AL. [222]). Studies on the ECM of the explanted hernia meshes constructed from PP, polyester and ePTFE shows lowered collagen type I/III and reduced tensile strength, a major reason for hernia recurrence (JUNGE ET AL. [140]). Though, altered ratios of collagen can be seen within fibroblasts located at the edges of recurrent hernia (KLOSTERHALFEN ET AL. [159]), yet it is not clear if the type of mesh used has any effect (BROWN AND FINCH [44]).

Mesh Wrinkling

Wrinkling of the mesh is caused by failure or inadequate mesh fixation in defected place. In the sutureless technique to repair abdominal hernia, meshes are placed flat on the floor of the abdomen. With insufficient dissection to insert the meshes, during physiological movement, meshes have a tendency to wrinkle or curl increasing the potential for the formation of dead spaces where unintended mesh overlap occurs, see Fig. 6.9a. This process augments the mesh relative movement from its total implanted position leaving gaps at the edges for the protrusion of tissues, causing hernia recurrence, see Fig. 6.9b. Further, the localized fibroblastic infiltration into mesh pores are greatly altered that mechanically cause inhomogeneous inelastic mesh deformation between the implant (stiffer scar tissue around mesh at dead spaces) and the underlying soft tissue and biologically a) leaves spaces for infection, b) chronic postoperative pain, and mesh deterioration. A wrinkled mesh may also add to adhesion problems with viscera which can result in the uneven distribution of stress on the mesh and cause an undesirable distortion, premature weakening of the mesh, and hence predispose the wound to infection (USHER AND GANNON [309]).

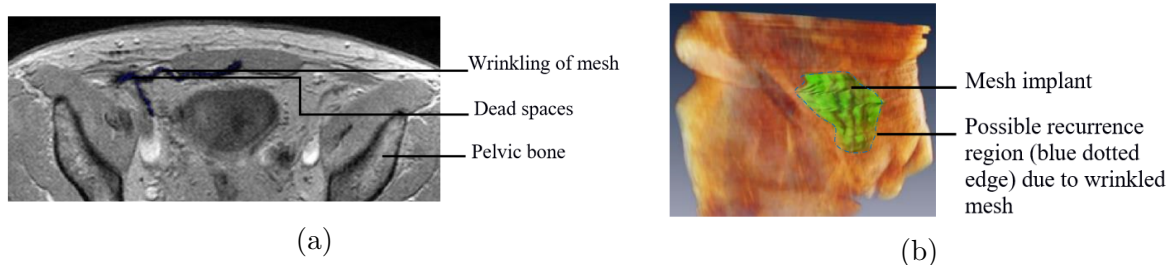


Figure 6.9: Abdominal hernia repair using mesh implant: a) MRI image showing mesh wrinkled after placed in the abdomen: superior view [with permission of N. A. Krämer]; b) Representation of the position of the wrinkled mesh in abdomen (anterior-lateral view) (BHATTARAI AND STAAT [28]).

Mesh shrinkage

Shrinkage is most common in the surgical repair with the use of heavyweight small pore size PP meshes. Studies assume that it is not the mesh which undergoes shrinkage (KLOSTERHALFEN ET AL. [159]), which is supported by our strain measurement on mesh implants. Assuming the thickness of the mesh to remain constant during test, the mesh area increases on stretching, see Fig. 6.10. Mesh shrinkage results due to contraction of scar tissue around the mesh, starting with a constant water loss, followed by a surface area decrease (AMID [5]). Depending on the properties (pore size, weight and filament type) of the prosthesis, shrinkage of the mesh implants due to wound contraction are observed to be within a wide range from 5% - 62% (JUNGE ET AL. [141], KLOSTERHALFEN ET AL. [159], SCHEIDBACH ET AL. [272]). Therefore, use of large implants to cover defects can justify the shrinkage effect, however, larger foreign body reactions, scarring, dyspareunia, shrinkage, mesh exposure and stiffening of the recipient host tissue can no longer be avoided (MARGULIES ET AL. [188]). Lightweight large

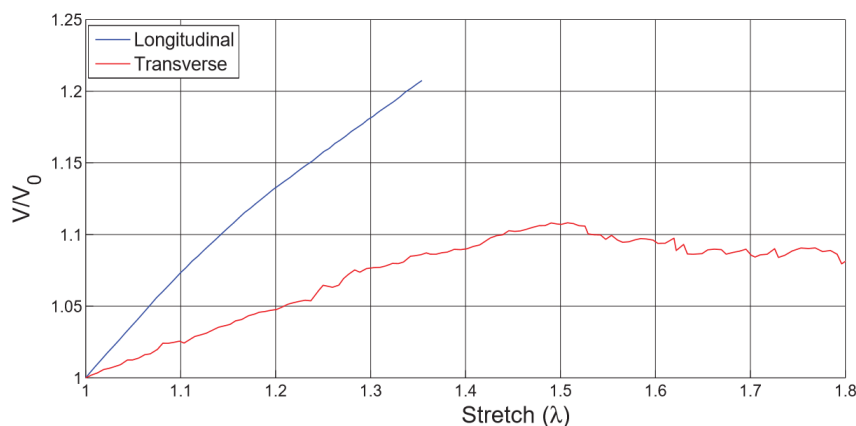


Figure 6.10: Area change under uniaxial tensile test on SIS direct soft mesh. A_0 and A are the initial and current surface area of the mesh (BHATTARAI AND STAAT [28]).

porous PP meshes are specifically designed to reduce the bridging and scar formation (KLINGE ET AL. [150]), however, the use of highly inert PVDF material is found to significantly reduce the wound contraction, (9.3%-19.9%) minimal loss of the original area (CONZE ET AL. [65], JUNGE ET AL. [141]) provide long-term stability as a result of lower foreign body reaction and maintain original strength after years of implantation (GÖRETZLEHNER AND MÜLLEN [111], KLINGE ET AL. [150], KLINK ET AL. [157]).

Pain

Biomaterials, such as mesh implants are associated with a potential risk of chronic pain, as they are recognized as foreign body by the host tissue immediately after repair. The reasons for chronic pain are still unclear and vary from patient to patient. Studies suggest pain associated with mesh surgery can be a) early pain immediately after surgery due to irritation from surgical material or nerve damage during surgery or b) chronic pain existing for more than 3 months after surgery (KLOSTERHALFEN ET AL. [159]). Repairs using small pore, heavyweight meshes with reduced effective porosity lead mainly to complaints about chronic pain that often requires the complete removal of the implant from the body (LAROCHÉ ET AL. [169], POOBALAN ET AL. [243]). Post-retrieval studies on such explants obtained from similar patients with failed repair indicate irritation and destruction of nerve fiber and fascicles by the inflammation at the interface with the mesh (KLOSTERHALFEN ET AL. [159]). Today's new generation meshes have been greatly improved using softer material, large pore and light weight meshes (KLINGE AND KLOSTERHALFEN [149]) which have proved to be a better mesh material with reduced level of inflammation and scar formation, which is directly related to pain (POST ET AL. [244]).

Infection

Infection is another common FBR in repair using mesh implants, hindering the local clearance from bacteria (CASEY [52], KLINGE ET AL. [153]) that leads to a chronic in-

flammatory wound with marked scarring, loss of compliance, mesh contraction, migration, physiochemical changes, seroma, and in some cases, eventual mesh removal to resolve the problem (LEBER ET AL. [171]). The incidence of chronic mesh infection is highly related to the type of mesh material, type of filament, pore size, and porosity (DELIGIANNIDIS ET AL. [75], POST ET AL. [244]). Generally, microporous and multifilament meshes with increased surface of the mesh area and small pores are at higher risk of infection than large porous monofilament meshes (>75 μ m). Macrophages and neutrophils are unable to enter small pores (<10 μ m) but allows bacteria (<1 μ m) to survive unchallenged within the pores. In contrast, there is some evidence that the persistence of the a) colonies of *Staphylococcus epidermis* bacteria at the surface of the polymer fibers (KLOSTERHALFEN ET AL. [159]), and b) acute/chronic inflammatory response beyond a 3 weeks period usually indicate higher risk of infection (ANDERSON ET AL. [8]). Chronic mesh infection following repair with small pore meshes or film like structures often requires removal of the infected mesh, which rarely results in hernia recurrence if sufficient fibrosis scarring remains (AMID [5]). Open pore meshes mostly can be treated conventionally.

7 Numerical Study of Stress Urinary Incontinence

In this chapter, the phenomenological development of the commonly known stress urinary incontinence (SUI) is presented. BHATTARAI AND STAAT [29] presented an improved 3D finite element model of the female pelvic floor which: considers the realistic support of the organs at the pelvic side walls, employs the improvement of their previous FE model (BHATTARAI ET AL. [24], BHATTARAI ET AL. [25]), and incorporates the realistic anatomy and boundary conditions of the endopelvic (pubocervical and rectovaginal) fascia. The mechanics of tissue constituents to characterize the mechanical behavior of the fascia using a constitutive mixture model is weighted by the volume fractions of the components as described in section 4.4. The influence of varying constituents, focusing mainly on the stiffest collagen to model the tissue impairment/weakness/laxity and different classes of the endopelvic fascia in craniocaudal direction has been studied. Several computations have been carried out by BHATTARAI AND STAAT [29] with the presented computational model with healthy and damaged supporting tissues, and comparisons have been made to understand the pathophysiology of the SUI.

7.1 Endopelvic fascia as a single unit

The endopelvic fascia as described in section 2.1.4 is a *single unit* of loose network of connective tissue strands which provide a firm base to maintain the proper position of the urethro-vesical junction, particularly during straining, to fill the organ-organ and the muscle-organ spaces in the pelvic floor by suspending the organs to the pelvic wall and muscles (OTCENASEK ET AL. [218]), and to prevent the urethral and the bladder hypermobility (RECHBERGER ET AL. [251]). For a more realistic mechanical structure, BHATTARAI AND STAAT [29] models fasciae as continuous tissue network and the respective thickening at different anatomical regions to the ligaments (Figure 7.1).

7.1.1 Pelvic fascia constituents

Histological studies found lax urethral support due to reduced collagen content on the SUI patients which did not appear on the cystocele subjects (FALCONER ET AL. [88], RECHBERGER ET AL. [251]). PETROS [239] suggested that the distal 2-3 cm of the endopelvic fascia around the vaginal length is collagen rich, and the superior part is rich in elastin and smooth muscle. This lights up the concept of the phenomenological differences of the urinary incontinence and (bladder and urethral) prolapse. Laxity of the PUL and the collagenous urethral support fascia fails to close the urethra during straining. Funneling of the proximal urethral occurs to leak the urine due to active longitudinal anal muscle contraction. Whereas, laxity or paravaginal damage in the upper elastic fascia drags the bladder into the vaginal canal, commonly known as cystocele. BHATTARAI AND STAAT [29] adopted the mixture model (section 4.4) in the constitutive level to describe the influence of the fascia constituents to describe SUI mechanically (Fig. 7.2a).

Pelvic connective tissues are made up of the extracellular matrix (ECM), macromolecules of biopolymers including elastin-collagen fibres and a varying amount of adipose (fat)

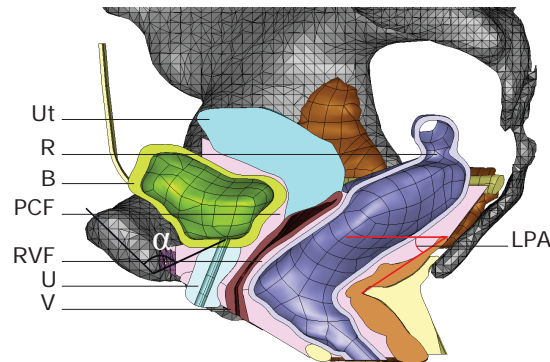


Figure 7.1: The organs, fasciae (pink) and muscles are cut in the sagittal plane (BHATTARAI AND STAAT [29]). For comparison of the fascia geometry refer to (OTCENASEK ET AL. [218]). The angle α measures the angle between the midpubic line to the bladder neck. Levator plate angle (LPA) is an angle subtended by the initial take off portion of the iliococcygeus from the coccyx to a horizontal reference line. Ut=Uterus; R=Rectum; B=Bladder; PCF=pubocervical fascia; RVF=rectovaginal fascia; U=Urethra; V=Vagina.

tissue and smooth muscle organized in a non-homogeneous fashion to form a complex composite microstructure. At structural level, its biomechanical behavior depends on the components, since each of them possess unique mechanics to one another; the collagen contributes significantly to the stiffening response (limited strain or stretch), elastin to the distensibility, the smooth muscle to the continuous contractility and the softest adipose tissue serves as a cushion with much lower stiffness than the other constituents. A homogenization approach to estimate the overall mechanical response of any non-linear multi-constituent soft tissue, the effect of collagen variation and tissue weakening are described in section 4.4, section 4.3.1 and section 4.5.

7.1.2 Finite element mesh of the female pelvic floor

Geometries of every pelvic structure are assembled and volume discretized to create three dimensional FE meshes considering the significant thickness of each pelvic constituent. A smooth FE mesh as shown in Figure 7.2b is constructed from 65,6563 linear tetrahedrons (4 node elements) except for the vagina, which has been discretized with 28,606 quadratic tetrahedral (10 node) elements for high smoothness in the analysis of self-contact between the anterior and posterior vaginal walls. The integrated FE model of the female pelvic floor consists of 24 structures: 8 ligaments, 5 organs, 8 muscles, 1 fasciae and 2 perineal structures (perineal membrane and perineal body).

7.1.3 Boundary conditions

The endopelvic fascia is connected to the pelvic diaphragm providing a firm support to the organs. *Pelvic bones are rigid structures because these are stiffer than pelvic tissues by orders of magnitude.* Therefore, they are included in the model as rigid points for the

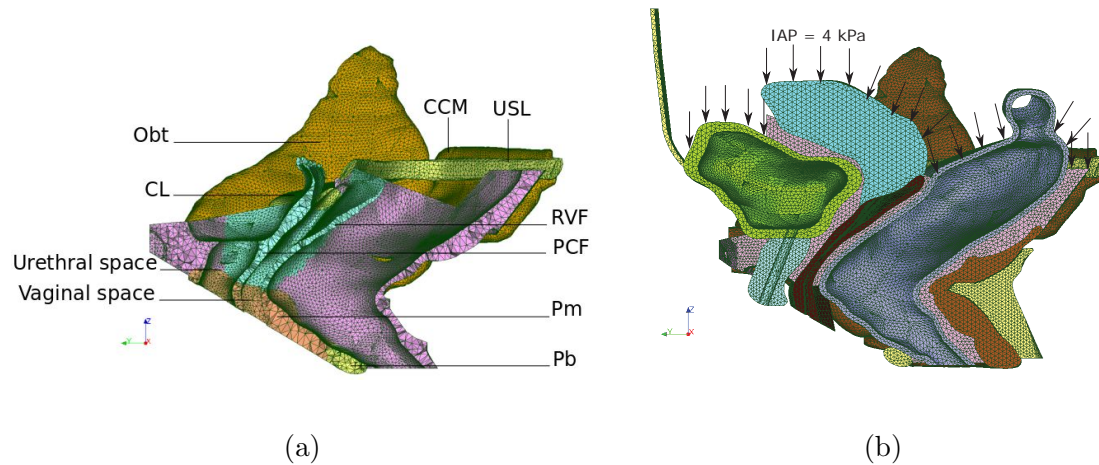


Figure 7.2: Sagittal section of the 3D finite element mesh showing a) pubocervical fascia (PCF) and rectovaginal fascia (RVF), ligaments and perineal structures, b) FE mesh loaded with intra-abdominal pressure (IAP). Endopelvic fascia is separated with different amount of elastin and collagen constituents, blue (elastin rich) and pink (collagen rich) (BHATTARAI AND STAAT [29]).

fixation of the muscles, ligaments and fasciae. The superior end of the umbilical ligament is connected to the umbilicus and is fixed for any movement. The piriformis muscle does not support the IAP and is not included in the model. However, the superior surfaces of the coccygeus muscles are connected to the piriformis and constrained in the horizontal plane. A frictionless sliding contact between the two walls of the vagina is considered.

The IAP of 40 cm of H₂O and 100 cm of H₂O during supine Valsalva manoeuvre and straining manoeuvre are applied on the upper surface of the organs (COBB ET AL. [63]). During normal micturition, the urethra is subjected to an average fluid pressure of 60 cm of H₂O to open the bladder neck (BUSH ET AL. [47]). Considering the linear anatomic profile of the urethra, the fluid pressure in the finite element simulation is dropping linearly from 60 cm of H₂O = 0.0058 MPa at the bladder neck to zero at the urethral exit. The inner surface of the bladder is also subjected to the same fluid pressure in the simulation. Based on the *Integral Theory*, the lateral vaginal wall transmits muscle contractions against suspensory ligaments; levator plate (LP) pulls the vagina and the bladder neck posteriorly against the PUL fulcrum, and the longitudinal muscle of anus (LMA) pulls downward against the USL. Ligaments and fasciae with laxity or weakness or reduced stiffness fail to maintain the normal position of the organs, which results in incontinence and prolapse.

7.2 Finite element simulations of SUI

In this section, the results of the computer simulations which test the capabilities of the FE female pelvic floor model are presented BHATTARAI AND STAAT [29]. The finite deformation simulations for the computational model (Fig. 7.2) are performed with the open source FE software, *Code_Aster*. The characteristic displaced positions of the pelvic organs are compared with its initial position at rest and verified with medical images

(Fig. 7.4) and clinical measurements. The study parameters are: the vertical (VUVJ) and horizontal (HUVJ) urethrovesical junction ($UVJ = \sqrt{(VUVJ)^2 + (HUVJ)^2}$) movements, the urethral axis with the vertical (U_r) and the angle α between the midpubic line to the bladder neck. The stiffness of the supporting endopelvic fascia and ligaments are sequentially reduced between (0% to 95%) to simulate possible pelvic floor disorders due to tissue laxity or weakening. The computational results presented here show the relative

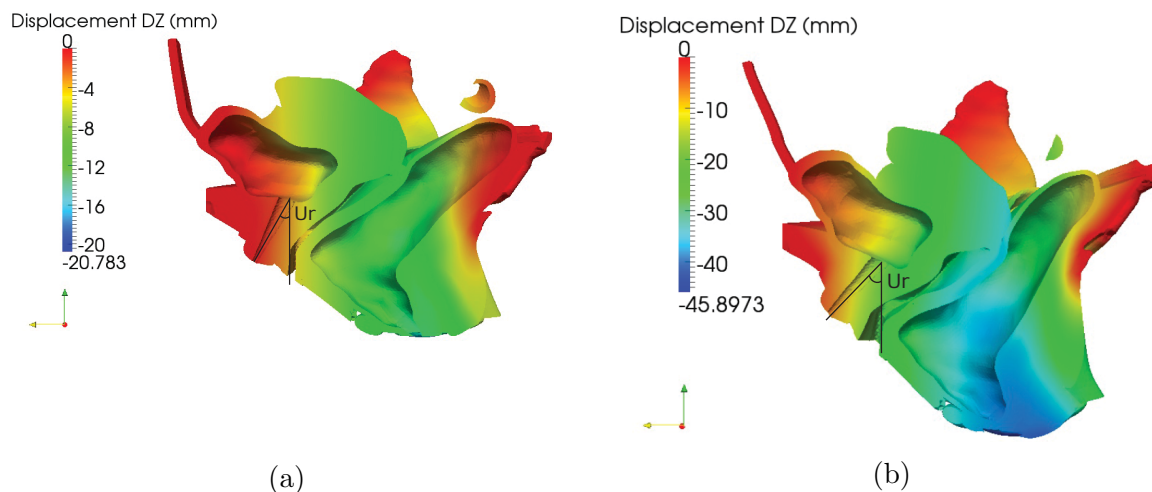


Figure 7.3: Sagittal section of a 3D pelvic model with results of the FE simulation showing the vertical movement of the pelvic floor during Valsalva maneuver for a) healthy tissues and b) 95% weakened ligaments and fasciae (BHATTARAI AND STAAT [29]). Urethral axis (U_r) $> 30^\circ$ with vertical line resembles positive Q-tip test. A great vertical descent ($DZ=38.79$ mm) of the anal orifice is observed in a dynamic MRI in a SUI patient (EL-GHARIB ET AL. [108]). The vertical displacement of the anal orifice in the SUI calculation (Fig. 7.4b) is 40.83 mm.

movement of the pelvic organs due to combined effects of the IAP, the detrusor pressure, impairment of the supporting system, and the active muscle opening forces as suggested by Petros in his so-called '*Integral Theory*'. The results offer the capability of a robust computational model of the female pelvic floor which poses a good start to improve our understanding of the SUI. The findings presented can be used to validate against medical examinations and surgical interventions that can profoundly improve both the health and quality of life of ageing women.

7.2.1 Mobility of the urethro-vesical junction

The impact of weakened pelvic support system during strain on the movement of the urethro-vesical junction in women with SUI is illustrated in Figures 7.3- 7.6. For all the simulation cases, the resting position of the urethro-vesical junction ($\alpha_{Rest} = 110^\circ$ in Fig. 7.1) and the urethral angle ($U_{r(Rest)} = 22^\circ$ in Fig. 7.4a) included between the urethral axis at resting and the vertical line are considered to be the reference values for comparisons. Under induced boundary conditions of the pressures and active muscle contraction forces during micturition, for healthy (asymptomatic) pelvic floor, the displacements of the

urethro-vesical junction are measured to be $VUVJ=3.76$ mm (inferiorly) and $HUVJ=3.44$ mm (posteriorly). The angle $Ur_{(Mict)}$ of the urethral axis with the vertical direction increased to 29.25° , the difference of $\Delta Ur = Ur_{(Mict)} - Ur_{(Rest)} = 7.25^\circ$ is in agreement with the X-ray examination of 8° during micturition (Fig. 7.4).

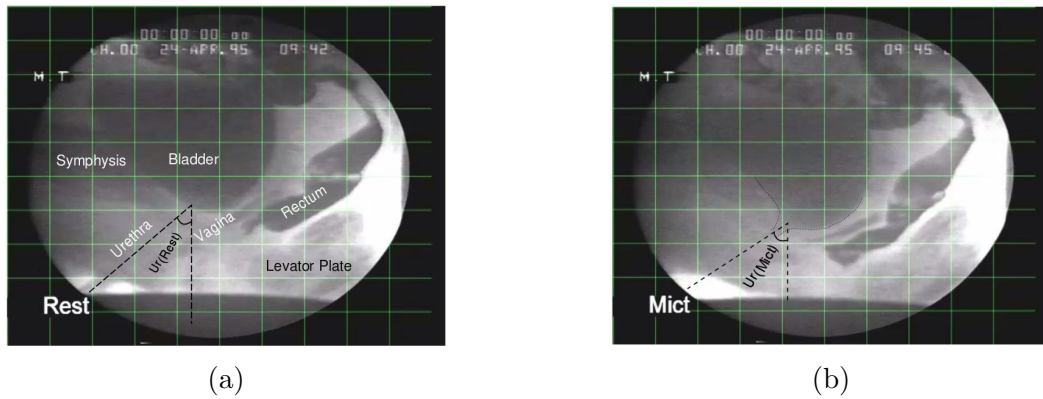


Figure 7.4: X-ray examination of an asymptomatic female pelvic floor urethral angle a) $Ur_{(Rest)}$ at rest and b) $Ur_{(Mict)}$ during micturition (PETROS [238], BHATTARAI AND STAAT [29]).

Fig. 7.5 shows the progressive movement of the bladder neck with increased tissue impairment. On Valsalva manoeuvre with an IAP of 40 cm of H_2O , the bladder neck mobility is markedly large (16.22 mm inferiorly and 6.54 mm posteriorly). The angle α is measured to be 138° (Fig. 7.6b). The results show that the movement of the UVJ is strongly increased after 50% weakness of all the supporting tissues (ligaments and fasciae). However, it is interesting to observe that the effect of the endopelvic fascia weakness alone is sufficient to cause large dislocations of the organs than the ligaments together (Figure 7.5). This represents the hypermobility of the organs and commonly initiates situations such as incontinence and prolapse.

7.2.2 Q-tip test for SUI

Clinically, the change in the urethral axis through the diagnostic Q-tip test is commonly considered as a measure to predict the type of SUI (LARRIEUX AND BALGOBIN [170]). Figure 7.6a shows a phenomenological effect of tissue impairment on the change of the urethral axis, Ur . An isolated impairment of the endopelvic fascia resulted in a more evident increase of the urethro-vesical junction mobility than weakened ligaments together including the pubourethral ligament which supports the mid-urethra. After 40% impairment of the fascial support, the urethral axis ($Ur_{(Mict)}$) increased dramatically beyond 30° with the vertical line which is normally considered to be a basic reference to predict the SUI due to urethral and vesical hypermobility.

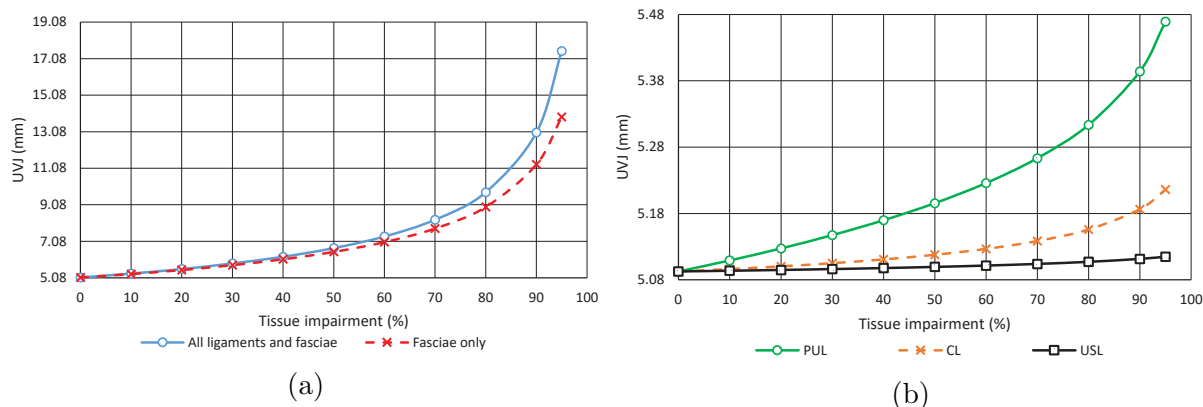


Figure 7.5: Effects of tissue impairment (*reduced stiffness*) on the vertical movement of the UVJ for the impairment of a) all connective tissues (fasciae and ligaments) b) and caused by individually impaired ligaments. *Maximum organ dislocation is achieved due to weakness in fasciae rather than the ligaments* (BHATTARAI AND STAAT [29]).

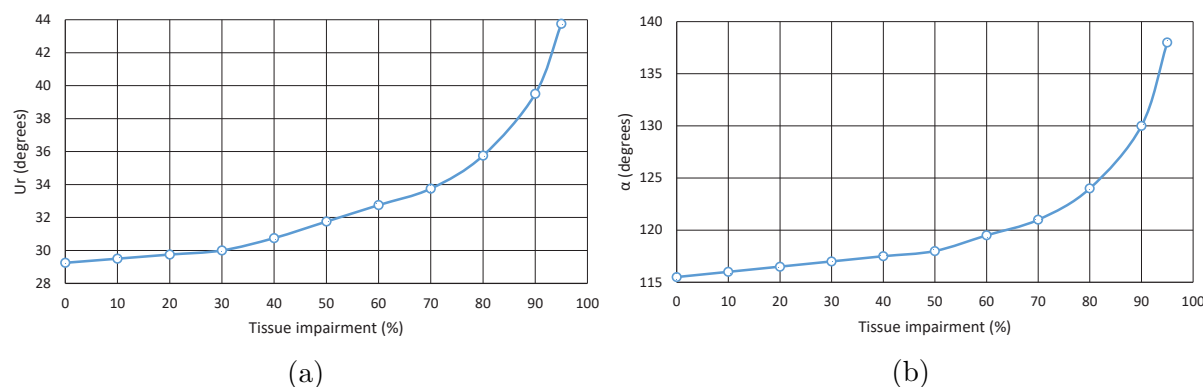


Figure 7.6: Plot of increased fascia impairment (*reduced stiffness*) on a) urethral axis, U_r and b) movement of the UVJ, (α) (BHATTARAI AND STAAT [29]).

7.2.3 Levator plate angulation

To measure the levator plate angle (LPA), a best fit line is placed for the levator plate at the initial take off portion of the iliococcygeus from the coccyx (Fig. 7.1). Between this line and a horizontal reference line, the LPA (subtended by the green line and the horizontal line in Fig. 7.7) at rest is measured to be 31.5° . In the female pelvic floor with healthy support, the measured levator plate angle is 42° . During Valsalva manoeuvre, women with simulated SUI showed statistically greater LPA compared to healthy tissue support (42° vs 54°) directed more caudally (Fig. 7.7).

7.2.4 Important discussions

The numerical studies performed on the fascia model differentiated with respect to varying elastin and collagen content supports the hammock hypothesis. The endopelvic fascia which covers most part of the pelvic diaphragm is found to restrain the induced IAP and

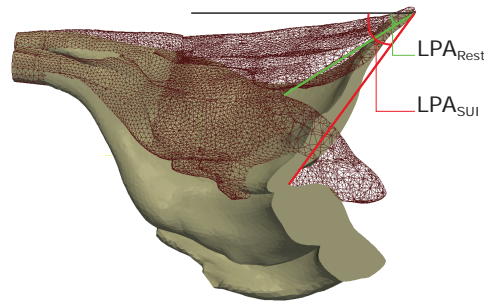


Figure 7.7: FE simulation results showing the sagittal section of increased levator plate angulation (LPA, the angle between the horizontal line and the line formed by two points between levator plate insertion point to the coccyx bone and anorectal junction) from rest (wireframe) to Valsalva manoeuvre (solid) for SUI female. Δ LPA=LPA_{SUI}-LPA_{Rest} = 22.5° is obtained between the rest (green) and during Valsalva manoeuvre (red) (BHATTARAI AND STAAT [29]).

its structural integrity is mainly responsible for the mobility of the pelvic organs.

Table 7.1: Comparison of the measured urethro-vesical junction movement (UVJ = $\sqrt{(\text{VUVJ})^2 + (\text{HUVJ})^2}$).

Reference	UVJ (mm)	
	Healthy	SUI
BHATTARAI AND STAAT [29]	5.1	17.5
BRANDÃO ET AL. [40]	5.7	12.0
HOWARD ET AL. [124]	12.4±4.7	14.8±6.4
PESCHERS ET AL. [233]	15±10	-
VIERECK ET AL. [311]	-	13.7 (2-30)
BRANDT ET AL. [41]	-	VUVJ=16.0±6.8 HUVJ=3.1±1.0

For normal micturition with intact support system, $\Delta U_r = 7.25^\circ$ is in agreement with the MRI examinations (Figures 7.3 and 7.4). The movement of the UVJ is 5.1 mm for the healthy support system in our study which is in good agreement with the MRI examination (5 mm) of a nulliparous (asymptomatic or healthy or continent) female without tissue impairment (BRANDÃO ET AL. [40]). Tables 8.3 and 7.2 illustrate the measurement of the UVJ and the angle alpha α , respectively. The measured values for the healthy female and for SUI simulations are within the ranges which are reported in the cited literature. The measured difference (22.5°) of the angle alpha between healthy and SUI Valsalva manoeuvre is similar to the references. Also, since the computed pelvic model has been constructed from a 72 years old female with no history of pelvic pathology, $\alpha_{\text{rest}} > 110^\circ$ for an elderly female is reasonable.

Results of the FE simulations validate the positive Q-tip test. An urethral angle of $U_r > 30^\circ$ during exertional activities indicates a hypermobile urethrovesical junction. Weak-

Table 7.2: Comparison of the angle between the midpubic line with the bladder neck (α). The difference of the angle alpha between healthy and SUI simulation is computed as $\Delta\alpha_{\text{Valsalva}} = \alpha_{\text{SUI}} - \alpha_{\text{healthy}}$.

Reference	α ($^{\circ}$)			
	α_{rest}	α_{healthy}	α_{SUI}	$\Delta\alpha_{\text{Valsalva}}$
BHATTARAI AND STAAT [29]	110	115.5	138	22.5
BRANDÃO ET AL. [40]	91.8	105.7	124.3	18.6
PREGAZZI ET AL. [245]	92.0±6.0	100.0±8	120.0±8	20.0
HOWARD ET AL. [124]	103	-	-	-
PENG ET AL. [230]	73	-	-	-

ness of the endopelvic fascia after 40% impairment is found to develop SUI, (Fig. 7.6a). Though representing a different physiopathological situation, a similar effect of the fascia impairment has been recently observed for the phenomenological development of the cystocele. Symptoms are dramatic after 40% impairment of the pubocervical fascia (LAMBLIN ET AL. [166]).

Petros emphasized the difference between the micturition in continent females and active opening in incontinent females, the latter is induced by a weak support system during increased IAP. BUSH ET AL. [47] found that the normal detrusor pressure alone is not sufficient to open the urethra in contrast to the conventional theory, which assumes that the female urethra opens uniquely because of the detrusor pressure. The numerical results presented support the proposition of the integral theory that together with an active muscle mechanisms, the increase of the detrusor pressure by two orders of magnitude is required to achieve the urethral funneling and urethrovesical hypermobility (Fig. 7.3). However, the mechanical stiffness around the bladder neck has not been reduced in our study, since increased bladder pressure alone resulted in urethral funneling. In addition, weakness of the internal urethral orifice involves a different form of SUI arising from the defect of the internal urethral sphincter, which is different due to damaged ligaments, muscles and fasciae. Also, the proximal 2/3rd of the urethral length and the lower portion of the urinary bladder is lined by transitional epithelium cells while the distal 1/3rd of the urethra is lined by stratified squamous epithelium cells (DAFTARY ET AL. [68]). Relatively softer transitional epithelium cells might open the urethral sphincter and move the proximal urethra more than the distal end.

Angulation of the levator plate in craniocaudal direction is obvious during pelvic maneuvers due to increased IAP and active muscle mechanisms. MRI examinations of patients with genuine SUI measured an increased angle $\Delta\text{LPA}=24.7^{\circ}$ from rest ($13.2^{\circ}\pm 11.9^{\circ}$) to straining ($-11.5^{\circ}\pm 15.5^{\circ}$) (HOYTE ET AL. [125]), where negative values represent a bladder neck inferior to the pubococcygeal line and positive values represent a bladder neck above the pubococcygeal line. During simulated Valsalva manoeuvre a 22.5° change in the LPA has been calculated (Fig. 7.7) which is in total agreement with the MRI examination.

8 Vaginal Vault Prolapse Correction

This chapter investigates the biomechanical efficacy of the vaginal vault suspension system after hysterectomy to correct apical prolapse using 3D finite element modeling as presented in BHATTARAI ET AL. [30], BHATTARAI AND STAAT [32]. The positions of the organs are calculated from the pubococcygeal line (PCL) as the reference line during Valsalva maneuver to verify the numerical approach of vaginal vault prolapse. The PCL is defined as the line joining the inferior border of the symphysis to the lowest possible coccygeal joint. Implant models of DynaMesh[®]-PRS soft and DynaMesh[®]-PRP soft from FEG Textiltechnik mbH, Aachen, Germany and Gynemesh[®] PS Nonabsorbable Prolene soft[®]^{12.)} and Ultrapro[®] from Ethicon, USA have been examined to correct apical prolapse suspending the vaginal cuff to the sacral bone.

8.1 Sacrocolpopexy implant

The computer model of a Y-shaped DynaMesh[®]-PRS soft mesh implant (length×width: 16 cm×2 cm or 23 cm×3 cm) as shown in Fig. 8.1 with two arms and a cylindrical mesh body is based on the specifications of FEG Textiltechnik mbH, Aachen, Germany for sacrocolpopexy. The PVDF fiber diameter ($\phi_{\text{fiber}} = 103.8\mu\text{m}$) and the total mesh thickness ($\phi_{\text{longitudinal}} = 333.6 \pm 36.2\mu\text{m}$ and $\phi_{\text{transversal}} = 174.2 \pm 21.7\mu\text{m}$) are measured using a digital microscope VHX-600 (Keyence, Japan) (BHATTARAI AND STAAT [28]). Depending on the stage of prolapse, the patient's anatomy and the surgeon's expertise, the standard mesh can be cut during surgery in order to fit to the pelvic floor. For the

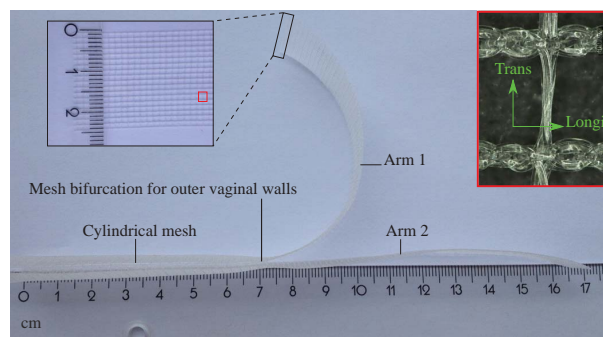


Figure 8.1: Dimensions of a standard DynaMesh[®]-PRS soft mesh implant with right red panel represents the higher magnification view of the red square on the black left panel showing PVDF polymer fibers using a digital microscope VHX-600 (Keyence, Japan) (BHATTARAI ET AL. [30]).

female pelvic model, a Y-shaped implant is modeled as a strip with adjusted dimension (length×width×thickness: (7+4) 11 cm×2 cm×0.04 cm) to fit up to the half length of the vagina and the other end is later pulled towards the S1 one below promontory for fixation or suture (Fig. 8.2).

^{12.)} Subsequently GYNECARE Gynemesh[®] PS Nonabsorbable PROLENE soft[®] is also abbreviated as Gynemesh and is adopted through out in this chapter.

8.2 Sacrocolpopexy implant in the pelvic floor model

The finite element model of the sacrocolpopexy implant as shown in Fig. 8.2 is included to support the vaginal stump after hysterectomy. Considering the thickness of pelvic organs, ligaments, muscles and fasciae, a volume discretization is adopted to generate 3D meshes.

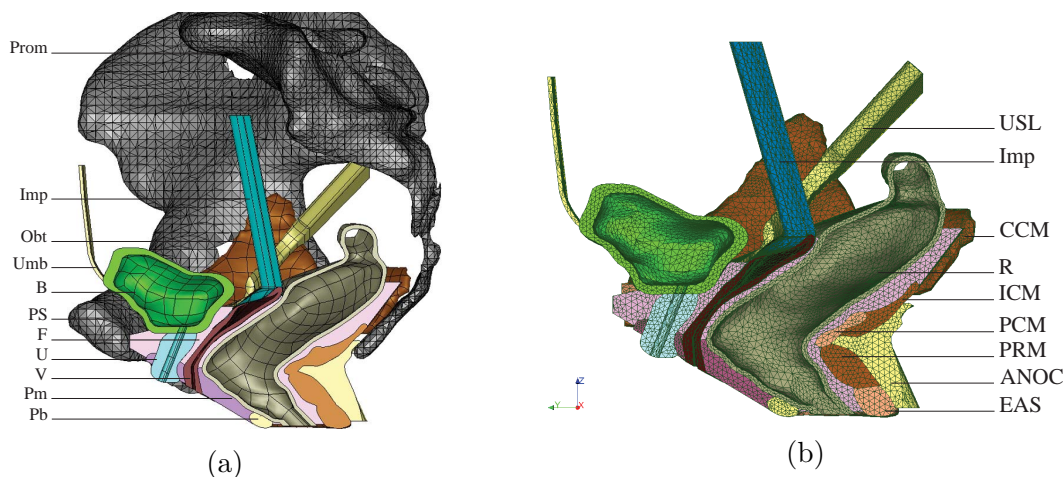


Figure 8.2: Sagittal section of the female pelvic floor showing a) the smoothed NURBS-based visualization geometry and b) the 3D FE mesh for simulation generated from smoothed NURBS-based geometry. Mesh implant suspends the vaginal cuff after hysterectomy from the first sacral (S1) bone (BHATTARAI ET AL. [30]). Prom=Promontory; Imp=DynaMesh[®]-PRS soft implant; Obt = Obturator internus muscle; Umb=Umbilical ligament; B=Bladder; PS=Pubic symphysis; F=Endopelvic fascia; U=Urethra; V=Vagina; Pm=Perineal membrane; Pb=Perineal body; USL=Uterosacral ligament; CCM=Coccygeus muscle; R=Rectum; ICM=Iliococcygeus; PCM=Pubococcygeus; PRM=Puborectalis; ANOC=Anococcygeal raphe; EAS=External anal sphincter.

8.3 Mechanical modeling of mesh implants

The industrial project partner FEG Textiltechnik mbH, Aachen, Germany provided force-elongation data for three popular meshes (DynaMesh[®]-PRS soft (FEG, Germany), Gynecare Gynemesh[®] Prolene soft (Ethicon, USA) and Ultrapro (Ethicon, USA)) which have been tested on a uniaxial tensile machine and are widely used to repair vaginal vault prolapse. The stress-stretch curve (Fig. 8.3) is derived from the force-elongation curve of the mesh implants that show nearly linear or nonlinear orthotropic behavior depending on the mesh pore deformation. For DynaMesh[®]-PRS soft with regular rectangular pores (Fig. 8.3), a slight deviation from the linearly elastic orthotropy is observed. Therefore, the Young's modulus is computed for each mesh loaded along longitudinal and transversal fiber bundles, see Table. 8.1. On the other hand, the Gynemesh[®] and Ultrapro[®] with large pore deformation along the loaded direction shows significant nonlinear mechanical

behavior. The stress-stretch curves for Gynemesh[®] along the longitudinal and transversal loaded directions are quite similar. On the other hand, the Ultrapro[®] showed distinct nonlinear orthotropy with higher stiffness along the loaded direction and is very compliant along the transversal direction. The isotropic hyperelastic constitutive equation (4.21) is used to model the mechanical behavior of the implants. The material parameters are listed in Table 8.1.

8.3.1 Parameters identification

The stress-strain curves of the pelvic structures are adopted from the experiments published in different literature and are fitted with three term polynomial hyperelastic function (Eqn. (4.21)) (RIVLIN ET AL. [257]) to obtain isotropic hyperelastic parameters which are used in the numerical study, see Table 4.3. The stress-stretch response of the mesh implants vary from nearly linear (DynaMesh[®]-PRS soft) to nonlinear (Gynecare Gynemesh[®] Prolene soft and Ultrapro[®]), see Fig. 8.3. The *linearly elastic orthotropic* and *isotropic hyperelastic material models* are used to characterize the mechanical behavior, see Table 8.1.

8.4 Mesh implant and suture position

Tissues with laxity (or weakness or reduced stiffness) fail to maintain the normal position of the organs which can be well stabilized again by using the Y-shaped mesh implants fixed at different levels of the sacrum bone below the sacral promontory (For example, S1 bone fixation in Fig. 8.2). Therefore, the stiffness of the supporting endopelvic fascia, ligaments, muscles and organs are reduced to simulate possible symptomatic pelvic floor (BRANDÃO ET AL. [40]). Attaching the mesh bifurcation to the vaginal cuff is a common

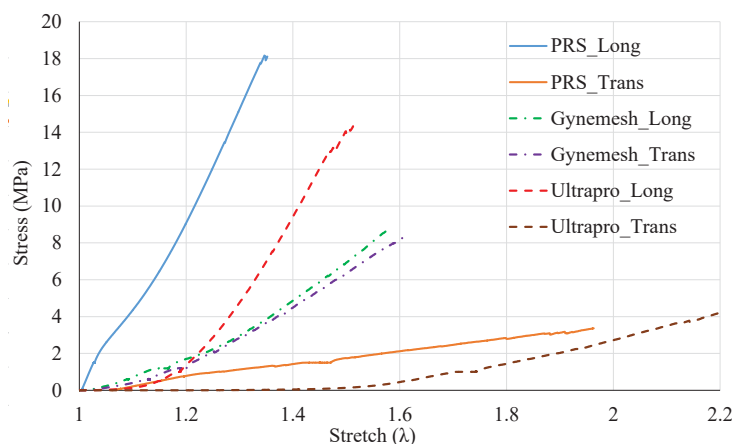


Figure 8.3: Uniaxial tensile Cauchy stress-stretch curves of DynaMesh[®]-PRS soft (with regular rectangular pores), Gynecare Gynemesh[®] Prolene soft and Ultrapro[®] (irregular hexagonal pores) mesh implants loaded in longitudinal (Long) and transversal (Trans) directions (BHATTARAI ET AL. [30]). The tensile tests data have been provided by FEG Textiltechnik mbH, Aachen, Germany as force-elongation data.

Table 8.1: Mechanical properties of prosthetic mesh implants fitted with elastic orthotropic and hyperelastic material behavior using eqn. (4.21) and Fig. 8.3.

Mesh implants	E_L (MPa)	E_T (MPa)	G_{LT} (MPa)	ν_{LT}
DynaMesh [®] -PRS soft	46.859	3.573	4.377	0.07
	C_{10} (MPa)	C_{01} (MPa)	C_{20} (MPa)	
Gynemesh [®]	0.9	0.25	1.75	
Ultrapro [®] (along stiffer longitudinal direction)	0.1	-	5.85	

surgical technique (Fig. 8.2b). The 7 cm cylindrical mesh length is short enough to reach the anterior aspect of the sacrum, the free end is carefully pulled towards the cranial body of the sacrum (S1). This situation of the pelvic floor after mesh implantation is considered the resting state in the numerical study. Later, pelvic organ movement is simulated under increased IAP during Valsalva maneuver as described in section 7.1.3. A mesh implant with good mechanical behavior holds the organs in their desired position.

8.5 Prolapse definition

Most researchers in radiography compare the dynamic pelvic floor movement with reference to the PCL line as an assessment of normal and the grading of the pelvic organ prolapse (FIELDING [95], FLETCHER ET AL. [98]). The PCL line is defined as the line between the inferior symphysis pubis and the last visible coccygeal joint (white line in Fig. 8.4). Prolapse is demonstrated in Fig. 8.4b when the organs (for example the vaginal cuff and the bladder base) herniate inferiorly below PCL (FIELDING [95]) and this is the author's preference. By convention, descent of any pelvic organ or structure and the severity of the prolapse is measured along the perpendicular line from the pubococcygeal line to the structure (FLETCHER ET AL. [98]).

8.5.1 Surgical reconstruction technique

Sacrocolpopexy is a standard surgical procedure for the treatment of vaginal vault prolapse in women. Reconstruction is achieved either with an open abdominal technique or with the use of minimally invasive techniques, such as laproscopic or robot-assisted surgery. This method connects two extraperitoneal structures, the sacrum and the apical portion of the vagina (or the vaginal cuff in patients after hysterectomy), see Fig. 8.5. The type of the treatment is decided by the surgeons before or during the surgery in accordance with the severity of the prolapse, its symptoms and postoperative mesh related complications. Conventional polypropylene (Gynemesh[®] and Ultrapro[®]) (ÖNOL ET AL. [216]) and modern PVDF (DynaMesh[®]-PRS soft) (ANDING ET AL. [9], HANSEN ET AL. [113]) meshes have been widely implemented to repair apical prolapse. The utilization of the MRI visible form of the PVDF mesh implant allows the visualization and animation of the surgical result (ANDING ET AL. [9]) and can be used to verify numerical studies.

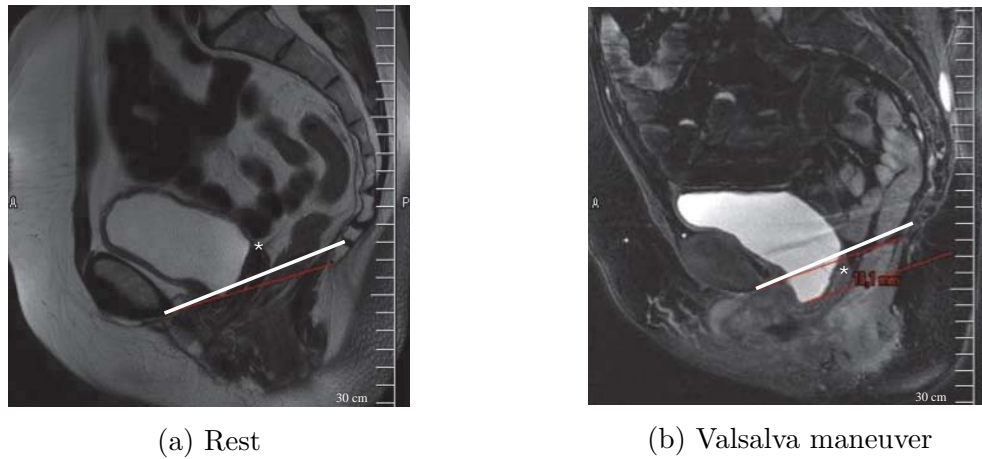


Figure 8.4: MRI of the pelvic floor from a symptomatic female showing organs a) at rest and b) movement during Valsalva maneuver (BHATTARAI ET AL. [30]). The PCL white line is drawn from the inferior border of the pubic symphysis to the last coccygeal joint. It is adopted as a reference line to compare the normal pelvic floor and the prolapse. Asterisk (*) illustrates the position of the vaginal cuff. Source: Dr. med. Ralf Anding.

8.5.2 Biomechanical simulation of prosthesis to support weak pelvic tissues

The simulation of the finite deformation of the prolapse condition and the sacrocolpopexy treatment using prosthetic mesh implants are performed within the open source FE software, *Code_Aster*. The finite element model of the female pelvic floor as shown in Fig. 8.2b consisted of a total of 547,932 linear tetrahedrons (4 node) and 28,833 quadratic tetrahedrons (6 node). Using parallel solver technology on a Linux-based multi-core processor, each simulation took about 6 hours with two Intel Xeon processor (8 core, 3.10GHz

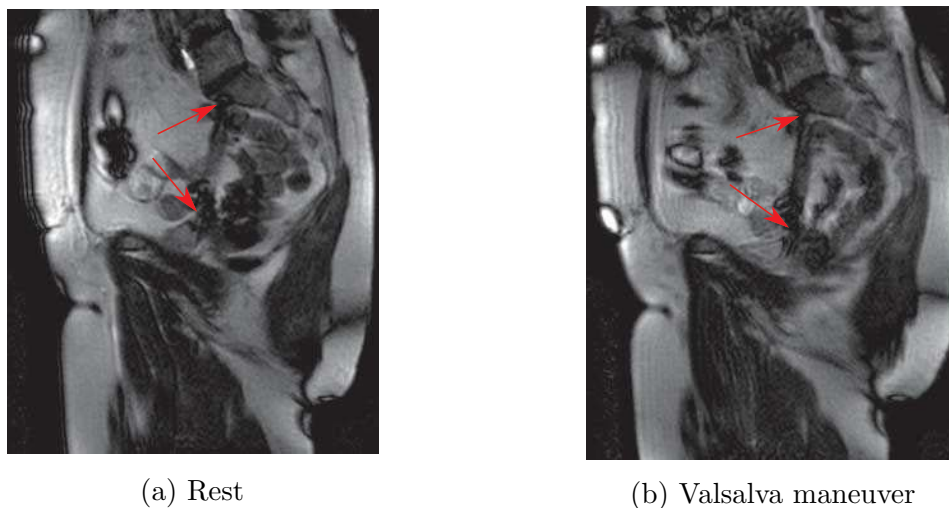


Figure 8.5: Sagittal section of MRI sequences with well depicted mesh (shown by red arrows) connecting the extraperitoneal structures, the sacral promontory and the vaginal cuff (BHATTARAI ET AL. [30]). Source: Dr. med. Ralf Anding.

Turbo, 20MB, 8.0 GT/s).

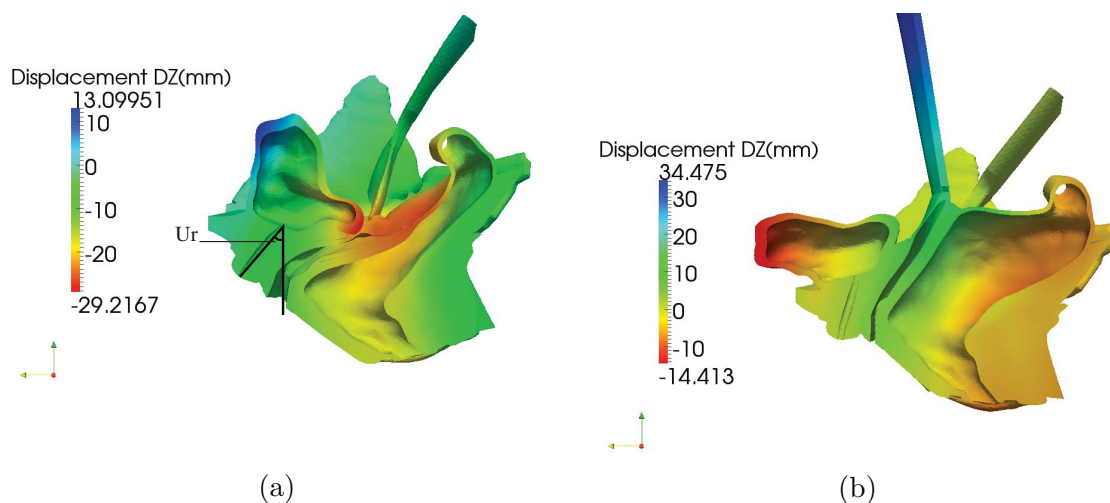


Figure 8.6: Finite element simulation of the weak female pelvic floor showing the pelvic organ movement a) before surgery (prolapse) and b) after sacrocolpopexy repair using DynaMesh[®]-PRS soft mesh implant suspended at S1 bone below promontory (BHATTARAI ET AL. [30]). Positions of the vaginal cuff, bladder and urethra are compared with respect to their movement (DZ in mm) in vertical direction during Valsalva maneuver. The change of the urethral axis is measured by angle $Ur(^{\circ})$ with vertical line.

The biomechanical simulation results of the symptomatic pelvic floor before and after surgery are shown in Fig. 8.6a and Fig. 8.6b, respectively. The pelvic dislocation during Valsalva maneuver and the angulation (urethral, vaginal and the ano-rectal axis) of the organ from their resting positions are critical during prolapse. The phenomena of organ dislocation is qualitatively similar to the one that can be observed in the MRI image (Fig. 8.4b) on the patient with prolapse after hysterectomy. For the verification of the prolapse, the distance from the organ to the reference PCL line is measured, see Fig. 8.7. A significant difference of the organ descent (bladder base and vaginal cuff, -9.19 mm and -10.03 mm, respectively) below the PCL line is calculated for presurgery or prolapse simulations during Valsalva maneuver. Here negative values represent the distance measured below the PCL line.

In contrast, after the surgical intervention with the use of Y-shaped DynaMesh[®]-PRS soft mesh suspended to the S1 bone (Fig. 8.6b), symptoms and the measured values are significantly modified. The critical dislocations of the bladder base and the vaginal cuff post-surgery are perfectly stabilized and are well above ($P_{Bb}=9.23$ mm and $P_{VC}=37.24$ mm) the PCL line, see Fig. 8.7. Two other polypropylene made Gynemesh[®] and Ultrapro[®] are also tested for the S1 fixation. Though, the elevation of the organs are above the PCL line, due to their mechanical behavior, the positions of the organs under Valsalva maneuver IAP are found to be lower than those obtained from the DynaMesh[®]-PRS soft mesh, see Table 8.3. In addition to the suspension of the vaginal cuff, the DynaMesh[®] is also able to stabilize the orientation of the urethral axis, Ur (8.17° vs 26.28° and 27.43°) better than the Gynemesh[®] and the Ultrapro[®] (Fig. 8.7). The urethral axis ($Ur>30^{\circ}$) and bladder

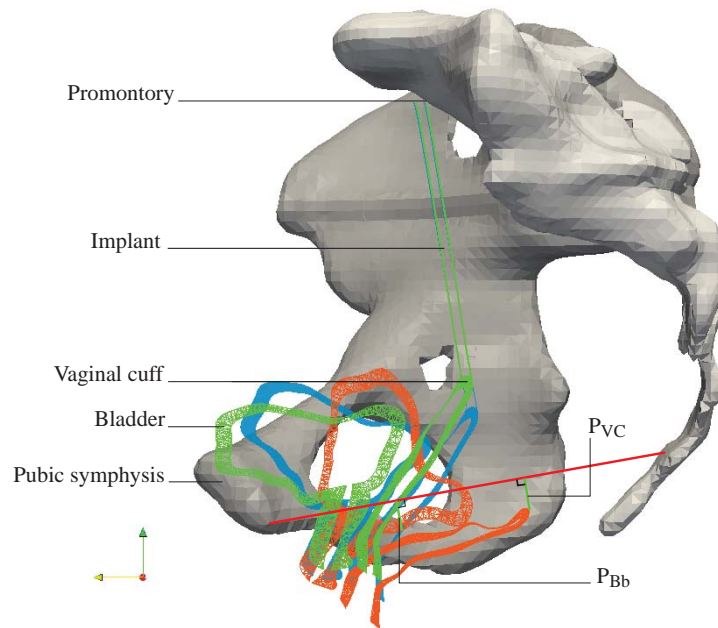


Figure 8.7: Sagittal slices showing the distances of the bladder base (P_{Bb}) and the vaginal cuff (P_{Vc}) from the reference PCL line (red line) inside the pelvic cavity before surgery or prolapse (orange), and after sacrocolpopexy repair using DynaMesh[®] (green) and Gynemesh[®] (blue) suspended at S1 bone below promontory (BHATTARAI ET AL. [30]).

hypermobility are considered to be the symptom of stress urinary incontinence. In all the cases, the sacrocolpopexy treatment using a Y-shaped implant suspended to the S1 bone maintain the vaginal axis, the vaginal cuff, bladder position and the orientation of the urethral axis (DynaMesh[®]).

8.5.3 Computational comparison of sacrocolpopexy with pectopexy technique

Obesity is associated with an increased risk for genital prolapse (IRVINE AND SHAW [130]), the sigmoid colon enlarged by fatty tissue provides less space for sacrocolpopexy. In obese patients, sacrocolpopexy technique (the mesh implanted between the sacrum and the vagina/cervical stump, Fig. 8.7) narrows the pelvic space, which might result in defecation disorders, adhesions, or trauma of the hypogastric nerves (AKLADIOS ET AL. [2]). Introduced for the first time in 2007 (BANERJEE AND NOÉ [16]), laparoscopic pectopexy minimizes such risks and has rapidly emerged as a promising technique for the prolapse repair in obese patients with good postoperative outcomes. This method uses the lateral parts of the iliopectineal ligament (Cooper ligament) for a bilateral mesh fixation (NOÉ ET AL. [212]). As shown in Fig. 8.8, the mesh implant carefully follows the direction of the round and broad ligaments without crossing or interfering sensitive areas such as the ureter, bowel or hypogastric trunk which offers zero restriction to the organ function by the implant. In this way, fixation at the stable and significantly stronger iliopectineal ligament than the

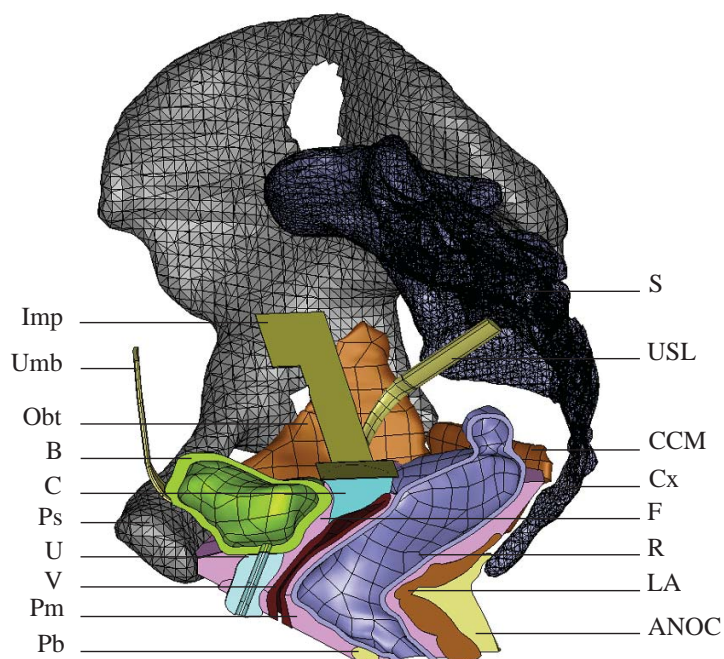


Figure 8.8: Sagittal section of the female pelvic floor showing the smoothed NURBS-based geometry with DynaMesh[®]-PRP soft implant (abbreviated as Imp) suspending the cervical stump after hysterectomy from the iliopectineal ligament. (BHATTARAI AND STAAT [32]) For other abbreviations, see Fig. 8.2.

sacrospinous ligament and arcus tendinosis fasciae pelvis ensures a more physiological axis of the vagina (NOÉ ET AL. [212], COSSON ET AL. [67]).

BHATTARAI AND STAAT [31] simulated and investigated the functional performance of the pectopexy after hysterectomy to correct the apical prolapse. Implant models (Fig. 8.9) are included in the pelvic floor model to examine the effectiveness of DynaMesh[®]-PRP soft, Gynemesh[®] and Ultrapro[®] mesh implants to correct apical prolapse by lifting the cervical stump. The positions of the vaginal vault and the urethral axis are measured and the result obtained are compared with sacrospinopexy repair technique (BHATTARAI ET AL. [30]).

8.5.4 Numerical simulation after pectopexy surgery

The FE simulations were performed with the open source FE software, *Code_Aster*^{13.)}. Using parallel solver technology on a Linux-based multi-core processor, each simulation took about 7 hours with two Intel Xeon processors (8 core, 3.10GHz Turbo, 20MB, 8.0 GT/s). After the surgical intervention with the use of pectopexy implants which are suspended bilaterally to the iliopectineal ligament, the stability of the post-hysterectomy vaginal cuff is expected. The biomechanical simulation results of the symptomatic pelvis after pectopexy surgery at rest (R/w) and during Valsalva maneuver (VM/w) are shown in Fig. 8.10 and Fig. 8.11, respectively (BHATTARAI AND STAAT [32]).

^{13.)} <http://www.code-aster.org>

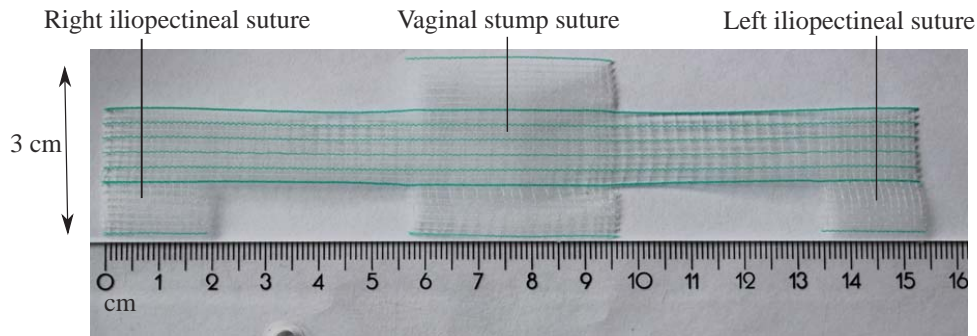


Figure 8.9: Dimensions of a standard DynaMesh[®]-PRP soft mesh implant (BHATTARAI AND STAAT [32]).

Rest state after surgery

Using DynaMesh[®]-PRP Soft, the bladder base (2.99 mm) and the post-pectopexy vaginal cuff (20.17 mm) are repositioned well above the PCL line at rest R/w (Figure 8.10a). The vaginal axis is aligned towards S3 bone making an angle of 49° with the vertical axis. Two other Ethicon meshes: Gynemesh[®] and Artisyn[®] which were comparatively softer material (see Fig. 8.10b) due to large mesh pore collapse under load were also tested in the pelvis model for which bladder and vaginal cuff positions were measured. Due to less stiff mechanical behavior, the lifting of the bladder base is just (2.62 mm and 2.61 mm) above the PCL line. However, the vaginal cuff is satisfactorily lifted high (15.69 mm above the PCL line for both meshes) and is directed towards the S3-S4 sacrum bone. The authors would like to emphasize that the results presented here reflect the approximate behavior of the Ethicon mesh products due to unavailability of actual mesh geometries for which mesh knitting patterns and pores architecture were different. A simple comparison of the differences in the mesh performance with respect to their elastic properties on a simplified mesh geometry were conducted.

Table 8.2: Measurement of the bladder base (P_{Bb}), vaginal cuff resting position (VCRP), urethral (U_r) and vaginal axis (V_{ax}) during rest state and Valsalva maneuver simulation for pectopexy repair using DynaMesh[®]-PRP soft, Gynemesh[®] and Artisyn[®] (BHATTARAI AND STAAT [32]). Distances of the organs are measured as the perpendicular distance with respect to the PCL line and the angles are measured with respect to the vertical axis. Positive values of P_{Bb} and P_{VC} represent the perpendicular distance measured above the PCL line and negative values represent the distance measured below the PCL line. SI represents the direction of the vaginal axis towards Ith sacrum bone.

	Rest state with mesh R/w (0.5 kPa)				Valsalva with mesh VM/w (4.5 kPa)			
	P_{Bb} (mm)	VCRP (mm)	U_r (°)	V_{ax} (°)	P_{Bb} (mm)	VCRP (mm)	U_r (°)	V_{ax} (°)
DynaMesh	2.99	20.17	20°	49° (S3)	0	17.18	24°	48° (S3)
GYNEMESH	2.62	15.69	23.5°	52.5° (S3-S4)	-1.87	11.95	28.5°	54° (S4)
Artisyn	2.61	15.69	23°	55° (S3-S4)	-1.49	6.72	29°	55.5° (S4)

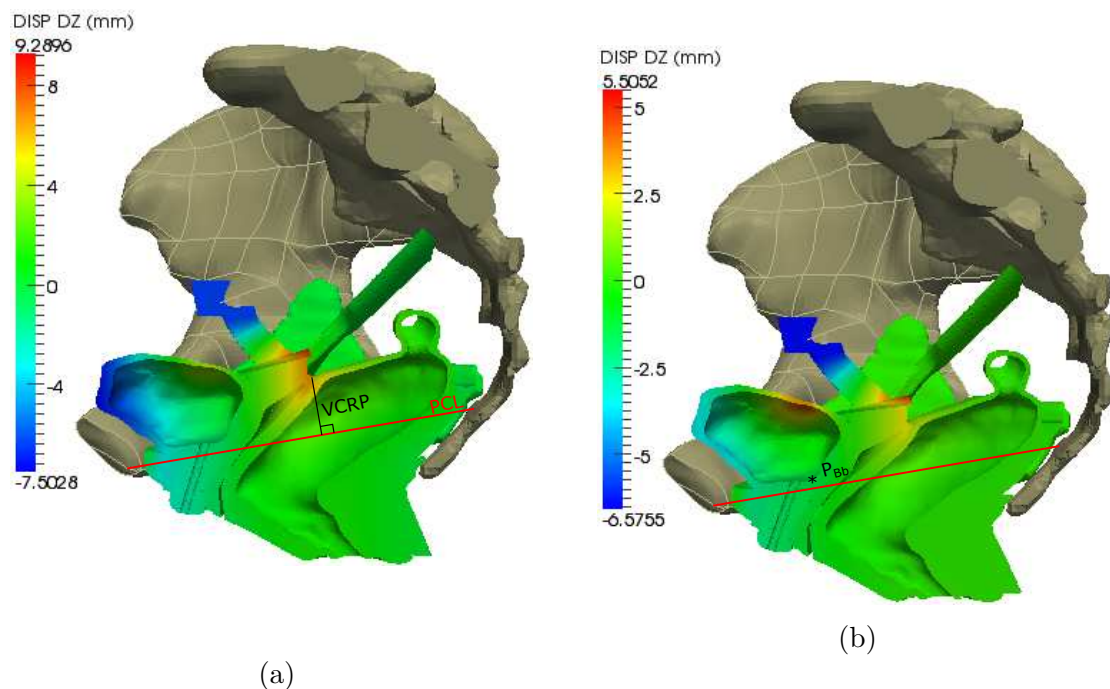


Figure 8.10: Finite element simulation of the pectopexy surgery after hysterectomy at rest, R/w (0.5 kPa) using a) DynaMesh®-PRP Soft and b) Gynecare Gynemesh® PS Nonabsorbable Prolene Soft® mesh materials (BHATTARAI AND STAAT [32]). DISP DZ represents the displacement in the vertical direction from the undeformed state. VCRP represents the perpendicular distance of the vaginal cuff resting position from red PCL line and * is drawn in Fig. 8.10b due to short perpendicular distance of bladder base from PCL.

Valsalva maneuver after surgery

In the second step, Valsalva maneuver (VM/w) with an IAP of 4.5 kPa is simulated (Figure 8.11). For all mesh materials, bladder base position changes significantly from the resting position after surgery with an IAP of 0.5 kPa (R/w): 2.99 mm for DynaMesh®-PRP Soft, 4.49 mm for Gynemesh® and 4.1 mm for Artisyn® (Table 8.2). With the DynaMesh®-PRP Soft, changes in the vaginal cuff resting position ($\Delta\text{VCRP} = 2.99$ mm), the urethral axis ($\Delta\text{Ur} = 4^\circ$) and the vaginal axis ($\Delta\text{V}_{\text{ax}} = -1^\circ$) are measured. However, for the Gynemesh® and Artisyn® significant changes in the VCRP ($\Delta\text{VCRP} = 3.74$ mm and 8.97 mm, respectively), Ur ($\Delta\text{Ur} = 5^\circ$ and 6° , respectively) and V_{ax} ($\Delta\text{V}_{\text{ax}} = 1.5^\circ$ and 0.5° , respectively) measurements are found. All tested mesh materials are found to stabilize the position of the vaginal cuff during Valsalva maneuver, however among them DynaMesh®-PRP Soft is found to functionally stable all the pelvic organs: the urethral axis is widely less than 30° ($\text{Ur} > 30^\circ$ clinically represents the symptoms of stress urinary incontinence [170]) and the new orientation of the vaginal axis is along the anatomical direction of the uterosacral ligament or the S3 bone (Figure 8.11a) which appears in the healthy pelvis.

After surgery, anatomically and physiologically correct positions of the vaginal cuff were

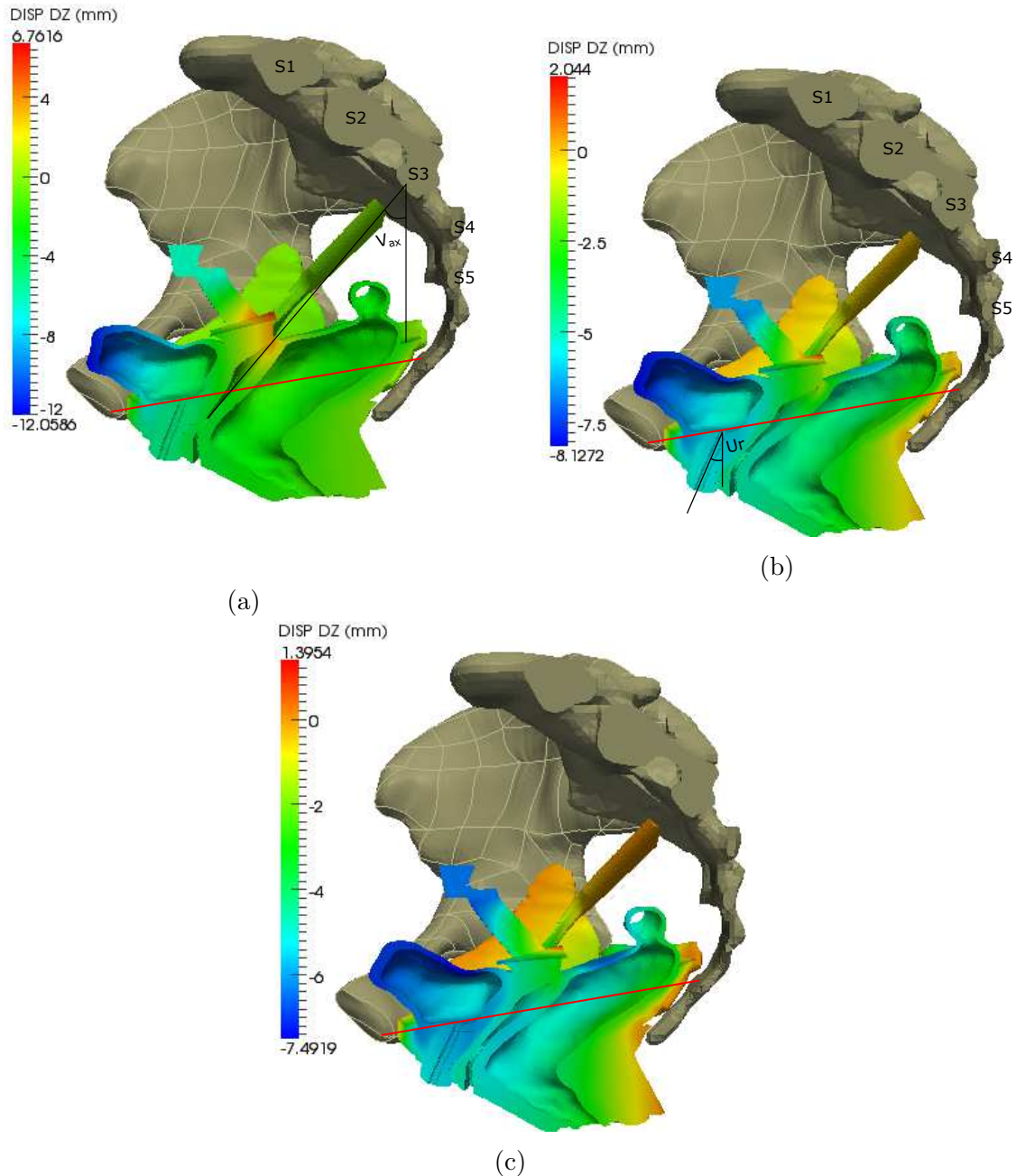


Figure 8.11: Finite element simulation of the pectopexy surgery after hysterectomy during Valsalva maneuver (4.5 kPa) using a) DynaMesh®-PRP Soft and b) Gynecare Gynemesh® PS Nonabsorbable Prolene Soft® c) Artisyn® mesh materials (BHATTARAI AND STAAT [32]). DISP DZ represents the displacement in the vertical direction from the undeformed state.

obtained during rest state (Fig. 8.10) and during Valsalva maneuver (Fig. 8.11). However, direct comparison of the simulation outcomes with corresponding pectopexy medical images has not been performed due to lack of such medical examinations. Therefore, results obtained, especially the vaginal-urethral axis and the bladder-vaginal cuff positions were

compared with the sacrocolpopexy technique after complete hysterectomy to treat vaginal cuff prolapse (Fig. 8.12) which has been simulated in our previous study [30]. Alike sacrocolpopexy, the pectopexy repair is found to provide adequate support to the vaginal cuff after hysterectomy in the weaker pelvis with lax supporting tissues.

The position of the vaginal cuff during the Valsalva maneuver after sacrocolpopexy (Fig. 8.12a-8.12c) and after pectopexy treatments (Fig. 8.12d-8.12f) are found to be significantly different. For uni-axially suspended sacrocolpopexy method using the Y-shaped DynaMesh[®]-PRS Soft, the vaginal cuff is much high (37.24 mm) above the PCL line than the Gynemesh[®] (27.12 mm) and the Artisyn[®] (25.72 mm) mesh materials. Whereas, the pectopexy method with lower bilateral suspension on the pelvic side walls than the sacrocolpopexy method repositioned 17.18 mm, 11.95 mm and 6.72 mm above the PCL line for DynaMesh[®]-PRP Soft, Gynemesh[®] and Artisyn[®] meshes, respectively. Also, the vaginal axis varies between S2-S3 (sacrocolpopexy) and S3 to S4 (pectopexy), resulting the variation in vaginal hammock to cause bladder hypermobility below the PCL line during Valsalva maneuver (Table 8.3).

Table 8.3: Measurements of the bladder base (P_{Bb} in mm) and urethral axis (U_r in degrees) during Valsalva maneuver simulation for sacrocolpopexy and pectopexy repair using DynaMesh[®]-PRS soft, DynaMesh[®]-PRP soft, Gynemesh[®] and Artisyn[®]. Sign convention for P_{Bb} is same as in Table 8.2.

	Sacrocolpopexy BHATTARAI ET AL. [30]			Pectopexy BHATTARAI AND STAAT [32]		
	PRS	Gynemesh	Artisyn	PRP	Gynemesh	Artisyn
P_{Bb} (mm)	9.23	2.3	1.25	0	-1.87	-1.49
U_r (°)	8.2°	26.3°	27.5°	24°	28.5°	29°

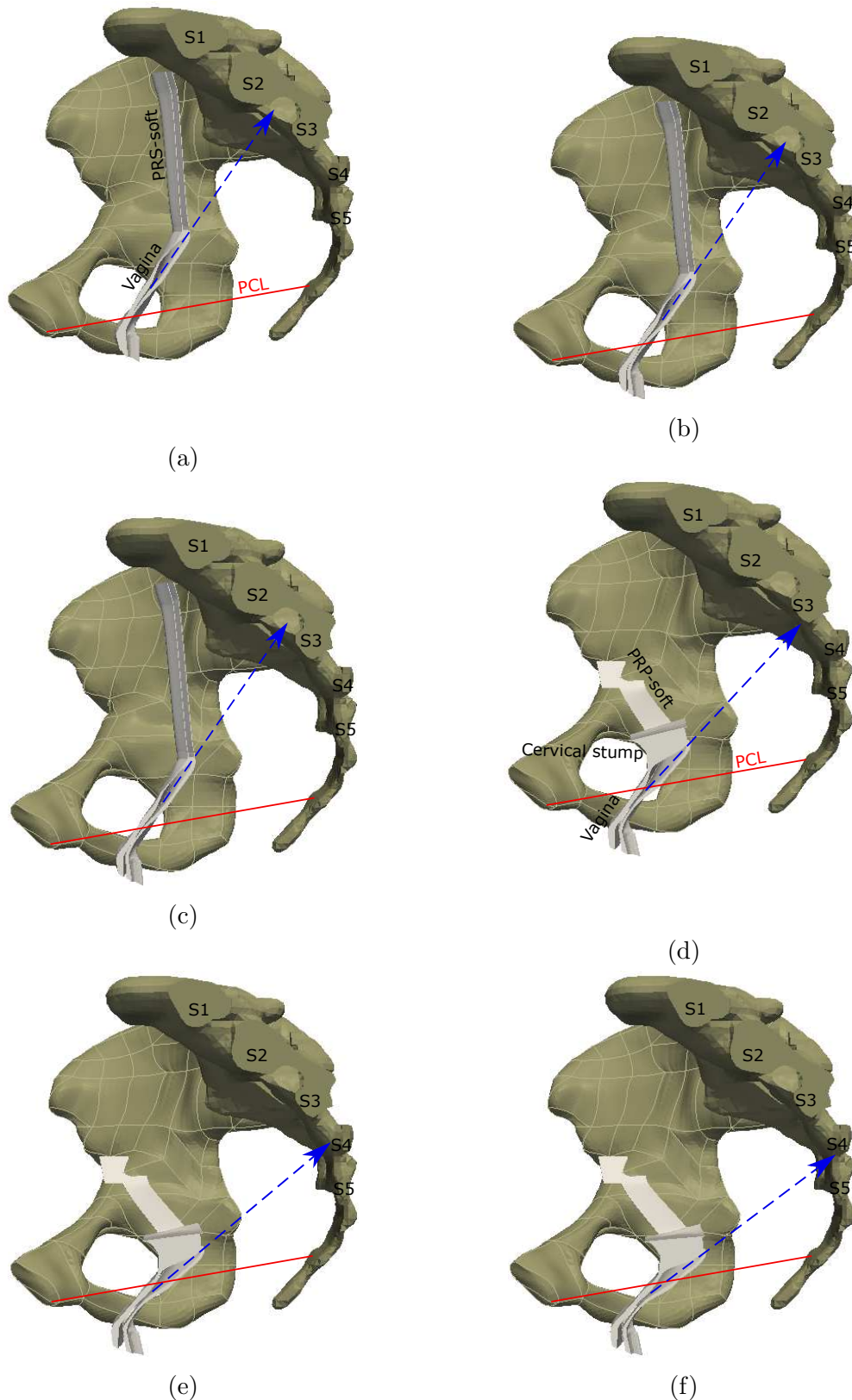


Figure 8.12: Finite element simulation results showing differences in the vaginal axis (blue arrow) after sacrocolpopexy (a-c) and pectopexy (d-f) treatment using the DynaMesh®-PRS (a), DynaMesh®-PRP (d), Gynemesh® (b, e) and Artisyn® (c, f) meshes. (a-c) shows complete and (d-f) shows partial hysterectomy (BHATTARAI AND STAAT [32]). The red PCL line is shown to visualize the position of the vaginal cuff after different prolapse repair technique.

9 Conclusions and Outlook

The presented work in this thesis deals with three major aspects. Firstly, the development of a three dimensional finite element model of the female pelvic floor using ultra-thin E12 sheet plastination technique and the novel representation and the inclusion of the fasciae geometry is presented. Secondly, this thesis concerns the applicability of the constructed model to understand the mechanical situations of a variety of normal and pathophysiological situations in the female pelvic floor. For this, the modeling of the nonlinear multi-constituent soft connective tissues using Voigt's isostrain homogenization approach is adapted to estimate their overall mechanical response. The soft tissue constituents, mainly elastin-collagen fiber compound, adipose tissue and smooth muscle are modeled as simple isotropic, incompressible and hyperelastic material which need to be extended to anisotropic material models if new tissue testing can provide the material data in future. And thirdly, this thesis also investigates testing and optimization of operations which use surgical mesh implants to restore healthy pelvic floor function avoiding discomfort, organ mobility resulting from implant mechanics and more importantly sufficient organ functionality. Nevertheless this thesis can be concluded with important remarks from following chapters.

Chapter 3: Development of computational model using plastinates

The plastination technique developed by Gunther von Hagens for the preservation and the representation of human or animal specimen for education and demonstration has been recently used as a research tool for the first time by M.C. Sora to develop a three-dimensional reconstructions of the female pelvic floor. The model generated from plastinated body slices offers a unique insight into the human body and to measure anatomic-topographic structures which can be used as a landmarks for surgical purposes. With few artefacts observed during three dimensional reconstruction, repairment with less effort has been possible using CAD softwares such as MeshLab and Rhino to construct better computational models. Thus, this thesis uses the capability of E12 plastination technique for the construction of finite element models and its applicability for numerical studies as alternative to other medical imaging procedures such as MRI, X-ray or ultrasound. The three dimensional computer model constructed and presented in this work shows its capability to understand the anatomy and the statics of the healthy female pelvic floor, the phenomena of some common pelvic floor disorders and the surgical treatment using prosthetic devices.

Chapter 4: Mathematical modeling of pelvic tissues

This thesis also deals with the homogenization of the nonlinear multi-constituent soft connective tissues to characterize their overall mechanical behavior on structural level.

Since, biological soft tissues are composed of elastin and collagen fibres embedded in the ground substance with varying amount of adipose tissue and smooth muscle, a pronounced anisotropy is associated with such tissues. In practice, it is not easy to obtain a stress-strain relation for all tissues which consider anisotropy, wherever possible every anisotropic nonlinear mechanical models are not readily available in such software. Also, sufficient histological studies and multi-axial deformation tests have not been performed with human tissue for all pelvic structures.

It is assumed that the pelvic structures are dominantly subjected to uniaxial tension during physiological pelvic movement and the required function is the load carrying and not the function of the organs, muscles and soft tissues themselves. Therefore, an isotropic non-linear hyperelastic formulation and the curve fit of tension tests in the direction of the dominating load direction can provide realistic representations of the load transfer in the pelvic floor. On this route we could base our analysis on a careful selection of recently published data of all tissues in the model. Therefore, numerical analysis presented in this work can be compared with studies of other research groups which used the same isotropic material models because all our improvements can be related to our most detailed representation of the geometry and the novel inclusion of the fasciae.

Chapter 5: Anisotropic modeling of levator ani muscle

In this chapter of the thesis, relevance of an intact support of the anococcygeal ligament and perineal structures to maintain the diameters of the urogenital and rectal hiatus is discussed. Pelvic floor dysfunctions (PFDs) such as incontinence and prolapse are often observed with widened hiatus that can be associated with permanent functional damage of such support system and reduced muscle tone as a consequence of birth-related injury and ageing. Passive stretching of the skeletal levator ani muscle is modeled by implementing the fibre based anisotropic constitutive model developed by Humphrey and Yin in the open-source FE software *Code_Aster*. The numerical results are closer to the clinical MRI values than those obtained by using isotropic material models. This explains the emerging necessity of the anisotropic constitutive model for the skeletal pelvic muscle to enhance our ability to model and to predict PFDs.

Further studies addressing the neural excitation of the pelvic muscle and variations in the fibre contractility are required in the model to determine the absolute phenomena of the PFDs. An improved active muscle model has been proposed so that it can be used in the future to modify the muscle deformation results, which should be useful for clinical applications.

Chapter 6: Prosthetic implants to treat stress urinary incontinence

Some popular prosthetic meshes used for the repair of PFDs and abdominal hernia are characterized in this thesis using standard uniaxial tensile test. Experiments on dry meshes

and gelatin-mesh compound shows that polyvinylidene fluoride meshes with appropriate pore geometry, adequate stiffness lead to a mechanically biocompatible structure during complex physiological conditions compared to conventional polypropylene meshes. Since the immune response and repair functions in the body are so complicated, it is not adequate to describe the biocompatibility of a single material in relation to a single tissue surrogate gelatin. However, these tests constitute an important step towards the laboratory animal testing and clinical trials that will determine the biocompatibility of different meshes with variations in pore geometry, structure and material composition in a given application. Considering these shortcomings, the perfect mesh design should consider sufficient tensile strength, anisotropy/isotropy, elasticity, and provide the appropriate biomimetic environment to ensure cell survival and at the same time should preserve its porosity under strain.

The normal process of wound healing creates a combined reparative layer of implant and fat or connective tissue, which is assumed to be achieved from meshes with sufficient pore dimension and minimum surface area. Small pore sized mesh intensifies the fibrosis forming thicker scar tissue with poor or no fat cell penetration to the pore. Mechanical response of such heterogeneous neo-scar tissue hugely differs from the anisotropic recipient host tissue that may increase the risk of infection, chronic pain, complete removal of the implant from the body, and recurrence. Under extreme physiological movements and straining processes, higher tensile and shear stresses on the ingrown tissue develops, which increase the risk of postoperative complications such as mesh wrinkling and mesh erosion. Moreover, if mesh pores are heavily deformed and wrinkling of the mesh occurs (Fig. 6.5b and 6.6c), large stresses are developed at the edges of the interface (Fig. 6.6c). During this process, the implanted mesh may wrap the host tissue and comes in contact with the adjacent organs to irritate, degenerate and even lead to dysfunction of the organs.

Specimens, constructed during surgery by cutting the desired dimension out of a large flat sheet to repair the defects often leave free edges that get separate out when they are stretched. The fibers once pulled out of the knitted mesh can no longer maintain their flat shape and start to stress the tissue locally. Successive tearing further debonds the ingrown tissue and the implanted mesh fails to perform the intended task in the body, see Fig. 6.6b. Repeated loading and unloading during rest and straining damages the ingrown tissue, impairing the mechanical biocompatibility of the implantation and finally leads to recurring damage. Thus, adequate structural stability as shown in Fig. 6.6a, which preserves the porosity under strain is essential for the proper function of such textile structures in a tensile environment *in vivo*.

The common trend in clinical practice for the reconstructive surgery has been the use of monofilamentous, lightweight large porous mesh in order to reduce the foreign body reaction and to minimize the risk of complications. Soft meshes with an adequate textile construction preserve their effective porosity and show structural stability under mechanical strain and lead to reduced scar formation. However, compliant meshes with additive softer material are often associated with intense pore deformation reducing the effective porosity (CIRITSIS ET AL. [60], HORBACH ET AL. [123]). Therefore, a good compromise of the mesh stiffness (formstability), polymer type and pore size should be maintained.

Rigorous clinical trials of such meshes should be done with respect to the deposition of physiologically regenerated tissue, for example, fat with the amount of stromal and fibroblasts, percentage of apoptotic cells and degree of foreign body response to compare the effectiveness of the available implants. This not only improves the behavior of existing meshes but insights to search for biomaterials with perfect biocompatibility in order to develop the ideal textile implants which can mimic the biomechanical properties of the tissues.

Chapter 7: Numerical study of stress urinary incontinence

Stress urinary incontinence, one of the pelvic floor dysfunction is simulated using the three dimensional finite element model of the female pelvic floor. The model shows its capability to better understand the dynamics of the female pelvic floor and the phenomena of stress urinary incontinence. Results showed that the weakness of the heterogeneous network of the endopelvic fasciae genuinely causes the abnormal dislocation of the pelvic organs. The phenomena of the SUI are associated with the urethral hypermobility, downward and clockwise urinary bladder rotation, rotation of the urethral axis towards the horizontal position and greater levator plate angulation during physiological Valsalva manoeuvre which are observed in incontinent females.

The isotropic hyperelastic tissue behavior has been adopted due to lack of sufficient experimental data for each and every pelvic tissue. Histological studies and multi-axial deformation tests have not been performed for all pelvic tissues; only few specimens extracted either from humans or animals are tested in such way (BECKER AND DE VITA [20], MANOOGIAN ET AL. [186], TAN ET AL. [300], TOKAR ET AL. [302], YAO ET AL. [333]). We have started to identify orthotropic data with own tests of porcine intestine and could relate the local behavior with the specific function of the different sections of the organ. However, we have not found published data on the orthotropic behavior of all structures in the human pelvic floor.

Also, the required function considered in this thesis is the load carrying and not the function of the organs themselves. Therefore, a curve fit of tension tests in the direction of the dominating load direction with isotropic material laws can provide realistic representations of the load transfer in the pelvic floor. On this route we could base our analysis on a careful selection of recently published data of all organs in the model. Therefore, our analysis can be compared with studies of other research groups which used the same isotropic material models because all our improvements can be related to our most detailed representation of the geometry and the novel inclusion of the fasciae.

Almost all biological soft tissues are associated with pronounced anisotropy and is the main difficulty in the biomechanical modeling. We have also implemented the orthotropic hyperelastic Holzapfel, Gasser, Ogden (HGO) model (HOLZAPFEL ET AL. [121]) in *Code_Aster* which represents the effect of fibre orientation in the tissues and made some developments to overcome unphysical behavior which may occur with this material model (DUONG ET AL. [84]). Recently we could show that the orthotropic compressible behavior

of two mesh implants for hernia repair could be represented by the polyconvex Itskov material model (HORBACH ET AL. [123]). Further testing and implementation in the FEM code has been already started. Since, biaxial material data on human or animal pelvic tissues are not completely tested yet, our pelvic floor model could be adapted to orthotropic tissue behavior as soon as data becomes available.

In any case to represent the material behavior of biological soft tissue accurately, orthotropic constitutive equations must ensure numerical stability in computer simulation. To prove the existence of solutions of boundary-value problems, the strain energy function should satisfy the Legendre-Hadamard or ellipticity conditions MARSDEN AND HUGHES [190]. For example the proposed HGO model for two fiber families has been proven to be polyconvex and satisfies the ellipticity condition (BALL [14], BALZANI [15], HOLZAPFEL ET AL. [122], SCHRÖDER, NEFF, BALZANI [274]). This means that the HGO model is polyconvex with its elasticity tensor satisfying the Legendre-Hadamard condition which guarantees the material stability.

Chapter 8: Vaginal vault prolapse correction

Last but not the least, this thesis has also studied the repair of the vaginal cuff prolapse after hysterectomy using prosthetic mesh implants to examine the effectiveness of the sacrocolpopexy and pectopexy technique. Firstly, the vaginal cuff prolapse situation is simulated and verified with the MRI scan of a symptomatic patient. With weak support system modeled by reduced tissue stiffness, the organs descended significantly below the reference PCL line. Computational models of Y-shaped meshes from two manufacturers FEG textiltechnik mbH (DynaMesh[®]-PRS soft), Germany and Ethicon, USA (Gynemesh[®] and Ultrapro[®]) are tested to support the vaginal cuff. Numerical outcomes are compared with the clinical outcomes to investigate the capability of each implant set in order to stabilize the position of the vaginal cuff in the weakened pelvic floor. The apical prolapse correction using the DynaMesh[®]-PRS soft suspended from the S1 bone below promontory is found to provide better support to the vaginal cuff after hysterectomy than the Gynemesh[®] and the Ultrapro[®]. Furthermore, the urinary bladder and the urethral axis is well positioned (angle Ur is much lesser than 30°) which may be beneficial for patients with stress urinary incontinence if present.

Similarly, the pectopexy technique is investigated using FE simulations to compare its performance with the sacrocolpopexy. Pectopexy uses the lateral parts of the iliopectineal ligament (Cooper ligament) for a bilateral mesh fixation. It is assumed to be favorable for the prolapse repair in obese patients with good postoperative outcomes and zero restriction to the organ function by the implant. The pectopexy results are moderate compared to the sacrocolpopexy technique: the urethral axis is not greatly improved whereas the vaginal axis is re-oriented properly along its normal or healthy state due to the DynaMesh[®]-PRP soft mesh elasticity.

Outlook

Despite better outcomes, the findings from this thesis can be employed in the future to predict potential complications such as mesh exposure into the viscera, injuries, irritation or infection of adjacent organs in the pelvic and peritoneal space, mesh shrinkage, bowel obstruction and wrinkling from mechanical response of the prosthetic device. Similarly, this study can also be extended to investigate the use of compliant meshes, meshes with ineffective fiber knots and the use of excessively stiffer meshes which limit the movement of the pelvic organs resulting in dyspareunia and urinary/fecal dysfunction. These critical factors may lead to failures of the surgical treatment of apical prolapse and in some cases can put patients at risk for recurrence or prolapse in different compartments for which re-operation is required. Therefore, the presented computational model can be used to select the best possible surgery and to investigate and minimize the post-operative complications which defines the success of the prolapse repair after implantation of prosthetic meshes during (minimally invasive) surgery.

References

- [1] S.D. Abramowitch, A. Feola, Z. Jallah, and P.A. Moalli. Tissue mechanics, animal models, and pelvic organ prolapse: a review. *Eur. J. Obstet. Gynecol. Reprod. Biol.*, 144 Suppl 1:S146–S158, 2009. doi: 10.1016/j.ejogrb.2009.02.022.
- [2] C.Y. Akladios, D. Dautun, C. Saussine, J.J. Baldauf, C. Mathelin, A. Wattiez. Laparoscopic sacrocolpopexy for female genital organ prolapse: establishment of a learning curve. *Eur. J. Obstet. Gynecol. Reprod. Biol.*, 149(2):218–221, 2010. doi: 10.1016/j.ejogrb.2009.12.012.
- [3] D.I. Alaedeen, J. Lipman, D. Medalie, and M.J. Rosen. The single-staged approach to the surgical management of abdominal wall hernias in contaminated fields. *Hernia*, 11(1):41–45, 2007. doi: 10.1007/s10029-006-0164-5.
- [4] N. Alkhouli, J. Mansfield, E. Green, J. Bell, B. Knight, N. Liversedge, J.C. Tham, R. Welbourn, A.C. Shore, K. Kos, and C.P. Winlove. The mechanical properties of human adipose tissues and their relationships to the structure and composition of the extracellular matrix. *Am. J. Physiol. Endocrinol. Metab.*, 305(12):E1427–E1435, 2013. doi: 10.1152/ajpendo.00111.2013.
- [5] P.K. Amid. Classification of biomaterials and their related complications in abdominal wall hernia surgery. *Hernia*, 1(1):15–21, 1997. doi: 10.1007/BF02426382.
- [6] P.K. Amid. Shrinkage: fake or fact? *Meshes: benefits and risks*, V. Schumpelick, and L.M. Nyhus (eds.), Springer, Berlin, 2004.
- [7] J.M. Anderson. Inflammatory response to implants. *ASAIO Trans.*, 34(2):101–107, 1988.
- [8] J.M. Anderson, A. Rodriguez, and D.T. Chang. Foreign body reaction to biomaterials. *Semin. Immunol.*, 20(2):86–100, 2008. doi: 10.1016/j.smim.2007.11.004.
- [9] R. Anding, S. Latz, S. Müller, R. Kirschner-Hermanns. Complete extraperitoneal sacrocolpopexy with PVDF visible mesh implant. In 41st IUGA. Annual Meeting, 2016.
- [10] M.V. Anurov, S.M. Titkova, and A.P. Oettinger. Biomechanical compatibility of surgical mesh and fascia being reinforced: dependence of experimental hernia defect repair results on anisotropic surgical mesh positioning. *Hernia*, 16(2):199–210, 2012. doi: 10.1007/s10029-011-0877-y.
- [11] J.A. Ashton-Miller, and J.O.L. DeLancey. Functional anatomy of the female pelvic floor. *Ann. N. Y. Acad. Sci.*, 1101:266–296, 2007. doi: 10.1196/annals.1389.034.
- [12] D. d’Aulignac, J.A.C. Martins and E.B. Pires. Physical modeling of the pelvic floor muscles using shell elements. In Proceedings of *European Congress on Computational Methods in Applied Sciences and Engineering* P. Neittaanmäki, T. Rossi, S. Korotov, E. Oñate, J. Périaux and D. Knörzer (eds.), 2004.

-
- [13] A. Baktir, O. Dogru, M. Girgin, E. Aygen, B.H. Kanat, D.O. Dabak, and T. Kuloglu. The effects of different prosthetic materials on the formation of collagen types in incisional hernia. *Hernia*, 17(2):249–253, 2013. doi: 10.1007/s10029-012-0979-1.
- [14] J.M. Ball. Convexity conditions and existence theorems in non-linear elasticity. *Arch. Ration. Mech. Anal.*, 63(4):337–403, 1977.
- [15] D. Balzani. Polyconvex anisotropic energies and modeling of damage applied to arterial walls. *PhD thesis*, TU Darmstadt, 2006.
- [16] C. Banerjee, and K.G. Noé. Laparoscopic pectopexy: a new technique of prolapse surgery for obese patients. *Arch. Gynecol. Obstet.*, 284(3):631–635, 2011. doi: 10.1007/s00404-010-1687-7.
- [17] M. Barber. Contemporary views on female pelvic anatomy. *Cleve. Clin. J. Med.*, 72 Suppl 4:S3–S11, 2005. doi: 10.3949/ccjm.72.Suppl_4.S3.
- [18] M. Barber. Symptoms and outcome measures of pelvic organ prolapse. *Clin. Obstet. Gynecol.*, 48(3):648–661, 2005. doi: 10.1097/01.grf.0000170424.11993.73.
- [19] Y. Barlow and J. Willoughby. Pathophysiology of soft tissue repair. *Br. Med. Bull.*, 48(3):698–711, 1992.
- [20] W.R. Becker and R. De Vita. Biaxial mechanical properties of swine uterosacral and cardinal ligaments. *Biomech. Model. Mechanobiol.*, 14(3):549–560, 2015. doi: 10.1007/s10237-014-0621-5.
- [21] R. Bendavid, and M. Kux. Seromas. In *Abdominal Wall Hernias: Principles and Management*, R. Bendavid, J. Abrahamson, M.E. Arregui, J.B. Flament, and E.H. Phillips. Springer, New York, 2001.
- [22] B. Berglas and I.C. Rubin. Histologic study of the pelvic connective tissue. *Sug. Gynecol. Obstet.*, 97(3):277–289, 1953.
- [23] D. Beyersdorff, T. Schiemann, M. Taupitz, H. Kooijman, B. Hamm, and V. Nicolas. Sectional depiction of the pelvic floor by CT, MR imaging and sheet plastination: computer-aided correlation and 3D model. *Eur. Radiol.*, 11(4):659–664, 2001. doi: 10.1007/s003300000561.
- [24] A. Bhattarai, R. Frotscher, M.C. Sora, and M. Staat. A 3D finite element model of the female pelvic floor for the reconstruction of the urinary incontinence. In *Proceedings of XI World Congress on Computational Mechanics*. E. Oñate, J. Oliver, and A. Huerta, (eds.), 923–934, 2014.
- [25] A. Bhattarai, R. Frotscher, and M. Staat. Biomechanical study of the female pelvic floor dysfunction using the finite element method. In *Proceedings of YIC GACM III ECCOMMAS-VI GACM*. S. Elgeti and J. Simon, (eds.), 2015. URN: urn:nbn:de:hbz:82-rwth-2015-039806. <http://nbn-resolving.de/urn:nbn:de:hbz:82-rwth-2015-039806>.

-
- [26] A. Bhattarai, R. Frotscher, and M. Staat, 2015. Significance of fibre geometry on passive-active response of pelvic muscles to evaluate pelvic dysfunction. In Proceedings of *BioMedWomen-Clinical and BioEngineering for Womens Health*. R.N. Jorge, T. Mascarenhas, J. Duarte, I. Ramos, M.E. Costa, M. Figueiral, O. Pinho, S. Brandão, T. Da Roza, and J.M.R.S. Tavares, (eds.), CRC Press, Boca Raton: pp. 185–188, 2015.
- [27] A. Bhattarai, R. Frotscher, and M. Staat. Computational analysis of pelvic floor dysfunction. In *Womens Health and Biomechanics: Where Medicine and Engineering meet*, S. Brandão, T. Da Roza, I. Ramos, and T. Mascarenhas, (eds.), Springer, New York, 29:217–230, 2018. doi: 0.1007/978-3-319-71574-2_17.
- [28] A. Bhattarai, and M. Staat. Mechanics of the soft tissue reactions to different textile mesh implants. In *Biological, Physical and Technical Basics of Cell Engineering*, G.M. Artmann, A. Temiz Artmann, A.A. Zhubanova, I.E. Digel, (eds.), Springer, Singapore: 251–275, 2018. doi: 10.1007/978-981-10-7904-7_11.
- [29] A. Bhattarai and M. Staat. Modelling of soft connective tissues to investigate female pelvic floor dysfunctions. *Comp. Math. Methods. Med.*, 2018, Article ID 9518076: 16 pages, 2018. doi: 10.1155/2018/9518076.
- [30] A. Bhattarai, M. Jabbari, R. Anding and M. Staat. Surgical treatment of vaginal vault prolapse using different prosthetic mesh implants: a finite element analysis. *tm-Technisches Messen*, 85(5):331–342, 2018. doi: 10.1515/teme-2017-0115.
- [31] A. Bhattarai, and M. Staat. Pectopexy to repair vaginal vault prolapse: a finite element approach. In Proceedings of *15th International Symposium on Computer Methods in Biomechanics and Biomedical Engineering and 3rd Conference on Imaging and Visualization, CMBBE2018*. P.R. Fernandes, and J.M. Tavares, (eds.), Lisbon, Portugal, 26–29 March, 2018.
- [32] A. Bhattarai and M. Staat. A computational study of organ relocation after laparoscopic pectopexy to repair posthysterectomy vaginal vault prolapse. *Computer Methods in Biomechanics and Biomedical Engineering: Imaging & Visualization*, 2019, to appear.
- [33] D.E. Birk, J.M. Fitch, J.P. Babiartz, K.J. Doane, and T.F. Linsenmayer. Collagen fibrillogenesis in vitro: interaction of types I and V collagen regulates fibril diameter. *J. Cell. Sci.*, 95(Pt 4):649–657, 1990.
- [34] C. Bleiler, P.P. Castañeda and O. Röhrle. A homogenisation method for the multi-scale modelling of transversely isotropic skeletal muscle tissue. *PAMM. Proc. Appl. Math. Mech.*, 17(1):183–184, 2018. doi: 10.1002/pamm.201710061.
- [35] S.S. Blemker and S.L. Delp. Three-dimensional representation of complex muscle architectures and geometries. *Ann. Biomed. Eng.*, 33(5):661–673, 2005.

- [36] M. Böl and S. Reese. A new approach for the simulation of skeletal muscles using the tool of statistical mechanics. *Materialwiss. Werkst.*, 38(12):955–964, 2007. doi: 10.1002/mawe.200700225.
- [37] M.K. Boreham, R.T. Miller, J.I. Schaffer, and R.A. Word. Smooth muscle myosin heavy chain and caldesmon expression in the anterior vaginal wall of women with and without pelvic organ prolapse. *Am. J. Obstet. Gynecol.*, 185(4):944–952, 2001. doi: 10.1067/mob.2001.117342.
- [38] M.K. Boreham, C.Y. Wai, R.T. Miller, J.I. Schaffer, and R.A. Word. Morphometric analysis of smooth muscle in the anterior vaginal wall of women with pelvic organ prolapse. *Am. J. Obstet. Gynecol.*, 187(1):56–63, 2002.
- [39] S.H. Boyles, A.M. Weber, and L. Meyn. Procedures for pelvic organ prolapse in the United States. *Am. J. Obstet. Gynecol.*, 188(1):108–115, 2003. doi: 10.1067/mob.2003.101.
- [40] S. Brandão, M. Parente, T. Mascarenhas, A.R. da Silva, I. Ramos, and R.N. Jorge. Biomechanical study on the bladder neck and urethral positions: simulation of impairment of the pelvic ligaments. *J. Biomech.*, 48(2):217–223, 2015. doi: 10.1016/j.jbiomech.2014.11.045.
- [41] F.T. Brandt, F.R. Lorenzato, L.V. Nóbrega, C.D. Albuquerque, R. Falcão, A.A. and Júnior. Intra-abdominal pressure measurement during ultrasound assessment of women with stress urinary incontinence: a novel model. *Acta. Cir. Bras.*, 21(4): 237–241, 2006.
- [42] M. Brieu, P. Chantreau, J. Gillibert, L. de Landsheere, P. Lecomte, and M. Cosson. A nonlinear-elastic constitutive model for soft connective tissue based on a histologic description: application to female pelvic soft tissue. *J. Mech. Behav. Biomed. Mater.*, 58:65–74, 2016. doi: 10.1016/j.jmbbm.2015.09.023.
- [43] M. Brincat, C.F. Moniz, J.W. Studd, A.J. Darby, A. Magos, and D. Cooper. Sex hormones and skin collagen content in postmenopausal women. *Br. Med. J. (Clin. Res. Ed.)*, 58(6402):1337–1338, 1983.
- [44] C.N. Brown and J.G. Finch. Which mesh for hernia repair? *Ann. R. Coll. Surg. Engl.*, 92(4):272–278, 2010.
- [45] J.L. Buller, J.R. Thompson, G.W. Cundiff, L. Krueger Sullivan, M.A. Schön Ybarra, and A.E. Bent. Uterosacral ligament: description of anatomic relationships to optimize surgical safety. *Obstet. Gynecol.*, 97(6):873–879, 2001.
- [46] R.C. Bump and P.A. Norton. Epidemiology and natural history of pelvic floor dysfunction. *Obstet. Gynecol. Clin. North. Am.*, 25(4):723–746, 1998.
- [47] M.B. Bush, B. Liedl, F. Wagenlehner, and P.E.P. Petros. A finite element model validates an external mechanism for opening the urethral tube prior to micturition in the female. *World J. Urol.*, 33(8):1151–1157, 2015. doi: 10.1007/s00345-014-1419-x.

-
- [48] S.A. Butler-Manuel, L.D. Buttery, R.P. A'Hern, J.M. Polak, and D.P. Barton. Pelvic nerve plexus trauma at radical hysterectomy and simple hysterectomy: the nerve content of the uterine supporting ligaments. *Cancer*, 89(4):834–841, 2000.
- [49] L. Boyadzhyan, S.S. Raman, S. Raz. Role of static and dynamic MR imaging in surgical pelvic floor dysfunction. *Radiographics*, 28(4):949–967, 2008. doi: 10.1148/rg.284075139.
- [50] J.L. Calvo-Gallego, J. Martínez-Reina, and J. Domínguez. A polynomial hyperelastic model for the mixture of fat and glandular tissue in female breast. *Int. J. Numer. Method Biomed. Eng.*, 31(9):e02723, 2015. doi: 10.1002/cnm.2723.
- [51] R.M. Campbell. The anatomy and histology of the sacrouterine ligaments. *Am. J. Obstet. Gynecol.*, 59(1):1–12, 1950. doi: 10.1016/0002-9378(50)90334-6.
- [52] E.M. Casey. Physical characterization of surgical mesh after function in hernia repair. Master Thesis, Clemson University, South Carolina, 2015.
- [53] P. Chantereau, M. Brieu, M. Kammal, J. Farthmann, B. Gabriel, and M. Cosson. Mechanical properties of pelvic soft tissue of young women and impact of aging. *Int. Urogynecol. J.*, 25(11):1547–1553, 2014. doi: 10.1007/s00192-014-2439-1.
- [54] P. Chapuis, L. Bokey, M. Fahrner, G. Sinclair, and N. Bogduk. Mobilization of the rectum: anatomic concepts and the bookshelf revisited. *Dis. Colon. Rectum.*, 45(1): 1–8, 2002.
- [55] B.H. Chen, Y. Wen, H. Li, and M.L. Polan. Collagen metabolism and turnover in women with stress urinary incontinence and pelvic prolapse. *Int. Urogynecol. J. Pelvic Floor Dysfunct.*, 13(2):80–87, 2002. doi: 10.1007/s001920200020.
- [56] E.H. Chen, E. Grote, W. Mohler, and A. Vignery. Cell-cell fusion. *FEBS Letters*, 581(11):2181–2193, 2007. doi: 10.1016/j.febslet.2007.03.033.
- [57] L. Chen, Y. Hsu, J.A. Ashton-Miller, and J.O.L. DeLancey. Measurement of the pubic portion of the levator ani muscle in women with unilateral defects in 3-D models from MR images. *Int. J. Gynaecol. Obstet.*, 92(3):234–241, 2006. doi: 10.1016/j.ijgo.2005.12.001.
- [58] L. Chen, J.A. Ashton-Miller, and J.O.L. DeLancey. A 3D finite element model of anterior vaginal wall support to evaluate mechanisms underlying cystocele formation. *J. Biomech.*, 42(10):1371–1377, 2009. doi: 10.1016/j.jbiomech.2009.04.043.
- [59] C.J. Chuong, M. Ma, R.C. Eberhart, and P. Zimmern. Viscoelastic properties measurement of the prolapsed anterior vaginal wall: a patient-directed methodology. *Eur. J. Obstet. Gynecol. Reprod. Biol.*, 173:106–112, 2014. doi: 10.1016/j.ejogrb.2013.11.012.

- [60] A. Ciritsis, A.J. Horbach, M. Staat, C.K. Kuhl, and N.A. Kraemer. Porosity and tissue integration of elastic mesh implants evaluated in vitro and in vivo. *J. Biomed. Mater. Res. B Appl. Biomater.*, 106(2):827–833, 2018. doi: 10.1002/jbm.b.33877.
- [61] W.S. Cobb, J.M. Burns, R.D. Peindl, A.M. Carbonell, B.D. Matthews, K.W. Kercher, and B.T. Heniford. Textile analysis of heavyweight, midweight, and lightweight polypropylene mesh in a porcine ventral hernia model. *J. Surg. Res.*, 136(1):1–7, 2006.
- [62] W.S. Cobb, K.W. Kercher, and B.T. Heniford. The argument for lightweight polypropylene mesh in hernia repair. *Surg. Innov.*, 12(1):63–69, 2005.
- [63] W.S. Cobb, J.M. Burns, K.W. Kercher, B.D. Matthews, H.J. Norton, and B. Todd Heniford. Normal intraabdominal pressure in healthy adults. *J. Surg. Res.*, 129(2):231–235, 2005. doi: 10.1016/j.jss.2005.06.015.
- [64] E.E. Cole, P.B. Leu, A. Gomelsky, P. Revelo, H. Shappell, H.M. Scarpero, and R.R. Dmochowski. Histopathological evaluation of the uterosacral ligament: is this a dependable structure for pelvic reconstruction? *BJU Int.*, 97(2):345–348, 2006. doi: 10.1111/j.1464-410X.2005.05903.x.
- [65] J. Conze, K. Junge, and C. Weiss, M. Anurov, A. Oettinger, U. Klinge, V. Schumpelick. New polymer for intra-abdominal meshes-PVDF copolymer. *J. Biomed. Mater. Res. B Appl. Biomater.*, 87(2):321–328, 2008. doi: 10.1002/jbm.b.31106.
- [66] M.M. Corton. Anatomy of pelvic floor dysfunction. *Obstet. Gynecol. Clin. North. Am.*, 36(3):401–419, 2009. doi: 10.1016/j.ogc.2009.09.002.
- [67] M. Cosson, M. Boukerrou, S. Lacaze, E. Lambaudie, J. Fasel, H. Mesdagh, P. Lobry, A. Ego. A study of pelvic ligament strength. *Eur. J. Obstet. Gynecol. Reprod. Biol.*, 109(1):80–87, 2003.
- [68] S. Daftary, S. Chakravati. *Manual of Obstetrics*. Elsevier Health Sciences, 2011.
- [69] J.O.L. DeLancey. Anatomical aspects of vaginal eversion after hysterectomy. *Am. J. Obstet. Gynecol.*, 166(6 Pt 1):1717–1724, 1992.
- [70] J.O.L. DeLancey. Structural support of the urethra as it relates to stress urinary incontinence: the hammock hypothesis. *Am. J. Obstet. Gynecol.*, 170(6):1713–1720, 1994.
- [71] J.O.L. DeLancey. Functional anatomy of the female pelvis. In *Female Urology*, E.D. Kursh, and E.J. McGuire (eds.), 1st Edition, Lippincott, Philadelphia, 1994.
- [72] J.O.L. DeLancey. The pathophysiology of stress urinary incontinence in women and its implications for surgical treatment. *World. J. Urol.*, 15(5):268–274, 1997.

-
- [73] J.O.L. DeLancey. Structural anatomy of the posterior pelvic compartment as it relates to rectocele. *Am. J. Obstet. Gynecol.*, 180(4):815–823, 1999.
- [74] J.O.L. DeLancey, J.M. Miller, R. Kearney, D. Howard, P. Reddy, W. Umek, K.E. Guire, R.U. Margulies, and J.A. Ashton-Miller. Vaginal birth and de novo stress incontinence: relative contributions of urethral dysfunction and mobility. *Obstet. Gynecol.*, 110(2 Pt 1):354–362, 2007. doi: 10.1097/01.AOG.0000270120.60522.55.
- [75] N. Deligiannidis, I. Papavasiliou, K. Sapolidis, I. Kesisoglou, S. Papavramidis, and O. Gamvros. The use of three different mesh materials in the treatment of abdominal wall defects. *Hernia*, 6(2):51–55, 2002.
- [76] D.Y. Deng. Urinary incontinence in women. *Med. Clin. North Am.*, 95(1):101–109, 2011. doi: 10.1016/j.mcna.2010.08.022.
- [77] H.P. Dietz and B. Clarke. Prevalence of rectocele in young nulliparous women. *Aust. N. Z. J. Obstet. Gynaecol.*, 45(5):391–394, 2005. doi: 10.1111/j.1479-828X.2005.00454.x.
- [78] H.P. Dietz and V. Lanzarone. Does vaginal childbirth cause defects of the rectovaginal septum? *Int. Urogynecol. J.*, 52(3):574, 2005.
- [79] T. Dimpfl, C. Jaeger, W. Mueller-Felber, C. Anthuber, A. Hirsch, R. Brandmaier, and B. Schuessler. Myogenic changes of the levator ani muscle in premenopausal women: the impact of vaginal delivery and age. *Neurourol. Urodynam.*, 17(3):197–205, 1998.
- [80] A.C. Diokno. Incidence and prevalence of stress urinary incontinence. *Adv. Stud. Med.*, 3(8E):S824–S827, 2003.
- [81] J. Dixon, and J. Gosling. Histomorphology of the pelvic floor muscle. In *Pelvic Floor Re-education: Principles and Practice*, B. Schuessler, J. Laycock; P. Norton, and S. Stanton (eds.), 38th Edition, Springer-Verlag, New York, 1994.
- [82] S.J. Downing and O.D. Sherwood. The physiological role of relaxin in the pregnant rat. IV. The influence on cervical collagen and glycosaminoglycans. *Endocrinology*, 118(2):471–479, 1986. doi: 10.1210/endo-118-2-471.
- [83] M.T. Duong, N.H. Nguyen, T.N. Tran, R.H. Tolba, and M. Staat. Influence of refrigerated storage on tensile mechanical properties of liver and spleen. *Int. Biomech.*, 2(1):79–88, 2015. doi: 10.1080/23335432.2015.1049295.
- [84] M.T. Duong, N.H. Nguyen, and M. Staat. Physical response of hyperelastic models for composite materials and soft tissues. *Asia. Pac. J. Comput. Eng.*, 2(3):1–18, 2015. doi: 10.1186/s40540-015-0015-x.

- [85] M.T. Duong, V. Seifarth, A. Temiz-Artmann, M. Staat. Growth modelling promoting mechanical stimulation of smooth muscle cells of porcine tubular organs in a fibrin-PVDF scaffold. In *Biological, Physical and Technical Basics of Cell Engineering*, G.M. Artmann, A. Temiz Artmann, A.A. Zhubanova, I.E. Digel (Eds.), Springer Nature, Singapore, 2018. doi: 10.1007/978-981-10-7904-7_9.
- [86] K. Elenskaia, K. Haidvogel, C. Heidinger, D. Doerfler, W. Umek, and E. Hanzal. The greatest taboo: urinary incontinence as a source of shame and embarrassment. *Wien. Klin. Wochenschr.*, 123(19–20):607–610, 2011. doi: 10.1007/s00508-011-0013-0.
- [87] A. Ercoli, V. Delmas, F. Fanfani, P. Gadonneix, M. Ceccaroni, A. Fagotti, S. Mancuso, and G. Scambia. Terminologia Anatomica versus unofficial descriptions and nomenclature of the fasciae and ligaments of the female pelvis: a dissection-based comparative study. *Am. J. Obstet. Gynecol.*, 193(4):1565–1573, 2005. doi: 10.1016/j.ajog.2005.05.007.
- [88] C. Falconer, G. Ekman, A. Malmström, and U.I. Ulmsten. Decreased collagen synthesis in stress-incontinent women. *Obstet. Gynecol.*, 84(4):583–586, 1994.
- [89] B. Fata, W. Zhang, R. Amini, and M.S. Sacks. Insights into regional adaptations in the growing pulmonary artery using a meso-scale structural model: effects of ascending aorta impingement. *J. Biomech. Eng.*, 136(2):021009, 2014. doi: 10.1115/1.4026457.
- [90] FDA. Urogynecologic surgical mesh: update on the safety and effectiveness of transvaginal placement for pelvic organ prolapse. 2011.
- [91] FDA. Surgical mesh for the treatment of women with pelvic organ prolapse and stress urinary incontinence: FDA executive summary. 2011.
- [92] P. Feil and M. Sora. A 3D reconstruction model of the female pelvic floor by using plastinated cross sections. *Austin. J. Anat.*, 1(5):4, 2014.
- [93] A. Feola, P. Moalli, M. Alperin, R. Duerr, R.E. Gandley, and S. Abramowitch. Impact of pregnancy and vaginal delivery on the passive and active mechanics of the rat vagina. *Ann. Biomed. Eng.*, 39(1):549–558, 2011. doi: 10.1007/s10439-010-0153-9.
- [94] A. Feola, W. Barone, P. Moalli, and S. Abramowitch. Characterizing the ex vivo textile and structural properties of synthetic prolapse mesh products. *Int. Urogynecol. J.*, 24(4):559–564, 2013. doi: 10.1007/s00192-012-1901-1.
- [95] J.R. Fielding. Practical MR imaging of female pelvic floor weakness. *Radiographics*, 22(2):295–304, 2002. doi: 10.1148/radiographics.22.2.g02mr25295.
- [96] T. Fischer, R. Ladurner, A. Gangkofer, T. Mussack, M. Reiser, and A. Lienemann. Functional cine MRI of the abdomen for the assessment of implanted synthetic mesh in patients after incisional hernia repair: initial results. *Eur. Radiol.*, 17(12):3123–3129, 2007. doi: 10.1007/s00330-007-0678-y.

-
- [97] R. Fleischmajer, J.S. Perlish, R.E. Burgeson, F. Shaikh-Bahai, and R. Timpl. Type I and type III collagen interactions during fibrillogenesis. *Ann. N. Y. Acad. Sci.*, 580:161–175, 1990.
- [98] J.G. Fletcher, A.E. Bharucha, H. Siddiki. Dynamic MR Imaging of the pelvic floor. In *Imaging pelvic floor disorders*, J. Stoker, S.A. Taylor, J.O.L. DeLancey, (eds.), 2nd, Springer, 2008.
- [99] D.W. Friedman, C.D. Boyd, J.W. Mackenzie, P. Norton, R.M. Olson, and S.B. Deak. Regulation of collagen gene expression in keloids and hypertrophic scars. *J. Surg. Res.*, 55(2):214–222, 1993. doi: 10.1006/jsre.1993.1132.
- [100] H. Fritsch and H. Hötzing. Tomographical anatomy of the pelvis, visceral pelvic connective tissue, and its compartments. *Clin. Anat.*, 8(1):17–24, 1995. doi: 10.1002/ca.980080103.
- [101] R. Frotscher and M. Staat. Stresses produced by different textile mesh implants in a tissue equivalent. *BioNanoMaterials*, 15(1–2):25–30, 2014. doi: 10.1515/bnm-2014-0003.
- [102] Y.C. Fung. *Foundations of Solid Mechanics*. Prentice Hall, New Jersey 1965.
- [103] Y.C. Fung, K. Fronek, and P. Patitucci. Pseudoelasticity of arteries and the choice of its mathematical expression. *Am. J. Physiol.*, 237(5):H620–H631, 1979.
- [104] Y.C. Fung. *Biomechanics: Mechanical Properties of Living Tissues*. Springer-Verlag, New York, 1993.
- [105] M.I. Funt, J.D. Thompson, and H. Birch. Normal vaginal axis. *South. Med. J.*, 71(12):1534–1552, 1979. doi: 10.1097/00007611-197812000-00026.
- [106] B. Gabriel, D. Denschlag, H. Göbel, C. Fittkow, M. Werner, G. Gitsch, and D. Wattermann. Uterosacral ligament in postmenopausal women with or without pelvic organ prolapse. *Int. Urogynecol. J. Pelvic. Floor. Dysfunct.*, 16(6):475–479, 2005. doi: 10.1007/s00192-005-1294-5.
- [107] P. Gadonneix, A. Ercoli, D. Salet-Lizée, O. Cotelle, B. Bolner, M. Van Den Akker, and R. Villet. Laparoscopic sacrocolpopexy with two separate meshes along the anterior and posterior vaginal walls for multicompartiment pelvic organ prolapse. *J. Am. Assoc. Gynecol. Laprosc.*, 11(1):29–35, 2004.
- [108] M.N. El-Gharib, M.A. Farahat, and M. Daoud. POP-Q system and dynamic MRI in assessment of female genital prolapse. *OJOG.*, 3(2):239–242, 2013. doi: 10.4236/ojog.2013.32045.
- [109] G. Green. On the laws of reflection and refraction of light at the common surface of two non-crystallised media. *Trans. Cambridge Phil. Soc.*, 7:1–24, 1839.

-
- [110] G. Green. On the Propagation of Light in Crystallized Media. *Trans. Cambridge Phil. Soc.*, 7:121–140, 1841.
- [111] U. Göretzlehner and A. Müllen. PVDF as an implant material in urogynaecology. *Biomaterialien*, 8(S1):28–29, 2007.
- [112] V.L. Handa, H.K. Pannu, S. Siddique, R. Gutman, J. VanRooyen, and G. Cundiff. Architectural differences in the bony pelvis of women with and without pelvic floor disorders. *Obstet. Gynecol.*, 102(6):1283–1290, 2003.
- [113] N.L. Hansen, A. Barabasch, M. Distelmaier, A. Ciritsis, N. Kuehnert, J. Otto, J. Conze, U. Klinge, R.D. Hilgers, C.K. Kuhl, N.A. Kraemer. First in-human magnetic resonance visualization of surgical mesh implants for inguinal hernia treatment. *Invest. Radiol.*, 48(11):770–778, 2013. doi: 10.1097/RLI.0b013e31829806ce.
- [114] T. Heidlauf and O. Röhrle. A geometrical model of skeletal muscle. *PAMM. Proc. Appl. Math. Mech.*, 12:119–120, 2012. doi: 10.1002/pamm.201210050.
- [115] S.L. Hendrix, A. Clark, I. Nygaard, A. Aragaki, V. Barnabei, and A. McTiernan. Pelvic organ prolapse in the women’s health initiative: gravity and gravidity. *Am. J. Obstet. Gynecol.*, 186(6):1160–1166, 2002.
- [116] A.V. Hill. The maximum work and mechanical efficiency of human muscles, and their most economical speed. *J. Physiol.*, 56(1–2):19–41, 1992.
- [117] N. Hinata, K. Hieda, H. Sasaki, T. Kurokawa, H. Miyake, M. Fujisawa, G. Murakami, and M. Fujimiya. Nerves and fasciae in and around the paracolpium or paravaginal tissue: an immunohistochemical study using elderly donated cadavers. *Anat. Cell. Biol.*, 47(1):44–54, 2014. doi: 10.5115/acb.2014.47.1.44.
- [118] E. Hirata, H. Fujiwara, S. Hayashi, A. Ohtsuka, S. Abe, G. Murakami, and Y. Kudo. Intergender differences in histological architecture of the fascia pelvis parietalis: a cadaveric study. *Clin. Anat.*, 24(4):469–477, 2011. doi: 10.1002/ca.21042.
- [119] Y. Hsu and J.O.L. DeLancey. Functional anatomy and pathophysiology of pelvic organ prolapse. In *Female Urology*, 3rd Edition, Elsevier, Philadelphia, 2008.
- [120] G.A. Holzapfel. Biomechanics of soft tissue. In *The Handbook of Materials Behavior Models*, J. Lemaitre (eds.), III Edition, Academic Press, Boston, 1994.
- [121] G.A. Holzapfel, T.C. Gasser, and R.W. Ogden. A new constitutive framework for arterial wall mechanics and a comparative study of material models. *J. Elasticity.*, 61(1–3):1–48, 2000.
- [122] G.A. Holzapfel, T.C. Gasser, and R.W. Ogden. Comparison of a multi/layer structural model for arterial walls with a Fung/type model, and issues of material stability. *J. Biomech. Eng.*, 126(2):264–275, 2004.

-
- [123] A.J. Horbach, M.T. Duong, and M. Staat. Modelling of compressible and orthotropic mesh implants based on optical stretch deformation measurement. *J. Mech. Behav. Biomed. Mater.*, 74:400–410, 2017. doi: 10.1016/j.jmbbm.2017.06.012.
- [124] D. Howard, J.M. Miller, J.O.L. DeLancey, J.A. Ashton-Miller. Differential effects of cough, valsalva, and continence status on vesical neck movement. *Obstet. Gynecol.*, 95(4):535–540, 2000.
- [125] L. Hoyte, L. Schierlitz, K. Zou, G. Flesh, and J.R. Fielding. Two-and 3-dimensional MRI comparison of levator ani structure, volume, and integrity in women with stress incontinence and prolapse. *Am. J. Obstet. Gynecol.*, 185(1):11–19, 2001. doi: 10.1067/mob.2001.116365.
- [126] D. Hull. *An introduction to composite materials*. Cambridge University Press, 1981.
- [127] J.D. Humphrey and F.C. Yin. On constitutive relations and finite deformations of passive cardiac tissue: I. A pseudostrain-energy function. *J. Biomech. Eng.*, 109(4): 298–304, 1987.
- [128] J.D. Humphrey. *Cardiovascular Solid Mechanics; Cells, Tissues, and Organs*. Springer, New York, 2002.
- [129] T. Hurme, H. Kalimo, M. Sandberg, M. Lehto, and E. Vuorio. Localization of type I and III collagen and fibronectin production in injured gastrocnemius muscle. *Lab. Invest.*, 64(1):76–84, 1991.
- [130] L.M. Irvine and R.W. Shaw. The effects of patient obesity in gynaecological practice. *Curr. Opin. Obstet. Gynecol.*, 13(3):179–184, 2003. doi: 10.1016/S0957-5847(03)00005-2.
- [131] R. Iwanaga, D.J. Orlicky, J. Arnett, M.K. Guess, K.J. Hurt, and K.A. Connell. Comparative histology of mouse, rat, and human pelvic ligaments. *Int. Urogynecol. J.*, 27(11):1697–1704, 2016. doi: 10.1007/s00192-016-3008-6.
- [132] S.R. Jackson, N.C. Avery, J.F. Tarlton, S.D. Eckford, P. Abrams, and A.J. Bailey. Changes in metabolism of collagen in genitourinary prolapse. *Lancet.*, 347(9016): 1658–1661, 1996.
- [133] J.S. Jameson, Y.W. Chia, M.A. Kamm, C.T. Speakman, Y.H. Chye, and M.M. Henry. Effect of age, sex and parity on anorectal function. *Br. J. Surg.*, 81(11):1689–1692, 1994.
- [134] S. Janda, F.C. van der Helm, and S.B. de Blok. Measuring morphological parameters of the pelvic floor for finite element modelling purposes. *J. Biomech.*, 36(6):749–757, 2003.
- [135] S. Janda. *Biomechanics of the Pelvic Floor Musculature*. PhD Thesis, Delft University of Technology, 2006.

- [136] T.N.A. Jeffcoate and H. Roberts. Stress incontinence of urine. *BJOG.*, 59(5):685–697, 1952. doi: 10.1111/j.1471-0528.1952.tb14748.x.
- [137] J. Jerabek, T. Novotny, K. Vesely, J. Cagas, V. Jedlicka, P. Vlcek, and I. Capov. Evaluation of three purely polypropylene meshes of different pore sizes in an onlay position in a New Zealand white rabbit model. *Hernia*, 18(6):855–864, 2014. doi: 10.1007/s10029-014-1278-9.
- [138] D. Jing, J.A. Ashton-Miller, and J.O.L. DeLancey. A subject-specific anisotropic viscohyperelastic finite element model of female pelvic floor stress and strain during the second stage of labor. *J. Biomech.*, 45(3):455–460, 2012. doi: 10.1016/j.jbiomech.2011.12.002.
- [139] N.H. Reay Jones, J.C. Healy, L.J. King, S. Saini, S. Shousha, and T.G. Allen-Mersh. Pelvic connective tissue resilience decreases with vaginal delivery, menopause and uterine prolapse. *Br. J. Surg.*, 90(4):466–472, 2003. doi: 10.1002/bjs.4065.
- [140] K. Junge, U. Klinge, R. Rosch, P.R. Mertens, J. Kirch, B. Klosterhalfen, P. Lynen, and V. Schumpelick. Decreased collagen type I/III ratio in patients with recurring hernia after implantation of alloplastic prostheses. *Langenbeck's Arch Surg*, 389(1):17–22, 2004. doi: 10.1007/s00423-003-0429-8.
- [141] K. Junge, M. Binnebösel, R. Rosch, M. Jansen, D. Kämmer, J. Otto, V. Schumpelick, and U. Klinge. Adhesion formation of a polyvinylidene fluoride/polypropylene mesh for intra-abdominal placement in a rodent animal model. *Surg. Endosc.*, 23(2):327–333, 2009. doi: 10.1007/s00464-008-9923-y.
- [142] K. Junge, M. Binnebösel, K.T. von Trotha, R. Rosch, U. Klinge, U.P. Neumann, and P. Lynen Jansen. Mesh biocompatibility: effects of cellular inflammation and tissue remodelling. *Langenbecks Arch. Surg.*, 397(2):255–270, 2012. doi: 10.1007/s00423-011-0780-0.
- [143] M.A. Kahn, and S.L. Stanton. Posterior vaginal wall prolapse and its management. *Contemp. Rev. Obstet. and Gynaecol.*, 9:303–310, 1997.
- [144] A.R. Kane and C.W. Nager. Midurethral slings for stress urinary incontinence. *Clin. Obstet. Gynecol.*, 51(1):124–135, 2008. doi: 10.1097/GRF.0b013e318161e687.
- [145] K. Kannan, A. McConnell, M. McLeod, and A. Rane. Microscopic alterations of vaginal tissue in women with pelvic organ prolapse. *J. Obstet. Gynaecol.*, 31(3):250–253, 2011. doi: 10.3109/01443615.2011.553690.
- [146] P.B. Kaplan, U. Usta, H.A. Inal, E. Tastekin, and B. Tokuc. Neuromuscular morphometry of the uterine ligaments and vaginal wall in women with pelvic organ prolapse. *Neurourol. Urodyn.*, 30(1):126–132, 2011. doi: 10.1002/nau.20972.
- [147] M. Kauer, V. Vuskovic, J. Dual, G. Szekeley, and M. Bajka. Inverse finite element characterization of soft tissues. *Med. Image. Anal.*, 6(3):275–287, 2002. doi: 10.1016/S1361-8415(02)00085-3.

-
- [148] M. Kirilova, S. Stoytchev, D. Pashkouleva, and V. Kavardzhikov. Experimental study of the mechanical properties of human abdominal fascia. *Med. Eng. Phys.*, 33(1):1–6, 2011. doi: 10.1016/j.medengphy.2010.07.017.
- [149] U. Klinge and B. Klosterhalfen. Modified classification of surgical meshes for hernia repair based on the analysis of 1,000 explanted meshes. *Hernia*, 16(3):251–258, 2012. doi: 10.1007/s10029-012-0913-6.
- [150] U. Klinge, B. Klosterhalfen, M. Müller, A.P. Ottinger, and V. Schumpelick. Shrinking of polypropylene mesh in vivo: an experimental study in dogs. *Eur J. Surg.*, 164(12):965–969, 1998. doi: 10.1080/110241598750005156.
- [151] U. Klinge, H. Zheng, Z.Y. Si, V. Schumpelick, R.S. Bhardwaj, and B. Klosterhalfen. Synthesis of type I and III collagen, expression of fibronectin and matrix metalloproteinases-1 and -13 in hernial sac of patients with inguinal hernia. *Int. J. Surg. Investig.*, 1(3):219–227, 1999.
- [152] U. Klinge, Z.Y. Si, H. Zheng, V. Schumpelick, R.S. Bhardwaj, and B. Klosterhalfen. Collagen I/III and matrix metalloproteinases (MMP) 1 and 13 in the fascia of patients with incisional hernias. *J. Invest. Surg.*, 14(1):47–54, 2001.
- [153] U. Klinge, B. Klosterhalfen, V. Birkenhauer, K. Junge, J. Conze, and V. Schumpelick. Impact of polymer pore size on the interface scar formation in a rat model. *J. Surg. Res.*, 103(2):208–214, 2002.
- [154] U. Klinge, M. Binnebosel, and S. Kuschel, and B. Schuessler. Demands and properties of alloplastic implants for the treatment of stress urinary incontinence. *Expert. Rev. Med. Devices.*, 4(3):349–359, 2007.
- [155] U. Klinge, J.K. Park, and B. Klosterhalfen. The ideal mesh? *Pathobiology*, 80(4):169–175, 2013. doi: 10.1159/000348446.
- [156] W. Klingler, M. Velders, K. Hoppe, M. Pedro, and R. Schleip. Clinical relevance of fascial tissue and dysfunctions. *Curr. Pain. Headache. Rep.*, 18(8):439, 2013. doi: 10.1007/s11916-014-0439-y.
- [157] C.D. Klink, K. Junge, M. Binnebösel, H.P. Alizai, J. Otto, U.P. Neumann, and U. Klinge. Comparison of long-term biocompatibility of PVDF and PP meshes. *J. Invest. Surg.*, 24(6):292–299, 2011. doi: 10.3109/08941939.2011.589883.
- [158] B. Klosterhalfen, U. Klinge, and V. Schumpelick. Functional and morphological evaluation of different polypropylene-mesh modifications for abdominal wall repair. *Biomaterials.*, 19(24):2235–2246, 1998.
- [159] B. Klosterhalfen, K. Junge, and U. Klinge. The lightweight and large porous mesh concept for hernia repair. *Expert. Rev. Med. Devices.*, 2(1):103–117, 2005. doi: 10.1586/17434440.2.1.103.

- [160] K.M. Knight, P.A. Moalli, A. Nolfi, S. Palcsey, W.R. Barone, and S.D. Abramowitch. Impact of parity on ewe vaginal mechanical properties relative to the non-human primate and rodent. *Int. Urogynecol. J.*, 27(8):1255–1263, 2016. doi: 10.1007/s00192-016-2963-2.
- [161] A. Kökçü, F. Yanik, and M. Cetinkaya, T. Alper, B. Kandemir, and E. Malatyalioglu. Histopathological evaluation of the connective tissue of the vaginal fascia and the uterine ligaments in women with and without pelvic relaxation. *Arch. Gynecol. Obstet.*, 266(2):75–78, 2002.
- [162] A. Kondo, M. Narushima, Y. Yoshikawa, and H. Hayashi. Pelvic fascia strength in women with stress urinary incontinence in comparison with those who are continent. *Neurourol. Urodyn.*, 13(5):507–513, 1994.
- [163] K.E. Krantz. The gross and microscopic anatomy of the human vagina. *Ann. N. Y. Acad. Sci.*, 83:89–104, 1959.
- [164] L. Krofta, L. Havelková, I. Urbánková, M. Krčmář, L. Hynčík, and J. Feyereisl. Finite element model focused on stress distribution in the levator ani muscle during vaginal delivery. *Int. Urogynecol. J.*, 28(2):275–284, 2017. doi: 10.1007/s00192-016-3126-1.
- [165] E. Kröner. Allgemeine Kontinuumstheorie der Versetzungen und Eigenspannungen. *Arch. Rational Mech. Anal.*, 4:273–334, 1960. doi: 10.1007/BF00281393.
- [166] G. Lamblin, O. Mayeur, G. Giraudet, J.E. dit Gautier, G. Chene, M. Brieu, C. Rubod, and M. Cosson. Pathophysiological aspects of cystocele with a 3D finite elements model. *Arch. Gynecol. Obstet.*, 294(5):983–989, 2016. doi: 10.1007/s00404-016-4150-6.
- [167] Y. Lanir. Structure-strength relations in mammalian tendon. *Biophys. J.*, 24(2): 541–554, 1978. doi: 10.1016/S0006-3495(78)85400-9.
- [168] M.C. Lapitan and P.L. Chye. The epidemiology of overactive bladder among females in Asia: a questionnaire survey. *Int. Urogynecol. J. Pelvic Floor. Dysfunct.*, 12(4): 226–231, 2001.
- [169] G. Laroche, Y. Marois, E. Schwarz, R. Guidoin, M.W. King, E. Pâris, and Y. Douville. Polyvinylidene fluoride monofilament sutures: can they be used safely for long-term anastomoses in the thoracic aorta? *Artif. Organs.*, 19(11):1190–1199, 1995.
- [170] J.R. Larrieux, and S. Balgobin. Effect of anatomic urethral length on the correlation between the Q-tip test and descent at point Aa of the POP-Q system. *Int. Urogynecol. J. Pelvic Floor Dysfunct.*, 19(2):273–276, 2008. doi: 10.1007/s00192-007-0429-2.

-
- [171] G.E. Leber, J.L. Garb, A.I. Alexander, and W.P. Reed. Long-term complications associated with prosthetic repair of incisional hernias. *Arch. Surg.*, 133(4):378–382, 1998.
- [172] C.C. Liang, Y.L. Chang, S.D. Chang, and T.S. Lo. Y.K. Soong. Pessary test to predict postoperative urinary incontinence in women undergoing hysterectomy for prolapse. *Obstet. Gynecol.*, 104(4):795–800, 2004. doi: 10.1097/01.AOG.0000140689.90131.01.
- [173] R. Liang, S. Abramowitch, K. Knight, S. Palcsey, A. Nolfi, A. Feola, S. Stein, and P.A. Moalli. Vaginal degeneration following implantation of synthetic mesh with increased stiffness. *BJOG.*, 120(2):233–243, 2013. doi: 10.1111/1471-0528.12085.
- [174] A. Liapis, P. Bakas, A. Pafiti, M. Frangos-Plemenos, N. Arnoyannaki, and G. Creatsas. Changes of collagen type III in female patients with genuine stress incontinence and pelvic floor prolapse. *Eur. J. Obstet. Gynecol. Reprod. Biol.*, 97(1):76–79, 2001.
- [175] Y.S. Lien, G.D. Chen, and S.C. Ng. Prevalence of and risk factors for pelvic organ prolapse and lower urinary tract symptoms among women in rural Nepal. *Int. J. Gynaecol. Obstet.*, 119(2):183–188, 2012. doi: 10.1016/j.ijgo.2012.05.031.
- [176] S.Y. Lin, Y.T. Tee, S.C. Ng, H. Chang, P. Lin, and G.D. Chen. Changes in the extracellular matrix in the anterior vagina of women with or without prolapse. *Int. Urogynecol. J. Pelvic Floor Dysfunct.*, 18(1):43–48, 2007. doi: 10.1007/s00192-006-0090-1.
- [177] Y.H. Lin, G. Liu, M. Li, N. Xiao, and F. Daneshgari. Recovery of continence function following simulated birth trauma involves repair of muscle and nerves in the urethra in the female mouse. *Eur. Urol.*, 57(3):506–512, 2010. doi: 10.1016/j.eururo.2009.03.020.
- [178] K.M. Luber, S. Boero, and J.Y. Choe. The demographics of pelvic floor disorders: current observations and future projections. *Am. J. Obstet. Gynecol.*, 184(7):1496–1501, 2001.
- [179] J. Luo, L. Chen, D.E. Fenner, J.A. Ashton-Miller, and J.O.L. DeLancey. A multi-compartment 3-D finite element model of rectocele and its interaction with cystocele. *J. Biomech.*, 48(9):1580–1586, 2015. doi: 10.1016/j.jbiomech.2015.02.041.
- [180] A.H. MacLennan, A.W. Taylor, D.H. Wilson, and D. Wilson. The prevalence of pelvic floor disorders and their relationship to gender, age, parity and mode of delivery. *BJOG.*, 107(12):1460–1470, 2000.
- [181] K.J. Macura, R.R. Genadry, D.A. Bluemke. MR imaging of the female urethra and supporting ligaments in assessment of urinary incontinence: spectrum of abnormalities. *Radiographics*, 26(4):1135–1149, 2006. doi: 10.1148/rp.264055133.
- [182] S. Madill. Biomechanical environment of the pelvic floor. In *Biomechanics of the Female Pelvic Floor*, L. Hoyte, and M. Damaser, (eds.), :239–255, 2006.

- [183] M. Maeta, K. Uno, and R. Saito. The potential of a plastination specimen for temporal bone surgery. *Auris. Nasus. Larynx.*, 30(4):413–416, 2003. doi: 10.1016/S0385-8146(03)00089-0.
- [184] C. Maher, B. Feiner, K. Baessler, C. Schmid. Surgical management of pelvic organ prolapse in women. *Cochrane Database Syst Rev.*, 30(4):CD004014, 2013. doi: 10.1002/14651858.CD004014.pub5.
- [185] J. Maigne. Treatment strategies for coccydynia. In *Musculoskeletal Science in Practice*, 12th International Congress of FIMM), 1998.
- [186] S.J. Manoogian, C. McNally, J.D. Stitzel, and S.M. Duma. Dynamic biaxial tissue properties of pregnant porcine uterine tissue. *Stapp. Car. Crash. J.*, 52:167–185, 2008.
- [187] J. Mant, R. Painter, and M. Vessey. Epidemiology of genital prolapse: observations from the oxford family planning association study. *Br. J. Obstet. Gynaecol.*, 104(5): 579–585, 1997.
- [188] R.U. Margulies, C. Lewicky-Gaupp, D.E. Fenner, E.J. McGuire, J.Q. Clemens, and J.O.L. DeLancey. Complications requiring reoperation following vaginal mesh kit procedures for prolapse. *Am. J. Obstet. Gynecol.*, 199(6):678.e1–678.e4, 2008. doi: 10.1016/j.ajog.2008.07.049.
- [189] A.D. Markland, H.E. Richter, C.W. Fwu, P. Eggers, and J.W. Kusek. Prevalence and trends of urinary incontinence in adults in the United States. *J. Urol.*, 186(2): 589–593, 2011. doi: 10.1016/j.juro.2011.03.114.
- [190] J.E. Marsden, and T.J.R. Hughes. *Mathematical foundations of elasticity*. Dover, New York, 1983.
- [191] J.A.C. Martins, E.B. Pires, R. Salvado, and P.B. Dinis. A numerical model of passive and active behavior of skeletal muscles. *Comput. Methods. Appl. Mech. Engrg.*, 151 (3–4), 1998. doi: 10.1016/S0045-7825(97)00162-X.
- [192] P.A. Martins, A.L. Filho, A.M. Fonseca, A. Santos, L. Santos, T. Mascarenhas, R.M. Jorge, and A.J. Ferreira. Uniaxial mechanical behavior of the human female bladder. *Int. Urogynecol. J.*, 22(8):991–995, 2011. doi: 10.1007/s00192-011-1409-0.
- [193] P. Martins, A.L. Silva-Filho, A.M. Fonseca, A. Santos, L. Santos, T. Mascarenhas, and R.M. Jorge, and A.M. Ferreira. Strength of round and uterosacral ligaments: a biomechanical study. *Arch. Gynecol. Obstet.*, 287(2):313–318, 2013. doi: 10.1007/s00404-012-2564-3.
- [194] B.D. Matthews, B.L. Pratt, H.S. Pollinger, C.L. Backus, K.W. Kercher, R.F. Sing, and B.T. Heniford. Assessment of adhesion formation to intra-abdominal polypropylene mesh and polytetrafluoroethylene mesh. *J. Surg. Res.*, 114(2):126–132, 2003.

-
- [195] S.G. McLean, A. Su, and A.J. van den Bogert. Development and validation of a 3-D model to predict knee joint loading during dynamic movement. *J. Biomech. Eng.*, 125(6):864–874, 2003.
- [196] P.S. Milley and D.H. Nichols. A correlative investigation of the human rectovaginal septum. *Anat. Rec.*, 163(3):443–451, 1969. doi: 10.1002/ar.1091630307.
- [197] K. Misof, G. Rapp, and P. Fratzl. A new molecular model for collagen elasticity based on synchrotron X-ray scattering evidence. *Biophys. J.*, 72(3):1376–1381, 1997. doi: 10.1016/S0006-3495(97)78783-6.
- [198] P.A. Moalli, L.C. Talarico, V.W. Sung, W.L. Klingensmith, S.H. Shand, L.A. Meyn, and S.C. Watkins. Impact of menopause on collagen subtypes in the arcus tendineus fasciae pelvis. *Am. J. Obstet. Gynecol.*, 190(3):620–627, 2004. doi: 10.1016/j.ajog.2003.08.040.
- [199] P.A. Moalli, N.S. Howden, J.L. Lowder, J. Navarro, K.M. Debes, S.D. Abramowitch, and S.L. Woo. A rat model to study the structural properties of the vagina and its supportive tissues. *Am. J. Obstet. Gynecol.*, 192(1):80–88, 2005. doi: 10.1016/j.ajog.2004.07.008.
- [200] M. Mohamed, A. Elmoghrabi, W.R. Shepard, M. McCann. Delayed onset seroma formation 'opting out' at 5 years after ventral incisional hernia repair. *BMJ. Case Rep.*, 2016. doi: 10.1136/bcr-2016-215034.
- [201] R.M. Mollen, C.J. Van Larrhoven, and J.H. Kuijpers. Pathogenesis and management of rectoceles. *Semin. Colorectal. Surg.*, 7(3):192–196, 1996.
- [202] D.M. Morgan, J. Iyengar, and J.O.L. DeLancey. A technique to evaluate the thickness and density of nonvascular smooth muscle in the suburethral fibromuscular layer. *Am. J. Obstet. Gynecol.*, 188(5):1183–1185, 2003.
- [203] T. Mühl, M. Binnebösel, U. Klinge, and T. Goedderz. New objective measurement to characterize the porosity of textile implants. *J. Biomed. Mater. Res. B Appl. Biomater.*, 84(1):176–183, 2008. doi: 10.1002/jbm.b.30859.
- [204] H. Nagase, R. Visse, and G. Murphy. Structure and function of matrix metalloproteinases and TIMPs. *Cardiovasc. Res.*, 69(3):562–573, 2006. doi: 10.1016/j.cardiores.2005.12.002.
- [205] I. Nagata, G. Murakami, D. Suzuki, K. Furuya, M. Koyama, and A. Ohtsuka. Histological features of the rectovaginal septum in elderly women and a proposal for posterior vaginal defect repair. *Int. Urogynecol. J.*, 18(8):863–868, 2007. doi: 10.1007/s00192-006-0249-9.
- [206] N.H. Nguyen, M.T. Duong, T.N. Tran, P.T. Pham, O. Grottke, R. Tolba, and M. Staat. Influence of a freeze-thaw cycle on the stress-stretch curves of tissues of porcine abdominal organs. *J. Biomech.*, 45(14):2382–2386, 2012. doi: 10.1016/j.jbiomech.2012.07.008.

- [207] R.A.J. Nievelstein, S.G.F. Robben, and J.G. Blickman. Hepatobiliary and pancreatic imaging in children—techniques and an overview of non-neoplastic disease entities. *Pediatr. Radiol.*, 41(1):55–75, 2011. doi: 10.1007/s00247-010-1858-5.
- [208] C. Niyibizi, K. Kavalkovich, T. Yamaji, and S.L. Woo. Type V collagen is increased during rabbit medial collateral ligament healing. *Knee Surg. Sports Traumatol. Arthrosc.*, 8(5):281–285, 2000. doi: 10.1007/s001670000134.
- [209] K. Noakes. *Anatomically Realistic Finite Element Models of the Pelvic Floor and Anal Canal: towards Understanding the Mechanisms of Defaecation*. PhD Thesis, 2007.
- [210] K.F. Noakes, A.J. Pullan, I.P. Bissett, and L.K. Cheng. Subject specific finite elasticity simulations of the pelvic floor. *J. Biomech.*, 41(14):3060–3065, 2008. doi: 10.1016/j.jbiomech.2008.06.037.
- [211] C. Noble, N. Smulders, N.H. Green, R. Lewis, M.J. Carré, S.E. Franklin, S. MacNeil, and Z.A. Taylor. Creating a model of diseased artery damage and failure from healthy porcine aorta. *J. Mech. Behav. Biomed. Mater.*, 60:378–393, 2016. doi: 10.1016/j.jmbbm.2016.02.018.
- [212] K.G. Noé, S. Schiermeier, I. Alkatout, M. Anapolski. Laparoscopic pectopexy: a prospective, randomized, comparative clinical trial of standard laparoscopic sacral colpopocervicopexy with the new laparoscopic pectopexy—postoperative results and intermediate-term follow-up in a pilot study. *J. Endourol.*, 29(2):210–215, 2015. doi: 10.1089/end.2014.0413.
- [213] P.A. Norton, J.E. Baker, H.C. Sharp, and J.C. Warenski. Genitourinary prolapse and joint hypermobility in women. *Obstet. Gynecol.*, 85(2):225–228, 1995. doi: 10.1016/0029-7844(94)00386-R.
- [214] T.M. Oelrich. The striated urogenital sphincter muscle in the female. *Anat. Rec.*, 205(2):223–232, 1983. doi: 10.1002/ar.1092050213.
- [215] A.L. Olsen, V.J. Smith, J.O. Bergstrom, J.C. Colling, and A.L. Clark. Epidemiology of surgically managed pelvic organ prolapse and urinary incontinence. *Obstet. Gynecol.*, 89(4):501–506, 1997. doi: 10.1016/S0029-7844(97)00058-6.
- [216] F.F. Önoel, E. Kaya, O. Köse, S.Y. Onol. A novel technique for the management of advanced uterine/vault prolapse: extraperitoneal sacrocolpopexy. *Int. Urogynecol. J.*, 22(7):855–861, 2011. doi: 10.1007/s00192-011-1378-3.
- [217] S.B. Orenstein, E.R. Saberski, D.L. Kreutzer, and Y.W. Novitsky. Comparative analysis of histopathologic effects of synthetic meshes based on material, weight, and pore size in mice. *J. Surg. Res.*, 176(2):423–429, 2012. doi: 10.1016/j.jss.2011.09.031.
- [218] M. Otcenasek, V. Baca, L. Krofta L, and J. Feyereisl. Endopelvic fascia in women: shape and relation to parietal pelvic structures. *Obstet. Gynecol.*, 111(3):622–630, 2008. doi: 10.1097/AOG.0b013e3181649e5c.

-
- [219] J. Otto, E. Kaldenhoff, R. Kirschner-Hermanns, T. Mühl, and U. Klinge. Elongation of textile pelvic floor implants under load is related to complete loss of effective porosity, thereby favoring incorporation in scar plates. *J. Biomed. Mater. Res. A*, 102(4):1079–1084, 2014. doi: 10.1002/jbm.a.34767.
- [220] O. Ozdegirmenci, Y. Karslioglu, S. Dede, S. Karadeniz, A. Haberal, O. Gunhan, and B. Celasun. Smooth muscle fraction of the round ligament in women with pelvic organ prolapse: a computer-based morphometric analysis. *Int. Urogynecol. J. Pelvic Floor Dysfunct.*, 16(1):39–43, 2005. doi: 10.1007/s00192-004-1215-z.
- [221] M.G. Pandy, F.E. Zajac, E. Sim, and W.S. Levine. An optimal control model for maximum-height human jumping. *J. Biomech.*, 23(12):1185–1198, 1990.
- [222] A. Pans, A. Albert, C.M. Lapière, and B. Nusgens. Biochemical study of collagen in adult groin hernias. *J. Surg. Res.*, 95(2):107–113, 2001. doi: 10.1006/jsre.2000.6024.
- [223] M.P.L. Parente, R.M. Natal Jorge, T. Mascarenhas, A.A. Fernandes, and J.A.C. Martins. The influence of the material properties on the biomechanical behavior of the pelvic floor muscles during vaginal delivery. *J. Biomech.*, 42(9):1301–1306, 2009. doi: 10.1016/j.jbiomech.2009.03.011.
- [224] H. Patel, D.R. Ostergard, and G. Sternschuss. Polypropylene mesh and the host response. *Int. Urogynecol. J.*, 23(6):669–679, 2012. doi: 10.1007/s00192-012-1718-y.
- [225] M.P.M. Pato and P. Areias. Active and passive behaviors of soft tissues: pelvic floor muscles. *Commun. Numer. Meth. Engng.*, 26(6):667–680, 2009. doi: 10.1002/cnm.1351.
- [226] P. Shanthi, D.V. Francis, and J. Suganthi. Colour plastinationa valuable tool for medical education. *Journal of the Anatomical Society of India*, 64(2):152–154, 2015. doi: 10.1016/j.jasi.2015.10.009.
- [227] G.W. Pearsall, and V.L. Roberts. Passive mechanical properties of uterine muscle (myometrium) tested in vitro. *J. Biomech.*, 11(4):167–171, 173–176, 1978. doi: 10.1016/0021-9290(78)90009-X.
- [228] E. Peña, B. Calvo, M.A. Martínez, P. Martins, T. Mascarenhas, R.M. Jorge, A. Ferreira, and M. Doblaré. Experimental study and constitutive modeling of the viscoelastic mechanical properties of the human prolapsed vaginal tissue. *Biomech. Model Mechanobiol.*, 9(1):35–44, 2010. doi: 10.1007/s10237-009-0157-2.
- [229] T.J. Pence and A. Wineman. On some connections between equivalent single material and mixture theory models for fiber reinforced hyperelastic materials. *International Journal of Non-Linear Mechanics*, 47(2):285–292, 2012. doi: 10.1016/j.ijnonlinmec.2011.06.011.
- [230] Y. Peng, R. Khavari, N.A. Nakib, T.B. Boone, and Y. Zhang. Assessment of urethral support using MRI-derived computational modeling of the female pelvis. *Int. Urogynecol. J.*, 27(2):205–212, 2016. doi: 10.1007/s00192-015-2804-8.

- [231] C. Persu, C.R. Chapple, V. Cauni, S. Gutue. and P. Geavlete. Pelvic organ prolapse quantification system (POP-Q)-a new era in pelvic prolapse staging. *J. Med. Life.*, 4(1):75–81, 2011.
- [232] U.M. Peschers, G.N. Schaer, J.O.L. DeLancey, and B. Schuessler. Levator ani muscle function before and after childbirth. *Br. J. Obstet. Gynaecol.*, 104(9):1004–1008, 1997.
- [233] U.M. Peschers, G. Fanger, G.N. Schaer, D.B. Vodusek, J.O.L. DeLancey, B. Schuessler. Bladder neck mobility in continent nulliparous women. *BJOG.*, 108(3):320–324, 2001.
- [234] P.E.P. Petros and U.I. Ulmsten. An integral theory of female urinary incontinence. Experimental and clinical considerations. *Acta. Obstet. Gynecol. Scand.*, 153:7–31, 1990.
- [235] P.E.P. Petros, and U.I. Ulmsten. Pregnancy effects on the intravaginal sling operation. *Acta. Obstet. Gynecol. Scand.*, 69(S153):77–78, 1990. doi: 10.1111/j.1600-0412.1990.tb08038.x.
- [236] P.E.P. Petros and U.I. Ulmsten. Role of the pelvic floor in bladder neck opening and closure I: muscle forces. *Int. Urogynecol. J. Pelvic Floor Dysfunct.*, 8(2):74–80, 1997.
- [237] P.E.P. Petros. The pubourethral ligaments—an anatomical and histological study in the live patient. *Int. Urogynecol. J. Pelvic Floor Dysfunct.*, 9(3):154–157, 1998.
- [238] P.E.P. Petros. The Integral Theory. MD Thesis, University of Sydney, 2003.
- [239] P.E.P. Petros. *The Female Pelvic Floor Function, Dysfunction and Management According to the Integral Theory*. Springer, 2010.
- [240] P.E.P. Petros. The integral system. *Cent. European J. Urol.*, 64(3):110–119, 2011. doi: 10.5173/cej.2011.03.art1.
- [241] M.J. Poellmann, E.K. Chien, B.L. McFarlin, and A.J. Wagoner Johnson. Mechanical and structural changes of the rat cervix in late-stage pregnancy. *J. Mech. Behav. Biomed. Mater.*, 17:66–75, 2013. doi: 10.1016/j.jmbbm.2012.08.002.
- [242] J. Pollak and G.W. Davila. Rectocele repair: the gynecologic approach. *Clin. Colon. Rectal. Surg.*, 16(1):61–70, 2003.
- [243] A.S. Poobalan, J. Bruce, W.C. Smith, P.M. King, Z.H. Krukowski, and W.A. Chambers. A review of chronic pain after inguinal herniorrhaphy. *Clin. J. Pain.*, 19(1): 48–54, 2003.
- [244] S. Post, B. Weiss, M. Willer, T. Neufang, and D. Lorenz. Randomized clinical trial of lightweight composite mesh for Lichtenstein inguinal hernia repair. *Br. J. Surg.*, 91(1):44–48, 2004. doi: 10.1002/bjs.4387.

-
- [245] R. Pregazzi, A. Sartore, P. Bortoli, E. Grimaldi, L. Troiano, S. Guaschino. Perineal ultrasound evaluation of urethral angle and bladder neck mobility in women with stress urinary incontinence. *BJOG.*, 109(7):821–827, 2002.
- [246] N. Price, A. Slack, and S.R. Jackson. Laparoscopic sacrocolpopexy: an observational study of functional and anatomical outcomes. *Int. Urogynecol. J.*, 22(1):77–82, 2011. doi: 10.1007/s00192-010-1241-y.
- [247] M.R. Rajasekaran, Y. Jiang, V. Bhargava, R. Littlefield, A. Lee, R.L. Lieber, and R.K. Mittal. Length-tension relationship of the external anal sphincter muscle: implications for the anal canal function. *Am. J. Physiol. Gastrointest. Liver Physiol.*, 295(2):G367–G373, 2008. doi: 10.1152/ajpgi.00033.2008.
- [248] R. Ramanah, M.B. Berger, B.M. Parratte, and J.O.L. DeLancey. Anatomy and histology of apical support: a literature review concerning cardinal and uterosacral ligaments. *Int. Urogynecol. J.*, 23(11):1483–1494, 2012. doi: 10.1007/s00192-012-1819-7.
- [249] E. Ramasamy, O. Avci, B. Dorow, S.Y. Chong, L. Gizzi, G. Steidle, F. Schick and O. Röhrle. An efficient modelling-simulation-analysis workflow to investigate stump-socket interaction using patient-specific, three-dimensional, continuum-mechanical, finite element residual limb models. *Front. Bioeng. Biotechnol.*, 6:126, 2018. doi: 10.3389/fbioe.2018.00126.
- [250] R.L. Range and R.T. Woodburne. The gross and microscopic anatomy of the transverse cervical ligaments. *Am. J. Obstet. Gynecol.*, 90:460–467, 1964.
- [251] T. Rechberger, K. Postawski, J.A. Jakowicki, Z. Gunja-Smith, and J.F. Jr Woessner. Role of fascial collagen in stress urinary incontinence. *Am. J. Obstet. Gynecol.*, 179 (6 Pt 1):1511–1514, 1998.
- [252] C. Reisenauer, T. Shiozawa, M. Oppitz, C. Busch, A. Kirschniak, T. Fehm, and U. Drews. The role of smooth muscle in the pathogenesis of pelvic organ prolapse an immunohistochemical and morphometric analysis of the cervical third of the uterosacral ligament. *Int. Urogynecol. J. Pelvic Floor Dysfunct.*, 19(3):383–389, 2008. doi: 10.1007/s00192-007-0447-0.
- [253] J.V. Ricci, J.R. Lisa, C.H. Thom, and W.L. Kron. The relationship of the vagina to adjacent organs in reconstructive surgery: a histological study. *Am. J. Surg.*, 74 (4):387–410, 1947. doi: 10.1016/0002-9610(47)90131-1.
- [254] A.C. Richardson. The rectovaginal septum revisited: its relationship to rectocele and its importance in rectocele repair. *Clin. Obstet. Gynecol.*, 36(4):976–983, 1993.
- [255] B.M. Riederer. Plastination and its importance in teaching anatomy. Critical points for long-term preservation of human tissue. *J. Anat.*, 224(3):309–315, 2014. doi: 10.1111/joa.12056.

- [256] G. Rivaux, C. Rubod, B. Dedet, M. Brieu, B. Gabriel, and M. Cosson. Comparative analysis of pelvic ligaments: a biomechanical study. *Int. Urogynecol. J.*, 24(1):135–139, 2013. doi: 10.1007/s00192-012-1861-5.
- [257] R.S. Rivlin, and D.W. Saunders. Large elastic deformations of isotropic materials VII. Experiments on the deformation of rubber. *Philos. Trans. Royal Soc. London Series A*, 243(865):251–288, 1951.
- [258] M.R. Roach, and A.C. Burton. The reason for the shape of the distensibility curve of arteries. *Can. J. Biochem. Physiol.*, 35(8):681–690, 1957.
- [259] H. Roberts. Observations on micturition in the female. *BJOG.*, 60(5):621–631, 1953. doi: 10.1111/j.1471-0528.1953.tb07251.x.
- [260] L.J. Romanzi, D.C. Chaikin, and J.G. Blaivas. The effect of genital prolapse on voiding. *J Urol.*, 161(2):581–586, 1999.
- [261] G.O. Rosato. Rectocele and perineal hernias. In *Fundamentals of Anorectal Surgery*, D.E. Beck, and S.D. Wexner (eds.), WB Saunders, London, 1998.
- [262] J.W. Ross and M. Preston. Laparoscopic sacrocolpopexy for severe vaginal vault prolapse: five-year outcome. *J. Minim. Invasive Gynecol.*, 12(3):221–226, 2005. doi: 10.1016/j.jmig.2005.03.017.
- [263] T.D. Roza, S. Brandão, D. Oliveira, T. Mascarenhas, M. Parente, J.A. Duarte, and R.N. Jorge. Football practice and urinary incontinence: Relation between morphology, function and biomechanics. *J. Biomech.*, 48(9):1587–1592, 2015. doi: 10.1016/j.jbiomech.2015.03.013.
- [264] C. Rubod, P. Lecomte-Grosbras, M. Brieu, G. Giraudet, N. Betrouni, and M. Cosson. 3D simulation of pelvic system numerical simulation for a better understanding of the contribution of the uterine ligaments. *Int. Urogynecol. J.*, 24(12):2093–2098, 2013.
- [265] C. Rubod, M. Boukerrou, M. Brieu, P. Dubois, and M. Cosson. Biomechanical properties of vaginal tissue part 1: new experimental protocol. *J. Urol.*, 178(1):320–325, 2007. doi: 10.1016/j.juro.2007.03.040.
- [266] C. Rubod, M. Brieu, M. Cosson, G. Rivaux, J.C. Clay, L. de Landsheere, and B. Gabriel. Biomechanical properties of human pelvic organs. *Urology*, 79(4):968.e17–968.e22, 2012. doi: 10.1016/j.urology.2011.11.010.
- [267] G. Salamone, L. Licari, A. Agrusa, G. Romano, G. Cocorullo, and G. Gulotta. Deep seroma after incisional hernia repair. Case reports and review of the literature. *Ann. Ital. Chir.*, 86, 2015.
- [268] M. Sankat, D.N. Bhardwaj, S. Lalwani, R. Kumar, and R. Dhingra. Plastination of human lungs using silicon polymer (s-10). *Journal of the Anatomical Society of India*, 65:s24–s25, 2016.

-
- [269] S. Sarma, T. Ying, K.H. Moore. Long-term vaginal ring pessary use: discontinuation rates and adverse events. *BJOG.*, 116(13):1715–1721, 2009. doi: 10.1111/j.1471-0528.2009.02380.x.
- [270] H. Sasaki, N. Hinata, T. Kurokawa, and G. Murakami. Supportive tissues of the vagina with special reference to a fibrous skeleton in the perineum: a review. *OJOG.*, 4(3):144–157, 2003. doi: 10.4236/ojog.2014.43025.
- [271] F. Scali, M.E. Pontell, L.G. Nash, and D.E. Enix. Investigation of meningomyo-vertebral structures within the upper cervical epidural space: a sheet plastination study with clinical implications. *Spine J.*, 15(11):2417–2424, 2015. doi: 10.1016/j.spinee.2015.07.438.
- [272] H. Scheidbach, C. Tamme, A. Tannapfel, H. Lippert, and F. Köckerling. In vivo studies comparing the biocompatibility of various polypropylene meshes and their handling properties during endoscopic total extraperitoneal (TEP) patchplasty: an experimental study in pigs. *Surg. Endosc.*, 18(2):211–220, 2004. doi: 10.1007/s00464-003-8113-1.
- [273] J. Schröder, and P. Neff. Invariant formulation of hyperelastic transverse isotropy based on polyconvex free energy functions. *Int. J. Solids Struct.*, 40(2):401–445, 2003. doi: 10.1016/S0020-7683(02)00458-4.
- [274] J. Schröder, P. Neff, and D. Balzani. A variational approach for materially stable anisotropic hyperelasticity. *Int. J. Solids Struct.*, 42(15):4352–4371, 2005. doi: 10.1016/j.ijsolstr.2004.11.021.
- [275] P.D. Scott, K.L. Harold, R.O. Craft, and C.C. Roberts. Postoperative seroma deep to mesh after laparoscopic ventral hernia repair: computed tomography appearance and implications for treatment. *Radiol. Case Rep.*, 3(1):128, 2008. doi: 10.2484/rcr.v3i1.128.
- [276] A.D. Shah, N. Kohli, S.S. Rajan, and L. Hoyte. The age distribution, rates, and types of surgery for pelvic organ prolapse in the USA. *Int. Urogynecol. J. Pelvic. Floor Dysfunct.*, 19(3):421–428, 2008. doi: 10.1007/s00192-007-0457-y.
- [277] S. Shoshan. Wound healing. *Int. Rev. Connect. Tissue Res.*, 9:1–26, 1981.
- [278] M.D. Shoulders and R.T. Raines. Collagen structure and stability. *Annu. Rev. Biochem.*, 78:929–958, 2009. doi: 10.1146/annurev.biochem.77.032207.120833.
- [279] I.R. Silitonga, M.R.A. Sukarsa, L.R. Pohan, E. Armawan, and B. Handono. Perbandingan kepadatan kolagen ligamentum sakrouterina pada pasien dengan dan tanpa prolaps uteri. *MKB.*, 47(4):212–217, 2015.
- [280] M.E. Silva, D.A. Oliveira, T.H. Roza, S. Brandão, M.P. Parente, T. Mascarenhas, and R.N. Jorge. Study on the influence of the fetus head molding on the biomechanical behavior of the pelvic floor muscles, during vaginal delivery. *J. Biomech.*, 48(9):1600–1605, 2015. doi: 10.1016/j.jbiomech.2015.02.032.

- [281] J.C. Simo and T.J.R. Hughes. *Computational Inelasticity*. Springer-Verlag, 1997.
- [282] J.H. Sinclair, and C.C. Chamis. Fracture models in off-axis fiber composites. *Polymer Compos.*, 2(1):45–52, 1981. doi: 10.1002/pc.750020109.
- [283] F.J. Smith, C.D. Holman, R.E. Moorin, and N. Tsokos. Lifetime risk of undergoing surgery for pelvic organ prolapse. *Obstet. Gynecol.*, 116(5):1096–1100, 2010. doi: 10.1097/AOG.0b013e3181f73729.
- [284] S.J. Snooks, M. Setchell, M. Swash, and M.M. Henry. Injury to innervation of pelvic floor sphincter musculature in childbirth. *Lancet*, 2(8402):546–550, 1984.
- [285] R.W. Soames. Skeletal system. In *Grays Anatomy. The Anatomical Basis of Medicine and Surgery*, P.L. Williams, L.H. Bannister, M.M. Berry, P. Collins, M. Dyson, J.E. Dussek, and M.W.J. Ferguson (eds.), 38th Edition, Elsevier, Churchill Livingstone, 1995.
- [286] M.C. Sora, P.C. Brugger, and B. Strobl. Shrinkage during E12 plastination. *J. Int. Soc. Plastination.*, 17:23–27, 2002.
- [287] M.C. Sora. Epoxy plastination of biological tissue: E12 ultra-thin technique. *J. Int. Soc. Plastination.*, 22:40–45, 2007.
- [288] M.C. Sora and P. Cook. Epoxy plastination of biological tissue E12 technique. *J. Int. Soc. Plastination.*, 22:31–39, 2007.
- [289] T. Spirka, K. Kenton, L. Brubaker, and M.S. Damaser. Effect of material properties on predicted vesical pressure during a cough in a simplified computational model of the bladder and urethra. *Ann. Biomed. Eng.*, 41(1):185–194, 2013. doi: 10.1007/s10439-012-0637-x.
- [290] L.A. Spyrou, M. Agoras, and K. Danas. A homogenization model of the Voigt type for skeletal muscle. *J. Theor. Biol.*, 414:50–61, 2016. doi: 10.1016/j.jtbi.2016.11.018.
- [291] M. Staat, E. Trenz, P. Lohmann, R. Frotscher, U. Klinge, R. Tabaza, and R. Kirschner-Hermanns. New measurements to compare soft tissue anchoring systems in pelvic floor surgery. *J. Biomed. Mater. Res. B Appl. Biomater.*, 100(4):924–933, 2012. doi: 10.1002/jbm.b.32654.
- [292] T.A. Stein, G. Kaur, A. Summers, K.A. Larson, and J.O.L. DeLancey. Comparison of bony dimensions at the level of the pelvic floor in women with and without pelvic organ prolapse. *Am. J. Obstet. Gynecol.*, 200(3):241.e1–241.e5, 2009. doi: 10.1016/j.ajog.2008.10.040.
- [293] L.L. Subak, L.E. Waetjen, S. van den Eeden, D.H. Thom, E. Vittinghoff, and J.S. Brown. Cost of pelvic organ prolapse in the United States. *Obstet. Gynecol.*, 98(4):646–651, 2001.

-
- [294] S. Susmallian, G. Gewurtz, T. Ezri, and I. Charuzi. Seroma after laparoscopic repair of hernia with PTFE patch: is it really a complication? *Hernia*, 5(3):139–141, 2001.
- [295] S. Swift, P. Woodman, A. O’Boyle, M. Kahn, M. Valley, D. Bland, W. Wang, and J. Schaffer. Pelvic organ support study (POSST): The distribution, clinical definition, and epidemiologic condition of pelvic organ support defects. *Am. J. Obstet. Gynecol.*, 192(3):795–806, 2005. doi: 10.1016/j.ajog.2004.10.602.
- [296] E.H. Sze, J. Meranus, N. Kohli, J.R. Miklos, and M.M. Karram. Vaginal configuration on MRI after abdominal sacrocolpopexy and sacrospinous ligament suspension. *Int. Urogynecol. J. Pelvic Floor Dysfunct.*, 12(6):375–379, 2001.
- [297] P. Takacs, M. Gualtieri, M. Nassiri, K. Candiotti, and C.A. Medina. Vaginal smooth muscle cell apoptosis is increased in women with pelvic organ prolapse. *Int. Urogynecol. J. Pelvic Floor Dysfunct.*, 19(11):1559–1564, 2008. doi: 10.1007/s00192-008-0690-z.
- [298] I.L. Tan, J. Stoker, A.W. Zwamborn, K.A. Entius, J.J. Calame, and J.S. Laméris. Female pelvic floor: endovaginal MR imaging of normal anatomy. *Radiology*, 206(3):777–783, 1998. doi: 10.1148/radiology.206.3.9494501.
- [299] T. Tan, F.M. Davis, D.D. Gruber, J.C. Massengill, J.L. Robertson, and R. De Vita. Histo-mechanical properties of the swine cardinal and uterosacral ligaments. *J. Mech. Behav. Biomed. Mater.*, 42:129–137, 2015. doi: 10.1016/j.jmbbm.2014.11.018.
- [300] T. Tan, N.W. Cholewa, S.W. Case, R. De Vita. Micro-structural and biaxial creep properties of the swine uterosacralcardinal ligament complex. *Ann. Biomed. Eng.*, 41(11):3225–3237, 2016. doi: 10.1007/s10439-016-1661-z.
- [301] T. Tansatit, P. Apinuntrum, T. Phetudom, and P. Phanchart. New insights into the pelvic organ support framework. *Eur. J. Obstet. Gynecol. Reprod. Biol.*, 166(2): 221–225, 2013. doi: 10.1016/j.ejogrb.2012.10.038.
- [302] S. Tokar, A. Feola, P.A. Moalli, and S. Abramowitch. Characterizing the biaxial mechanical properties of vaginal maternal adaptations during pregnancy. In Proceedings of ASME. *Summer Bioengineering Conference*, Paper No. SBC2010-19394: 689–690, 2010. doi: 10.1115/SBC2010-19394.
- [303] P. Toozs-Hobson, K. Boos, L. Cardozo. Management of vaginal vault prolapse. *Br. J. Obstet. Gynaecol.*, 105(1):13–17, 1998.
- [304] L.R.G. Treolar. The elasticity and related properties of rubbers. *Reports on Progress in Physics*, 36(7), 1973.
- [305] C. Truesdell, and W. Noll. *The Non-Linear Field Theories of Mechanics*. In Handbuch der Physik, Vol. III/3. Springer-Verlag, 1965.

- [306] R. Tunn, J.O.L. DeLancey, and E.E. Quint. Visibility of pelvic organ support system structures in magnetic resonance images without an endovaginal coil. *Am. J. Obstet. Gynecol.*, 184(6):1156–1163, 2001. doi: 10.1067/mob.2001.112972.
- [307] E. Uhlenhuth, W.M. Wolfe, E.M. Smith, and E.B. Middleton. The rectogenital septum. *Surg. Gynecol. Obstet.*, 86:148–163, 1948.
- [308] N. Uldbjerg, U. Ulmsten, and G. Ekman. The ripening of the human uterine cervix in terms of connective tissue biochemistry. *Clin. Obstet. Gynecol.*, 26(1):14–26, 1983.
- [309] F.C. Usher and J.P. Gannon. Marlex mesh, a new plastic mesh for replacing tissue defects: I. Experimental studies. *AMA. Arch. Surg.*, 78(1):131–137, 1959.
- [310] M.D. Vardy, T.R. Gardner, F. Cosman, R.J. Scotti, M.S. Mikhail, A.O. Preiss-Bloom, J.K. Williams, J.M. Cline, and R. Lindsay. The effects of hormone replacement on the biomechanical properties of the uterosacral and round ligaments in the monkey model. *Am. J. Obstet. Gynecol.*, 192(5):1741–1751, 2005. doi: 10.1016/j.ajog.2004.10.639.
- [311] V. Viereck, M. Nebel, W. Bader, L. Harms, R. Lange, R. Hilgers, G. Emons. Role of bladder neck mobility and urethral closure pressure in predicting outcome of tension-free vaginal tape (TVT) procedure. *Ultrasound Obstet. Gynecol.*, 28(2): 214–220, 2006. doi: 10.1002/uog.2834.
- [312] J.Y. Vink, S. Qin, C.O. Brock, N.M. Zork, H.M. Feltovich, X. Chen, P. Urie, K.M. Myers, T.J. Hall, R. Wapner, J.K. Kitajewski, C.J. Shawber, and G. Gallos. A new paradigm for the role of smooth muscle cells in the human cervix. *Am. J. Obstet. Gynecol.*, 215(4):478.e1–478.e11, 2016. doi: 10.1016/j.ajog.2016.04.053.
- [313] W. Voigt. *Lehrbuch der kristallphysik (mit ausschluss der kristalloptik)*. B.G. Teubner, Leipzig, 1910.
- [314] G. von Hagens. Impregnation of soft biological specimens with thermosetting resins and elastomers. *Anat. Rec.*, 194(2):247–255, 1979. doi: 10.1002/ar.1091940206.
- [315] G. von Hagens. *Heidelberg Plastination Folder: Collection of Technical Leaflets of Plastination*. 2nd Edition, Springer, Heidelberg, 1986.
- [316] G. von Hagens, K. Tiedemann, and W. Kriz. The current potential of plastination. *Anat. Embryol. (Berl.)*, 175(4):411–421, 1987.
- [317] M. von Zeissl. Innervation of urinary bladder. *Arch. Ges. Physiol.*, 53:500, 1893.
- [318] D. Vu, B.T. Haylen, K. Tse, and A. Farnsworth. Surgical anatomy of the uterosacral ligament. *Int. Urogynecol. J.*, 21(9):1123–1128, 2010. doi: 10.1007/s00192-010-1147-8.
- [319] L. Wall, P. Norton, and J. Delancey. *Practical Urogynecology*. Williams and Wilkins, 1993.

-
- [320] A.M. Weber and H.E. Richter. Pelvic organ prolapse. *Obstet. Gynecol.*, 106(3): 615–634, 2005. doi: 10.1097/01.AOG.0000175832.13266.bb.
- [321] A.M. Weber and M.D. Walters. Anterior vaginal wall prolapse: review of anatomy and techniques of surgical repair. *Obstet. Gynecol.*, 89(2):311–318, 1997. doi: 10.1016/S0029-7844(96)00322-5.
- [322] R.J. Wenstrup, J.B. Florer, E.W. Brunskill, S.M. Bell, I. Chervoneva, and D.E. Birk. Type V collagen controls the initiation of collagen fibril assembly. *J. Biol. Chem.*, 279(51):53331–53337, 2004. doi: 10.1074/jbc.M409622200.
- [323] S.L. Wesnes, S. Hunskar, and G. Rortveit. Epidemiology of urinary incontinence in pregnancy and postpartum. *Urinary Incontinence*, A. Alhasso (eds.), InTech, Rijeka, 2012.
- [324] W.E. Whitehead, L. Borrud, P.S. Goode, S. Meikle, E.R. Mueller, A. Tuteja, A. Weidner, M. Weinstein, and W. Ye. Fecal incontinence in u.s. adults: epidemiology and risk factors. *Gastroenterology*, 137(2):512.e2–517.e2, 2009. doi: 10.1053/j.gastro.2009.04.054.
- [325] G.T. Williams and W.J. Williams. Granulomatous inflammation—a review. *J. Clin. Pathol.*, 36(7):723–733, 1983.
- [326] P.L. Williams, R. Warwick, M. Dyson, and L.H. Bannister. *Gray’s Anatomy*. 37th Edition, Churchill Livingstone, 1989.
- [327] C.J. Wilson, R.E. Clegg, D.I. Leavesley, and M.J. Percy. Mediation of biomaterial-cell interactions by adsorbed proteins: a review. *Tissue Eng.*, 11(1–2):1–18, 2005. doi: 10.1089/ten.2005.11.1.
- [328] R.T. Woodburne. *Essentials of Human Anatomy*. 4th Edition, Oxford University Press, New York, 1971.
- [329] J.M. Wu, S. Stinnett, R.A. Jackson, A. Jacoby, L.A. Learman, and M. Kuppermann. Prevalence and incidence of urinary incontinence in a diverse population of women with noncancerous gynecologic conditions. *Female Pelvic Med. Reconstr. Surg.*, 16(5):284–289, 2010. doi: 10.1097/SPV.0b013e3181ee6864.
- [330] Y. Yabuki, H. Sasaki, N. Hatakeyama, and G. Murakami. Discrepancies between classic anatomy and modern gynecologic surgery on pelvic connective tissue structure: harmonization of those concepts by collaborative cadaver dissection. *Am. J. Obstet. Gynecol.*, 193(1):7–15, 2005. doi: 10.1016/j.ajog.2005.02.108.
- [331] X. Yan, J.A. Kruger, P.M. Nielsen, and M.P. Nash. Effects of fetal head shape variation on the second stage of labour. *J. Biomech.*, 48(9):1593–1599, 2015. doi: 10.1016/j.jbiomech.2015.02.062.

- [332] A. Yang, J.L. Mostwin, N.B. Rosenshein, and E.A. Zerhouni. Pelvic floor descent in women: dynamic evaluation with fast MR imaging and cinematic display. *Radiology*, 179(1):25–33, 1991. doi: 10.1148/radiology.179.1.2006286.
- [333] W. Yao, K. Yoshida, M. Fernandez, J. Vink, R.J. Wapner, C.V. Ananth, M.L. Oyen, and K.M. Myers. Measuring the compressive viscoelastic mechanical properties of human cervical tissue using indentation. *J. Mech. Behav. Biomed. Mater.*, 34:18–26, 2014. doi: 10.1016/j.jmbbm.2014.01.016.
- [334] K. Yoshida, M. Mahendroo, J. Vink, R. Wapner, and K. Myers. Material properties of mouse cervical tissue in normal gestation. *Acta. Biomater.*, 36:195–209, 2016. doi: 10.1016/j.actbio.2016.03.005.
- [335] C.A. Yucesoy, B.H. Koopman, P.A. Huijig, and H.J. Grootenboer. Three-dimensional finite element modeling of skeletal muscle using a twodomain approach: linked fibre-matrix mesh model. *J. Biomech.*, 35(9):1253–1262, 2002.
- [336] R.F. Zacharin. The suspensory mechanism of the female urethra. *J. Anat.*, 97(Pt 3):423–427, 1963.
- [337] F.E. Zajac. Muscle and tendon: properties, models, scaling, and application to biomechanics and motor control. *Crit. Rev. Biomed. Eng.*, 17(4):359–410, 1989.
- [338] S. Zeinali-Davarani, M.J. Chow, R. Turcotte, and Y. Zhang. Characterization of biaxial mechanical behavior of porcine aorta under gradual elastin degradation. *Ann. Biomed. Eng.*, 41(7):1528–1538, 2013. doi: 10.1007/s10439-012-0733-y.
- [339] H. Zheng, Z. Si, R. Kasperk, R.S. Bhardwaj, V. Schumpelick, U. Klinge, and B. Klosterhalfen. Recurrent inguinal hernia: disease of the collagen matrix? *World J. Surg.*, 26(4):401–408, 2002. doi: 10.1007/s00268-001-0239-5.
- [340] R. Zimmerman. Surgery under scrutiny: What went wrong with vaginal mesh. *WBUR.*, 2011. <http://commonhealth.wbur.org/2011/11/surgery-under-scrutiny-what-went-wrong-with-vaginal-mesh>.

Der Lebenslauf ist in der Online-Version aus Gründen des Datenschutzes nicht enthalten.

In dieser Schriftenreihe bisher erschienene Berichte:

- Nr. 1 (2004) *Ein Modell zur Beschreibung finiter anisotroper elastoplastischer Deformationen unter Berücksichtigung diskreter Rissausbreitung*, J. Löblein, Dissertation, 2004.
- Nr. 2 (2006) *Polyconvex Anisotropic Energies and Modeling of Damage applied to Arterial Walls*, D. Balzani, Dissertation, 2006.
- Nr. 3 (2006) *Kontinuumsmechanische Modellierung ferroelektrischer Materialien im Rahmen der Invariantentheorie*, H. Romanowski, Dissertation, 2006.
- Nr. 4 (2007) *Mehrskalen-Modellierung polykristalliner Ferroelektrika basierend auf diskreten Orientierungsverteilungsfunktionen*, I. Kurzhöfer, Dissertation, 2007.
- Nr. 5 (2007) *Proceedings of the First Seminar on the Mechanics of Multifunctional Materials*, J. Schröder, D.C. Lupascu, D. Balzani (Ed.), Tagungsband, 2007.
- Nr. 6 (2008) *Zur Modellierung und Simulation diskreter Rissausbreitungsvorgänge*, O. Hilgert, Dissertation, 2008.
- Nr. 7 (2009) *Least-Squares Mixed Finite Elements for Solid Mechanics*, A. Schwarz, Dissertation, 2009.
- Nr. 8 (2010) *Design of Polyconvex Energy Functions for All Anisotropy Classes*, V. Ebbing, Dissertation, 2010.
- Nr. 9 (2012) *Modeling of Electro-Mechanically Coupled Materials on Multiple Scales*, M.-A. Keip, Dissertation, 2012.
- Nr. 10 (2012) *Geometrical Modeling and Numerical Simulation of Heterogeneous Materials*, D. Brands, Dissertation, 2012.
- Nr. 11 (2012) *Modeling and simulation of arterial walls with focus on damage and residual stresses*, S. Brinkhues, Dissertation, 2012.
- Nr. 12 (2014) *Proceedings of the Second Seminar on the Mechanics of Multifunctional Materials*, J. Schröder, D.C. Lupascu, M.-A. Keip, D. Brands (Ed.), Tagungsband, 2014.
- Nr. 13 (2016) *Mixed least squares finite element methods based on inverse stress-strain relations in hyperelasticity*, B. Müller, Dissertation, 2016.

- Nr. 14 (2016) *Electromechanical Modeling and Simulation of Thin Cardiac Tissue Constructs*, R. Frotscher, Dissertation, 2016.
- Nr. 15 (2017) *Least-squares mixed finite elements for geometrically nonlinear solid mechanics*, K. Steeger, Dissertation, 2017.
- Nr. 16 (2017) *Scale-Bridging of Elasto-Plastic Microstructures using Statistically Similar Representative Volume Elements*, L. Scheunemann, Dissertation, 2017.
- Nr. 17 (2018) *Modeling of Self-healing Polymers and Polymeric Composite Systems*, S. Specht, Dissertation, 2017.
- Nr. 18 (2018) *Proceedings of the Third Seminar on the Mechanics of Multifunctional Materials*, J. Schröder, D.C. Lupascu, H. Wende, D. Brands (Ed.), Tagungsband, 2018.
- Nr. 19 (2018) *Least-squares finite element methods with applications in fluid and solid mechanics*, C. Nisters, Dissertation, 2018.
- Nr. 20 (2018) *A two-scale homogenization scheme for the prediction of magneto-electric product properties*, M. Labusch, Dissertation, 2018.
- Nr. 21 (2019) *Modeling the passive mechanical response of soft tissues: constitutive modeling approaches, efficient parameter selection and subsequent adjustments due to residual stresses*, M. von Hoegen, Dissertation, 2019